1
Crystal Chemistry of Mullite and Related Phases

1.1
The Mullite-type Family of Crystal Structures

R. X. Fischer and H. Schneider

1.1.1
Introductory Remarks

Mullite in the strict sense, with the composition $3Al_2O_3 \cdot 2SiO_2$, has been the subject of numerous crystal structure and crystal-chemical studies, not only for basic reasons but also because of its outstanding electrical, mechanical and thermal properties, and its wide use in traditional and advanced ceramics.

The fundamental building unit in mullite is the chain of edge-sharing AlO_6-octahedra. The topological arrangement of these chains is a common feature of a whole group of compounds with various chemical compositions. From its most prominent member, this group is designated as the "mullite-type structure family" or just the "mullite-type family". The individual members can have various chemical compositions and different linkages of the chains by cations and cationic groups. They are distinguished by their crystallographic subgroup relationships as described in Section 1.1.2. However, there are some specific requirements that define the mullite-type structural arrangement:

(1) The space group of a mullite-type structure must be a subgroup of the aristotype in space group *P*4/*mbm* (see Section 1.1.2).

(2) The chains[1] of edge-sharing MO_6 octahedra (M = octahedrally coordinated cation, see Tables in Section 1.1.3 for examples of observed cations) must be linear representing single Einer-chains in their highest topological symmetry in space group *P*4/*mbm*.

(3) The axis through the terminating atoms (non-edge-sharing atoms) of the octahedra must point towards the edges (parallel to the chain direction) of adjacent octahedra ($30° \leq \omega \leq 90°$).

---

[1] Note that the overall composition of the chain is MO_4 because of the edge-sharing linkage of the MO_6 octahedra where two neighboring octahedra share two O-atoms.

(4) The chain structure should resemble the orthogonal metric of the aristotype perpendicular to the chain direction as closely as possible ($\gamma' = 90 \pm 5°$).

The third criterion is strictly achieved only in those cases where the octahedral axes in the *ab*-plane are perpendicular to each other (see Fig. 1.1.1a). The typical angle ω between the octahedral axes of neighboring octahedra in the mullites listed in Table 1.1.16 is close to 60°. Essentially all chain structures with angles between the respective octahedral axes from >0° to 90° match criterion (3). At exactly 0° the structure assumes *Cmmm* symmetry which is not a translationengleiche subgroup of *P*4/*mbm* (Note that the hypothetical II.2 structure listed in Fig. 1.1.4 in space group *Cmmm* has a different unit cell setting and consequently does conform to the subgroup relationships). Therefore, we have set an arbitrary limit of 30° intermediate between 0° and 60° representing the limiting angle above which a structure is considered to belong to the mullite-type family. Fig. 1.1.2 shows the frequency of occurrence of the inclination angles ω of neighboring octahedra observed in the crystal structures listed in Section 1.1.3. The angles are grouped in bars rounded in steps of 5°. The highest bar represents the mullites with angles close to 60°. No compounds were found with angles less than 40° except those close to 0° resembling the *Cmmm* type of structures. Therefore, 30° seems to be a suitable value representing the gap between the two structure types. Consequently, structures like, for example, $Na_2Li_3CoO_4$ (Fig. 1.1.1c, Birx and Hoppe 1991), which crystallize in the andalusite-type space group *Pnnm* with chains of edge-sharing NaO_6 octahedra 5.8° inclined to each other, essentially resemble the *Cmmm* symmetry and are therefore not assigned to the mullite-type family. The *Cmmm* type is represented by the cadmium uranate compound $CdUO_4$ (Yamashita et al. 1981) which consists of two subsets of chains of octahedra, the UO_4 chains and the bigger CdO_4 chains perpendicularly oriented to each other as shown in Fig. 1.1.1d. The linkage of the two subsets corresponds to the rutile-type of crystal structures with edge-sharing MO_6 octahedra (TiO_6 in rutile).

Table 1.1.1 Atomic coordinates and site definitions of the chain structure in *P*4/*mbm* ($a = b = 8.0862$ Å, $c = 2.6659$ Å) calculated from distance least square refinement (DLS).

Atom	*x*	*y*	*z*	Site symmetry	Wyckoff position	No. of atoms in unit cell
Al 1	0	0	0	*m.mm*	2(d)	2
O1	0.38348	*x*	$^1/_2$	*m.2m*	4(h)	4
O2	0.16492	*x*	0	*m.2m*	4(g)	4

Nonstandard setting with origin at center (2/*m*) at 2/*m* 1 2/*m*, $^1/_2$ 0 0 from 4/*m* at 4/*m* 1 2_1/*g*.
Symmetry operators:
x, y, z $\quad -y+^1/_2, x+^1/_2, z$ $\quad -x, -y, z$ $\quad y+^1/_2, -x+^1/_2, z$ $\quad -x+^1/_2, y+^1/_2, z$
y, x, z $\quad x+^1/_2, -y+^1/_2, z$ $\quad -y, -x, z$
and equivalent positions related by center of symmetry $\bar{1}$

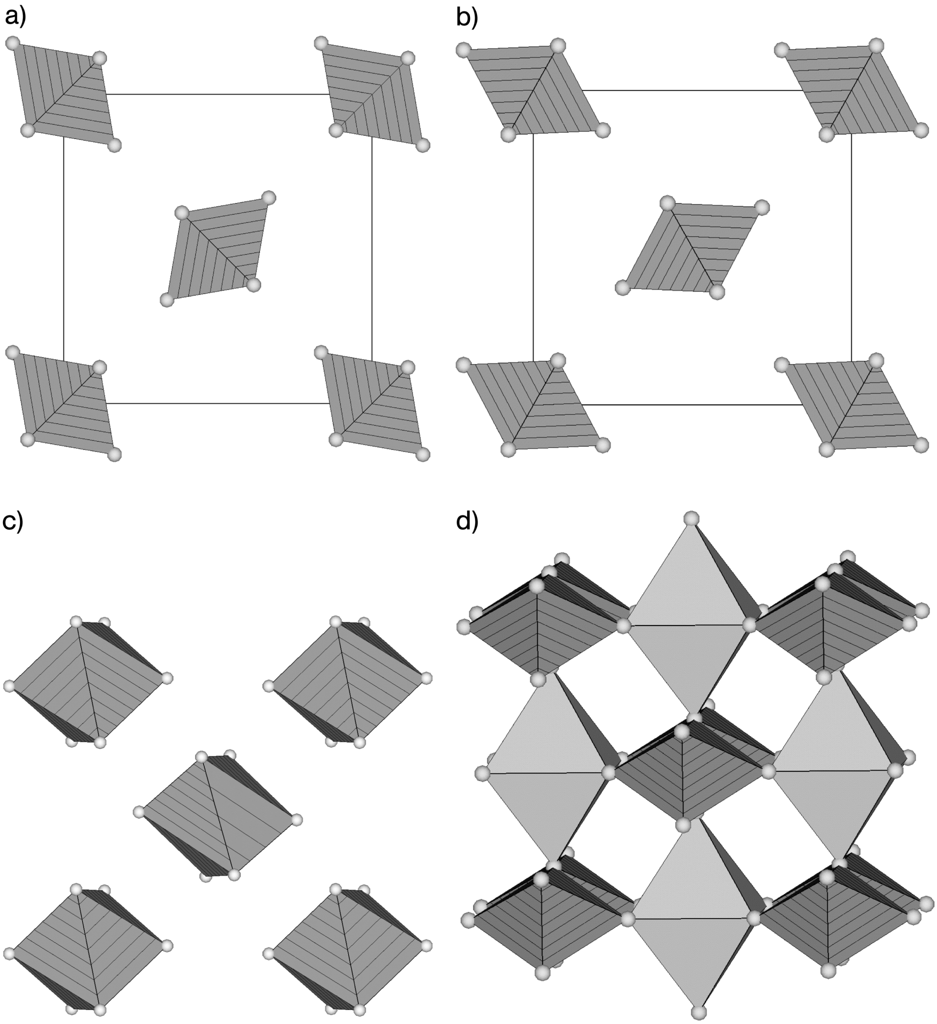

Fig. 1.1.1 Various chain structures with octahedral inclination angles ω between 90° and 0°. (a) The aristotype structure in *P*4/*mbm* (see chapter 1.1.2). ω = 90°. (b) The mullite structure in *Pbam*. (Angel and Prewitt, 1986). ω = 59.6°. (c) The $Na_2Li_3CoO_4$ structure in *Pnnm* (Birx and Hoppe, 1991). ω = 5.8°. (d) The $CdUO_4$ structure in *Cmmm* (Yamashita et al. 1981). ω = 0°. CdO_6 octahedra are light grey, UO_6 octahedra are dark grey and hatched.

The fourth criterion concerning the orthogonal metric is applied, for example, when the lattice symmetry is nonorthogonal. Consequently, werdingite (Section 1.1.3.15) with an angle of γ' = 92.0° between the basis vectors of the unit cell projected onto the plane perpendicular to the chain axes (the cross-section of the unit cell) is assigned to the mullite family whereas the epidote minerals

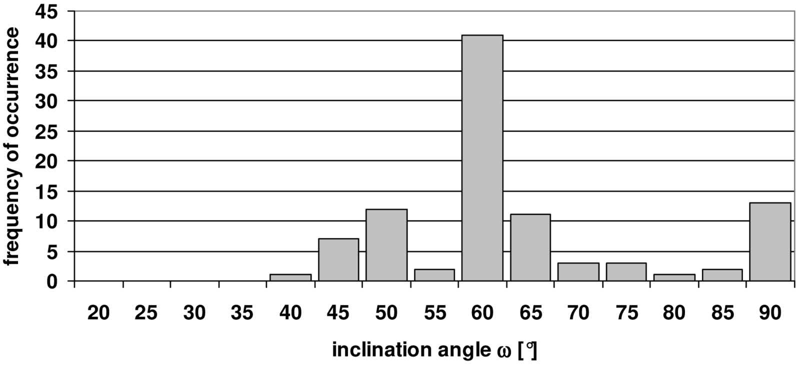

Fig. 1.1.2 Frequency of occurrence of inclination angles ω in mullite-type crystal structures listed in Section 1.1.3.

($Ca_2Al_2Fe(OH)Si_3O_{12}$) are excluded. The monoclinic chain structure of epidote (Kvick et al. 1988) in $P2_1/m$ could be derived from the aristotype as a subgroup of index 2 of *Pbnm* (sillimanite, IV.32) if the epidote unit cell is transformed according to –**a**, **a**+**c**, **b**. Even the angle ω = 41.0° between adjacent octahedra matches criterion 3. However, the angle $\gamma = \gamma' = 116°$ between the **a** and **b** axes of the unit cell after transformation is too far away from 90° and, therefore, epidote is not assigned to this family. Arbitrarily, the angle is assumed here to be within $\gamma' = 90 \pm 5°$ but it could deviate for individual compounds if, for example, their physical properties are mullite-like.

Close structural relationships with mullite have been described frequently in the literature, as, for example, for sillimanite, andalusite, grandidierite, werdingite, the boron and alkali aluminates and gallates, and X-SiAlON. Other phases exhibiting the same topology of the octahedral chain configuration, however, have not yet been assigned to this structure family. Therefore we propose a general definition of the mullite-type structure family. It has the advantage of including the above described phases and to be open for other compounds not yet identified.

It is the aim of this part of the book to define the structural features forming the mullite-type family of crystal structures, to show the group-subgroup relationships between these structures and to describe the individual crystal structures in a general context within this family. In order to achieve an optimal platform for the descriptions of the mullite-type family members, the crystal structures of the individual compounds are derived from the hypothetical tetragonal aristotype structure which represents the highest possible topological symmetry of the octahedral root structure.

1.1.2
The Derivation of Mullite-type Crystal Structures

The most commonly used and generally applicable standardization procedure for inorganic crystal structure data was introduced in 1984 by Parthé and Gelato

(1984) and further developed in the computer program STRUCTURE TIDY (Gelato and Parthé 1987) as a tool for standardizing crystal structures. However, the standardization is applied to unit cell settings and atomic coordinates just within a given space group and does not consider structural relationships between related phases crystallizing in different space groups. Therefore, the comparison and the statistical evaluation of crystal structures within a framework-type family remains difficult even when standardization routines such as STRUCTURE TIDY are applied.

The standardization method used for the mullite-type family classification is that introduced by Baur and Fischer (2000, 2002) and Fischer and Baur (2004) for zeolite-type structures. The approach can easily be applied to the mullite-type crystal structures, since the zeolites are standardized according to their framework structure and the mullite-type compounds are described based on their octahedral chains. The individual symmetry in either case is determined by the additional groups linking the framework atoms or the chains, respectively.

The following rules are applied to the standardization of the mullite-type family adopted from Baur and Fischer (2000) following the concept of Bärnighausen (1980):

(1) The hypothetical structure with the highest possible topological symmetry of the pure chain structure is called the “aristotype” (Fig. 1.1.3).

(2) Crystal structures are assigned to the mullite-type family if their chain structure can be described in a subgroup of the aristotype.

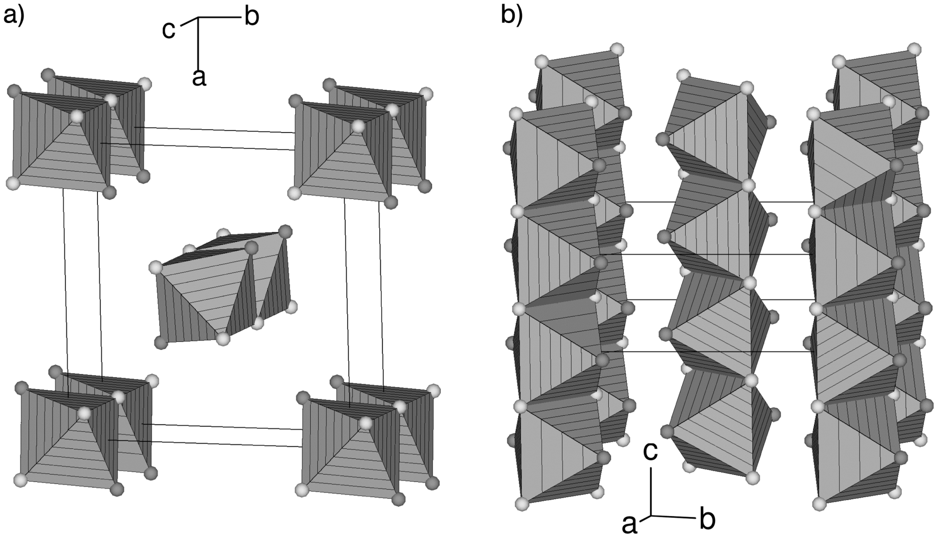

Fig. 1.1.3 The chain structure of mullite in the highest possible topological symmetry *P*4/*mbm*. O1 atoms are light grey, O2 atoms are dark grey. (a) View parallel **c** rotated by 20° about **a** and 20° about **b**. (b) View parallel **a** rotated by 10° about **b** and 5° about **c**. Chains extend in **c**.

Table 1.1.2 Atomic site relationships of the mullite-type crystal structures. Branch 11 in Figure 1.1.4.

MUL-I ***P4/mbm***	**MUL-II.1** **$P4_2/mbc$**	**MUL-VI.11** **$P4_2/mbc$**
M1 [2(d), *m.mm*]	M1 [4(d), 2.22]	M11 [4(d), 2.22]
		M12 [8(f), 2..]
O1 [4(h), *m.2m*]	O1 [8(h), *m*..]	O11 [8(h), *m*..]
		O12 [16(i), 1]
O2 [4(g), *m.2m*]	O2 [8(g), ..2]	O21 [8(g), ..2]
		O22 [16(i), 1]

Table 1.1.3 Atomic site relationships of the mullite-type crystal structures. Branch 12 in Figure 1.1.4.

MUL-I ***P4/mbm***	**MUL-II.1** **$P4_2/mbc$**	**MUL-IV.12** ***Pbam***	**MUL-VIII.12** ***Pbam***
M1 [2(d), *m*.mm]	M1 [4(d), 2.22]	M1 [4(f), ..2]	M11 [4(f), ..2]
			M12 [4(f), ..2]
O1 [4(h), *m.2m*]	O1 [8(h), *m*..]	O11 [4(g), ..*m*]	O11a [4(g), ..*m*]
			O11b [4(h), ..*m*]
		O12 [4(h), ..*m*]	O12 [8(i), 1]
O2 [4(g), *m.2m*]	O2 [8(g), ..2]	O2 [8(i), 1]	O21 [8(i), 1]
			O22 [8(i), 1]

(3) Space group and unit cell setting of the aristotype are chosen to conform to the setting of the mullite type-material which crystallizes in *Pbam*.
(4) The O-atoms in the aristotype are sorted according to the descending order of their Wyckoff-site symbols.
(5) Atom positions listed in the subgroups follow strictly the sequence assigned in the corresponding aristotype, independently of their Wyckoff notation.
(6) The names of atoms in the subgroups carry the root name of the corresponding name in the aristotype appended by numbers and characters. That way, for example, an oxygen position designated O1 in the aristotype setting might be split into an O11 and an O12 site in the subgroup, perhaps further transformed to O11a, O11b, O12a, and O12b in another subgroup of lower index.

This standardization procedure is applied to all derivations listed in Fig. 1.1.4 and Tables 1.1.2 to 1.1.10 as a tool for an easy comparison of the structures in different space groups and different unit cell settings. However, it should be admitted that the systematic classification is not as rigorous as in the case of zeolites, where the

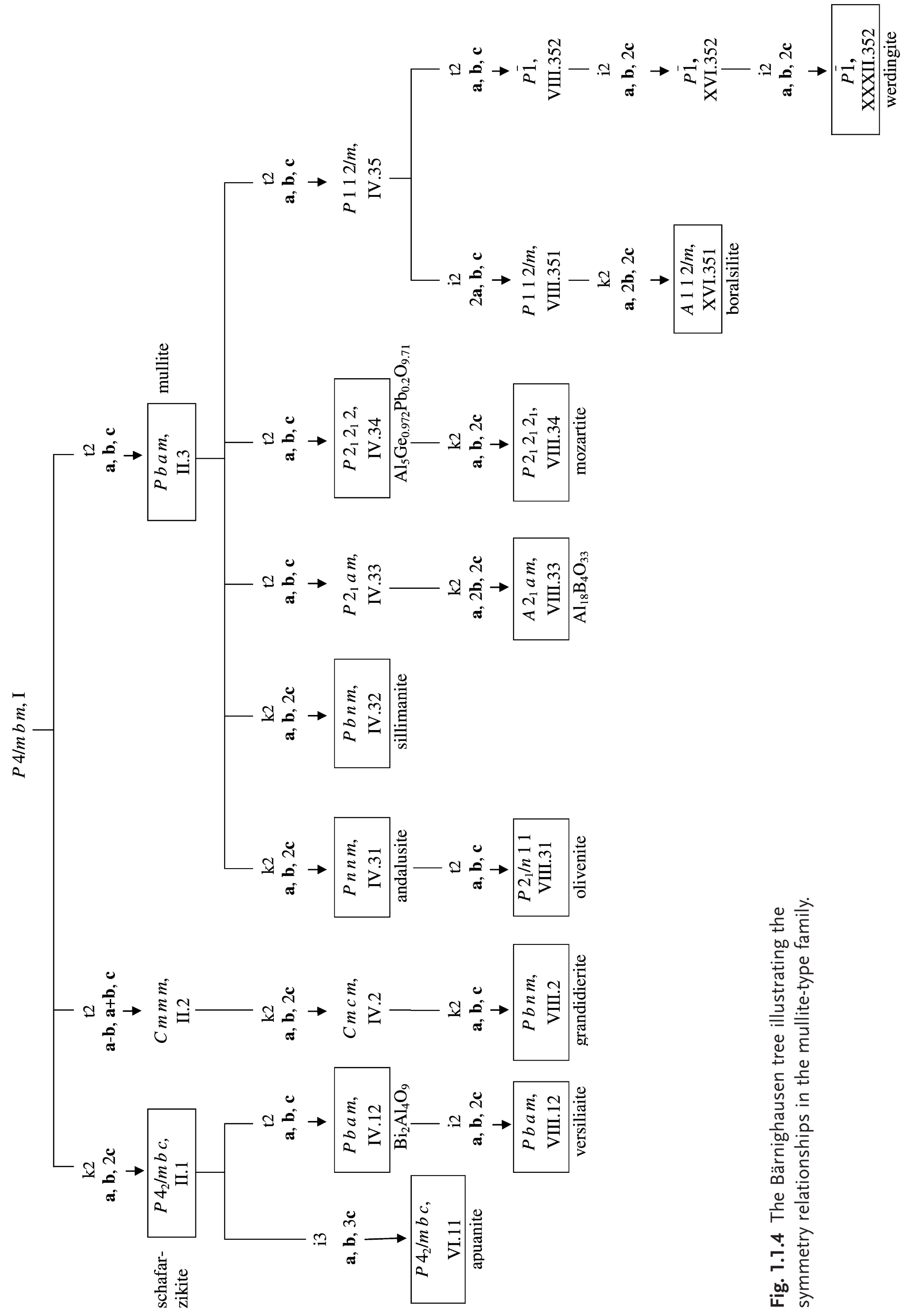

Fig. 1.1.4 The Bärnighausen tree illustrating the symmetry relationships in the mullite-type family.

Table 1.1.4 Atomic site relationships of the mullite-type crystal structures. Branch 2 in Figure 1.1.4.

MUL-I	**MUL-II.2**	**MUL-IV.2**	**MUL-VIII.2**
P4/mbm	***Cmmm***	***Cmcm***	***Pbnm***
M1 [2(d), *m.mm*]	M11 [2(a), *mmm*]	M11 [4(a), 2/*m*..]	M11 [4(a), $\bar{1}$]
	M12 [2(b), *mmm*]	M12 [4(b), 2/*m*..]	M12 [4(b), $\bar{1}$]
O1 [4(h), *m*.2*m*]	O11 [4(h), 2*mm*]	O11 [8(g), ..*m*]	O11a [4(c), ..*m*]
			O11b [4(c), ..*m*]
	O12 [4(j), *m*2*m*]	O12a [4(c), *m*2*m*]	O12a [4(c), ..*m*]
		O12b [4(c), *m*2*m*]	O12b [4(c), ..*m*]
O2 [4(g), *m*.2*m*]	O21 [4(g), 2*mm*]	O21 [8(e), 2..]	O21 [8(d), 1]
	O22 [4(i), *m*2*m*]	O22 [8(f), *m*..]	O22 [8(d), 1]

Table 1.1.5 Atomic site relationships of the mullite-type crystal structures. Branch 31 in Figure 1.1.4.

MUL-I	**MUL-II.3**	**MUL-IV.31**	**MUL-VIII.31**
***P*4/mbm**	***Pbam***	***Pnnm***	$P2_1/n11$
M1 [2(d), *m.mm*]	M1 [2(a), ..2/*m*]	M1 [4(e), ..2]	M1 [4(e), 1]
O1 [4(h), *m*.2*m*]	O1 [4(h), ..*m*]	O11 [4(g), ..*m*]	O11 [4(e), 1]
		O12 [4(g), ..*m*]	O12 [4(e), 1]
O2 [4(g), *m*.2*m*]	O2 [4(g), ..*m*]	O2 [8(h), 1]	O21 [4(e), 1]
			O22 [4(e), 1]

Table 1.1.6 Atomic site relationships of the mullite-type crystal structures. Branch 32 in Figure 1.1.4.

MUL-I	**MUL-II.3**	**MUL-IV.32**
P4/mbm	***Pbam***	***Pbnm***
M1 [2(d), *m.mm*]	M1 [2(a), ..2/*m*]	M1 [4(a), $\bar{1}$]
O1 [4(h), *m*.2*m*]	O1 [4(h), ..*m*]	O11 [4(c), ..*m*]
		O12 [4(c), ..*m*]
O2 [4(g), *m*.2*m*]	O2 [4(g), ..*m*]	O2 [8(d), 1]

family members in one group exhibit exactly the same topology and are commonly described in the same fashion. Here we are dealing with individual compounds of different chemical compositions, some of which have significantly different properties. Therefore, we are not aiming for a complete standardization of the mullite-type compounds and we are describing the individual type-materials in Section

Table 1.1.7 Atomic site relationships of the mullite-type crystal structures. Branch 33 in Figure 1.1.4.

MUL-I ***P4/mbm***	**MUL-II.3** ***Pbam***	**MUL-IV.33** $P2_1am$	**MUL-VIII.33** $A2_1am$
M1 [2(d), *m.mm*]	M1 [2(a), ..2/*m*]	M1 [2(a), ..*m*]	M1 [8(b), 1]
O1 [4(h), *m.2m*]	O1 [4(h), ..*m*]	O11 [2(b), ..*m*]	O11a [4(a), ..*m*]
			O11b [4(a), ..*m*]
		O12 [2(b), ..*m*]	O12a [4(a), ..*m*]
			O12b [4(a), ..*m*]
O2 [4(g), *m.2m*]	O2 [4(g), ..*m*]	O21 [2(a), ..*m*]	O21 [8(b), 1]
		O22 [2(a), ..*m*]	O22 [8(b), 1]

Table 1.1.8 Atomic site relationships of the mullite-type crystal structures. Branch 34 in Figure 1.1.4.

MUL-I ***P4/mbm***	**MUL-II.3** ***Pbam***	**MUL-IV.34** $P2_12_12$	**MUL-VIII.34** $P2_12_12_1$
M1 [2(d), *m.mm*]	M1 [2(a), ..2/*m*]	M1 [2(a), ..2]	M1 [4(a), 1]
O1 [4(h), *m.2m*]	O1 [4(h), ..*m*]	O1 [4(c), 1]	O11 [4(a), 1]
			O12 [4(a), 1]
O2 [4(g), *m.2m*]	O2 [4(g), ..*m*]	O2 [4(c), 1]	O21 [4(a), 1]
			O22 [4(a), 1]

1.1.3 usually in their original settings (see also discussion in last paragraph of Section 1.1.3.10 for the sillimanite group compounds).

The symmetry derivations with complete group-subgroup relationships are illustrated in Fig. 1.1.4 by Bärnighausen trees (Bärnighausen, 1980). This is a generally accepted and widely used concept to represent structural relationships (see, for example, the symmetry relationships between various ABW type structures (Kahlenberg et al. 2001), the complex relationships among the derivative structures of perovskite (Bock and Müller, 2002) or the rutile-type structures (Baur, 1994)). All space groups are given as maximal subgroups derived from the space group representing the highest possible topological symmetry (i. e. *P*4/*mbm*, Fig. 1.1.4, Table 1.1.1). Branches contain information on the type of the subgroup relationship (isomorphic (i), translationengleich (t), or klassengleich (k)) with the respective subgroup index representing the factor of the symmetry reduction or the number of cosets derived from the supergroup.

The hierarchical order of the space groups is represented by roman numerals assigned to the space group symbols. The aristotype has the number I, while the subgroups have numerals corresponding to their index of symmetry reduction

Table 1.1.9 Atomic site relationships of the mullite-type crystal structures. Branch 351 in Figure 1.1.4.

MUL-I ***P*4/*mbm***	**MUL-II.3** ***Pbam***	**MUL-IV.35** ***P*112/*m***	**MUL-VIII.351** ***P*112/*m***	**MUL-XVI.351** ***A*112/*m***
M1 [2(d), *m.mm*]	M1 [2(a), .. 2/*m*]	M11 [1(a), 2/*m*]	M11a [1(a), 2/*m*]	M11a [4(e), $\bar{1}$]
			M11b [1(c), 2/*m*]	M11b [4(f), $\bar{1}$]
		M12 [1(g), 2/*m*]	M12 [2(m), *m*]	M12 [8(j), 1]
O1 [4(h), *m*.2*m*]	O1 [4(h), .. *m*]	O11 [2(n), *m*]	O11a [2(n), *m*]	O11a1 [4(i), *m*]
				O11a2 [4(i), *m*]
			O11b [2(n), *m*]	O11b1 [4(i), *m*]
				O11b2 [4(i), *m*]
		O12 [2(n), *m*]	O12a [2(n), *m*]	O12a1 [4(i), *m*]
				O12a2 [4(i), *m*]
			O12b [2(n), *m*]	O12b1 [4(i), *m*]
				O12b2 [4(i), *m*]
O2 [4(g), *m*.2*m*]	O2 [4(g), .. *m*]	O21 [2(m), *m*]	O21a [2(m), *m*]	O21a [8(j), 1]
			O21b [2(m), *m*]	O21b [8(j), 1]
		O22 [2(m), *m*]	O22a [2(m), *m*]	O22a [8(j), 1]
			O22b [2(m), *m*]	O22b [8(j), 1]

Table 1.1.10 Atomic site relationships of the mullite-type crystal structures. Branch 352 in Figure 1.1.4.

MUL-II.3 ***Pbam***	**MUL-IV.35** ***P112/m***	**MUL-VIII.352** **$P\bar{1}$**	**MUL-XVI.352** **$P\bar{1}$**	**MUL-XXXII.352** **$P\bar{1}$**
M1 [2(a), ..2/*m*]	M11 [1(a), 2/*m*]	M11 [1(a), $\bar{1}$]	M11a [1(a), $\bar{1}$]	M11a1 [1(a), $\bar{1}$]
				M11a2 [1(b), $\bar{1}$]
			M11b [1(b), $\bar{1}$]	M11b [2(i), 1]
	M12[1(g), 2/*m*]	M12 [1(e), $\bar{1}$]	M12a[1(e), $\bar{1}$]	M12a1 [1(e), $\bar{1}$]
				M12a2 [1(h), $\bar{1}$]
			M12b [1(h), $\bar{1}$]	M12b [2(i), 1]
O1 [4(h), ..*m*]	O11 [2(n), *m*]	O11 [2(i), 1]	O11a [2(i), 1]	O11a1 [2(i), 1]
				O11a2 [2(i), 1]
			O11b [2(i), 1]	O11b1 [2(i), 1]
				O11b2 [2(i), 1]
	O12 2(n), *m*]	O12 [2(i), 1]	O12a [2(i), 1]	O12a1 [2(i), 1]
				O12a2 [2(i), 1]
			O12b [2(i), 1]	O12b1 [2(i), 1]
				O12b2 [2(i), 1]
O2 [4(g), ..*m*]	O21 [2(m), *m*]	O21 [2(i), 1]	O21a [2(i), 1]	O21a1 [2(i), 1]
				O21a2 [2(i), 1]
			O21b [2(i), 1]	O21b1 [2(i), 1]
				O21b2 [2(i), 1]
	O22 [2(m), *m*]	O22 [2(i), 1]	O22a [2(i), 1]	O22a1 [2(i), 1]
				O22a2 [2(i), 1]
			O22b [2(i), 1]	O22b1 [2(i), 1]
				O22b2 [2(i), 1]

relative to the aristotype. Entries with the same index are drawn on the same height, thus representing members of the same hierarchical order. Members on one level occurring in different branches are distinguished by arabic numerals. Furthermore, the set of basis vectors is given which describes the transformation of a unit cell to its setting in the subgroup. Space groups representing observed crystal structures are put in frames. Space groups presented without frames are needed to indicate intermediate steps in describing symmetry transformations. The atomic site relationships are tabulated based on the derivations in the Bärnighausen tree. Arrows indicate the splitting of atom sites upon symmetry reduction. Wyckoff positions and site symmetries are given in square brackets according to the notation in the International Tables for Crystallography (Hahn, 2002). Atom names are derived from the corresponding names in the aristotype, keeping the numeral assigned to the atom in its highest symmetry and adding a second numeral expressing the second level derivation. If an atom site is affected by the symmetry reduction, it keeps the name of its supergroup root name. Upon further reduction of symmetry, lower case letters are added to the atom names. If further subdivisions are needed, numerals and lower case letters follow each other consecutively.

The highest possible topological symmetry for the pure chain structure of edge-sharing MO_6 octahedra of mullite-type compounds can be described in the tetragonal space group $P4/mbm$. Atomic parameters are calculated by distance least squares (DLS) methods using the program DLS76 (Baerlocher et al. 1976). Distances are prescribed by Al–O = 1.885 Å corresponding to the sum of the ionic radii of Al and O (Shannon, 1976), and O–O = 2.666 Å calculated from the octahedral geometry. The distance between O atoms of neighboring octahedra (the distance between O1 and O2 atoms with the coordinates given in Table 1.1.1) is arbitrarily set to 2.833 Å corresponding to the O–O distance in an AlO_4 tetrahedron assumed to bridge adjacent octahedra. Lattice constants refined to $a = b =$ 8.0862 Å and $c = 2.6659$ Å and final atomic parameters are listed in Table 1.1.1. The distance least squares residual is $R = 0.0003$ expressing the ideal geometry of this refined chain structure shown in Fig. 1.1.3.

1.1.3
Members of the Mullite-type Family of Crystal Structures

1.1.3.1 Introduction

In the following chapters compounds are described which are proven by crystal-structure refinements to belong to the mullite-type family. Individual members are sorted into groups of the same subgroup symmetry. The groups are named after their most prominent member. However, neither the number of groups nor the number of entries within these groups is aiming at completeness. Unit cell settings and cell parameters are standardized to the most abundant compound within this group preferably matching the setting of the aristotype as closely as possible. However, many of the type-materials are established in the literature with their own history and their own individual unit cell settings independent of the mullite-type standardization. Therefore, we describe the type-materials in their original setting in the text and the figures. Chemical compositions are given in two notations. In the first column of the tables, the chemical composition is listed as given in the original literature. In the second column, the chemical composition is given as the unit cell contents with the octahedrally coordinated M cation listed as the first element. The atomic positions of oxygen atoms are according to strict geometrical rule. Their designations (e.g. 01, 02 ...) allow easy description of subgroups (e.g. 01 → 011, 012 ..., 02 → 021, 022 ...). However, an other setting (e.g. 0(A,B), 0(D) ...) has also frequently been in literature. Both settings correlate in the way given in Table 1.1.17.

Crystal structure drawings are performed with the program STRUPLO (Fischer and Messner, 2004) as part of the BRASS program package (Birkenstock et al. 2004). MO_6 coordinations forming the MO_4 chains are drawn in polyhedral representation with the O ligands marked as small circles. Extra chain cations are drawn as spheres with a radius of about half their ionic radius (Shannon, 1976).

1.1.3.2 MUL-II.1, $P4_2/mbc$: Schafarzikite Group

This group consists of the crystals of the highest symmetry (except for orthorhombic mullite, which has the same index of symmetry reduction) observed so far in the mullite-type family of crystal structures, crystallizing in a tetragonal space group. Schafarzikite ($FeSb_2O_4$) is a prominent member of this group. The FeO_4 chains of edge-sharing FeO_6 octahedra are the mullite-type backbones of this structure. A characteristic feature of these compounds is the presence of ions with lone-

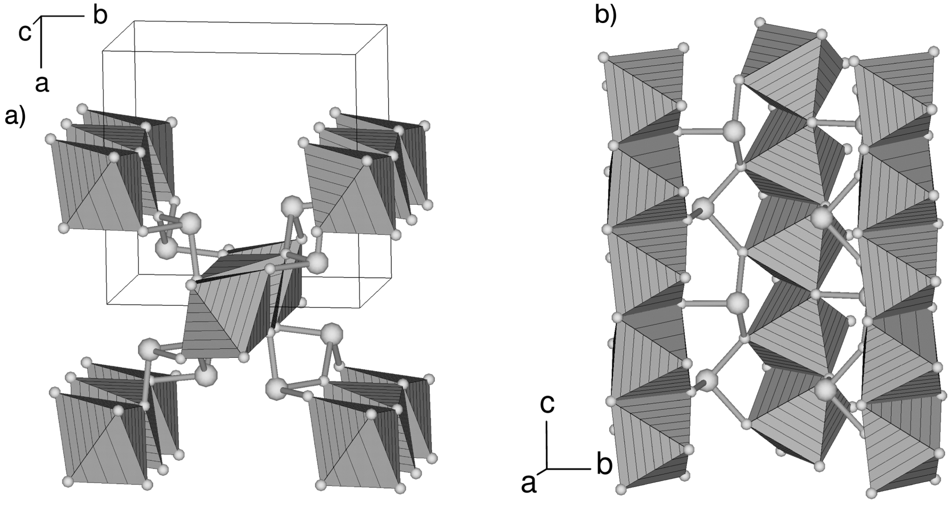

Fig. 1.1.5 Projections of the crystal structure of schafarzikite (Fischer and Pertlik, 1975). Sb atoms are shown as spheres bonded to three O atoms of the AlO_6 octahedra. (a) View parallel **c** rotated by 10° about **a** and **b**. (b) View parallel **a** rotated by 12° about **b** and 10° about **c**.

Table 1.1.11 MUL-II.1 compounds: Schafarzikite group.

Chemical composition	Unit cell contents	Mineral name	*a* [Å]	*c* [Å]	*V* [Å³]	ω [°]	Reference
$MnSb_2O_4$	$Mn_4Sb_8O_{16}$		8.7145(2)	6.0011(2)	455.74	90	Chater and Gavarri (1985)
$FeSb_2O_4$	$Fe_4Sb_8O_{16}$	Schafarzikite	8.590(5)	5.913(5)	436.31	90	Fischer and Pertlik (1975)
		synthetic	8.6181(2)	5.9225(2)	439.87	90	Chater et al. (1985)
$NiSb_2O_4$	$Ni_4Sb_8O_{16}$		8.3719(3)	5.9079(3)	414.08	90	Gavarri (1981)
$CuAs_2O_4$	$Cu_4As_8O_{16}$	Trippkeite	8.592(4)	5.573(4)	411.41	90	Pertlik (1975)
$ZnSb_2O_4$	$Zn_4Sb_8O_{16}$		8.527(2)	5.942(2)	432.04	90	Puebla et al. (1982)
Pb_3O_4	$Pb_4Pb_8O_{16}$		8.811(5)	6.563(3)	509.51	90	Gavarri and Weigel (1975)

pair electrons. These cations form three short bonds to neighboring oxygen atoms completed by the lone-pair electrons to an approximately tetrahedral coordination. In Fig. 1.1.5 the chains of corner-sharing SbO_3 groups are shown crosslinking the octahedral pillars. Other compounds of this group with NiO_4, CuO_4, PbO_4, ZnO_4 and MnO_4 chains are given in Table 1.1.11. There, the chains are crosslinked by SbO_3, AsO_3, and PbO_4 groups with cations above the center of the planes formed by the O atoms.

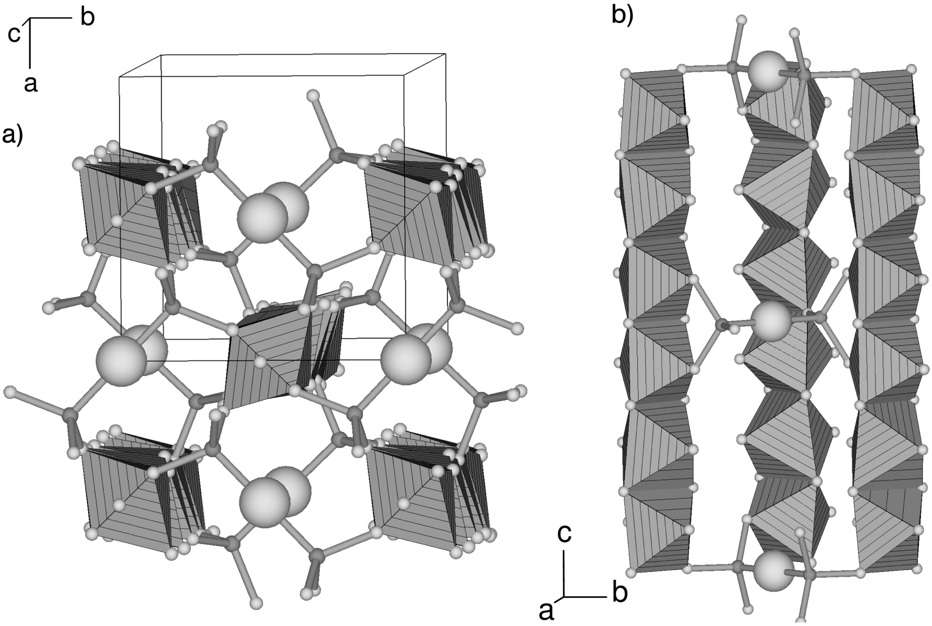

Fig. 1.1.6 Projections of the crystal structure of apuanite with a subset of Fe cations and S anions (Mellini and Merlino, 1979). Big spheres are S atoms, small spheres are Fe atoms. (a) View parallel **c** rotated by 2° about **b** and 4° about **a**. (b) View parallel **a** rotated by 5° about **b** and 8° about **c**.

1.1.3.3 **MUL-VI.11, $P4_2/mbc$: Apuanite Group**

Apuanite can be regarded as a derivative structure of schafarzikite (MUL-II.1) by substituting one-quarter of the antimony (Sb) atoms by iron (Fe) and adding sulphide ions bridging adjacent iron cations. The insertion of sulfur atoms yields four-coordinated iron, while the remaining antimony atoms remain bonded to three oxygen atoms of the octahedral chain. Owing to the ordered distribution of iron and sulfur, lattice constant *c* is tripled relative to the schafarzikite cell (Figs. 1.1.6 and 1.1.7, Table 1.1.12). Apuanite is found as massive black aggregates in veinlets at the contact between dolomite and phyllite as a product of a metasomatic process (Mellini and Merlino, 1979).

Table 1.1.12 MUL-VI.11 compound: Apuanite group.

Chemical composition	**Unit cell contents**	**Mineral name**	***a* [Å]**	***c* [Å]**	***V* [Å³]**	**ω [°]**	**Reference**
$Fe_5Sb_4O_{12}S$	$(Fe_{4.15}Zn_{0.32}Fe_{7.40})$ $(Fe_{6.87}Sb_{15.64}As_{1.49})$ $O_{48}S_{3.57}$	Apuanite	8.372(5)	17.974(10)	1259.80	90	Mellini and Merlino (1979)

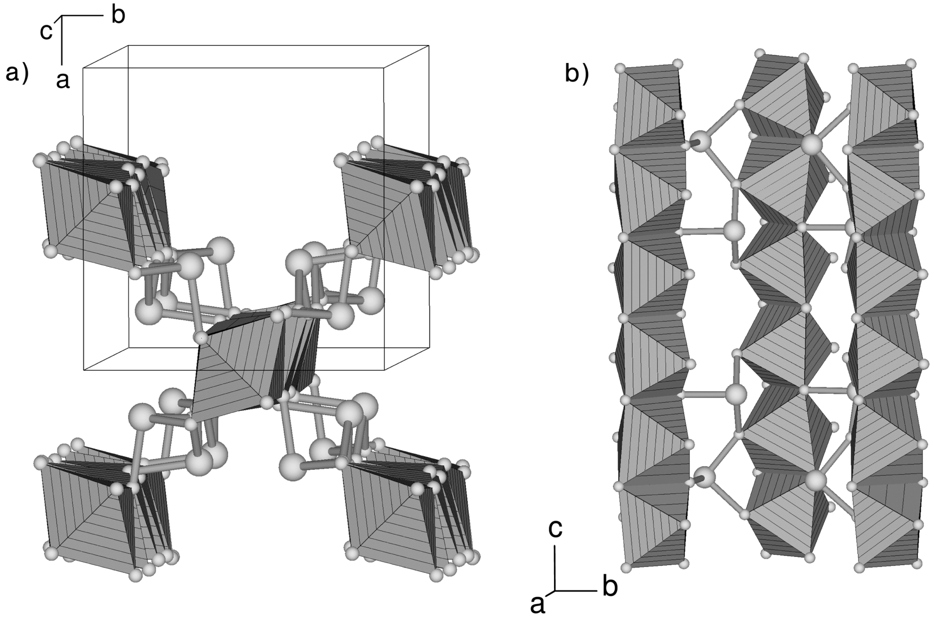

Fig. 1.1.7 Projections of the crystal structure of apuanite with a subset of Sb cations shown as medium sized spheres (Mellini and Merlino, 1979). (a) View parallel **c** rotated by 2° about **b** and 4° about **a**. (b) View parallel **a** rotated by 5° about **b** and 8° about **c**.

1.1.3.4 MUL-IV.12, *Pbam*: $Bi_2M_4O_9$ Group

In $Bi_2M_4O_9$ (M = Al^{3+}, Ga^{3+}, Fe^{3+}) and $Bi_2Mn_4O_{10}$ the mullite-type columns of edge-shared MO_6 octahedra are linked by dimers of MO_4 tetrahedra ($Bi_2M_4O_9$) or MO_5 square-pyramidal polyhedra ($Bi_2Mn_4O_{10}$), respectively. Perpendicular to the octahedral chain axes the polyhedra form five-membered rings of three tetrahedra or pyramids and two octahedra. The Bi^{3+} atoms are located in the structural channels running parallel to the octahedral chains (Fig. 1.1.8). $Bi_2Al_4O_9$, $Bi_2Ga_4O_9$ and $Bi_2Fe_4O_9$ show complete solid solution (Niizeki and Wachi, 1968).

On the basis of infrared studies, Voll et al. (2005) provide some interesting ideas on the distribution of the tetrahedrally bound Al^{3+} and Fe^{3+} cations in $Bi_2(Al,Fe)_4O_9$ mixed crystals. This has been derived from the portion of the infrared spectrum which is exclusively associated with stretching vibrations of tetrahedrally coordinated Al^{3+} (near 915 cm^{-1}) and Fe^{3+} (near 810 cm^{-1}). However, while the end members of the solid solution $Bi_2Al_4O_9$ and $Bi_2Fe_4O_9$ display single and sharp signals at the expected wave numbers, the mixed crystals with $Bi_2(Al_2Fe_2)O_9$ composition show an infrared band being splitted into three components, centering near to those of the aluminum and iron end members and to an average position near 860 cm^{-1} (Fig. 1.1.9). The sub-bands occurring in the $Bi_2(Al_2Fe_2)O_9$ phase near to the band positions of the end members $Bi_2Al_4O_9$ and $Bi_2Fe_4O_9$ are ascribed to tetrahedral Al-Al and Fe-Fe clusters whereas the infrared peak in between those of the end members is ascribed to the contacts between tetrahedral Al-Al and Fe-Fe clusters.

The crystal structure of $Bi_2Mn_4O_{10}$ deviates slightly from that of $Bi_2M_4O_9$ because manganese occurs in two oxidation states (Mn^{3+} and Mn^{4+}, Nguyen et al.

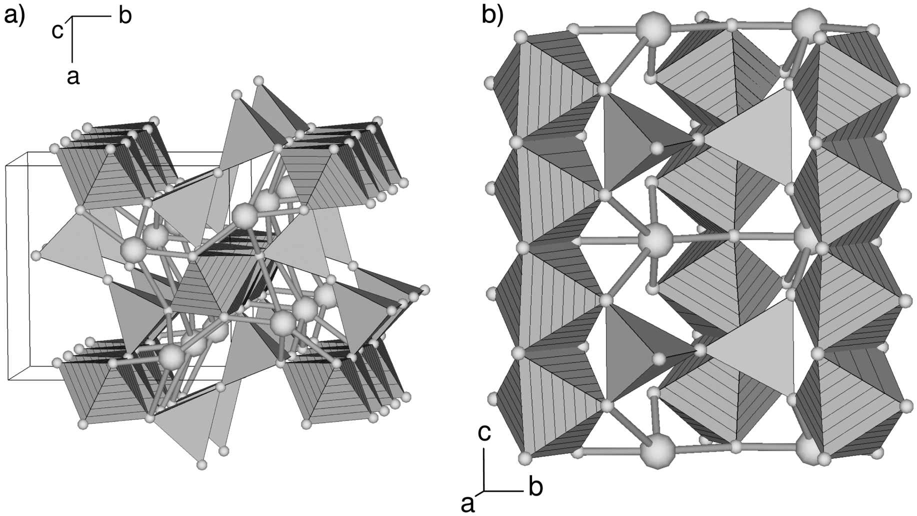

Fig. 1.1.8 Projections of the crystal structure of $Bi_2Al_4O_9$ (Abrahams et al. 1999). (a) View parallel **c** rotated by 5° about **b** and 8° about **a**. (b) View parallel **a** rotated by 5° about **b** and 8° about **c**.

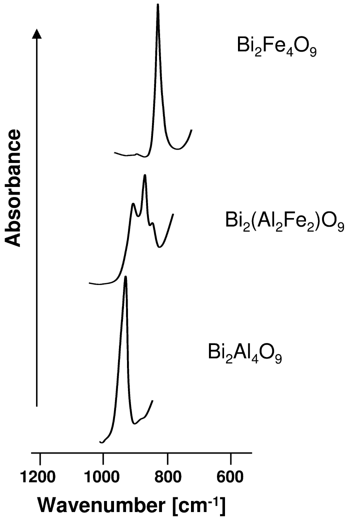

Fig. 1.1.9 Infrared absorption spectra of $Bi_2M_4O_9$ phases (M = Al^{3+}, Fe^{3+}), showing the region of stretching vibrations of TO_4 tetrahedra. Note the splitting of the signal of the $Bi_2(Al_2Fe_2)O_9$ compound, which is associated with the occurrence of tetrahedrally coordinated aluminum and iron clusters (after Voll et al. 2005).

1999). The end members of phases form mixed crystals (e.g. Giaquinta et al. 1995), or can be doped by other cations (e.g. Sr^{2+}, Ti^{4+}, Zha et al. 2003).

$Bi_2M_4O_9$ phases exhibit good oxygen conductivity. This can be explained structurally by the sequence of tetrahedral dimers and of large voids in the octahedral chain direction. A schematic view of the one-dimensional oxygen conductivity of $Bi_2M_4O_9$ after Abrahams et al. (1999) is given in Fig. 1.1.10. It involves hopping of oxygen atoms bridging MO_4 dimers (O_{bri} = bridging oxygen atom) to a vacancy in between two adjacent dimers. In a second step these dislocated O_{bri} atoms migrate to an available regular O_{bri} site. No Bi^{3+} conductivity has been taken into account, possibly due to the asymmetric polarization of the Bi^{3+} electronic shell (see Abrahams et al. 1999). According to Zha et al. (2003), the electrical conductivity achieves a maximum if 20% of Bi^{3+} is replaced by Sr^{2+}. $Bi_2M_4O_9$ ceramic conductors are suitable materials for membranes, electrodes and sensors. Of special interest is its potential use for electrodes in solid oxide fuel cells (SOFCs) for intermediate temperature operation.

The oxygen conduction mechanism in $Bi_2M_4O_9$ is also interesting with respect to a potential high-temperature oxygen conductivity, especially in Al_2O_3-rich aluminum-silicon mullite, with its high number of oxygen vacancies. Al_2O_3-rich aluminum-silicon mullites display a sequence of tetrahedral dimers and of oxygen vacancies in the octahedral chain direction quite similar to that in $Bi_2M_4O_9$. Although this sequence is disordered and incomplete in the former case, but ordered and complete in the latter, it may indicate similar oxygen conduction mechanisms in $Bi_2M_4O_9$ and mullite in the strict sense.

Besides the above described compounds, a number of phases with PbO_6 and especially MnO_6 octahedra, connected by SnO_4 or various rare earth oxygen polyhedra, has been mentioned in the literature. Prominent representatives are summarized in Table 1.1.13.

Table 1.1.13 MUL-IV.12 compounds: $Bi_2M_4O_9$ group.

Chemical composition	Unit cell contents	*a* [Å]	*b* [Å]	*c* [Å]	*V* [Å^3]	ω [°]	Reference
$Bi_2Al_4O_9$	$Al_4Al_4Bi_4O_{18}$	7.7134(1)	8.1139(2)	5.6914(1)	356.20	61.1	Abrahams et al. (1999)
$Bi_2Fe_2Al_2O_9$	$(Al_2Fe_2)Bi_4Fe_2Al_2O_{18}$	7.8611(3)	8.2753(3)	5.8535(3)	380.80	59.7	Giaquinta et al. (1995)
$Bi_2Ga_4O_9$	$Ga_4Ga_4Bi_4O_{18}$	7.934	8.301	5.903	388.77	61.7	Müller-Buschbaum and Chales de Beaulieu (1978)
$BiMn_2O_5$	$Mn_4Mn_4Bi_4O_{20}$	7.540(5)	8.534(5)	5.766(5)	371.02	59.6	Niizeki and Wachi (1968)
$LaMn_2O_5$	$Mn_4Mn_4La_4O_{20}$	7.6891(7)	8.7142(7)	5.7274(5)	383.76	43.8	Alonso et al. (1997a)
$PrMn_2O_5$	$Mn_4Mn_4Bi_4O_{20}$	7.5583(9)	8.6481(9)	5.7119(6)	373.36	42.3	Alonso et al. (1997a)
$NdMn_2O_5$	$Mn_4Mn_4Nd_4O_{20}$	7.5116(8)	8.6270(8)	5.7060(5)	369.76	46.7	Alonso et al. (1997a)
$SmMn_2O_5$	$Mn_4Mn_4Sm_4O_{20}$	7.4332(7)	8.5872(7)	5.6956(5)	363.55	44.3	Alonso et al. (1997a)
$EuMn_2O_5$	$Mn_4Mn_4Eu_4O_{20}$	7.3986(8)	8.5666(9)	5.6925(6)	360.80	47.3	Alonso et al. (1997a)
$TbMn_2O_5$	$Mn_4Mn_4Tb_4O_{20}$	7.3251(2)	8.5168(2)	5.6750(2)	354.04	46.5	Alonso et al. (1997b)
$HoMn_2O_5$	$Mn_4Mn_4Ho_4O_{20}$	7.2643(3)	8.4768(3)	5.6700(2)	349.15	47.2	Alonso et al. (1997b)
$ErMn_2O_5$	$Mn_4Mn_4Er_4O_{20}$	7.2360(2)	8.4583(2)	5.6655(1)	346.75	47.5	Alonso et al. (1997b)
$Bi_2Fe_4O_9$	$Fe_4Fe_4Bi_4O_{18}$	7.950(5)	8.428(5)	6.005(5)	402.35	62.4	Niizeki and Wachi (1968)
$Bi_2Fe_2Ga_2O_9$	$(Fe_{2.4}Ga_{1.6})Bi_4Fe_{1.6}Ga_{2.4}O_{18}$	7.946(1)	8.335(1)	5.929(1)	393.62	64.0	Giaquinta et al. (1992)
$SnPb_2O_4$	$Sn_4Pb_8O_{16}$	8.7215(3)	8.7090(3)	6.2919(3)	477.90	84.9	Gavarri et al. (1981)
Pb_3O_4	$Pb_4Pb_8O_{16}$	8.8189(3)	8.8068(2)	6.5636(1)	509.77	89.3	Gavarri et al. (1978)

1.1.3.5 MUL-VIII.12, *Pbam*: Versiliaite Group

Versiliaite is orthorhombic with space group *Pbam* (see Table 1.1.14). With respect to its physical, chemical and crystallographical properties the phase is closely related to schafarzikite (MUL-II.1) and apuanite (MUL-VI.11). Octahedral chains are connected by $Fe^{3+}O_4$ tetrahedral chains, in which, however, every forth Fe^{3+} ion is replaced by Sb^{3+}. Adjacent tetrahedral chains are in turn linked by $Fe_2^{3+}O_7$ groups, with S^{2-} ions bridging both tetrahedra. Charge balance is achieved by partial Fe^{3+} for Fe^{2+} substitution at octahedral sites (Fig. 1.1.11). Versiliaite belongs to the same metasomatic paragenesis as apuanite and occurs, for example, at the contact between dolomite and phyllite (see Mellini and Merlino, 1979).

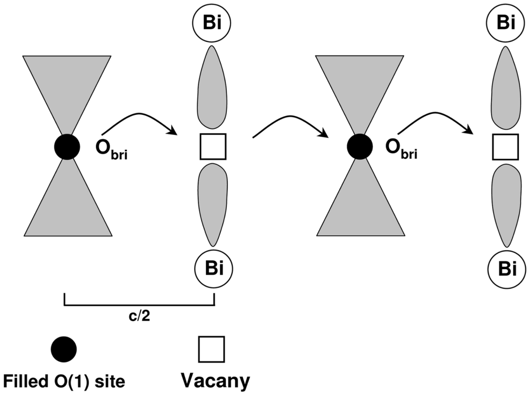

Fig. 1.1.10 Schematic view of the conduction mechanism of bridging oxygen atoms (O_{bri}) of the $Bi_2M_4O_9$ phases. Filled triangles represent oxygen tetrahedra and pestles signify electron orbitals of bismuth (after Abrahams et al. 1999).

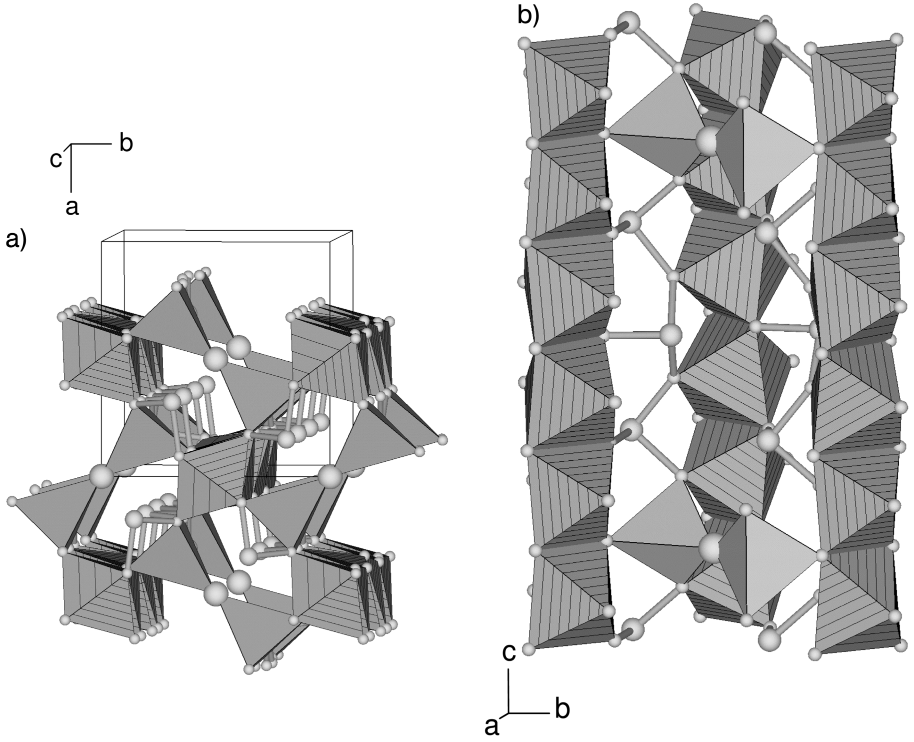

Fig. 1.1.11 Projections of the crystal structure of versiliaite (Mellini and Merlino, 1979). (a) View parallel **c** rotated by 2° about **b** and 4° about **a**. (b) View parallel **a** rotated by 10° about **b** and 8° about **c**.

Table 1.1.14 MUL-VIII.12 compound: Versiliaite group.

Chemical composition	**Unit cell contents**	**Mineral name**	***a* [Å]**	***b* [Å]**	***c* [Å]**	***V* [Å^3]**	**ω [°]**	**Reference**
$Fe_6Sb_6SO_{16}$	$(Fe_7Zn)Fe_3$ $Sb_{12}AsS_2O_{32}$	Versiliaite	8.492(5)	8.326(5)	11.938(7)	844.07	89.5 79.4	Mellini and Merlino (1979)

1.1.3.6 **MUL-VIII.2, *Pbnm*: Grandidierite Group**

Grandidierite occurs in nature as large elongated bluish-green crystals. It has orthorhombic symmetry like most mullite-type phases (Table 1.1.15). Grandidierite, with the ideal composition $MgAl_3BSiO_9$, can schematically be derived from andalusite $Al_4Si_2O_{10}$ by a combined substitution of $B^{3+} = Si^{4+} + 0.5\ O^{2-}$ and $Mg^{2+} = Al^{3+} + 0.5\ O^{2-}$ in the ratio 1 : 1 (Stephenson and Moore, 1968). The mullite-type edge-shared AlO_6 octahedral chains are linked by a complex array of polyhedra: AlO_5

Table 1.1.15 MUL-VIII.2 compounds: Grandidierite group.

Chemical composition	Unit cell contents	Mineral name	*a* [Å]	*b* [Å]	*c* [Å]	*V* [Å^3]	ω [°]	Reference
(Mg,Fe)Al_3SiBO_9	$Al_8Al_4Mg_{3.6}Fe_{0.4}Si_4B_4O_{36}$	Grandidierite	10.335(2)	10.978(2)	5.760(2)	653.52	86.8 88.1	Stephenson and Moore (1968)
(Fe,Mg)Al_3SiBO_9	$Al_8Al_4Fe_{3.4}Mg_{0.4}Mn_{0.1}Si_4B_4O_{36}$ with traces of P	Ominelite	10.343(2)	11.095(1)	5.7601(8)	661.01	87.5 88.1	Hiroi et al. (2002)

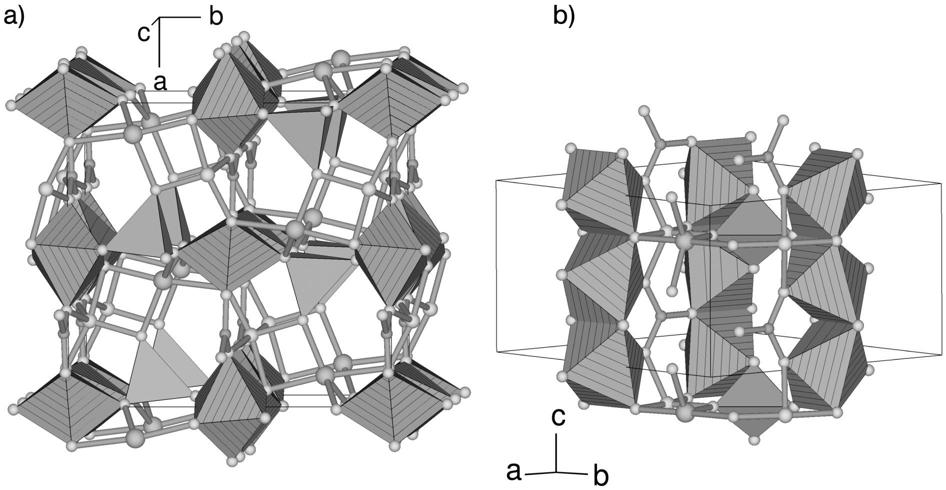

Fig. 1.1.12 Projections of the crystal structure of grandidierite (Stephenson and Moore, 1968). (a) View parallel [001] rotated by 4° about [010] and 6° about [100]. (b) View parallel [110] rotated by 2° about [001] and 6° about [$\bar{1}$10].

and MgO_5 bipyramids, SiO_4 tetrahedra and BO_3 triangles (Fig. 1.1.12). Ominelite is the iron-rich analogue of grandidierite with a Fe/Mg ratio of about 8.5, while grandidierite displays values near 0.1.

1.1.3.7 **MUL-II.3, *Pbam*: Mullite Group**

Mullite and mullite solid solution Mullite was first mentioned by Bowen and Greig (1924) as a natural mineral on the island of Mull occurring at the contact zone of a hot magma with Al_2O_3-rich clay sediments. It is worth noting that the phase has been described much earlier (Oschatz and Wächter, 1847, Deville and Caron, 1865,

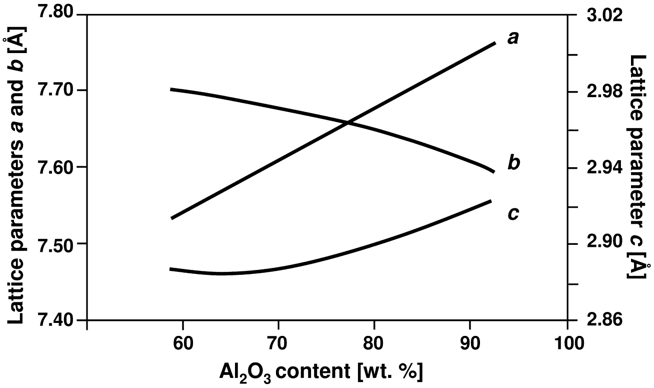

Fig. 1.1.13 Development of the lattice constants *a*, *b* and *c* of mullite with the Al_2O_3 content (after Fischer et al. 1994).

Vernadsky, 1890, Thomas, 1922), although it has been mistaken for sillimanite. Since the first citation in 1924, an enormous number of papers has been published on the synthesis, properties, phase equilibria and crystal chemistry of mullite, on mullite ceramics and mullite matrix composites (see also the General Introduction). Most of this work has been focused on synthetic materials.

Mullite is an aluminosilicate with a variable aluminum to silicon ratio represented by the solid solution series $Al_2[Al_{2+2x}Si_{2-2x}]O_{10-x}$. The composition of mullite observed so far ranges between $0.18 \leq x \leq 0.88$, corresponding to 57 to 92 mol% Al_2O_3 (Fischer et al. 1996). The chemical composition of mullite can be derived from its lattice constant *a* according to the linear relationship $m = 144.5\ a - 1029.5$ (Fischer et al. 1996), where *m* denotes the molar content of Al_2O_3 in mol%. Fig. 1.1.13 shows the relationship between the lattice parameters of mullite and the molar Al_2O_3 content.

Table 1.1.16 gives an overview of the crystal structure refinements performed on mullite and other MUL-II.3 compounds. Mullites have been described in two different unit cell settings. Burnham (1963a) introduced a unit cell setting shifted by 1/2, 1/2, 0 relative to the origin in the initial structure determination of Ďurovič (1962a) and Sadanaga et al. (1962). Most of the subsequent structure refinements are based on the Burnham setting which is also used here. It has the advantage to conform to the setting and the origin of the closely related sillimanite. The atomic parameters of the two different settings can be considered enantiomorphous, related to each other by an inversion center $\bar{1}$ in 1/4, 1/4, 0 which is equivalent with an origin shift of 1/2, 1/2, 0. All entries in Table 1.1.16 referring to the initial setting by Ďurovič (1962a), Sadanaga et al. (1962) and by Brunauer et al. (2001) are marked by an asterisk.

The average crystal structure of mullite can be best described by comparison with the closely related but structurally simpler sillimanite (composition Al_2SiO_5, i.e. $Al_2O_3 \cdot SiO_2$, see Section 1.1.3.10 for further details). In sillimanite, the aluminum oxygen (AlO_6) octahedral chains are crosslinked by alternating AlO_4 and SiO_4

Table 1.1.16 MUL-II.3 compounds: Mullite group.

Chemical composition	Unit cell contents	Mineral / compound name	*a* [Å]	*b* [Å]	*c* [Å]	*V* [Å^3]	ω [°]	Reference
$Al_{4.6}Si_{1.4}O_{9.7}$	$Al_2Al_{2.6}Si_{1.4}O_{9.7}$	Mullite-ss*	7.549(8)	7.681(8)	2.884(3)	167.23	58.5	Ďurovič (1962a)
$Al_{4.8}Si_{1.\ 2}O_{9.6}$	$Al_2Al_{2.8}Si_{1.\ 2}O_{9.6}$	Mullite-ss*	7.583(2)	7.681(2)	2.8854(5)	168.06	59.6	Sadanaga et al. (1962)
$Al_{5.38}Si_{2.44}O_{9.70}$	$Al_2Al_{3.38}Si_{2.44}O_{9.70}$	Mullite-ss	7.584(3)	7.693(3)	2.890(1)	168.61	59.5	Burnham (1963a)
$Al_{5.66}Si_{2.16}O_{9.70}$	$Al_2Al_{3.66}Si_{2.16}O_{9.70}$	Mullite-ss	7.584(3)	7.693(3)	2.890(1)	168.61	59.5	Burnham (1963a)
$Al_{4.72}Si_{1.32}O_{9.66}$	$Al_2Al_{2.72}Si_{1.32}O_{9.66}$	Mullite-ss*	7.566(5)	7.682(5)	2.884(2)	167.62	59.4	Ďurovič (1969)
$Al_{4.5}Si_{1.5}O_{9.75}$	$Al_2Al_{2.5}Si_{1.5}O_{9.75}$	3/2 mullite*	7.553(1)	7.686(1)	2.8864(7)	167.56	59.0	Saalfeld and Guse (1981)
$Al_{4.72}Si_{1.32}O_{9.66}$	$Al_2Al_{2.72}Si_{1.32}O_{9.66}$	Mullite-ss	7.5785(6)	7.6817(7)	2.8864(3)	168.04	59.8	Angel and Prewitt (1986)
$Al_{4.8}Si_{1.\ 2}O_{9.6}$	$Al_2Al_{2.8}Si_{1.\ 2}O_{9.6}$	2/1 mullite	7.588(2)	7.688(2)	2.8895(6)	168.56	59.8	Angel et al. (1991)
$Al_{4.95}Si_{1.05}O_{9.53}$	$Al_2Al_{2.95}Si_{1.05}O_{9.53}$	Mullite-ss	7.6110(3)	7.6803(4)	2.8872(1)	168.77	60.8	Ban and Okada (1992)
$Al_{4.98}Si_{1.02}O_{9.51}$	$Al_2Al_{2.98}Si_{1.02}O_{9.51}$	Mullite-ss	7.6156(6)	7.6780(6)	2.8859(2)	168.75	61.7	Ban and Okada (1992)
$Al_{4.87}Si_{1.13}O_{9.57}$	$Al_2Al_{2.87}Si_{1.13}O_{9.57}$	Mullite-ss	7.5964(5)	7.6803(5)	2.8824(2)	168.17	60.5	Ban and Okada (1992)
$Al_{4.64}Si_{1.36}O_{9.68}$	$Al_2Al_{2.64}Si_{1.36}O_{9.68}$	Mullite-ss	7.5640(4)	7.6923(4)	2.8806(1)	167.61	61.1	Ban and Okada (1992)
$Al_{4.75}Si_{1.25}O_{9.63}$	$Al_2Al_{2.75}Si_{1.25}O_{9.63}$	Mullite-ss	7.5811(3)	7.6865(3)	2.8821(1)	167.95	60.1	Ban and Okada (1992)
$Al_{4.59}Si_{1.41}O_{9.70}$	$Al_2Al_{2.59}Si_{1.41}O_{9.70}$	Mullite-ss	7.5539(2)	7.6909(2)	2.88391(6)	167.54	59.2	Ban and Okada (1992)
$Al_{4.54}Si_{1.46}O_{9.73}$	$Al_2Al_{2.54}Si_{1.46}O_{9.73}$	Mullite-ss	7.5421(1)	7.6957(1)	2.88362(5)	167.37	59.1	Ban and Okada (1992)
$Al_{4.52}Si_{1.48}O_{9.74}$	$Al_2Al_{2.52}Si_{1.48}O_{9.74}$	Mullite-ss	7.5459(2)	7.6937(2)	2.88346(7)	167.40	59.0	Ban and Okada (1992)
$Al_{4.56}Si_{1.44}O_{9.72}$	$Al_2Al_{2.56}Si_{1.44}O_{9.72}$	Mullite-ss	7.5473(1)	7.6928(1)	2.88391(4)	167.44	58.9	Ban and Okada (1992)
$Al_{4.5}Si_{1.5}O_{9.75}$	$Al_2Al_{2.5}Si_{1.5}O_{9.75}$	3/2 mullite	7.54336(6)	7.69176(6)	2.88402(2)	167.34	58.9	Balzar and Ledbetter (1993)
$Al_{5.65}Si_{0.35}O_{9.175}$	$Al_2Al_{3.65}Si_{0.35}O_{9.175}$	Mullite-ss	7.7391(6)	7.6108(5)	2.9180(1)	171.87	64.5	Fischer et al. (1994)
$Al_{4.82}Si_{1.18}O_{9.59}$	$Al_2Al_{2.82}Si_{1.18}O_{9.59}$	Mullite-ss	7.5817(8)	7.6813(9)	2.8865(5)	168.10	60.0	Voll et al. (2001)
$Al_{4.68}Si_{1.32}O_{9.66}$	$Al_2Al_{2.68}Si_{1.32}O_{9.66}$	Mullite-ss	7.5655(4)	7.6883(4)	2.8851(2)	167.81	59.1	Voll et al. (2001)
$Al_{4.98}Si_{1.02}O_{9.51}$	$Al_2Al_{2.98}Si_{1.02}O_{9.51}$	Mullite-ss	7.616(2)	7.678(2)	2.8891(4)	168.97	63.0	Johnson et al. (2001)
$Al_{5.16}Si_{0.84}O_{9.42}$	$Al_2Al_{3.16}Si_{0.84}O_{9.42}$	Mullite-ss	7.606(1)	7.682(1)	2.8871(4)	168.70	61.4	Johnson et al. (2001)
$Al_{4.68}Si_{1.32}O_{9.66}$	$Al_2Al_{2.68}Si_{1.32}O_{9.66}$	Mullite-ss	7.5454(2)	7.6956(2)	2.88398(6)	167.46	58.6	Johnson et al. (2001)
$Al_{4.66}Si_{1.34}O_{9.67}$	$Al_2Al_{2.66}Si_{1.34}O_{9.67}$	Mullite-ss	7.5499(3)	7.6883(3)	2.88379(9)	167.39	58.5	Johnson et al. (2001)

Table 1.1.16 (cont.)

Chemical composition	Unit cell contents	Mineral / compound name	*a* [Å]	*b* [Å]	*c* [Å]	*V* [Å^3]	ω [°]	Reference
$Al_{4.67}Si_{1.17}P_{0.17}O_{9.76}$	$Al_2Al_{2.67}Si_{1.17}P_{0.17}O_{9.76}$	P-doped mullite	7.5722(4)	7.6960(4)	2.8856(1)	168.16	60.0	Ronchetti et al. (2001)
$Al_{4.20}Fe_{0.30}Si_{1.50}O_{9.74}$	$Al_2Al_{2.20}Fe_{0.30}Si_{1.50}O_{9.74}$	Fe-doped mullite	7.5693(2)	7.7159(2)	2.89470(5)	169.06	58.5	Ronchetti et al. (2001)
$Al_{4.43}Fe_{0.1.50}Si_{1.35}P_{0.08}O_{9.76}$	$Al_2Al_{2.43}Fe_{0.1.50}Si_{1.35}P_{0.08}O_{9.76}$	Fe,P-doped mullite	7.5673(2)	7.7016(2)	2.88895(6)	168.37	59.1	Ronchetti et al. (2001)
$Al_{4.52}Ge_{1.48}O_{9.74}$	$Al_2Al_{2.52}Ge_{1.48}O_{9.74}$	Ge-aluminate	7.650(2)	7.779(2)	2.925(2)	174.06	61.5	Ďurovič and Fejdi (1976)
$Al_{4.72}Ge_{1.28}O_{9.64}$	$Al_2Al_{2.72}Ge_{1.28}O_{9.64}$	Ge-aluminate	7.6530(4)	7.7779(4)	2.9252(2)	174.12	61.5	Voll et al. (2001)
$Al_{4.5}Ge_{1.5}O_{9.75}$	$Al_2Al_{2.5}Ge_{1.5}O_{9.75}$	Ge-aluminate	7.644	7.779	2.925	173.93	61.5	Saalfeld and Gerlach (1991)
$Al_{4.76}Ge_{1.24}O_{9.62}$	$Al_2Al_{2.76}Ge_{1.24}O_{9.62}$	Ge-aluminate	7.644(1)	7.760(1)	2.923(1)	173.38	61.8	Saalfeld and Gerlach (1991)
$Al_{3.92}Cr_{0.5}Si_{1.58}O_{9.79}$	$Al_2Al_{1.92}Cr_{0.5}Si_{1.58}O_{9.79}$	Cr-doped mullite	7.56712(6)	7.70909(6)	2.90211(2)	169.30	58.2	Fischer and Schneider (2000)
$Ga_{4.62}Ge_{1.38}\ O_{9.69}$	$Ga_2Ga_{2.62}Ge_{1.38}\ O_{9.69}$	Ge-gallate	7.8674(4)	8.0305(4)	3.0148(2)	190.47	61.0	Voll et al. (2001)
Al_5BO_9	$Al_2Al_3BO_9$	B-aluminate	7.621	7.621	2.833	164.54	77.3	Mazza et al. (1992)
$Al_4B_2O_9$	$Al_2Al_2B_2O_9$	B-aluminate	7.617	7.617	2.827	164.02	71.1	Mazza et al. (1992)
$Al_6NaO_{9.5}$	$Al_2Al_4NaO_{9.5}$	Na-aluminate	7.640	7.640	2.937	171.43	59.5	Mazza et al. (1992)
$Al_6Na_{0.67}O_{9.33}$	$Al_2Al_4Na_{0.67}O_{9.33}$	Na-aluminate	7.6819(4)	7.6810(4)	2.91842(8)	172.20	63.8	Fischer et al. (2001)
$Al_6KO_{9.5}$	$Al_2Al_4KO_{9.5}$	K-aluminate	7.708	7.708	2.906	172.65	73.7	Mazza et al. (1992)
$Al_6K_{0.67}O_{9.33}$	$Al_2Al_4K_{0.67}O_{9.33}$	K-aluminate	7.6934(3)	7.6727(3)	2.93231(7)	173.09	66.1	Fischer et al. (2001)
$Ga_6Rb_{0.67}O_{9.33}$	$Ga_2Ga_4Rb_{0.67}O_{9.33}$	Rb-gallate	8.0087(3)	8.0177(3)	3.04158(6)	195.30	65.5	this work

An asterisk in the mineral name column indicates that the unit cell setting corresponds to the setting introduced by Ďurovič (1962a).

tetrahedra forming double chains of tetrahedra running parallel to **c**. The double chains of ordered AlO_4 and SiO_4 tetrahedra in sillimanite are replaced in mullite by a disordered arrangement of $(Al,Si)O_4$ tetrahedra.

Formally mullite can be derived from sillimanite by the coupled substitution

$$2Si^{4+} + O^{2-} \rightarrow 2Al^{3+} + \text{vacancy } (\square) \qquad (1)$$

The reaction involves removal of oxygen atoms from the structure and the formation of oxygen vacancies. Structure refinements have shown that the oxygen atoms bridging two polyhedra in the tetrahedral double chain (so called O(C) oxygen sites, corresponding to O3 in this work) are removed. As a consequence the two tetrahedral (T) sites are displaced to a position designated as T* (large arrows in Fig. 1.1.14a,b) and O3 becomes threefold coordinated by cations forming T_3O groups (so called triclusters).

The cation occupation at the T* sites of mullite is a point of controversy. According to the basic work of Angel and Prewitt (1986) the occupancy of silicon in tetrahedral T* sites is very small or even zero. In order to maintain charge balance, the removal of O3 oxygen atoms is accompanied by replacement of tetrahedrally coordinated silicon by aluminum. Thus, the introduction of an oxygen vacancy causes the two tetrahedral cation (T) atom sites to migrate towards adjacent oxygen O3 atoms which are pulled towards these cations. These oxygen atoms, slightly displaced from the special position (Wyckoff site 2(d) in space group *Pbam*) have been designated O(C*) corresponding to O4 in the new configuration. According to Angel and Prewitt (1986) the number of oxygen vacancies corresponds to the x value of the mullite mixed crystal series $Al_{4+2x}Si_{2-2x}O_{10-x}$. The c lattice constant of mullite is halved compared with the corresponding parameter in sillimanite because silicon and aluminum atoms are randomly distributed over the tetrahedral cation sites. The structural data obtained for 3/2-mullite ($x = 0.25$) and 2/1-mullite ($x = 0.40$), respectively, are compiled in Tables 1.1.17 and 1.1.18.

The crystal structure analysis from X-ray or neutron diffraction data is based on the deconvolution of electron densities of a large number of atoms projected into one unit cell. The local structural order of oxygen vacancies and of the aluminum to silicon distribution, however, may deviate from the average situation. Information on the structural short-range-order can be obtained from the additional diffuse scattering of mullite ("superstructure reflections"). This additional scattering has been attributed to partial ordering of O3 oxygen vacancies and to aluminum and silicon distribution over tetrahedral (T) sites. According to Paulmann (1996) the ordering scheme of the oxygen vacancies in mullite is very stable persisting up to the melting point. A hypothetically ordered mullite, with all tetrahedrally bound cations in T_3O triclusters, is shown in Fig. 1.1.14. Order-disorder phenomena in mullite are associated with its real structure which is considered in Section 1.2. Information on the degree of the tetrahedral aluminum to silicon ordering in mullite has also been derived from ^{29}Si nuclear magnetic resonance (NMR) spectroscopy by Schmücker et al. (2005). The silicon spectrum of mullite displays three well resolved maxima near –88, –92 and –95 ppm. Schmücker et al. assigned the

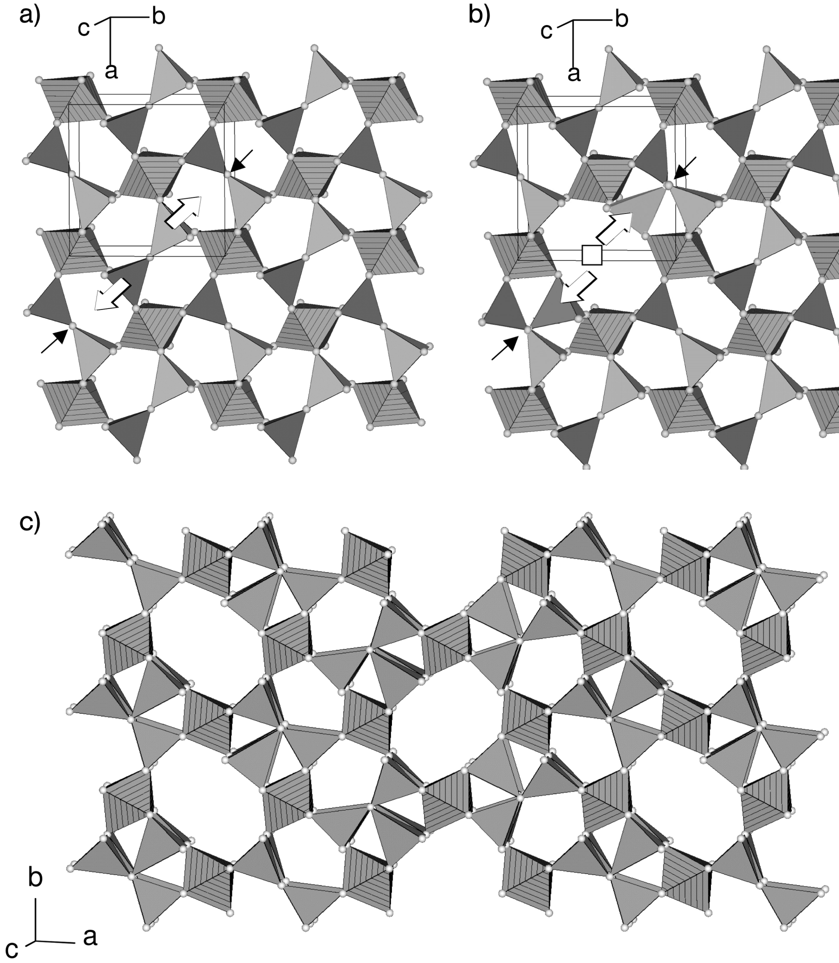

Fig. 1.1.14 The crystal structures of mullite solid solution compounds derived from sillimanite. All projections viewed parallel to **c** rotated by 4° about **a** and **b**. (a) Linkage of octahedral chains in sillimanite by T_2O_7 groups. Big arrows indicate the migrations directions of the T-atoms, thin arrows point to the O atoms which are dislocated off the special position. (b) Modeling of an oxygen vacancy in the layer shown in (a). Big arrows indicate the migration directions corresponding to (a), thin arrows indicate the dislocation directions of the O3 atoms migrating to the O4 position. The square indicates the oxygen vacancy. (c) Hypothetically ordered crystal structure of a 4/1-mullite (**x** = 0.67) corresponding to a $3 \times a$ orthorhombic supercell (after Fischer et al. 1994). All octahedra are linked by T_3O-groups.

Table 1.1.17 Atomic coordinates and occupancy factors for the average structure of 3/2- (x = 0.25) and 2/1-mullite (x = 0.40).

Atom name §	**Alternative designations commonly used §**	***x***		***y***		***z***		**Occupancy**	
		3/2-mullite	**2/1-mullite**	**3/2-mullite**	**2/1-mullite**	**3/2-mullite**	**2/1-mullite**	**3/2-mullite**	**2/1-mullite**
Al 1	Al	0.0	0.0	0.0	0.0	0.0	0.0	1.0	1.0
(Al,Si)	T	0.1485	0.14901(2)	0.3411	0.34026(2)	0.5	0.5	0.863	0.56 Al 0.25 Si
(Al,Si)*	T*	0.2621	0.26247(9)	0.2057	0.20529(9)	0.5	0.5	0.137	0.13 Al 0.06 Si
O1	O(A,B)	0.3579	0.3590(1)	0.4221	0.4218(1)	0.5	0.5	1.0	1.0
O2	O(D)	0.1265	0.1273(1)	0.2201	0.2186(1)	0.0	0.0	1.0	1.0
O3	O(C)	0.0	0.0	0.5	0.5	0.5	0.5	0.590	0.39
O4	O(C*)	0.4507	0.4498(4)	0.0518	0.0505(4)	0.5	0.5	0.137	0.19

References:
3/2-mullite data: Saalfeld and Guse (1981), unit cell transformed to the setting used by Angel and Prewitt (1986), Al and Si are not distinguished
2/1-mullite data: Angel and Prewitt (1986).
§ Both designations are used in this book depending on literature reference.

Table 1.1.18 Interatomic distances and bond angles for the average structures of 3/2- ($x = 0.25$) and 2/1-mullite ($x = 0.40$).

	Distances [Å]				Angles [°]		
	3/2-mullite	**2/1-mullite**	**Multiplicity**	**Structural site**	**3/2-mullite**	**2/1-mullite**	**Multiplicity**
M1-site				**M1**			
Al 1–O1	1.896	1.8936(5)	4×	O1–Al 1–O1	180	180	2×
Al 1–O2	1.943	1.9366(9)	2×	O2–Al 1–O2	180	180	1×
mean	1.912	1.908		O1–Al 1–O1	99.17	99.31(2)	2×
				O1–Al 1–O1	80.83	80.69(2)	2×
				O1–Al 1–O2	89.80	89.65(3)	4×
				O1–Al 1–O2	90.20	90.35(3)	4×
T-site				**T**			
(Al,Si)–O1	1.700	1.7102(8)	1×	O1–(Al,Si)–O3	111.08	111.15(3)	1×
(Al,Si)–O2	1.725	1.7273(5)	2×	O1–(Al,Si)–O2	106.69	106.66(3)	2×
(Al,Si)–O3	1.658	1.6676(2)	1×	O2–(Al,Si)–O2	113.56	113.34(5)	1×
mean	1.702	1.708		O2–(Al,Si)–O3	109.39	109.50(3)	2×
T*-site				**T***			
Al*–O1	1.814	1.8169(10)	1×	O1–(Al,Si)*–O4	106.19	106.21(7)	1×
Al*–O2	1.773	1.7728(6)	2×	O1–(Al,Si)*–O2	99.97	100.37(5)	2×
Al*–O4	1.852	1.8518(31)	1×	O2–(Al,Si)*–O4	118.96	118.68(5)	2×
mean	1.803	1.804		O2–(Al,Si)*–O2	108.96	109.01(6)	1×

References:
3/2-mullite data: Saalfeld and Guse (1981)
2/1-mullite data: Angel and Prewitt (1986).

signal near –88 ppm with the highest intensity to three AlO_4 tetrahedra in the next nearest environment of SiO_4, similar to the situation in sillimanite. The nuclear magnetic resonance peaks near –92 and –95 ppm have been assigned respectively to two AlO_4 and one SiO_4 tetrahedra, and to one AlO_4 and two SiO_4 tetrahedra being next nearest neighbors of SiO_4. Comparison of the measured data with simulated nuclear magnetic resonance data yields a moderate degree of aluminum to silicon odering in the tetrahedra of mullite.

Burnham (1964a) remarked that the mullite structure theoretically fits any composition between (disordered) sillimanite ($x = 0.00$) and aluminum oxide (ι-alumina, $x = 1.00$), and that there is no obvious reason why the composition should be restricted to 3/2-mullite ($x = 0.25$) and 2/1-mullite ($x = 0.40$), or to mixed crystals between them. In reality, mullite mixed crystal formation is limited towards SiO_2-rich compositions ($x \approx 0.20$). The existence of the miscibility gap between sillimanite and mullite has been explained by the different ordering schemes of sillimanite and mullite. The extent of the miscibility gap has remained a point of dispute. Mullites with a composition midway between sillimanite and 3/2-mullite (termed Al_2O_3-rich sillimanite) were described in a contact metamorphosed rock (lithomarge from Rathlin Island, Northern Ireland, Cameron, 1976a) and in iron-rich and titanium-poor compounds (see Cameron, 1977b). A complete solubility between sillimanite and mullite, which has been described as occuring at higher pressures (Hariya et al. 1969, Grigor'ev, 1976), seems to be less probable.

If mullites are simple solid solutions with little structural variation, their cell parameters should depend linearly on the Al_2O_3 content. The plot of the a constant versus the Al_2O_3 content has frequently been used for discussion of the dependence (Fig. 1.1.13). Many authors (Trömel et al. 1957, Gelsdorf et al. 1961, Ďurovič 1962b, Hariya et al. 1969, Cameron 1977c, Schneider and Wohlleben, 1981, Schneider, 1990, Ban and Okada, 1992, Fischer et al. 1994, Rehak et al. 1998) have shown that the a lattice constants of mullites in the composition range 60–74 mol% Al_2O_3 actually increases linearly with the Al_2O_3 content, while the b constant decreases slightly and non-linearly. Extrapolation of the curves towards lower Al_2O_3 content results in the a and b constants of sillimanite (50 mol% Al_2O_3). Continuing the a and b curves of the mullite solution series against higher Al_2O_3 contents shows that the lines cross at about 80 mol% Al_2O_3 ($x \approx 0.67$). Actually a compound with $a = b$ was first described by Ossaka (1961), and was designated as tetragonal mullite phase. In spite of the coincidental identity of a and b lattice constants this mullite is orthorhombic. Therefore it could be designated as "pseudo-tetragonal" mullite (see Schneider and Rymon-Lipinski, 1988). To be precise, it should read mullite with "pseudo-tetragonal metric", since the symmetry of the crystal structure is clearly orthorhombic.

Only a few results are available on the phase relations of Al_2O_3-rich mullites beyond the "pseudo-tetragonal" point. Alumina phases with mullite-like structures (ι-alumina) have been discussed in the literature and were believed to be either tetragonal (Cameron, 1977a, Foster, 1959, Perrotta and Young, 1974), or they have been assigned to orthorhombic symmetry (Saalfeld, 1962, Duvigneaud, 1974). Careful own microchemical studies have shown that such phases belong to the

Table 1.1.19 Site occupancies in mullite phases.

	$x \le 0.67$	$x \ge 0.67$
No. of T atoms (Si + Al)	$4 - 2x$	$4 - 2x$
No. of T* atoms (all Al)	$2x$	$2 - x$
No. of T** atoms (all Al)	0	$-2 + 3x$
No. of Al atoms in T site	2	2
No. of Si atoms in T site	$2 - 2x$	$2 - 2x$
No. of O3 [O(C)] atoms	$2 - 3x$	0
No. of O4 [O(C*)] atoms	$2x$	$2 - x$

After Fischer et al. (1994).

mullite-type alkali aluminates rather than to mullites. Investigations on Al_2O_3-rich mullite precursors synthesized via a specific chemical route from aluminum-*sec*-butylate and silicon chloride yielded mullites that have unusual lattice constants with $a > b$ ($a = 7.760$ Å, $b = 7.595$ Å, $c = 2.9192$ Å, data from a sample annealed at 1000 °C, Schneider et al. 1993a), corresponding to Al_2O_3 up to about 89 mole% Al_2O_3 ($x = 0.83$ corresponding to a 9/1-mullite composition of $Al_{5.65}Si_{0.35}O_{9.18}$) which lies far beyond the crossover of the a and b curves ($a > b$ at about 80 mol% Al_2O_3, Fig. 1.1.13). A low temperature orthorhombic mullite, probably with $a > b$, has also been described by Huling and Messing (1992).

Understanding the crystal structure of the $a > b$ phase turned out to be difficult, since the conventional structure model of mullite is restricted to $x \le 0.67$ (≤ 80 mol% Al_2O_3, Angel and Prewitt 1986), where all possible O3 vacancies have formed. Angel and Prewitt mentioned that at $x > 0.67$ some additional Al^{3+} ions are incorporated at interstitial sites. Another approach to accommodating the additional Al involves the formation of T_4O groups (so-called tetraclusters), where four(!) tetrahedra are connected via a common oxygen atom. Fischer et al. (1994) performed a structure refinement of the mullite with a very high Al_2O_3 content ($x = 0.83$ i. e. 9/1-mullite see Tables 1.1.19 and 1.1.20), and proved that the average

Table 1.1.20 Chemical compositions and site assignments for selected compounds in the mullite solid solution series.

Compound	x	Composition of octahedral chain	Residue	No. of groups		
				T_2O	T_3O	T_4O
Sillimanite	0	Al_2O_8	$Al_2Si_2O_2$	2	0	0
3/2-mullite	0.25	Al_2O_8	$Al_{2.5}Si_{1.5}O_{1.75}$	1.25	0.5	0
2/1-mullite	0.4	Al_2O_8	$Al_{2.8}Si_{1.2}O_{1.6}$	0.8	0.8	0
4/1-mullite	0.67	Al_2O_8	$Al_{3.33}Si_{0.67}O_{1.33}$	0	1.33	0
9/1-mullite	0.825	Al_2O_8	$Al_{3.65}Si_{0.35}O_{1.175}$	0	0.7	0.475
ι-Al_2O_3	1	Al_2O_8	Al_4O	0	0	1

After Fischer et al. (1994).

structure remained orthorhombic. Although tetrahedral T_4O arrangements are not favored on the basis of energy calculations (Padlewski et al. 1992a), Fischer and coworkers preferred this model. They suggested that these extremely Al_2O_3-rich mullites contain sillimanite-like T_2O dimers of tetrahedra with additional pairs of AlO_4 tetrahedra (T^* and T^{**}, i. e. T_3O and T_4O groups, respectively). T_3O and T_4O groups are linked to the bridging oxygen atom, which is loosely bound with long distances to the octahedral chains. T^* and T^{**} sites can alternatively be interpreted as fivefold coordinated. In order to get further structural information on the $a > b$-mullite ($x = 0.83$) a plane image reconstruction has been carried out in comparison to that of 2/1-mullite. The theoretical background of this procedure is based on the so-called videographic simulation and reconstruction of the real structure of mullite (e. g. Rahman, 1993a, see Section 1.2). The reconstructed image of the $a > b$-mullite ($x = 0.83$) derived from its diffraction patterns (Fig. 1.1.15) is given in Fig. 1.1.16 and compared with 2/1-mullite ($x = 0.40$). The structures of both mullites are believed to consist of domains with high O3 oxygen vacancy concentrations (bright areas containing light dots) distributed in a matrix with relatively low O3 oxygen vacancy concentrations (dark areas). The domains as well as the cells in individual domains partly exhibit a quasi-antiphase relationship. The antiphase relationships are referred to the O3 sublattice in the mullite structure, whereby the "antiphase boundaries" run parallel to [001] for 2/1-mullite ($x = 0.40$), and parallel [100] for the $a > b$-mullite. The domains are distributed quasi randomly in the case of 2/1-mullite whereas for $a > b$-mullite a clear correlation distance along [101] and $[\bar{1}01]$ (inter-domain vectors) exists, forming an irregular twin boundary along the main directions.

The near-tetragonal arrangement of structural units perpendicular to the **c** axis of mullite suggests that the a and b cell dimensions display comparable developments with increasing Al_2O_3 content. However, as shown in Fig. 1.1.13, a increases linearly while b decreases slightly and non-linearly (see also above). Clockwise and counter-clockwise rotations of polyhedra are unlikely to explain these phenomena since they would cause a strong deformation of the structure. Also the theory of rigid unit modes (RUMs, Hammonds et al. 1998), which says that the stiff tetrahedral units of a silicate structure show little tendency to rotate if they are

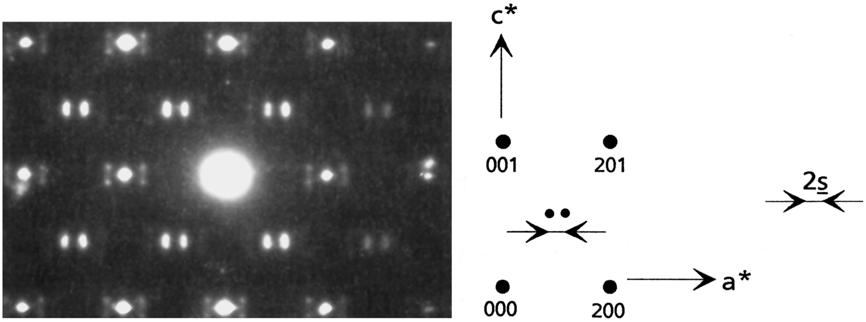

Fig. 1.1.15 **a*c*** electron diffraction pattern of Al_2O_3-rich mullite ($a > b$, $x = 0.83$, from Schneider et al. 1994a).

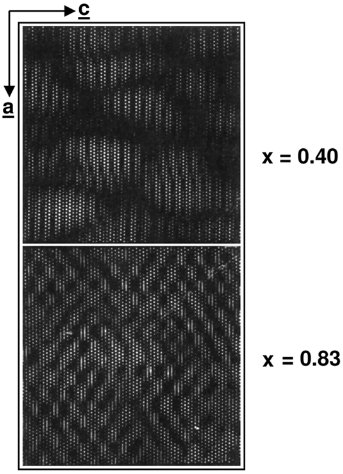

Fig. 1.1.16 Reconstructed image for the *a* > *b*-mullite ($x = 0.83$) in comparison with 2/1-mullite ($x = 0.40$). Information on the procedure, its theoretical background and its significance are given in the text (see also Section 1.2, from Schneider, 1994a).

stabilized by octahedra, contradicts the rotational approach. Random Al^{3+} and Si^{4+} distribution over the tetrahedral sites with the amount of tetrahedral Al^{3+} increasing with the *x*-value of mullite can also not produce the observed development, because it has a similarly increasing effect on both lattice constants. As a last influencing factor the distribution of O3 oxygen vacancies may be considered. The number and distribution of O3 vacancies are important, since they increase the compressibility in the specific lattice direction, which in turn works against incorporation-induced expansion. Again, randomly distributed vacancies would have similar expansion-reducing effects in both **a** and **b** directions. However, things change if structurally anisotropic vacancy distributions are taken into account in a way that the number of O3 oxygen vacancies along **b** increases more strongly than along **a** in going from 3/2- to 2/1-mullite. Since the vacancies work against the expansion induced by aluminum for silicon substitution, this would have the result of a less strong expansion parallel to **b** than parallel to **a**.

Various types of mullites depending on their synthesis routes have been described as relevant for ceramics and technical processes:

Sinter-mullites, which have Al_2O_3 contents with a frequency maximum at about 60 mol% Al_2O_3 (72 wt.% Al_2O_3). These mullites have been designated as *3/2-mullite* ($3Al_2O_3 \cdot 2SiO_2$, $x = 0.25$) or stoichiometric mullite. The term sinter-mullite describes a mullite that has been produced from the starting materials essentially by solid-state reactions. The Al_2O_3 content of sinter-mullites is influenced by sintering temperatures, the duration of heat treatment, the initial bulk composition, the nature, grain size and efficiency of mixing of the starting materials, and whether α-alumina nucleated (see also Section 3.1).

Fused-mullites[2] which have Al_2O_3 contents with a frequency maximum at about

---

[2] The term *fused-mullite* has frequently been used in the literature (e.g. Cameron, 1977c), although it is misleading and can be mistaken for molten mullite, i.e. a glass phase with mullite composition. A hyphen should therefore be put between the terms "fused" and "mullite".

64 mole% Al_2O_3 (76 wt.% Al_2O_3) and the ideal composition 66.7 mol% Al_2O_3 (78 wt.% Al_2O_3). These mullites have been designated as *2/1-mullites* ($2Al_2O_3 \cdot SiO_2$, $x = 0.40$). The term fused-mullite describes mullites that are produced either by melting the raw materials in an electric arc furnace above 2000 °C with subsequent crystallization of mullite during cooling of the bath, or by laboratory scale crystal growth techniques (see Section 4.1.2). Higher Al_2O_3 contents can be achieved by rapid quenching, or alternatively by a very slow cooling process. The composition of mullites crystallized from liquids is primarily a function of temperature and to a lesser degree of the initial composition (see Cameron, 1977c): Guse (1974) and Guse and Mateika (1974) investigated the solid solution range of Czochralski-grown fused-mullites by varying the starting chemical composition of the melt between 77.3 and 71.8 wt.% Al_2O_3 (22.7 to 28.2 wt.% SiO_2). In spite of this rather large variation, the Al_2O_3 content of corresponding mullites changed only from about 77.5 to 75.5 wt.%, both compositions lying close to that of 2/1-mullite. A conclusion of Guse's observation is that the formation of 2/1- or, alternatively, 3/2-type mullite is controlled by the synthesis process, while the bulk chemical composition of the system plays a less important role.

Chemical-mullites, or solution-sol-gel-derived mullites of which the chemical composition greatly depends on the starting materials and on the formation temperature. Al_2O_3 contents over 83 mol% have been described (see above and Section 4.1.3). Chemical mullites are formed from organic and inorganic precursors by polymerization and ceramization. Mullitization takes place at low temperatures between about 900 and 1300 °C, with the "low temperature" mullites normally being Al_2O_3-rich.

Germanium mullite The chemical similarity of Si^{4+} and Ge^{4+}, especially the comparable ionic radii (Si^{4+}: 0.26 Å, Ge^{4+}: 0.39 Å) imply that germanium mullite, isotypic with silicon mullite, does exist. Actually, Gelsdorf et al. (1958) were the first to synthesize a 3/2-type germanium mullite ($3Al_2O_3 \cdot 2GeO_2$). They also described a complete solid solution between 3/2-silicon ($3Al_2O_3 \cdot 2SiO_2$) and 3/2-germanium mullite ($3Al_2O_3 \cdot 2GeO_2$). Detailed data on germanates with mullite structure were published by Perez Y Jorba (1968, 1969), and Schneider and Werner (1981, 1982). A structural refinement of a germanate ($3.08Al_2O_3 \cdot 2GeO_2$) isostructural with 2/1-mullite has been performed by Ďurovič and Fejdi (1976).

Complete gallium (Ga^{3+}) and partial iron (Fe^{3+}) substitution for aluminum (Al^{3+}) in the germanates was reported by Schneider and Werner (1981, 1982). The incorporations cause cell edge expansion, especially along **b**. This was taken as evidence for a preferred octahedral incorporation of gallium and iron, producing strong expansion along the elastic M1-O2 (M(1)-O(D)) bond lying about 30° to either side of the **b** axis but to about 60° of **a** (Fig. 1.1.14). Tetrahedral incorporation also occurs in the case of gallium. The expansion anisotropy, being much stronger in iron-substituted mullites than in gallium-substituted mullites, however, indicates that tetrahedral incorporation is much less probable for iron. There is a linear dependence between the mean radius of trivalent cations and cell volumes of the mullites. Infrared spectroscopic studies carried out by Schneider (1981) and Voll et al. (2001) on different silicon and germanium mullites showed notable band broadenings in the $3Al_2O_3 \cdot 2GeO_2$ absorption diagram, while $3Al_2O_3 \cdot 2SiO_2$ and $3Ga_2O_3 \cdot 2GeO_2$ exhibit bands with smaller half-widths. This was taken as evidence for a higher degree of cation disorder in Al,Ge-mullite. Only phases with near-stoichiometric 3/2-compositions of the germanium mullites (i.e. $3M_2O_3 \cdot 2GeO_2$, M = Al,Ga) have so far been identified. This is striking, since the radii of fourfold-coordinated cations are very similar (Al^{3+}: 0.39 Å, Ga^{3+}: 0.47 Å, Ge^{4+}: 0.39 Å). Further research is required to solve this point.

Alkali aluminates and gallates Angerer (2001) studied the synthesis of mullite-type alkali aluminates $Al_6Na_{0.67}O_{9.33}$, $Al_6K_{0.67}O_{9.33}$ and $Al_6Rb_{0.67}O_{9.33}$. He showed that complete binary and ternary miscibility exists between these end members. Angerer also synthesized the alkali gallates $Ga_6Na_{0.67}O_{9.33}$, $Ga_6K_{0.67}O_{9.33}$ and $Ga_6Rb_{0.67}O_{9.33}$ which are isotypic with alkali aluminates. No alkaline earth aluminates and gallates, or aluminates and gallates with threefold-charged cations (except B^{3+}) with mullite-type structures have been described yet.

Fischer et al. (2001) performed structure refinements of the end members and of the mixed crystal of the series $Al_6Na_{0.67}O_{9.33}$–$Al_6K_{0.67}O_{9.33}$. The structure consists exclusively of AlO and GaO networks, respectively. Because of the charge deficiency of the networks, sodium and potassium atoms reside in the vacant O3 oxygen sites. Na^+ occurs at a split site slightly off the special position, while K^+ enters the ideal non split site. This was explained by Fischer et al. (2001) by the fact that Na^+ is too small to completely fill the large oxygen vacancies, while the larger K^+ cations fit well. The alkali ions are restricted to 2 atoms per 3 unit cells, and as a consequence a fixed number of 0.66 vacancies per unit cell occurs.

1.1.3.8 **MUL-IV.31, *Pnnm*: Andalusite Group**

Andalusite is an orthorhombic natural mineral occurring in high-grade metamorphic Al_2O_3-rich rocks with the composition Al_2SiO_5 ($Al_2O_3 \cdot SiO_2$). The mullite-specific chains of edge-sharing AlO_6 octahedra in andalusite are linked by edge-sharing AlO_5 bipyramids which alternate with SiO_4 tetrahedra (Burnham and Buerger, 1961, see Fig. 1.1.17). Fivefold-coordinated cations in MO_5 polyhedra have frequently been observed in mullite-type phases, e.g. grandidierite (Section 1.1.3.6), werdingite (Section 1.1.3.15), boralsilite (Section 1.1.3.14), boron aluminates (Section 1.1.3.11). The arrangement of AlO_5 bipyramids and of SiO_4 tetrahedra formally resembles the sequence of mullite-type "Zweier double chains" (M-chains according to Saalfeld, 1979), if the AlO_5 bipyramids are replaced by $(Al,Si)_2O_5$ tetrahedral groups.

Schneider and Werner (1982), Fischer and Schneider (1992) and Voll et al. (2001) described germanates of the composition Ga_2GeO_5 isotypic with andalusite. Schneider and Werner stated that about 25% of the Ga^{3+} can be replaced by Al^{3+}. There is a group of OH-bearing phosphates and arsenates with the andalusite structure and the general composition M_2TO_4OH (M = Cu^{2+}, Mn^{2+}, Zn^{2+}, Co^{2+};

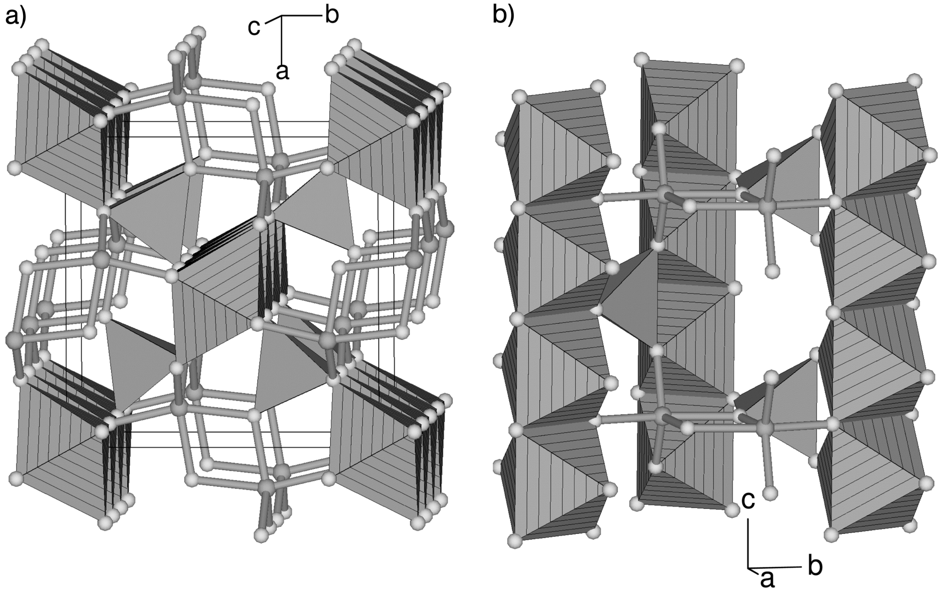

Fig. 1.1.17 Projections of the crystal structure of andalusite (Pilati et al. 1997). (a) View parallel **c** rotated by 4° about **b** and 6° about **a**. (b) View parallel **a** rotated by 10° about **b** and **c**.

Table 1.1.21 MUL-IV.31 compounds: Andalusite group.

Chemical composition	**Unit cell contents**	**Mineral name**	***a* [Å]**	***b* [Å]**	***c* [Å]**	***V* [Å^3]**	**ω [°]**	**Reference**
Al_2SiO_5	$Al_4Al_4Si_4O_{20}$	Andalusite	7.7992(6)	7.9050(6)	5.5591(5)	342.73	60.9	Pilati et al. (1997)
$Al_5Fe_3Ge_4O_{20}$	$(Al_{2.2}Fe_{1.8})Al_{2.8}Fe_{1.2}Ge_4O_{20}$		8.0376(1)	8.1673(2)	5.7726(1)	378.95	59.7	Fischer and Schneider (1992)
$Cu_2(OH)PO_4$	$Cu_4Cu_4(OH)_4P_4O_{16}$	Libethenite	8.062(5)	8.384(4)	5.881(2)	397.51	65.2	Cordsen (1978)
$Zn_2(OH)AsO_4$	$Zn_4Zn_4(OH)_4As_4O_{16}$	Adamite	8.306(4)	8.524(6)	6.043(3)	427.85	63.0	Hill (1976)
$Mn_2(OH)AsO_4$	$Mn_4Mn_4(OH)_4As_4O_{16}$	Eveite	8.57(1)	8.77(1)	6.27(1)	471.25	68.4	Moore and Smyth (1968)
$(Cu_{0.42}Zn_{0.58})_2(OH)AsO_4$	$(Cu_{3.36}Zn_{0.64})Zn_4(OH)_4As_4O_{16}$		8.50(2)	8.52(2)	5.99(1)	433.80	62.7	Toman (1978)
$(Mn_{0.86}Al_{1.14})SiO_5$	$(Mn_{2.96}Al_{1.04})Mn_{0.48}Al_{3.52}Si_4O_{20}$	Kanonaite	7.959(2)	8.047(2)	5.616(1)	359.68	60.8	Weiss et al. (1981)

T = P^{5+}, As^{5+}). Prominent members of this group are libethenite, eveite and adamite (Table 1.1.21). M atoms occur in both sixfold and fivefold coordination, corresponding to Al^{3+} in andalusite, while T cations are fourfold coordinated as is Si^{4+} in andalusite. $MO_4(OH)_2$ octahedra form the edge-shared mullite-type chains, which are connected by $MO_4(OH)$ bipyramids and TO_4 tetrahedra as in andalusite. It is not known whether the phosphates and arsenates can transform to mullite-type phases at elevated temperatures. However, their relatively low thermal stability, at least at atmospheric pressure, makes this rather unlikely.

1.1.3.9 **MUL-VIII.31, *P*2₁/*n*11: Olivenite Group**

Olivenite is a hydroxyl copper arsenate (Table 1.1.22) which has been found in the oxidation zone of copper-bearing ore bodies. Olivenite is structurally related to adamite and libethenite, and thus in a wider sense belongs to the andalusite group. The structure is composed of edge-shared CuO_6 octahedra and CuO_5 bipyramids similar to the relationships in andalusite (see Figs. 1.1.17 and 1.1.18).

Table 1.1.22 MUL-VIII.31 compound: Olivenite group.

Chemical composition	Unit cell contents	Mineral name	*a* [Å]	*b* [Å]	*c* [Å]	α [°]	*V* [Å³]	ω [°]	Reference
Cu_2OHAsO_4	$Cu_4Cu_4(OH)_4$ As_4O_{16}	Olivenite	8.5894(2)	8.2073(2)	5.9285(1)	90.088(3)	417.93	63.1 2×	Burns and Hawthorne (1995)

1.1.3.10 **MUL-IV.32, *Pbnm*: Sillimanite Group**

In nature sillimanite tends to form from pelitic rocks during low- or medium-pressure metamorphism. It is one of the three polymorphs with composition $Al_2O_3 \cdot SiO_2$ (i.e. Al_2SiO_5), the other two polymorphs being andalusite (Section 1.1.3.8) and kyanite, the latter not belonging to the mullite structure family. The orthorhombic phase contains the mullite-type AlO_6 octahedral chains running parallel to the crystallographic **c** axis. Octahedral chains are connected by double chains of tetrahedra with aluminum and silicon alternating in an ordered sequence (Fig. 1.1.19). The similarity between sillimanite and mullite is remarkable (see, for example, Burnham, 1963b, 1964a), and many properties are quite similar. However, there is no complete solubility between sillimanite and mullite, at least at atmospheric pressure (see also Section 1.1.3.7).

The synthetic $PbMBO_4$ phases also have an orthorhombic sillimanite-type structure with chains of edge-sharing MO_6 octahedra. These octahedra have two highly asymmetric O-M-O bridging angles but a constant M-M distance of 2.97 Å. The explanation of the deformation of the octahedra is the rigid nature of the BO_3 groups connecting octahedral chains (Fig. 1.1.20). Octahedral cations are Al^{3+}, Ga^{3+}, Fe^{3+}, Cr^{3+} and Mn^{3+} (Park and Barbier, 2001, Park et al. 2003b). The large

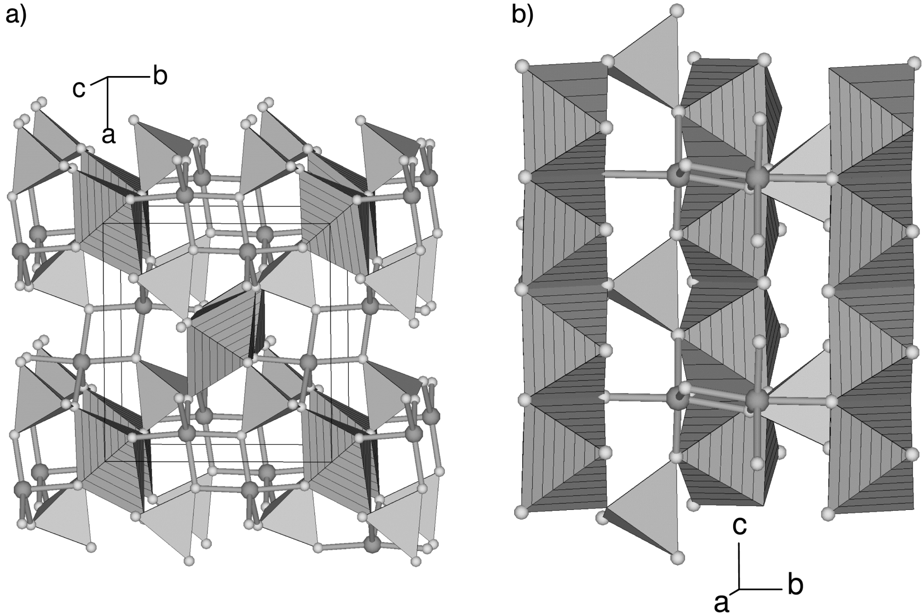

Fig. 1.1.18 Projections of the crystal structure of olivenite (Burns and Hawthorne, 1995). (a) View parallel **c** rotated by 6° about **a** and **a** × **c**. (b) View parallel **a** rotated by 2° about **a** × **c** and 4° about **c**.

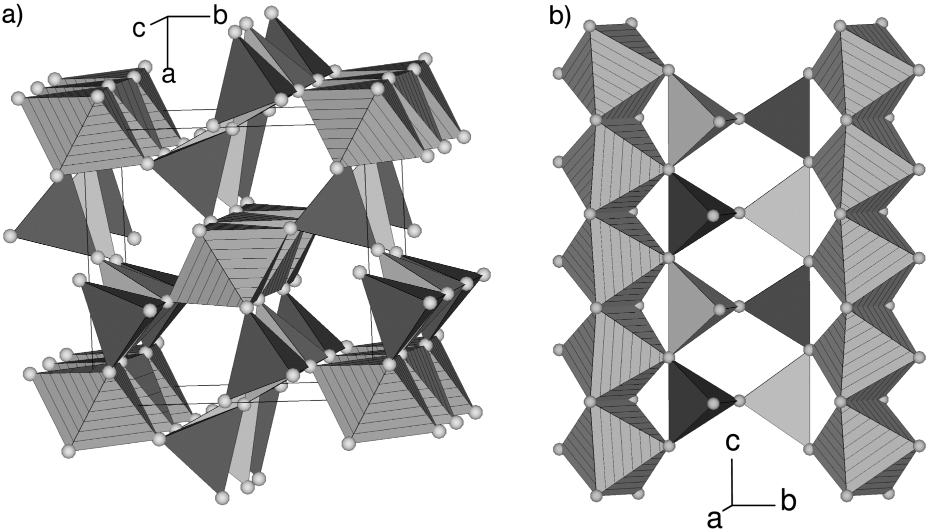

Fig. 1.1.19 Crystal structure projections of sillimanite (Yang et al. 1997). AlO_4 tetrahedra are light gray, SiO_4 tetrahedra are dark gray. (a) View parallel **c** rotated by 10° about **a** and 5° about **b**. (b) View parallel **a** rotated by 2° about **b** and **c**. Chains extended in **c**.

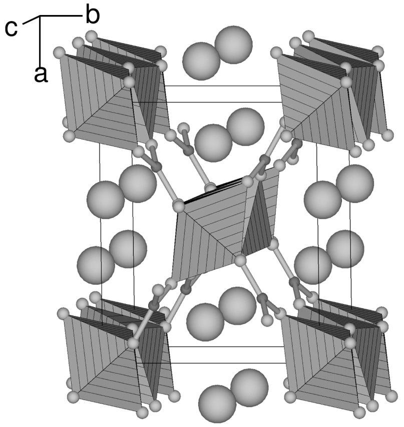

Fig. 1.1.20 Crystal structure projections of $PbGaBO_4$ (Park and Barbier, 2001). B and Pb atoms are represented by small and large spheres, respectively. View parallel **c** rotated by 10° about **a** and 5° about **b**.

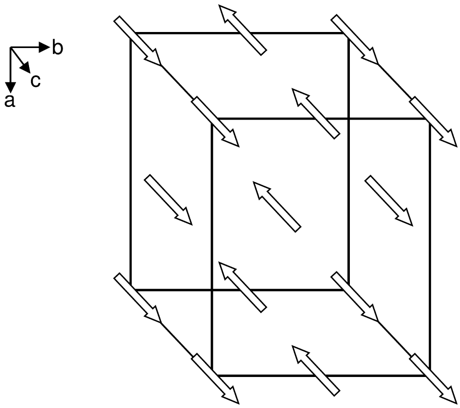

Fig. 1.1.21 The magnetic structure of $PbFeBO_4$ showing antiferromagnetism. Arrows indicate areas of equal magnetization (after Park et al. 2003a).

lead atoms enter the structural channels for charge compensation and geometrical stabilization reasons. As a result of the transition metal incorporation the octahedral chains of the $PbMBO_4$ phases display one-dimensional magnetic behavior. The chromium and iron compounds are characterized by intrachain antiferromagnetism (Fig. 1.1.21), whereas the manganese shows ferromagnetic coupling. Interchain correlations are always ferromagnetic, which means that these phases belong to the class of insulating ferromagnets.

The sillimanite-group compounds are listed in Table 1.1.23. While in sillimanite the octahedral axes in the **ab**-plane are closer to the **b** axis, and the *a* lattice constant is slightly smaller than *b*, the situation is reversed in the other compounds of this group. This could be adjusted by transforming the unit cell interchanging **a** and **b** yielding a strictly standardized setting. However, the space group of the resulting structure in the new setting would be *Pnam* and therefore would represent a new branch in the Bärnighausen tree in Fig. 1.1.4. For simplicity and convenience such a strict standardization is neither applied here nor in other groups.

1.1.3.11 **MUL-VIII.33, $A2_1am$: A_9B_2 Boron Aluminates**

The boron aluminate usually designated as A_9B_2 (i.e. $9Al_2O_3 \cdot 2B_2O_3$) is a synthetic compound not yet identified in nature (Table 1.1.24). It directly forms from the oxides or by transformation of $Al_{6-x}B_xO_9$ above about 1050 °C (see Section 1.1.3.14). Without any atomic deficiency or atomic replacement, its calculated composition is $10Al_2O_3 \cdot 2B_2O_3$. However, if less than 2% of the aluminum in the structure are replaced by boron atoms this may result in a composition near $9Al_2O_3 \cdot 2B_2O_3$. Since it is extremely difficult to determine the chemical composi-

Table 1.1.23 MUL-IV.32 compounds: Sillimanite group.

Chemical composition	Unit cell contents	Mineral name	*a* [Å]	*b* [Å]	*c* [Å]	*V* [Å³]	ω [°]	Reference
Al_2SiO_5	$Al_4Al_4Si_4O_{20}$	Sillimanite	7.4857(8)	7.6750(9)	5.7751(7)	331.80	57.3	Yang et al. (1997)
$Pb(Fe,Mn)(VO_4)OH$	$(Fe_{0.8}Mn_{0.2})4Pb_4V_4O_{16}(OH)_4$	Čechite	9.435	7.605	6.099	437.62	52.1	Pertlik (1989)
$PbZn(VO_4)OH$	$Zn_4Pb_4V_4O_{16}(OH)_4$	Descloizite	9.416(2)	7.593(2)	6.057(1)	433.05	52.4	Hawthorne and Faggiani (1979)
$(Pb_{2.8}Fe_{1.2})Cu_4O_{1.6}(VO_4)_4(OH)_2$	$(Cu_4Pb_{2.8}Fe_{1.2}V_4O_{17.6}(OH)_2$	Mottramite	9.640(5)	7.525(7)	5.900(3)	427.99	48.1	Permer et al. (1993)
$Pb(Cu_{0.81}Zn_{0.12})VO_4(OH)$	$(Cu_{0.85}Zn_{0.15})_4Pb_4V_4O_{16}(OH)_4$	Mottramite	9.316(4)	7.667(4)	6.053(2)	432.34	49.6	Cooper and Hawthorne (1995)
$PbMnVO_4(OH)$	$Mn_4Pb_4V_4O_{16}(OH)_4$	Pyrobelonite	9.507(2)	7.646(2)	6.179(1)	449.15	51.9	Kolitsch (2001)
$PbGaBO_4$	$Ga_4Pb_4B_4O_{16}$		8.2495(11)	6.9944(10)	5.8925(8)	340.00	74.4	Park and Barbier (2001)
$PbCrBO_4$	$Cr_4Pb_4B_4O_{16}$		8.1386(11)	6.9501(10)	5.9410(8)	336.05	75.1	Park et al. (2003b)
$PbMnBO_4$	$Mn_4Pb_4B_4O_{16}$		8.6418(11)	6.7062(9)	5.9429(8)	344.41	69.8	Park et al. (2003b)
$PbFeBO_4$	$Fe_4Pb_4B_4O_{16}$		8.3339(17)	7.0089(14)	5.9412(12)	347.03	72.5	Park et al. (2003b)
$PbAlBO_4$	$Al_4Pb_4B_4O_{16}$		8.0215(6)	6.9209(5)	5.7134(4)	317.19	77.8	Park et al. (2003a)

Table 1.1.24 MUL-VIII.33 compounds: A_9B_2 boron aluminates group.

Chemical composition	Unit cell contents	*a* [Å]	*b* [Å]	*c* [Å]	*V* [Å³]	ω [°]	Reference
$Al_{18}B_4O_{33}$	$Al_8Al_{11.6}B_{4.4}O_{36}$	7.6942(1)	15.0110(2)	5.6689(1)	654.74	67.5	Garsche et al. (1991)
$Al_{16.6}Cr_{1.4}B_4O_{33}$	$Al_8Al_{10.1}Cr_{1.5}B_{4.4}O_{36}$	7.7051(1)	15.0637(2)	5.7001(1)	661.60	66.9	Garsche et al. (1991)

tion of these nano-sized compounds the actual composition of these phases remains a point of dispute and may vary to a certain extent from sample to sample. Nevertheless it is reasonable to retain the general designation A_9B_2. Owing to the stability of A_9B_2 boron aluminate up to about 1200 °C, its low thermal expansion coefficient and the low thermal conductivity, and because of the corrosion resistance against molten B_2O_3-rich glasses, A_9B_2 boron aluminates have been widely used as refractory linings and for thermal insulation (see Wada et al. 1993, 1994, Rymon-Lipinski et al. 1985). A_9B_2 boron aluminate forms whiskers via a gas-transport reaction, thus making it available for, for example, reinforcement of metal matrices for automotive engine parts.

Ihara et al. (1980) and Garsche et al. (1991) found a A_9B_2 boron aluminate ($x = 1$) with a doubled b parameter. The mullite-type AlO_6 octahedral chains in A_9B_2 display a repeat distance of about 5.7 Å, indicating a sequence of two octahedra to identity. The octahedral chains are linked by edge-sharing AlO_5 bipyramids alternating with isolated AlO_4 tetrahedra and BO_3 triangles (Ihara et al. 1980, Garsche et al. 1991, Fig. 1.1.22). The occurrence of AlO_6, AlO_5 and AlO_4 polyhedra has been confirmed by ^{27}Al NMR satellite transition spectroscopy (SATRAS, Kunath et al. 1992). Garsche et al. found that A_9B_2 is able to incorporate up to about 10 wt.% Cr_2O_3, with Cr^{3+} substituting Al^{3+} in the octahedra.

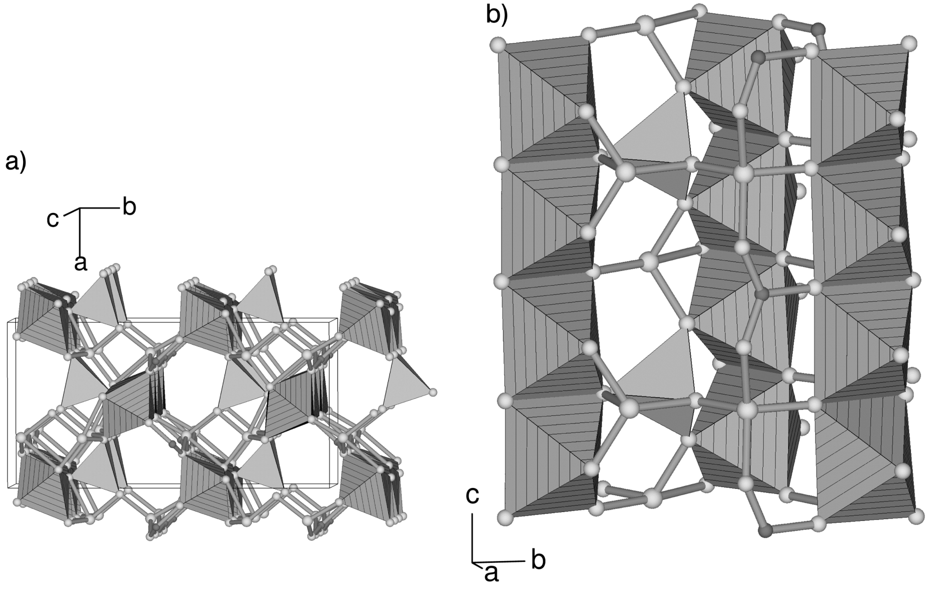

Fig. 1.1.22 Projections of the crystal structure of $Al_{18}B_4O_{33}$ (A_9B_2) (Garsche et al. 1991). (a) View parallel **c** rotated by 2° about **b** and 4° about **a**. (b) View parallel **a** rotated by 10° about **b** and **c**.

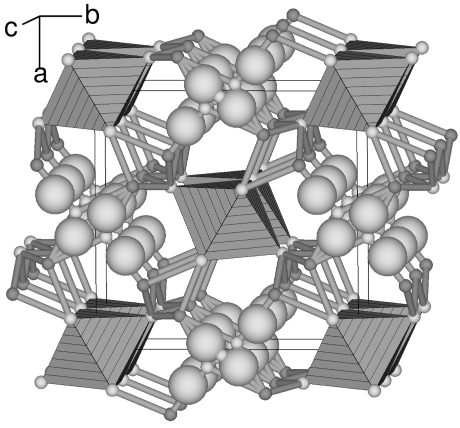

Fig. 1.1.23 Projections of the crystal structure of $Al_5Ge_{0.972}Pb_{0.2}O_{9.71}$ (Saalfeld and Klaska, 1985). View parallel to **c** rotated by 4° about **a** and **b**.

1.1.3.12 MUL-IV.34, $P2_12_12$: $Al_5Ge_{0.972}Pb_{0.2}O_{9.71}$ Phase

Saalfeld and Klaska (1985) described an Al_2O_3-rich germanium mullite with 8.2 wt.% PbO and 2.4 wt.% Nd_2O_3 (Table 1.1.25). It has been shown that the large Pb^{2+} and Nd^{3+} ions are incorporated at O3 oxygen vacancies in the mullite structure (Figs. 1.1.14b and 1.1.23), thus representing a partially filled structure. The investigations provide further evidence for the mullite structure's ability to incorporate foreign cations at various structural sites. Depending on the size and charge of the cations, they may enter octahedral or tetrahedral sites substituting Al^{3+}, or are incorporated interstitially in the structural channels running parallel to the crystallographic **c** axis or in structural voids produced by O3 oxygen vacancies.

1.1.3.13 MUL-VIII.34, $P2_12_12_1$: Mozartite Group

A large variety of mullite-type phases of the composition $CaM(OH)TO_4$ has been described (octahedrally coordinated cations M = Al^{3+}, Mn^{3+}, Cu^{2+}, Zn^{2+}, tetrahedrally coordinated cations T = Si^{4+}, V^{5+}, As^{5+}, see Table 1.1.26). Prominent members are mozartite ($CaMn(OH)SiO_4$), vuagnatite ($CaAl(OH)SiO_4$) and adelite ($Ca(Cu,Ni,Zn)(OH)(V,As)O_4$). The silicates mozartite and vuagnatite differ from the vanadates and arsenates of the adelite group (Table 1.1.26) by their charge distribution. In mozartite and vuagnatite the edge-sharing octahedral chains are formed by the trivalent cations Al^{3+} and Mn^{3+} (Fig. 1.1.24), whereas in adelite the divalent Cu^{2+}, Ni^{2+} and Zn^{2+} ions enter the octahedral sites. In the latter case the positive charge deficit is balanced by the tetrahedral cations As^{5+} and V^{5+}, while Si^{4+} occurs in mozartite and vuagnatite. The higher valence state of tetrahedral cations in adelite leads to electrostatically more saturated oxgygen atoms of the tetrahedra. The divalent octahedral cations of these compounds, on the other hand, produce a slight undersaturation of the octahedral oxygen atoms and causes an affinity for protonization. This favors the formation of octahedrally bound hydroxyl (OH) groups.

Of special crystallochemical interest are compounds showing Jahn-Teller distor-

Table 1.1.25 MUL-IV.34 compound: $Al_5Ge_{0.972}Pb_{0.2}O_{9.71}$ phase.

Chemical composition	Unit cell contents	*a* [Å]	*b* [Å]	*c* [Å]	*V* [Å³]	ω [°]	Reference
$Al_{5.03}Ge_{0.97}Pb_{0.15}\ Nd_{0.06}O_{9.71}$	$Al_2Al_3Ge_{0.972}Pb_{0.2}O_{9.71}$	7.6648(4)	7.7914(3)	2.9213(1)	174.46	61.4	Saalfeld and Klaska (1985)

Table 1.1.26 MUL-VIII.34 compounds: Mozartite group.

Chemical composition	Unit cell contents	Mineral name	*a* [Å]	*b* [Å]	*c* [Å]	*V* [Å³]	ω [°]	Reference
$CaAlOHSiO_4$	$Al_4Ca_4(OH)_4Si_4O_{16}$	Vuagnatite	7.055(6)	8.542(7)	5.683(5)	342.48	52.3	McNear et al. (1976)
$CaMnOHSiO_4$	$Mn_4Ca_4(OH)_4Si_4O_{16}$	Mozartite	7.228(1)	8.704(1)	5.842(1)	367.53	46.3	Nyfeler et al. (1997)
$PbZnOHAsO_4$	$Zn_4Pb_4(OH)_4As_4O_{16}$	Arsen-descloizite	7.646(2)	9.363(2)	6.077(1)	435.05	52.6	Keller et al. (2003)
$CaZnOHAsO_4$	$Zn_4Ca_4(OH)_4As_4O_{16}$	Austinite	7.5092(8)	9.0438(9)	5.9343(8)	403.01	49.8	Clark et al. (1997)
$CaNiOHAsO_4$	$Ni_4Ca_4(OH)_4As_4O_{16}$	Nickel-austinite	7.455(3)	8.955(3)	5.916(2)	394.95	52.1	Cesbron et al. (1987)
$CaMgOH(V,As)O_4$	$Mg_4Ca_4(OH)_4V_3AsO_{16}$	Gottlobite	7.510(4)	9.004(5)	5.948(3)	402.20	51.2	Witzke et al. (2000)
$PbCuOHAsO_4$	$Cu_4Pb_4(OH)_4As_4O_{16}$	Duftite	7.768(1)	9.211(1)	5.999(1)	429.23	51.0	Kharisun et al. (1998)
$CaCuOHAsO_4$	$Cu_4Ca_4(OH)_4As_4O_{16}$	Conichalcite	7.4	5.842	9.21	398.16	47.6	Qurashi and Barnes (1963)
$CaCuOH(V,As)O_4$	$Cu_4Ca_4(OH)_4(V_{2.36}As_4)_{16}$	Calciovolborthite[a]	5.836(1)	7.430(2)	9.347(1)	405.30	47.9	Basso et al. (1989)

a) The name tangeite was proposed by Basso et al. (1989)

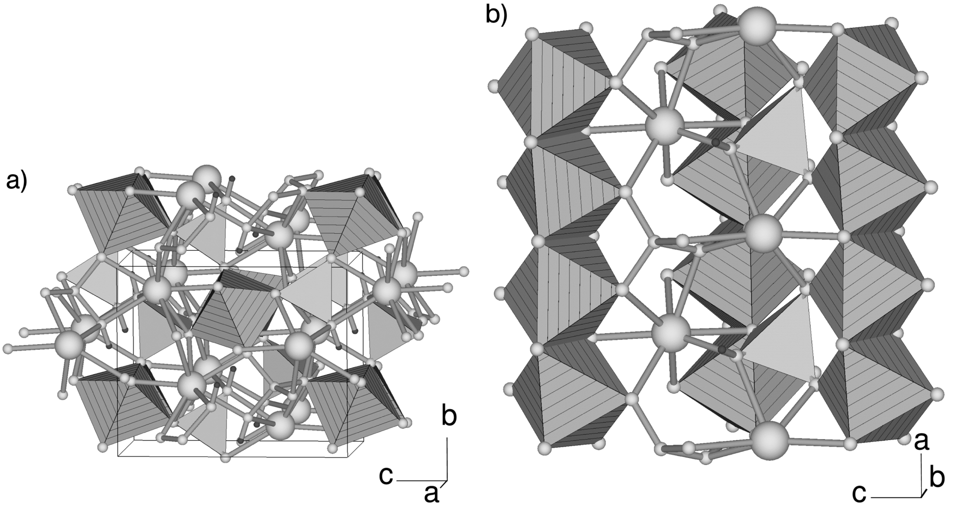

Fig. 1.1.24 Projections of the crystal structure of mozartite (Nyfeler et al. 1997). (a) View parallel **a** rotated by 6° about **b** and **c**. (b) View parallel **b** rotated by 5° about **c** and 10° about **a**.

tion of the octahedra. The $Mn^{3+}O_6$ octahedra of mozartite display approximately orthorhombic geometry, which is explained by the combination of a tetragonally compressed Jahn-Teller effect and lattice-induced stress. Comparison with the isostructural vuagnatite, with no electronically induced distortions, indicates that the distorted octahedral geometry in mozartite causes shifts of the valence sums of oxygen atoms being hydrogen bonded. As a consequence the OH groups in mozartite are located at the isolated SiO_4 apex and not bonded to the octahedra as in some of the isostructural phases. Owing to the specific structural arrangement of mozartite the OH–O distance in mozartite is very short (<2.5 Å). The compounds of the adelite group with tetrahedral As^{5+} and V^{5+} show a different Jahn-Teller distortion with tetragonally elongated geometry for $Cu^{2+}O_6$.

1.1.3.14 **MUL-XVI.351, *A*112/*m*: Boralsilite Group**

Boralsilite The natural mineral boralsilite, with the ideal composition $Al_{16}B_6Si_2O_{37}$, occurs as a high temperature phase in pegmatites of the granulite facies in metapelitic rocks. The basic mullite-type AlO_6 octahedra chains determine a lattice constant of about 5.6 Å (in the boralsilite setting this is the *b* constant), reflecting twice the periodicity of the AlO_6 octahedron (twice the O–O edge length in the octahedron of about 2.8 Å). A number of inter-chain units connect the octahedral chains in boralsilite: dimers of corner-sharing SiO_4 and AlO_4 tetrahedra, and dimers of edge-sharing AlO_5 bipyramids joined above by BO_3 triangles and laterally by BO_4 tetrahedra. Thus Al occurs in tetrahedral, bipyramidal and

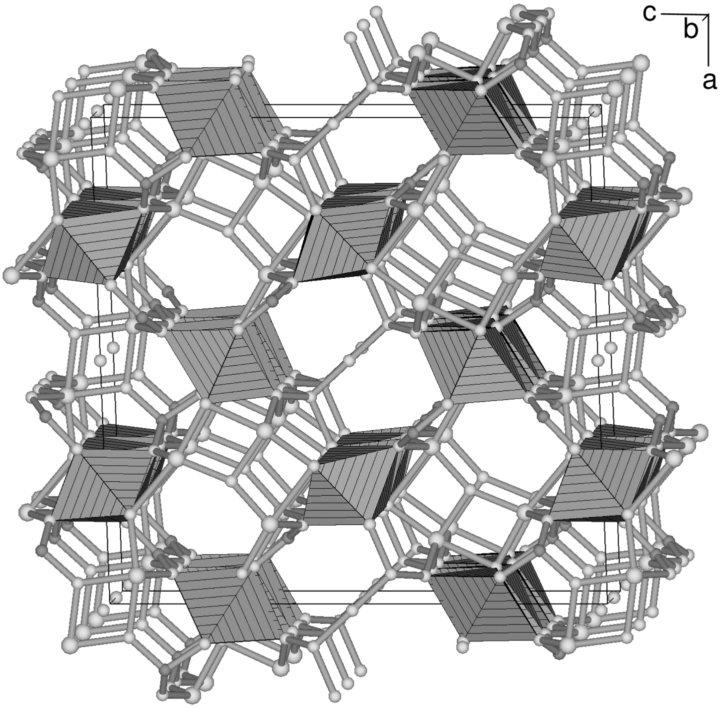

Fig. 1.1.25 Projection of the crystal structure of boralsilite. View parallel **b** rotated by 4° about **a** × **c** and **c** (Peacor et al. 1999).

octahedral coordination (Peacor et al. 1999, Fig. 1.1.25). Substitutions of Mg^{2+}, Fe^{2+} and Fe^{3+} for Al^{3+} and of Al^{3+} for Si^{4+} allows a wide range of mixed crystal formation. Furthermore, partial site occupancies in boralsilite may give rise to a solid solution with werdingite, the boron aluminates $Al_{6-x}B_xO_9$ and A_9B_2, and with aluminum-silicon mullite (mullite in the strict sense).

$Al_{6-x}B_xO_9$ boron aluminates Scholze (1956) was among the first to describe $Al_{6-x}B_xO_9$ with $x = 2$ (i. e. $Al_4B_2O_9$). Mazza et al. (1992) described members of the solid-solution series $Al_{6-x}B_xO_9$ with $1 < x < 3$ crystallizing in space group *Pbam* with lattice constants similar to mullite. According to Mazza et al. these boron aluminates display a pseudo-tetragonal metric with $a = b$. Fischer et al. (2005), however, found that the compound with $x \approx 2$ is monoclinic with space group A $2/m$. Fischer et al. (2005) also suggested that the structure of this boron aluminate is strongly related to boralsilite, with Si^{4+} being replaced by Al^{3+}, and with the lattice constants being doubled ($a = 15.05$ Å, $b = 14.81$ Å, $c = 5.54$ Å, monoclinic angle $\gamma = 90.9°$) with respect to Mazza's unit cell. The mullite-type backbone of the structure, the edge-sharing AlO_6 octahedral chains, are crosslinked by AlO_4 and BO_4 tetrahedra, AlO_5 bipyramids and BO_3 triangles. One oxygen atom is disordered on an interstitial site. Voll et al. (2005) showed that a complete solid solution

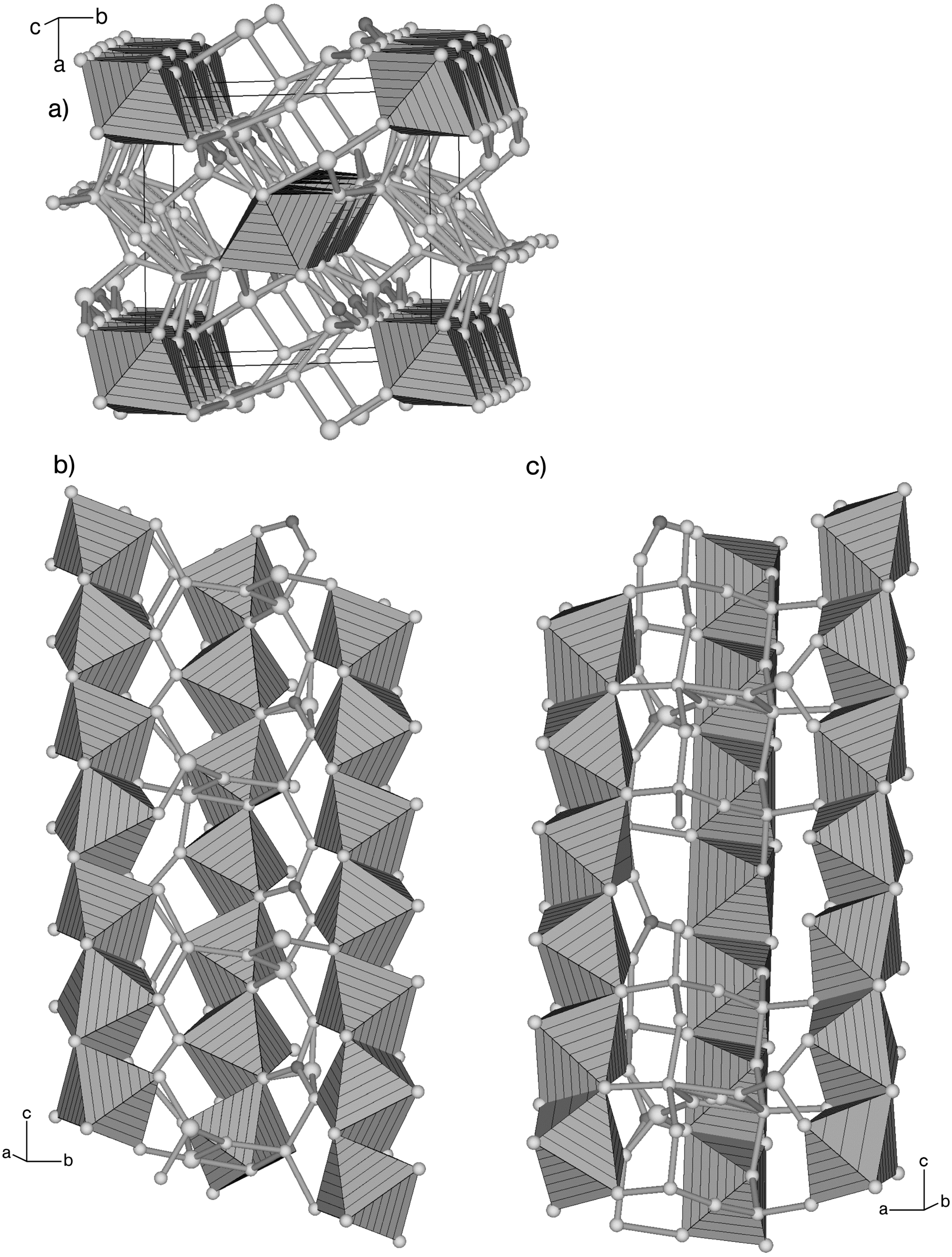

Fig. 1.1.26 Projections of the crystal structure of werdingite (Niven et al. 1991). (a) View approximately parallel **c**. (b) View approximately parallel **a**. (c) View approximately parallel **b**.

Table 1.1.27 MUL-XVI.351 compound: Boralsilite group.

Chemical composition	Unit cell contents	Mineral name	*a* [Å]	*b* [Å]	*c* [Å]	γ [°]	*V* [Å^3]	Reference
$Al_{16}B_6Si_2O_{37}$	$Al_{12}Al_{20}B_{12}Si_4O_{74}$	boralsilite	15.079(1)	14.767(1)	5.574(1)	91.96(1)	1240.4	Peacor et al. (1999)

Table 1.1.28 MUL-XXXII.352 compound: Werdingite group.

Chemical composition	Unit cell contents	Mineral name	a [Å]	*b* [Å]	*c* [Å]	α [°]	β [°]	γ [°]	*V* [Å^3]	Reference
$(Mg_{0.84}Fe_{0.16})2Al_{12}(Al_{0.79}Fe_{0.21})_2Si_4B_2(B_{0.77}Al_{0.23})_2O_{37}$	$Al_8(Mg_{0.84}Fe_{0.16})2Al_4(Al_{0.79}Fe_{0.21})_2Si_4B_2(B_{0.77}Al_{0.23})_2O_{37}$	Werdingite	7.995(2)	8.152(1)	11.406(4)	110.45(2)	110.85(2)	84.66(2)	650.5	Niven et al. (1991)

exists between Al_5BO_9 ($x = 1$, Al_2O_3-rich) and $Al_4B_2O_9$ ($x = 2$, B_2O_3-rich). Nuclear magnetic resonance inspection clearly shows that the Al_2O_3-rich compound Al_5BO_9 has boron in triangular coordination only, while the B_2O_3-rich phase $Al_4B_2O_9$ contains both triangular and tetrahedrally coordinated boron. The $Al_{6-x}B_xO_9$ phases are stable in a small temperature region (950 to 1050 °C). At higher temperatures they transform to A_9B_2 boron-aluminate ($Al_{18}B_4O_{33}$, see Section 1.1.3.11). Since both compounds belong to the mullite structure family a topotactical transformation with preservation of the octahedral chains is predicted.

1.1.3.15 **MUL-XXXII.352, $P\bar{1}$: Werdingite Group**

Werdingite (ideal formula: $Mg_2Al_{14}Si_4B_4O_{37}$, Moore et al. 1990) occurs in nature in high grade Al_2O_3-rich metamorphic rocks of the granulite facies. In the triclinic phase (space group: $P\bar{1}$) part of Mg^{2+} can be substituted by Fe^{2+}, although the pure magnesium end member of werdingite has been synthesized at elevated temperatures and pressures as well (Werding and Schreyer, 1992). In werdingite the mullite-type octahedral AlO_6 chains are crosslinked by Si_2O_7 and $(Al,Fe)_2O_7$ dimers with typical Si-Si, Al-Al, and (Al,Fe)-(Al,Fe) pairs, $(Al,Mg)O_5$ bipyramids and by BO_3 triangles (Fig. 1.1.26). Formally, the werdingite crystal structure can be derived from that of mullite by the following substitutions:

$$Al^{3+} \rightarrow Si^{4+} + 0.5\ O^{2-}; \qquad B^{3+} \rightarrow Si^{4+} + 0.5\ O^{2-}; \qquad Mg^{2+} \rightarrow Al^{3+} + 0.5\ O^{2-}$$

Cation substitutions go along with the formation of oxygen vacancies (Niven et al. 1991). Because of the various cation substitutions a wide range of mixed crystals can form with coupled cation replacements of Fe^{2+} for Mg^{2+}, Fe^{3+} for Al^{3+} and Al^{3+} for B^{3+} and with various cation ordering schemes. In spite of similar local arrangements no long-range structural correspondence exists between werdingite and grandidierite, andalusite and the boron-aluminates $Al_{6-x}B_xO_9$ and A_9B_2.

Acknowledgments

We thank Werner H. Baur (Evanston) for his comments on the manuscript and for his valuable suggestions, and Elke Eggers (Bremen) for typesetting and formatting the tables.

1.2

The Real Structure of Mullite

S. Rahman and S. Freimann

1.2.1

Introduction

X-ray and electron diffraction patterns of 3/2- and 2/1-mullite show besides the Bragg reflections diverse diffuse scattering phenomena in nearly the whole reciprocal space. The reason for such diffuse scattering is structure disorder. The diffuse scattering in mullite is caused by a certain distribution of oxygen vacancies coupled with cation shifts, resulting in a complicated real-structure configuration. Generally, a real structure cannot be described by a single structure unit (unit cell), which repeats periodically in all three dimensions. In fact, the real structure contains many structure variants, which are distributed by certain rules or functions.

The physical (electrical, mechanical, thermal, optical) properties of crystalline solids depend on the atomic structure. According to the disorder type (point defects, stacking faults, modulations, short-range order, domain formation) a deviation from the ideal structure is present and hence the physical properties are influenced. In order to describe the physical behavior of a crystalline solid a real-structure determination is needed. In the case of mullite, the complex diffuse scattering phenomena cannot be interpreted by classical disorder theories (Daniel and Lipson, 1944, Jagodzinski, 1949, 1964a, 1964b, Kunze, 1959, Korekawa, 1967, Korekawa et al. 1970, De Wolff, 1974, Böhm, 1977, Boysen et al. 1984). For evaluation of the mullite real structure, X-ray single-crystal diffraction and high-resolution electron microscopy (HREM) were applied. The results obtained from the X-ray and HREM investigations were used as input data for a simulation and reconstruction technique, called the videographic method (Rahman, 1991), to determine and describe the real structure of 3/2- and 2/1-mullite.

1.2.2
High-resolution Electron Microscopy

High-resolution electron microscopy (HREM) is one of the most important experimental methods for determining the real structure of disordered single crystals. Deviations from the ideal periodic arrangement (point defects, modulations, short-range order, domain boundaries, etc.) are typical examples that can be examined applying HREM. A proper interpretation of the experimental real-structure images is only possible via contrast simulations using predefined superstructure models.

HREM investigations of mullite were first performed for Al-rich mullite ($0.25 < x < 0.4$, see Section 1.1.3.7) by Nakajima et al. (1975), who directly correlated varying spot intensities with different vacancy concentrations along [010]. The authors ascertained a periodic arrangement of increased vacancy concentrations every third or fourth layer parallel to [100]. Based upon image simulations, Ylä-Jääski and Nissen (1983) observed in mullites with $x = 0.48$ and 0.54 antiphase domain boundaries running parallel to [100] and slightly inclined against [601], respectively. In an investigation of 1.71/1-mullite, which was obtained from sintering Al_2O_3 and $ZrSiO_4$, Schryvers et al. (1988) reported a random distribution of vacancies without any direct correlation between contrast pattern and vacancy distribution. Comparable results to Schryvers et al. (1988) were published for 3/2-mullite by Epicier et al. (1990) and Epicier (1991), who stated that less than 50% vacancies cannot be detected along [001] and the vacancies are randomly

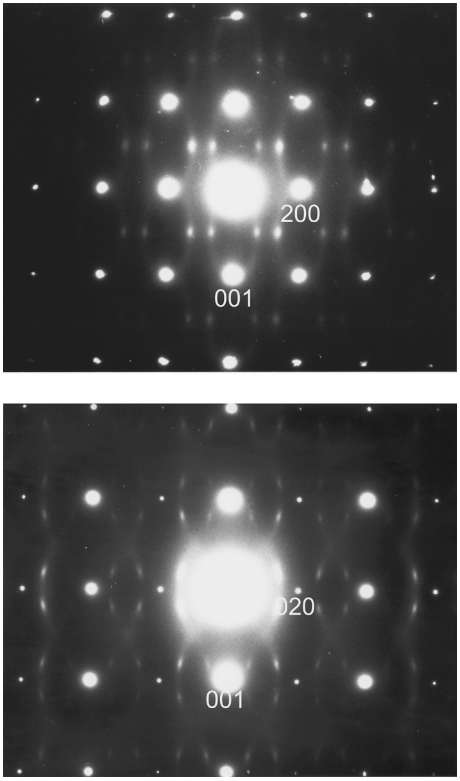

Fig. 1.2.1 Electron diffraction pattern (top) *h*0*l* plane, (bottom) 0*kl* plane of 2/1-mullite.

distributed. However, a random distribution of oxygen vacancies in the mullite structure would cause a monotone diffuse background in contrast to the observed diffuse maxima with different shapes in the diffraction patterns of mullite (Fig. 1.2.1).

Using systematically developed structure models, an attempt was made by Rahman and Weichert (1990) and Rahman (1993b, 1994a) to determine the arrangement of oxygen vacancies semi-quantitatively (always coupled to an occupation of an Al* site) by analyzing observed differences of the image contrast in HREM images of the *ab* plane. In further investigations (Paulmann et al. 1994, Rahman et al. 1996) 200-kV and 300-kV HREM images of mullite with beam direction parallel to [010] and [100] have been compared with extensive multi-slice calculations of structure models with different oxygen-vacancy arrangements.

This section presents the experimental results of HREM and their interpretation regarding the oxygen-vacancy distribution in the three main planes via contrast simulation. Hitachi H-800 and H-9000 electron microscopes operating at 200 and 300 kV, respectively, were used for the high-resolution observations. Both microscopes were equipped with LaB_6 cathodes and top-entry high-resolution specimen stages with a ±15° tilting angle. The images were recorded either on photographic film or, in special cases (image reconstruction), by using a video unit connected to

Table 1.2.1 Microscopic constants (H-800 and H-9000) used for image simulations.

	H-800	H-9000
Accelerating voltage [kV]	200	300
Wavelength λ [nm]	0.0025079	0.0019688
Spherical aberration C_s	1.0	0.9
Chromatic aberration C_c	1.1	1.5
Focus spread Δ [nm]	5	5
Divergence α [rad]	5×10^{-4}	5×10^{-4}

an image-processing system. All of the HREM images were taken from very thin mullite crystals ($t = 2$-4 nm, $x = 0.25$ and 0.4) with the electron beam parallel to the [001], [010] and [100] zone axes. Preparation of the crystallites for the investigations was carried out by crushing them with propanol in an agate mortar and transferring the suspension onto copper grids covered with a perforated carbon film. The microscope constants adopted for the image simulations are listed in Table 1.2.1. The image contrast simulations were done using the program system SIM40 (Rahman and Rodewald, 1992) based upon the multi-slice approximation (Cowley and Moodie, 1957). The program system was specially developed for the contrast simulation of real structures.

Diffuse scattering with different intensity distributions is observed when *h*0*l* and 0*kl* electron-diffraction patterns are examined (Fig. 1.2.1). The diffuse maxima of the *h*0*l* plane at the positions $2h\pm2/3$, 0, $l\pm1/2$ were interpreted in the past by several authors (McConnell and Heine, 1985, Angel and Prewitt, 1987, Angel et al. 1991, Padlewski et al. 1992b) as satellite reflections, indicating a twofold modulation of the *c* axis and an incommensurate modulation along the *a* axis. Such an interpretation, assuming maximal ordering, ignored the diffuse streaks running approximately parallel to the c^* axis. However, the 0*kl* diffraction pattern shows diffuse maxima at positions 0, $2k\pm2/3$, $l\pm1/5$, which does not agree with a doubling of the *c* lattice constant within this plane. Furthermore, many other diffuse figures are present, for example cross-shaped streaks in the 0*kl* plane, and many complicated diffuse scattering phenomena in reciprocal planes perpendicular to c^* (Freimann and Rahman, 2001), which will be presented and discussed in Section 1.2.3.

In order to interpret the experimental HREM images and to determine the oxygen vacancy distribution, contrast simulations with predefined structure models were calculated for the three main directions. To investigate the influence of contrast variation with different concentrations of vacancies along the beam direction, calculations with a $5a \times 5b \times 6c$ super cell were performed with individual slice sequences as shown schematically in Fig. 1.2.2a (only the vacancy positions are shown). To avoid cut-off effects in calculations of the (010) and (100) plane, the first and last slice were chosen to be vacancy-free. The projected vacancy distributions and concentrations are presented schematically in Fig. 1.2.2b–d, while the corre-

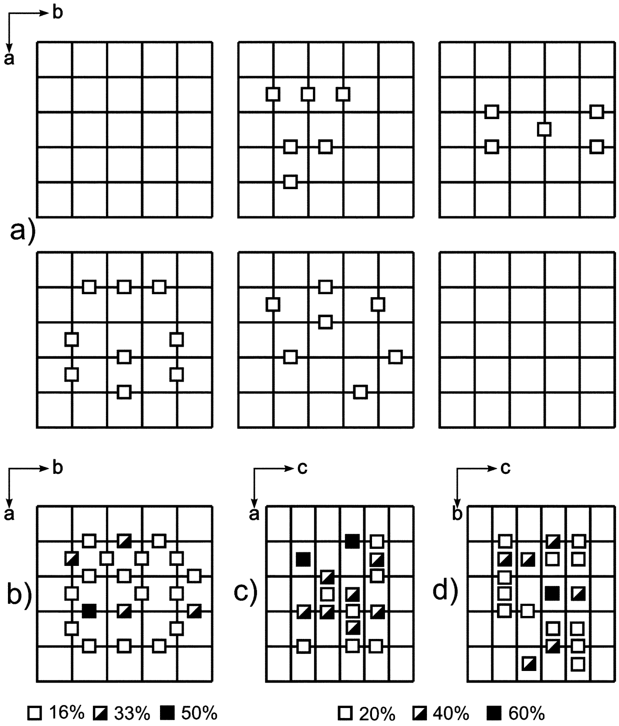

Fig. 1.2.2 (a) Slice sequences for HREM contrast simulation of vacancy distributions; (b) Vacancy concentrations projected on (001); (c) Vacancy concentrations projected on (010); (d) Vacancy concentration projected on (100).

sponding calculated images along [010], [100] and [001] are shown in Figs. 1.2.3 and 1.2.4, respectively. Depending on the actual defocus value (–35 nm, –75 nm), an accurate detection of about 20% vacancy concentration is possible in [010] and [100] (Fig. 1.2.3).

In the case of (010) simulations (Fig. 1.2.3) the contrast maxima directly coincide with the projected O_C (i.e. O3) positions and higher vacancy concentrations cause an easily detectable intensity enhancement of the corresponding dot in the calculated image due to the associated cation shifts (Al*) near the oxygen vacancy. Similarly in (100) simulations (Fig. 1.2.3) oxygen vacancies are responsible for the appearance of an additional dot between the main maxima. A simultaneous shifting of the neighbouring main maxima results in a broad dot of higher intensity with enhanced dark regions along [010] in the immediate vicinity of a vacancy position.

In comparison, simulations of the (001) plane (Fig. 1.2.4) are characterized by four more-or-less elongated maxima within a mullite unit cell, best resolved at defocus values of –50 nm and –55nm. As discussed earlier in more detail (Rahman and Weichert, 1990, Rahman, 1993b, Rahman, 1994a), the maxima can be

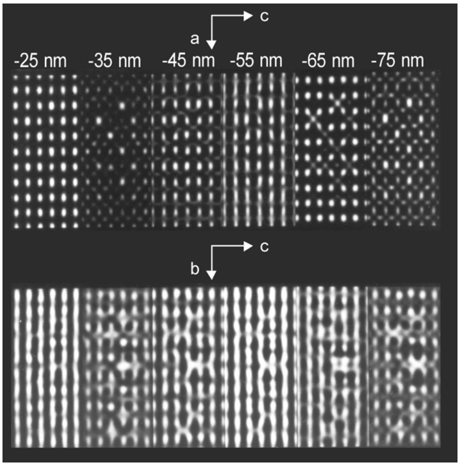

Fig. 1.2.3 HREM contrast simulations along [010] (top) and [100] (bottom) of the 3D structure model shown in Fig. 1.2.2a (thickness = 3.84 nm and 3.78 nm).

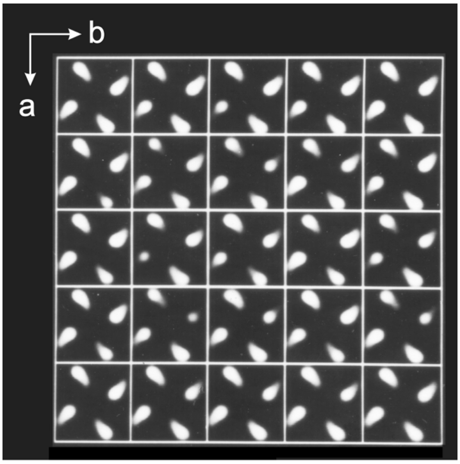

Fig. 1.2.4 HREM contrast simulation along [001] of the 3D structure models shown in Fig. 1.2.2a (thickness = 3.46 nm, $\Delta F = -50$ nm). The simulated contrast becomes reduced in the vicinity of an oxygen vacancy.

directly correlated with channels beside the O_c (O3) positions. The channels are further enhanced by introducing an oxygen vacancy and cause the contrast located clockwise next to an oxygen vacancy to become less intense. A correlation with occupied Al* positions is obvious, so that contrast changes are mainly affected by cation shifts. This simple relationship and the correspondence of the simulated contrast pattern (Fig. 1.2.4) with the experimental structure image (Fig. 1.2.5) permit a semi-quantitative determination of enhanced vacancy concentrations along [001] for a thin mullite crystal. Since comparable results with negligible differences were obtained for multi-slice simulations along the main crystallographic direc-

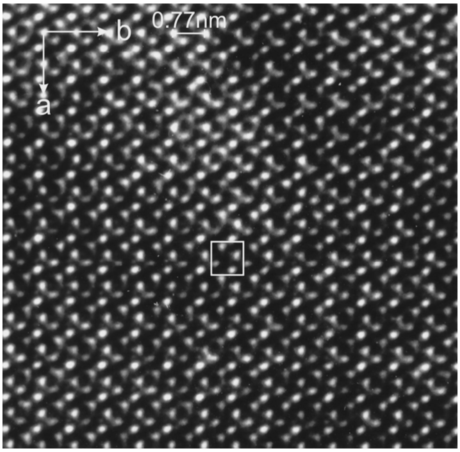

Fig. 1.2.5 HREM image (200 kV) of the *ab* plane of 3/2-mullite. One unit cell is outlined.

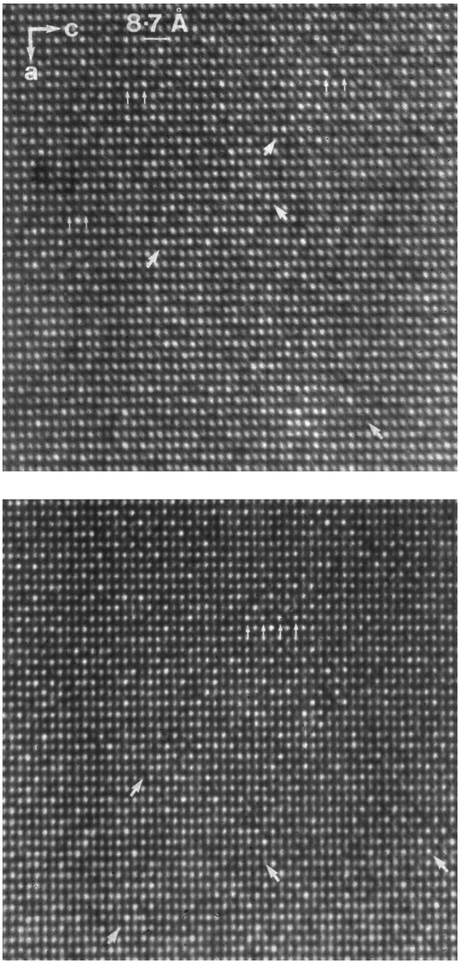

Fig. 1.2.6 200-kV HREM images of 3/2-mullite (top) and 2/1-mullite (bottom) along [010]. The arrows indicate the preferred orientations of oxygen vacancies along <102>. Small arrows indicate the twofold periodicity along [001] in the projection.

tions with an accelerating voltage of 300 kV, a separate presentation is not required.

HREM images of 3/2- and 2/1-mullite with a beam direction parallel to [010] and an approximate defocus value of -25 nm, are presented in Fig. 1.2.6. Although both images exhibit intensity variations of the contrast pattern, these variations are more pronounced in the image of Al-rich 2/1-mullite, whereas the contrast pattern of 3/2-mullite shows minor intensity deviations. Bearing the above mentioned features of 200-kV HREM contrast simulations in mind, it is obvious that an enhancement of certain dots must be attributed to higher vacancy concentrations along [010]. The most striking property of HREM images of the (010) plane are linear arrangements of enhanced dots with preferred orientations parallel to <102>. With an extension between 0.40 nm to 2.42 nm in 2/1-mullite and 0.40 nm to 1.20 nm in 3/2-mullite, the length of the rows are found to be closely related to

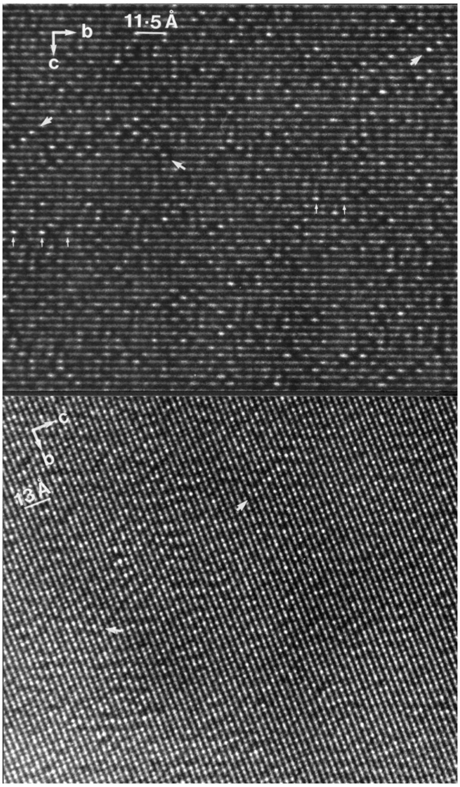

Fig. 1.2.7 HREM images of 2/1-mullite along [100] (top 200 kV, bottom 300 kV). The arrows indicate the preferred orientations along <012> (top) and <013> (bottom). Small arrows indicate the period of 1.5 *b*.

the chemical composition of the investigated mullite. More conspicuous in HREM images of 2/1-mullite, the ordering scheme of columns with enhanced vacancy concentrations along [010] furthermore often reveals a period of 1.5*a* and 2*c*.

In contrast to the appearance of distinct white spots in HREM images of the (010) plane, 200-kV images along [100] (Fig. 1.2.7) do not show a definite period parallel to [010], because the 020 reflections (d_{020} = 0.384 nm) are relatively weak, whereas the stronger 040 reflections (d_{040} = 0.192 nm) do not contribute to image formation owing to a point-to-point resolution of 0.23 nm. However, brighter dots in HREM images at a defocus value of -0.25 nm indicate higher vacancy concentrations along the illumination direction. Preferred orientations parallel to <012> and <001> are marked by arrows in Fig. 1.2.7. By examining a 300-kV image (point-to-point resolution of about 0.17 nm), arrangements of enhanced vacancy concentrations exhibit an undulatory form with an average direction along <013> (Fig. 1.2.7). Consistent with the positions of diffuse maxima in 0*kl* diffraction patterns, the average distances between these arrangements reveal an interval of 1.5*b* and a five- to sixfold periodicity along [001].

Summarizing the results of the HREM investigation and analysis of the electron diffraction pattern, it is evident that mullite does not exhibit a perfectly ordered arrangement of oxygen vacancies. Weak diffuse regions as well as the diffuse max-

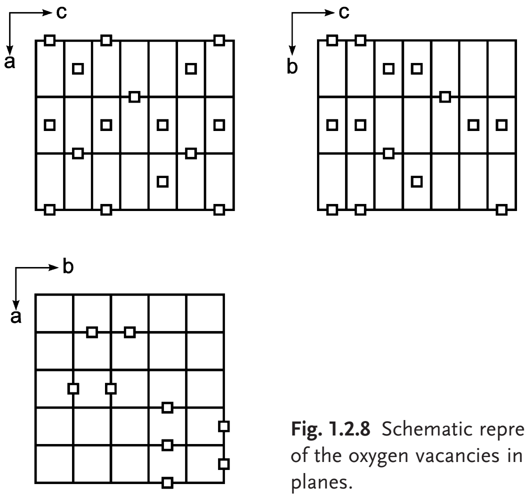

Fig. 1.2.8 Schematic representation of the ordering schemes of the oxygen vacancies in the three main crystallographic planes.

ima in *h*0*l* and 0*kl* diffraction patterns imply the formation of short-range-order regions. The real structure is characterized by partly ordered regions ("domains") with enhanced vacancy concentrations showing a specific correlation along preferred directions, as indicated in experimental HREM images. A schematic representation of the vacancy arrangements in the main crystallographic planes is presented in Fig. 1.2.8.

Although HREM investigations yield valuable information about preferred vacancy arrangements, one has to deal with some restrictions regarding the 3D interpretation of the contrast pattern, since they are caused by a projection of the structure along the incident beam. However, the HREM results in the three main crystallographic directions give important parameters as input data for two-dimensional and three-dimensional videographic real-structure simulations, as discussed in Section 1.2.4.

1.2.3
X-ray Investigation

In order to solve the real structure of mullite the diffuse scattering in the whole reciprocal space was determined. To get an overview of the position of the diffuse scattering, an X-ray rotation photograph (Mo Kα) about the *c* axis for mullite with $x = 0.4$ is presented in Fig. 1.2.9. The rotation photograph shows diffuse layers with $l = 1/2$, 1/3, 1/4, 1/6. To give an impression of the complicated diffuse intensity distribution in these reciprocal planes a precession photograph with quartz monochromator for the *hk*1/4 plane is given in Fig. 1.2.10. In this precession photograph there are diffuse circular arcs around the positions 1,0,0.25 and 0,1,0.25 and diffuse streaks parallel to the directions <110>*. Without going into details such a complicated diffuse scattering distribution cannot be explained by the known disorder theories (Daniel and Lipson, 1944, Jagodzinski, 1949, 1964a,b,

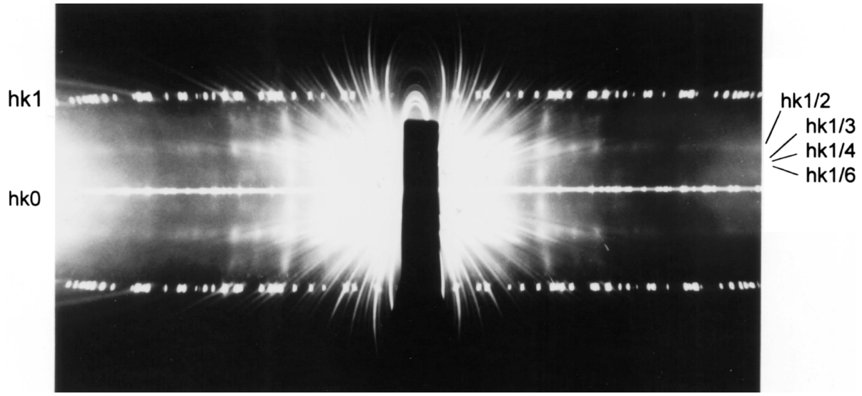

Fig. 1.2.9 X-ray rotation photograph about the *c*-axis for 2/1-mullite.

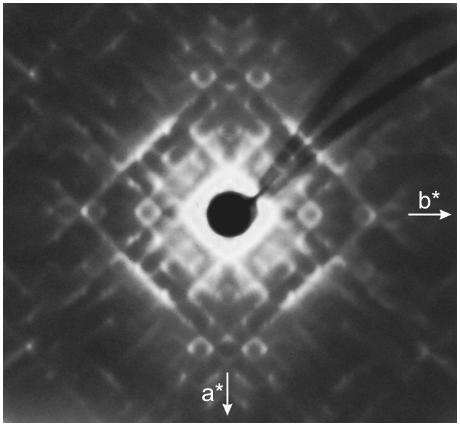

Fig. 1.2.10 X-ray precession photograph (Mo Kα) of the *hk*1/4 reciprocal plane of 2/1-mullite (h, $k \leq 8$).

Kunze, 1959, Korekawa, 1967, Korekawa et al. 1970, De Wolff, 1974, Böhm, 1977, Boysen et al. 1984).

The lack of 3/2-mullite single crystals for X-ray investigations made it impossible to obtain diffraction patterns (four-circle diffractometer) for all reciprocal planes as in the case of 2/1-mullite. In order to overcome these difficulties Rahman et al. (2001) prepared a 3/2-mullite single crystal from a sillimanite single crystal by slow thermal heating and annealing at 1600 °C for 24 h. For a complete characterization of the diffuse scattering in 3/2- and 2/1-mullite, a four-circle diffractometer was used to measure the intensity distribution in *hk*1/2, *hk*1/3, *hk*1/4 and *hk*1/6. The experimental results of the four-circle measurements for *hk*1/4 are presented in Fig. 1.2.11. The inner part (close to the incident beam spot) of the four-circle diffraction pattern is better resolved than in the precession photograph (Fig. 1.2.10). Comparing the diffraction patterns of 3/2 and 2/1-mullite it can be seen that both compositions in principle show the same scattering phenomena; however, the diffuse figures of 3/2-mullite are broadened and have weaker relative

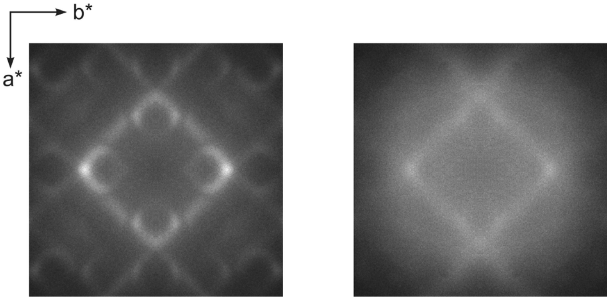

Fig. 1.2.11 X-ray diffraction pattern of 2/1-mullite (left) and 3/2-mullite (right) for *hk*1/4 (*h*, *k* ≤ 2.5) showing complicated diffuse scattering.

intensities. Furthermore the exact positions of the maxima of intensity are slightly different in 2/1- and 3/2-mullite.

The information about the real-structure configuration in mullite is implicitly contained in the shape and intensity distribution of the diffuse scattering patterns. A direct method of solving the real structure of mullite with such complicated diffuse scattering phenomena is not available. In less complicated cases these difficulties can be overcome by applying optical Fourier transforms or Monte-Carlo simulations using predefined structural models. In the case of mullite, representative structure models cannot be easily derived because of the great number of varieties of the model. Rahman (1991) suggested, that the vacancy distribution in mullite can be described by inter-vacancy correlation vectors. Butler and Welberry (1994) calculated SRO parameters of mullite from the intensities of the diffuse scattering. The diffuse scattering was measured in the area *hkl* with $h,k < 4.5$ and $0.5 < l < 1.0$ and analyzed using least-squares techniques by deriving an equation for the diffuse scattering that only involves the local order of the oxygen vacancies. The calculated diffraction patterns of a Monte-Carlo simulation, in which 12 interaction energies were adjusted to fit 12 of the 18 presented SRO parameters, show some similarities to the experimental patterns but still show some differences. However, a complete description of the mullite real structure is not given. In the next section a simulation and reconstruction method will be applied to mullite in order to solve and describe the real structure.

1.2.4

Real-structure Determination Using Videographic Reconstruction and Simulation Techniques

The videographic method is a simulation and reconstruction procedure that uses a statistical mathematical approach and computer graphics to aid the interpretation of diffuse scattering (X-ray, electron, neutron) from a disordered crystal and to solve the real structure. A detailed description of the videographic method was given by Rahman (1991, 1992, 1993a, 1994b) and Rahman and Rodewald (1995), so the method will only be briefly outlined here.

1.2.4.1 **The Videographic Method**

The basic principle of the videographic method is the representation of the real structure as a computer graphic, where different atoms are replaced by picture elements (pixels) of different grey levels according to their scattering power. As the videographic method of 1991 was developed, a special graphic adapter was needed to display the image with 256 grey levels. Moreover, an array processor was used for the time-consuming calculations (Fourier transforms). Nowadays these components are no longer necessary, because most personal computers are able to meet the above-mentioned requirements. The videographic method contains two procedures complementing each other, the videographic simulation of the real structure and the videographic reconstruction, which enables to draw conclusions from the diffraction pattern about the atomic arrangements.

Videographic simulation is performed by the distribution of structure variants, which can be derived from the average structure according to the approach that an average structure $<\varphi>$ can be described as a superposition of n possible structure variants φ_j:

$$<\varphi(x,y,z)> = \frac{1}{N}\sum_{j=1}^{n}\varphi_j(x,y,z)\times N_j \tag{2}$$

where N = total number of structure variants and N_j = number of the structure variants j.

These structure variants are distributed using a random variable J taking the values j (j = 1, ..., n) with certain probabilities determined by the distribution function of J. The distribution function is defined in terms of the combination probabilities W_{ij} (Rahman, 1991) for the direct combination of two structure variants along the three main simulation directions a, b and c. For the distribution behind the first shell an input of influence factors for any correlation vectors is used (Rahman and Rodewald, 1995). With the aid of the influence factors f_v a structure variant A (or φ_i) can directly influence the probability of the occurrence of the structure variant B (or φ_j) at the position of a correlation vector lmn:

$$P_\mathrm{B}(lmn) = P_\mathrm{B}^\mathrm{Tab}\times f_\mathrm{v} \tag{3}$$

where $P_\mathrm{B}{}^\mathrm{Tab}$ = probability of structure variant B according to the tables containing the combination probabilities and lmn = components of the correlation vector between A and B.

In this way preferences beyond the first or second shell can be considered. A three-dimensional simulation field $S(L,M,N)$ with L rows, M columns and N layers can be expressed as

$$S(L,M,N) = \sum_{l}^{L}\sum_{m}^{M}\sum_{n}^{N}\varphi_{lmn}(J_{lmn}) \tag{4}$$

where $\varphi_{lmn}(J_{lmn})$ = structure variant of type J at an lmn position, J_{lmn} = random variable for an lmn position and l, m, n = integers.

The videographic real-structure image $S(x,y)$ can be obtained by replacing every structure variant by a videographic pixel pattern. To check the result of a simulation, the Fourier transformation of the real-structure image $F[S(x,y)]$ is calculated:

$$Q(u, v) = F\left[S(x, y)\right] = \frac{1}{LR}\sum_{x=0}^{L-1}\sum_{y=0}^{R-1} S(x, y)\, \exp\left[-2\pi i\left(x\frac{u}{L} + y\frac{v}{R}\right)\right] \tag{5}$$

where L, R = number of rows and columns of the videographic image, x, y = coordinates of the videographic image and u, v = coordinates in Fourier space.

The Fourier transforms $Q(u,v)$ are displayed for comparison with the experimental diffraction patterns. The input parameters (combination probabilities and influence factors) are systematically varied until a best fit between simulation and experiment is reached. It must be pointed out that the simulation field must have an appropriate size [(L, M, N, Eq. (4)] in order to obtain representative results. In a further step the 3D simulation field is analyzed to obtain the frequencies of correlation vectors lmn and control the chemical composition (frequency of each structure variant).

To enable the calculation of diffraction patterns for any reciprocal layers (in the case of mullite for example $hk1/6$, $hk1/4$, $hk1/3$, $hk1/2$) the 3D simulation field can be converted into a floating point data file containing the coordinates (x, y, z) of the atoms and the temperature factors. The positions of the atoms (x, y, z coordinates) contained in the files (of the variants) are converted according to the position of the variant in the simulation field into atomic positions related to the supercell of the 3D simulation field. Using the atom coordinates of the real structure (supercell) the structure factors F_{hkl} can be calculated for every reciprocal plane conventionally.

In order to get structural information for the input parameters of the simulation, the videographic reconstruction can be applied, which enables recovery of real-structure configurations by filter operations in reciprocal space. The principal idea in a reconstruction of an unknown real structure is that the diffuse scattering in the diffraction pattern of a partly ordered structure is a subset of the monotone diffuse background for a random disorder (Rahman, 1992). For this reason, a randomly disordered structure is usually assumed as a starting model. In addition to the Bragg peaks $Q(u,v)_\mathrm{B}$, its Fourier transform shows a monotone diffuse background $\Delta Q(u,v)_\mathrm{d}$. Image reconstruction of the real structure $S(x,y)$ can be achieved by selective filtering of certain frequencies by means of the transfer function. In this case $Q(u,v)_\mathrm{B}$ or $\Delta Q(u,v)_\mathrm{d}$ can be multiplied by the transfer functions $G_1(u,v)$ and $G_2(u,v)$, respectively:

$$F\left[\varphi(x,y)\right] = Q(u,v)_\mathrm{B} \times G_1(u,v) + \Delta Q(u,v)_\mathrm{d} \times G_2(u,v) \tag{6}$$

The values of the transfer functions can be chosen to select either the diffuse regions, parts of the diffuse regions or the Bragg reflections, which are accounted for by a backward Fourier transform. In order to obtain information about the real-structure arrangements causing the diffuse scattering in mullite, specific frequencies of the diffuse background $\Delta Q(u,v)_\mathrm{d}$ are selected by the transfer function

$G_2(u,v)$. The positions of the selected areas are chosen according to the positions of diffuse scattering in the experimental diffraction pattern in mullite; the other frequencies of $\Delta Q(u,v)_d$ are excluded except the Bragg reflections. The transfer function can be expressed as a convolution between the reciprocal lattice function $F(u,v)$ and a window function $W(u,v)$, which determines the coordinates of the selected areas and corresponds to a filter mask.

$$G(u,v) = F(u,v) * W(u,v) \tag{7}$$

The backward Fourier transform of an image with L rows and R columns shows a reconstructed real-structure image $S'(x,y)$ with a different contrast distribution compared to the starting model.

$$S'(x,y) = \int\limits_{\mathrm{u}}\int\limits_{\mathrm{v}} \left(Q(u,v)_{\mathrm{B}} \cdot G_1(u,v) + \Delta Q(u,v)_{\mathrm{d}} \cdot G_2(u,v) \right) \cdot \exp\Omega \cdot dudv$$

$$\text{where } W = 2\pi i\left(x\frac{u}{L} + y\frac{y}{R} \right) \tag{8}$$

By visual inspection of the reconstructed real-structure images, preferred atomic arrangements in the real structure can be determined, but no quantitative results regarding the frequencies of correlation vectors are available. For this reason a correlation function $P(X,Y)$ can be calculated from the Fourier transforms of the reconstructed images:

$$P(X,Y) = \sum_{u=0}^{L-1}\sum_{v=0}^{R-1} \left| Q(u,v) \right|^2 \quad \cos 2\pi\left(X\frac{u}{L} + Y\frac{v}{R} \right) \tag{9}$$

where X,Y = coordinates of the correlation function.

Analysing the intensities of the correlation (Patterson) function the frequencies of correlation vectors can be estimated and used as input parameters for a new videographic simulation.

To attain a complete characterization of the ordering scheme in the mullite real-structure, 2D reconstructions for the main planes were first performed, and these results were tested by 2D videographic simulations. In order to describe the oxygen vacancy correlations in the real structure, the *lmn* correlation vectors between oxygen vacancies are defined as:

$$l = 1/2a,\ m = 1/2b,\ n = \mathrm{c}\ (a,\ b \text{ and } c \text{ are the lattice constants}). \tag{10}$$

Then a 3D ordering scheme was derived containing the most important correlation vectors. Via 3D simulations of the mullite real structure this ordering scheme was refined and confirmed. The results of the videographic simulation and reconstruction method will be presented in the following sections.

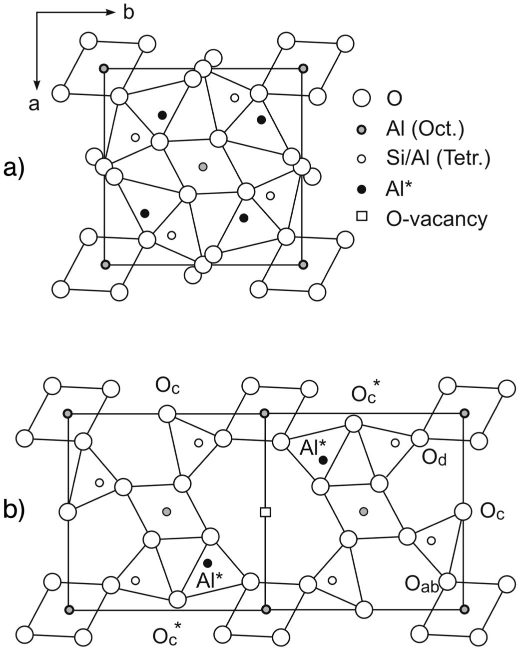

Fig. 1.2.12 Structure of mullite (a) Average structure (Angel and Prewitt 1986); the origin of the unit cell is displaced by *a*+1/2 and *b*+1/2 against Angel and Prewitt 1986); (b) Atomic displacements around an oxygen vacancy (following the nomenclature of Angel and Prewitt 1986 for the atomic positions).

1.2.4.2 Structure Variants of Mullite

The structure variants are derived from the average structure [Fig. 1.2.12a, Eq. (2)] considering crystal-chemical rules for bond lengths, atomic distances and coordination number. To derive the structure variants the following restrictions were applied: The occupation of the tetrahedral Si/Al and Al* sites depends on the position of oxygen atoms or vacancies. If the O_c site is occupied, the two adjacent Si/Al sites are occupied too. However, next to a vacancy the adjacent Al* sites are occupied instead of the Si/Al sites, and the coordinating oxygen atoms shift from the O_c to the O_c* position (Fig. 1.2.12b). Structure variants with two vacancies building the correlation vector <110> are not allowed, because an Al or Si atom would only be threefold coordinated. Si/Al-O_c* bond lengths of 0.173 and 0.178 nm lead to a tetrahedral occupation by Al, whereas 0.167 nm for the Si/Al-O_c bond gives Si occupation of the T position.

Considering these rules and different O_c and O_c* occupations, 34 structure variants (Fig. 1.2.13) result from the decomposition of the mullite average structure. Each four variants (1-4, 5-8, 9-12, 13-16) exhibit an oxygen vacancy on the same cell edge and different O_c and O_c* occupations on the remaining three edges. Structure variants 17 to 32 are vacancy-free, but with a variation on the O_c/O_c* sites. Variants 33 and 34 represent the silica free ι-Al_2O_3 modification proposed by Saalfeld (1962).

Since it is difficult to handle simulations with such a great number of structure variants (large combination tables with a great number of combination probabilities and complicated conditional probabilities leading to great deviations between

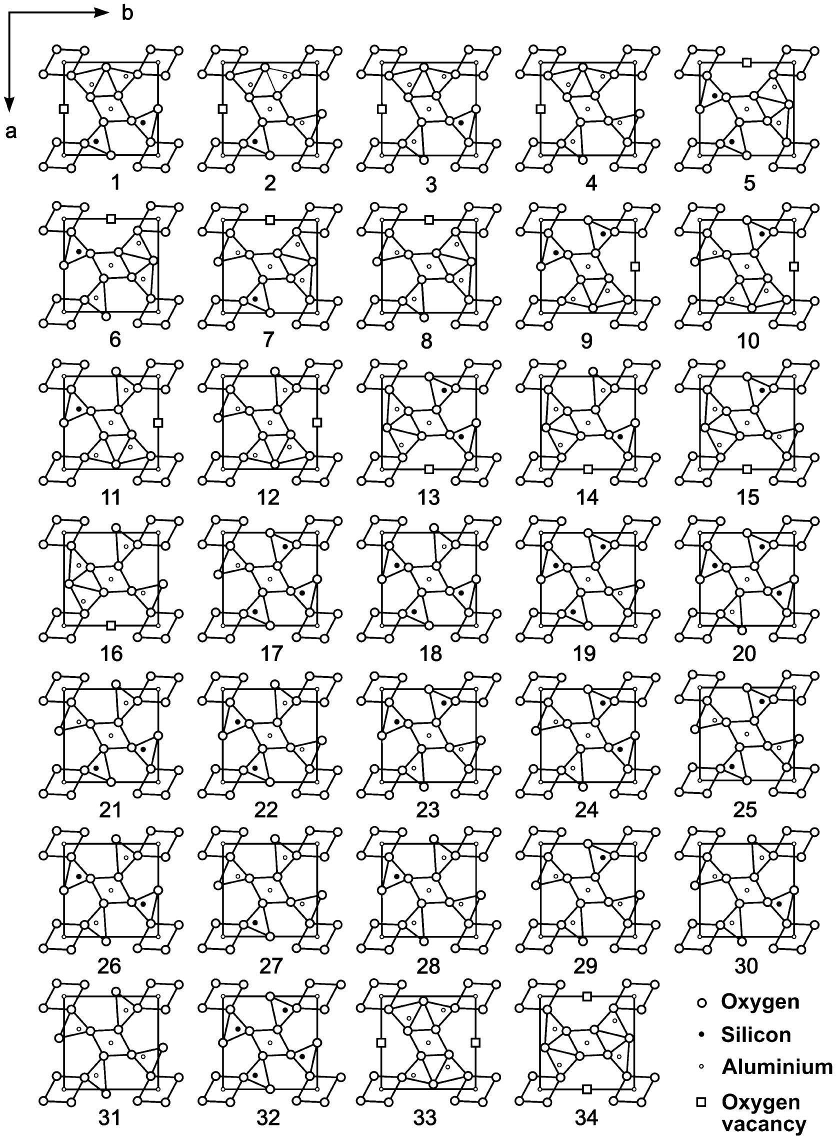

Fig. 1.2.13 34 structure variants of mullite.

the input and output parameters), the number of structure variants can be reduced to 7 by neglecting the O_c^* positions. Fig. 1.2.14 shows seven structure variants for mullite, which differ in the position of oxygen vacancies. Variants 1 to 4 have one vacancy on one edge of the unit cell, in variant 5 all O_c positions are occupied and variants 6 and 7 have two vacancies on opposite edges. Since the occupation of the O_c^* site is coupled with the occurrence of vacancies, it is possible to generate a

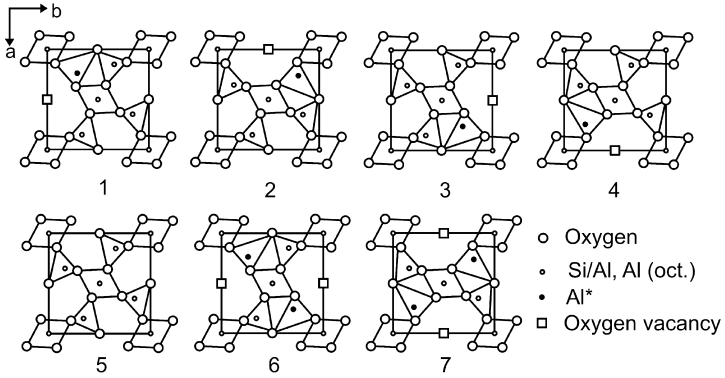

Fig. 1.2.14 7 structure variants of mullite neglecting the O_c* position.

simulation field with the seven structure variants and subsequent convert the seven into the 34 different variants (Freimann, 2001). In this way the Fourier transforms of the videographic simulations are calculated for the correct representation of the structure.

1.2.4.3 **Two-dimensional Videographic Reconstructions**

For the videographic reconstruction of the *ac* and *bc* planes a simplified starting model, consisting only of oxygen atoms and vacancies [both on the O_c site], was used. The oxygen atoms and vacancies were distributed randomly and the Fourier transform showed a diffuse background alongside the Bragg reflections. The selected regions in the filter masks coincide with the diffuse regions of the experimental diffraction patterns for *h*0*l* and 0*kl*. According to Eq. (7) the filter masks are convoluted with the Fourier transform of the starting model. The filter masks contain the Bragg reflections, the diffuse maxima and the diffuse streaks. All other frequencies that are not included in the filter mask (not present in the experimental diffraction pattern) are set to zero and only the selected areas are considered for backward Fourier transformation (Fig. 1.2.15a). The resulting reconstructed real-structure images (Fig. 1.2.15b) reveal an intensity distribution typical for the applied filter masks. In the reconstructed image of the *ac* plane, specific arrangements of pixels with relatively high intensities building the correlation vectors <3*m*0>, <0*m*2> and <1*m*1> can be observed. The reconstructed image of the *bc* plane shows preferred arrangements along the approximate direction <*l*23> often in a distance of 3*b* and 5*c*. In order to determine the frequencies of correlation vectors (*lmn*) the correlation function [Eq. (9)] is calculated from the reconstructed image. Parts of the correlation (Patterson) functions for the *ac* and *bc* planes are presented in Fig. 1.2.15c. The intensities in the correlation functions are proportional to the frequencies of correlation vectors. Analysing the intensity distribution of the correlation functions the following most frequent 2D correlation vectors were estimated for the *ac* and *bc* planes:

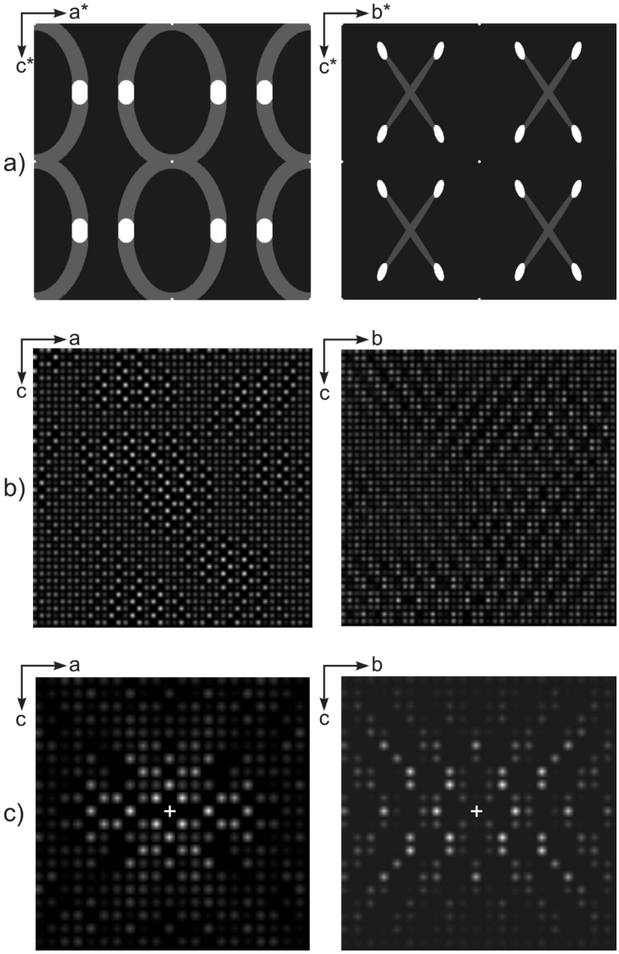

Fig. 1.2.15 (a) Filter masks for the selection of the diffuse scattering as obtained from the experimental diffraction pattern (h, $k \leq 2$, $l \leq 1$); (b) reconstructed real structure images of the *ac* and *bc* planes; (c) calculated correlation functions for vectors l, m, $n \leq 10$.

ac plane: <3*m*0>, <1*m*1>, <0*m*2>
bc plane: <*l*30>, <*l*22>, <*l*23>, <*l*05>.

The 2D correlation vectors obtained from the videographic reconstruction were used as input parameters for 2D videographic simulations. The Fourier transforms of the 2D simulations are in good agreement with the experimental diffraction patterns shown in Fig. 1.2.1, which indicates the correctness of the reconstruction procedure. Videographic reconstructions were also performed for the *hk*1/2, *hk*1/3, *hk*1/4 and *hk*1/6 reciprocal planes of 2/1-mullite (Freimann et al. 1996, Freimann, 2001). Without going into details the most frequent correlation vectors were determined for each layer as shown in Fig. 1.2.16. It must be noted, that the 2D reconstruction of *hk*1/2, *hk*1/3, *hk*1/4 and *hk*1/6 only have a two-dimensional character and cannot be directly used for 3D simulation.

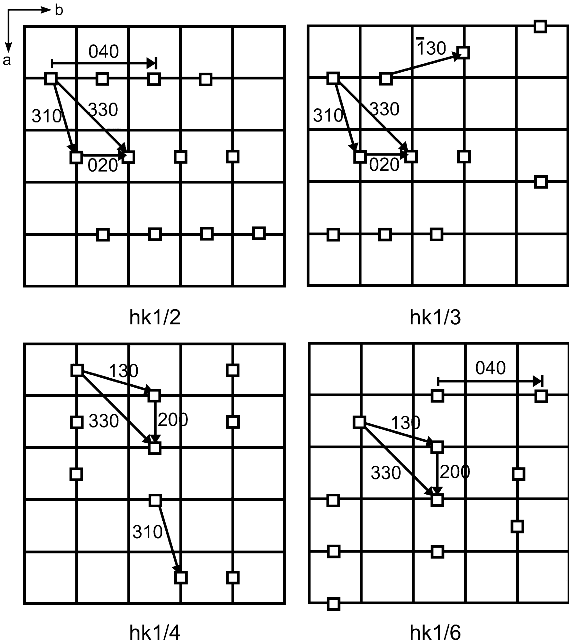

hk1/2 hk1/3

hk1/4 hk1/6

Fig. 1.2.16 Schematic representation of the oxygen vacancy correlation vectors obtained from the reconstruction for *hk*1/2, *hk*1/3, *hk*1/4 and *hk*1/6.

1.2.4.4 Three-dimensional Videographic Simulations for 2/1-and 3/2-mullite

In order to obtain representative results for the distribution function, a simulation field containing 48 × 48 × 96 structure variants, was chosen for videographic 3D simulations. From the results presented in the previous sections (HREM, X-ray, videographic 2D reconstructions and simulations) 2D correlation vectors for the three main planes were obtained, which allowed the derivation of the 3D correlation vectors presented in Table 1.2.2. The 1.5-fold period along [100] and [010] in *h*0*l* and 0*kl* diffraction pattern (Fig. 1.2.1) are caused by a preference of the <310>, <130> and <330> correlation vectors. Furthermore, it can be assumed that the twofold period along [001] in *h*0*l* patterns originates from more frequent <022> correlation vectors, which already appear in (100) HREM images as preferred arrangements along the [012] and [0-12] crystallographic directions (Fig. 1.2.7). Thus, a projection of the <022> vector onto (010) results in a twofold period along [001].

The preferred vacancy arrangements along the crystallographic directions [102] and [-102] observed in HREM images of the *ac* plane (Fig. 1.2.6) can be achieved by a preference of the <111> correlation vector in agreement with the 2D reconstruction and simulation of the *ac* plane with the high frequency of the 2D vector <1*m*1>. The preference of the 3D correlation vector <201> corresponds to a high frequency of <2*m*1> in the reconstruction of the *ac* plane and - in projection on (100) - to a vacancy arrangement along [001], which appears in (100) HREM images. In addition, the correlation vectors <131> are preferred in the 3D simulations.

Table 1.2.2 Derivation of the preferred 3D correlation vectors (*lmn*) from the most frequent 2D vectors.

ab	*ac*	*bc*	3D
<31*n*>	<3*m*0>		<310>
<33*n*>	<3*m*0>	<*l*30>	<330>
<13*n*>		<*l*30>	<130>
	<1*m*1>	<*l*11>	<111>
	<2*m*1>	<*l*01>	<201>
	<1*m*1>	<*l*31>	<131>
<02*n*>	<0*m*2>	<*l*22>	<022>
<31*n*>	<3*m*2>	<*l*12>	<312>

The 3D videographic simulations [Eq. (4)] were carried out first for 2/1-mullite using the 3D vectors presented in Table 1.2.2. The correctness of the simulated structure was tested by comparing its Fourier transforms with the experimental diffraction patterns (precession photographs and four-circle diffractometer). The simulations were successively refined until the best fit was found (Rahman et al. 1996, Freimann and Rahman, 2001). The Fourier transforms calculated after projecting the 3D videographic simulation field onto the *ac* and *bc* plane are presented in Fig. 1.2.17 together with the corresponding X-ray precession photographs. In both the X-ray precession pattern and the calculated Fourier transform of the *h*0*l* plane there are the rounded streaks with the maximum intensities at the approximate positions 1.3 a^* and 0.5 c^*. In the calculated 0*kl* plane the cross-shaped streaks and the diffuse maxima agree in position (1.4 b^* and 0.19 c^*) and relative intensity distribution with the precession pattern. The differences at greater scattering angles may result from the fact that the calculated Fourier transforms do not include the dependence of intensity on the scattering angle.

In order to compare the agreement in the reciprocal planes perpendicular to c^*, Fig. 1.2.18 presents the experimental diffraction patterns of 2/1-mullite and the Fourier transforms for the 3D simulation. In all these planes a very good agreement is observed. The calculated *hk*1/2 plane shows the diffuse maxima at the correct position on the a^* axis at $1.3a^*$, corresponding to the diffuse maxima in the *h*0*l* plane. In the *hk*1/3 plane the maximum intensities are at the same position but additional diffuse circular arcs around the reciprocal coordinates 1, 0, 1/3 and 0, 1, 1/3 appear. In the *hk*1/4 plane the diffuse arcs change into angular shapes and there are streaks parallel to the direction <110>*, which are also present in the *hk*1/6 plane. In both the *hk*1/4 and *hk*1/6 planes the maxima of diffuse intensity are on the b^* axis at approximately $1.4b^*$.

Because of the good agreement between the Fourier transforms and the experimental patterns, this 3D simulation gives a good representation of the vacancy distribution in 2/1-mullite. The simulation field was analyzed for all correlation

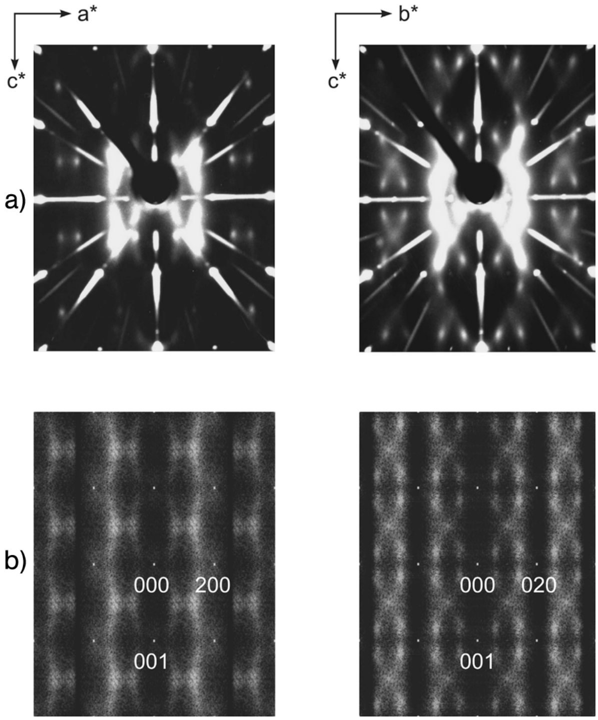

Fig. 1.2.17 (a) X-ray diffraction patterns *h*0*l* and 0*kl* of 2/1-mullite (precession photograph Mo Kα); (b) Fourier transforms *h*0*l* and 0*kl* of the 3D simulation of 2/1-mullite.

vectors *l*,*m*,*n* ≤ 6 (Freimann, 2001). Hence the simulation and the real structure can be completely described. The frequencies of correlation vectors (up to 060) are given in Fig. 1.2.20. It is remarkable, that the preferred vectors indeed have the highest frequencies (<310>, <111>, <022>, <201>, <330>). For some of the vectors it is possible to describe their influence on specific details of the diffuse scattering: For example the diffuse maxima in the *h*0*l* and *hk*1/2 plane can be explained with the vectors <310> and <022>, in which <310> is responsible for the location along the *a** axis at 1.3*a** and <022> for the location along the *c** axis at 1/2*c**.

The single-crystal diffraction patterns for the planes *hk*1/2, *hk*1/3, *hk*1/4 and *hk*1/6 of 3/2-mullite are shown on the left in Fig. 1.2.19. Comparing this with the diffraction pattern of 2/1-mullite (Fig. 1.2.18) it can be seen that both compositions (2/1- and 3/2-mullite) in principle show the same scattering phenomena, although the diffuse figures of 3/2-mullite are broadened and have weaker relative intensities. Furthermore the exact positions of the maxima of intensity are slightly different in 2/1- and 3/2-mullite. Because of the similar diffraction patterns of 3/2-mullite we supposed that the results for 2/1-mullite were also valid for 3/2-mullite. Thus 3D simulations for 3/2-mullite were performed preferring the same correlation vectors but with reduced frequencies because of the lower concentration of vacancies. Again the simulation was refined by varying the frequencies of the preferred vectors until the Fourier transforms of the simulation showed the best agreement with the experimental diffraction patterns. In Fig. 1.2.19, the

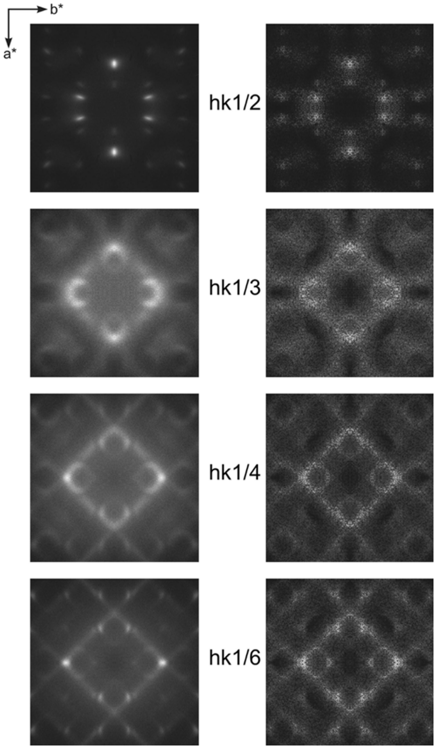

Fig. 1.2.18 (Left) X-ray diffraction pattern of 2/1-mullite; (right) Fourier transforms of the 3D simulation of 2/1-mullite (h, $k \leq 2.5$).

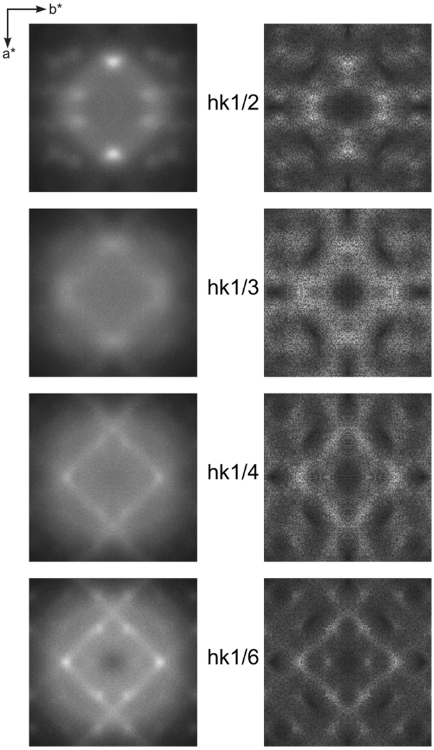

Fig. 1.2.19 (Left) X-ray diffraction pattern of 3/2-mullite; (right) Fourier transforms of the 3D simulation of 3/2-mullite (h, $k \leq 2.5$).

experimental diffraction patterns of 3/2-mullite are presented on the left and the calculated patterns from the 3D simulation are shown on the right. The shapes and the maximum intensities of the diffuse scattering are very similar in the experiment and the simulation. The simulation field was analyzed and the vector frequencies are presented in Fig. 1.2.20. Comparing the frequencies of inter-vacancy correlation vectors in this simulation with those for 2/1-mullite, it is clear that both graphs in Fig. 1.2.20 have a similar shape, indicating that the vacancy distribution in both compositions generally obeys the same rules, except that the frequencies of the correlation vectors are lower in 3/2-mullite. There are only small differences in the sequence of correlation vectors (the sequence of 2/1-mullite: <310>, <111>, <022>, <201>, <330>; the sequence of 3/2-mullite: <022>, <201>, <111>, <310>, <130>). Hence it is evident that 2/1- and 3/2-mullite have very similar ordering schemes of oxygen vacancies and the real structures can be described via inter-vacancy correlation vectors (with slightly different frequencies). A schematic representation of the 3D ordering scheme, which is constructed with the most important correlation vectors, is given in Fig. 1.2.21.

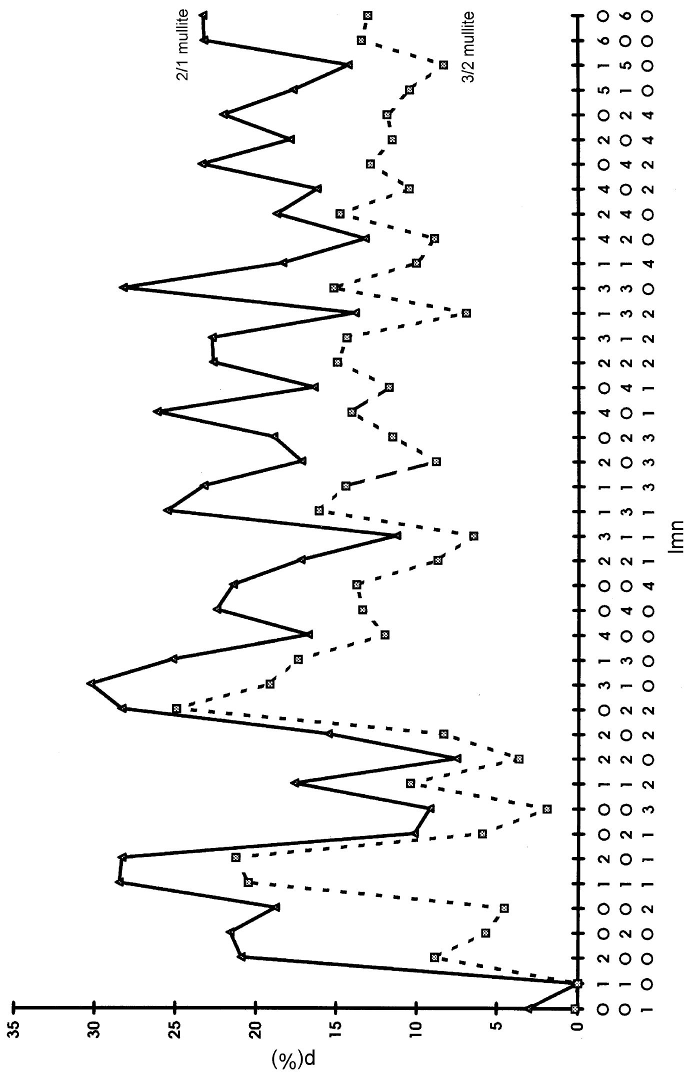

Fig. 1.2.20 Frequencies of inter-vacancy correlation vectors determined from the analysis of the 3D simulation fields for 3/2 and 2/1-mullite [p = probability (%) of finding another oxygen vacancy at the end of an *lmn* correlation vector].

1.2.4.5 **Conclusions**

Videographic 3D simulations were performed for 2/1- and 3/2-mullite, whose Fourier transforms reproduce the diffuse scattering in all examined reciprocal planes as observed in the experimental patterns (Fig. 1.2.17, 1.2.18 and 1.2.19). The 3D simulation fields are built up by 48 × 48 × 96 structure variants and include 221 184 unit cells with about 3.5 million atoms. By analysing the 3D simulation

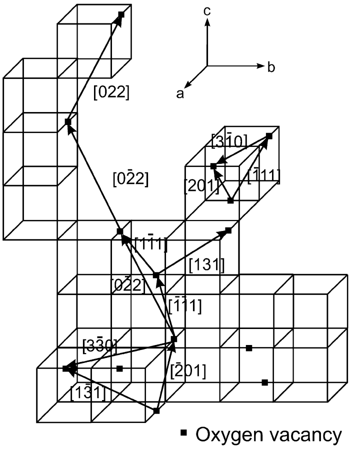

Fig. 1.2.21 3D ordering scheme of the oxygen vacancies.

fields the vacancy distribution in 2/1- and 3/2-mullite could be described completely in terms of inter-vacancy correlation vectors. For this reason mullite is the first non-metallic mineral in which the diffuse scattering can be completely explained by short-range ordering. Short-range-order parameters (correlation vectors) are usually used to describe the real structure of intermetallic alloys above the critical temperature, T_c. In most cases the first three short-range-order parameters are adequate to describe the short-range-order state. In mullite, with T_c above the melting point, the three shortest correlation vectors are not sufficient to describe the oxygen vacancy ordering scheme. In this case, higher order inter-vacancy correlation vectors (Fig. 1.2.20) are important for the complete interpretation of the mullite real structure. Unlike alloys, the short-range ordering process in mullite is related to vacancies coupled with cation displacements.

Knowledge of the real structure may help to explain some physical properties of mullite. In a part of the simulation field for 2/1-mullite (Fig. 1.2.22) differences in the vacancy arrangements along the *a* and *b* axes can be observed. In one *ab* layer (Fig. 1.2.22 top) the differences in probabilities of correlation vectors (p_{lmn}) are small: There are linear arrangements along the *a* axis with the vectors <200> and <130> as well as linear arrangements along the *b* axis with the vectors <020> and <310>. The frequencies of <200> and <020> are very similar, the vector <310> is more frequent than <130>, but both are preferred. However, for a proper description of the physical behavior of a bulk crystal it is more realistic to consider not only one layer with correlation vectors *lm*0 but at least two subsequent layers. The superposition of two subsequent layers (Fig. 1.2.22 bottom) with the correlation vectors *lm*0 and *lm*1 clearly shows differences in the vacancy arrangements (concentrations) in projection on the *a* and *b* directions. The vector <201> is very frequent (marked with black lines in Fig. 1.2.22), but the vector <021> is rare, while <131> is frequent, <311> rare. Therefore the dependence of several physical properties on the direction may be explained with the given distribution of oxygen vacancies, which can be well described with the help of inter-vacancy correlation vectors.

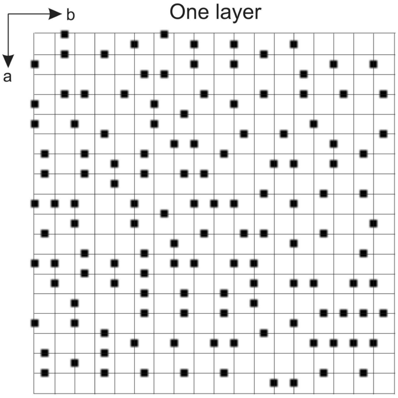
One layer

<lmn>	p/%
<020>	21,60
<200>	20,91
<130>	25,21
<310>	30,30
<040>	22,48
<400>	16,78

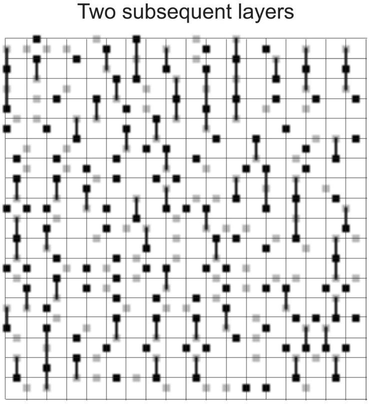
Two subsequent layers

<021>	10,19
<201>	28,33
<131>	25,53
<311>	11,29
<041>	16,39
<401>	26,15

Fig. 1.2.22 Part of the simulation field for 2/1-mullite.

The results presented above reflect the importance of real-structure determination in material science in order to characterize the behavior of physical properties in the case of disorder.

1.3
Foreign Cation Incorporation in Mullite
H. Schneider

1.3.1
Transition Metal Incorporation

Natural mullites contain iron, titanium, and occasionally chromium as foreign components. The foreign cation content is usually low, though Fe_2O_3- and TiO_2-rich mullites have also been described (Agrell and Smith, 1960, Table 1.3.1).

Synthesis experiments carried out at varying temperatures and atmospheres have shown that a large variety of transition metals does enter the mullite struc-

Table 1.3.1 Chemical composition of naturally occurring mullite (wt. %)[a].

	1	2	3	4	5	6
SiO_2	30	32	29	29	31	29
TiO_2	1.29	2.27	0.55	0.79	0.70	0.80
Al_2O_3	68	65	64	70	68	70
Fe_2O_3	0.62	0.94	5.90	0.50	0.50	0.30
Cr_2O_3	n. d.	n. d.	n. d.	n. d.	–	0.30

a) Total iron expressed as Fe_2O_3; n. d. = not determined.
1 = Rudh'a' Chromain, Carsaig Bay, Mull, Scotland (Agrell and Smith, 1960).
2 = Carrickmore, west of Ballycastle, Northern Ireland (Agrell and Smith, 1960).
3 = Tievebulliagh, County Antrim, Northern Ireland (Agrell and Smith, 1960).
4 = Seabank Villa, Mull, Scotland (Bowen and Greig, 1924).
5 = Rudh'a' Chromain, Loch Scridain, Mull, Scotland (Cameron, 1976b).
6 = Bushfeld Complex, Thorncliffe and Maandagshoek, South Africa (Cameron, 1976b).

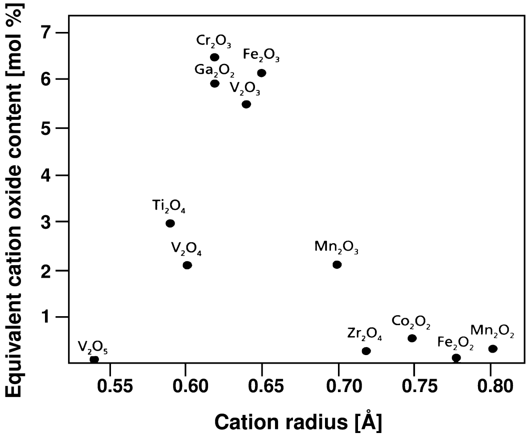

Fig. 1.3.1 Transition metal incorporation in mullite, given as maximum equivalent cation oxide contents and plotted versus the radii of substituting transition metal cations. Gallium incorporation (given as Ga_2O_3) is presented for comparison (from Schneider et al. 1994).

ture. Depending on synthesis conditions mullite may incorporate Ti^{3+}, Ti^{4+}, V^{3+}, V^{4+}, Cr^{3+}, Mn^{2+}, Mn^{3+}, Fe^{2+}, Fe^{3+} and Co^{2+}, though in strongly differing amounts (see Schneider, 1990). The upper solubility limit is controlled by the radii and oxidation states of transition metal ions: The highest degrees of incorporation are observed for V^{3+}, Cr^{3+} and Fe^{3+} followed by Ti^{4+}, while only very low amounts of Mn^{2+}, Fe^{2+} and Co^{2+} ions enter the mullite structure (Fig. 1.3.1). No systematic studies on the incorporation of scandium (Sc^{3+}), cobalt (Co^{3+}, Co^{2+}) and nickel (Ni^{3+}, Ni^{2+}) have been published so far.

Knowledge of equilibrium data for oxygen-transition metal systems with several states of oxidation are helpful for understanding the cation incorporation proc-

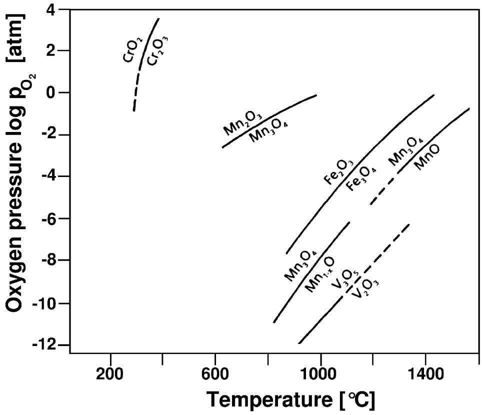

Fig. 1.3.2 Stability relations of transition metal oxides with different oxidation stages of chromium (Wilhelmi, 1975), manganese (Schwerdtfeger and Muan, 1975, Hübner and Sato, 1970), iron (Darken and Gurry, 1945, 1946) and vanadium (Anderson and Kahn, 1975) as function of temperature and oxygen pressure (from Schneider et al. 1994).

esses. A graph comparing the stabilities of Mn_2O_3/Mn_3O_4 and Mn_3O_4/MnO reaction pairs with those of Fe_2O_3/Fe_3O_4, CrO_2/Cr_2O_3 and V_3O_5/V_2O_3 as a function of temperature and oxygen partial pressure (p_{O_2}) is shown in Fig. 1.3.2. This shows that Cr^{3+} is the only stable oxidation state of chromium at higher temperatures regardless of the oxygen partial pressure, while the stability field of Fe^{3+} extends up to about 1400 °C at $p_{O_2} = 0.2$ atm. V^{3+} occurs above about 1600 °C at $p_{O_2} = 0.2$ atm, but is stable under a reducing atmosphere at lower temperatures. The experimental results on vanadium, chromium and iron incorporation into mullite obtained under varying reaction temperatures and atmospheres are in good accordance with the thermodynamic data (e.g.: Schneider, 1990, Rager et al. 1990, Schneider and Rager, 1986). Experimental data (e.g.: Schneider, 1990, Rager et al. 1993), moreover, suggest that the TiO_2/Ti_2O_3 reaction pair displays a similar temperature and oxygen partial pressure-dependent redox behavior to V_3O_5/V_2O_3. The equilibrium data of the manganese oxides show that Mn^{3+} is stable only below about 1000 °C. This may explain why Mn^{3+} incorporation into mullite by oxide reaction sintering is not possible, since it would require temperatures above 1200 °C, which is beyond the stability field of Mn^{3+}. However, a possible way to incorporate Mn^{3+} in mullite is the sol-gel route synthesis at low temperatures ($\leq$ 900 °C, Schneider and Vasudevan, 1989). The same synthesis technique may allow incorporation of Co^{3+} and Ni^{3+} into mullite. Another method of producing Mn^{3+}-, Co^{3+}- and Ni^{3+}-doped mullites may be synthesis by the hydrothermal technique, using oxidizing buffer systems.

Nucleation and growth, and associated shapes and sizes of the transition metal-doped mullite crystals, are controlled by the synthesis procedure, the synthesis temperature and atmosphere, and by the type and amount of transition metal incorporated. The size of the mullite crystals prepared from oxide powder mixtures with excess SiO_2 by reaction sintering increases within the sequence vanadium, chromium, titanium and iron. Within the same series the shapes of the mullite crystals change from small equiaxed to larger tabular grains (Fig. 1.3.3a–c). The influences controlling nucleation and growth of transition metal-doped mullites are probably complex. Growth is probably enhanced by the decreasing viscosities

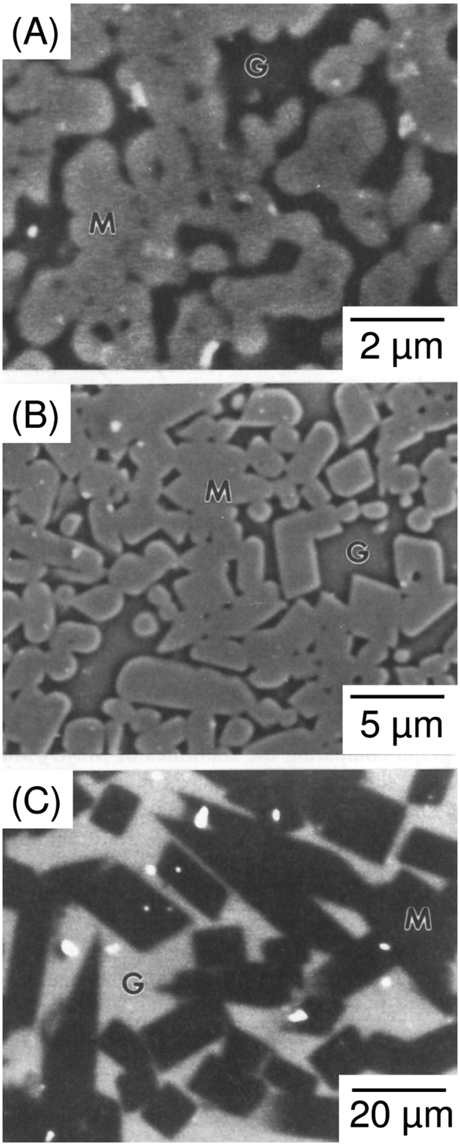

Fig. 1.3.3 Electron microprobe photographs of ceramics consisting of mullite (M) and glass phase (G). (a) Vanadium-rich ceramic with mullite containing 8.7 wt.% V_2O_3. The mullite crystals are very small with reniform contours; (b) Chromium-rich ceramic with mullite containing 11.5 wt.% Cr_2O_3. The mullite crystals are small with rounded-off contours; (c) Iron-rich ceramic with mullite containing 10.3 wt.% Fe_2O_3 (from Schneider et al. 1994).

of the partial melts coexisting with mullite in going from vanadium- to iron-rich oxide mixtures, and the associated higher velocities of diffusion species. Solid-state sintering studies show that low reaction rates and the microstructural development of samples are not only controlled by the presence of a low-viscosity liquid phase but at least in the case of the Cr_2O_3–Al_2O_3–SiO_2 system is a property inherent to transition metal-doped mullite itself (Saruhan and Schneider, 1993).

1.3.1.1 Titanium Incorporation

The extent of titanium solubility in mullite ranges between about 2 and 6 wt.% TiO_2, depending on the synthesis conditions (Gelsdorf et al. 1958, Murthy and Hummel, 1960, Green and White, 1974, Bohn, 1979, Baudin et al. 1983). Schneider and Rager (1984), Schneider (1986a, 1990), and Rager et al. (1993) found that both, Ti^{3+} and Ti^{4+} cations enter the structure.

Schneider (1986a, 1990) provided data on the dependence between the amounts of Ti_2O_3 and TiO_2 incorporated in mullite and the Al_2O_3 and SiO_2 concentrations of the phase (Fig. 1.3.4). It has been shown that a reciprocal and equimolar dependence exists between Ti_2O_3 and Al_2O_3, but not between Ti_2O_3 and SiO_2. The chemical interdependences were interpreted as implying that the entry of Ti^{3+} into mullite goes along with the removal of the same number of Al^{3+} ions from the structure. According to EPR studies, and because of the similar cation radii of octahedrally bound Al^{3+} and Ti^{3+} ions ($^{[6]}Al^{3+}$: 0.53 Å, $^{[6]}Ti^{3+}$: 0.64 Å; all cation radii are from Shannon 1976) $Ti^{3+} \rightarrow Al^{3+}$ substitution at octahedral sites is taken into account. The dependences between TiO_2 and Al_2O_3 and SiO_2, respectively, are contrary to those described above, with a reciprocal and equimolar dependence between TiO_2 and SiO_2, but not between TiO_2 and Al_2O_3 (Fig. 1.3.4). Probable Ti^{4+} incorporation mechanisms are $Ti^{4+} \rightarrow Al^{3+}$ or $Ti^{4+} \rightarrow Si^{4+}$ substitution. The cation radii of $^{[4]}Si^{4+}$ (0.26 Å), $^{[6]}Al^{3+}$ (0.53 Å), and $^{[6]}Ti^{4+}$ (0.605 Å) strongly suggest an entry of Ti^{4+} into the oxygen octahedra. An $^{[4]}Al^{3+} \rightarrow {}^{[4]}Si^{4+}$ substitution necessary for charge compensation, if Ti^{4+} enters octahedral sites may explain the higher incorporation-induced expansion of the *a* rather than the *b* lattice constant, which is characteristic for Ti^{4+}-doped mullite (Table 1.3.2).

Electron paramagnetic resonance (EPR) studies carried out on Ti^{3+}-doped mullite yielded interesting details (Rager et al. 1993): Two components of the EPR peak

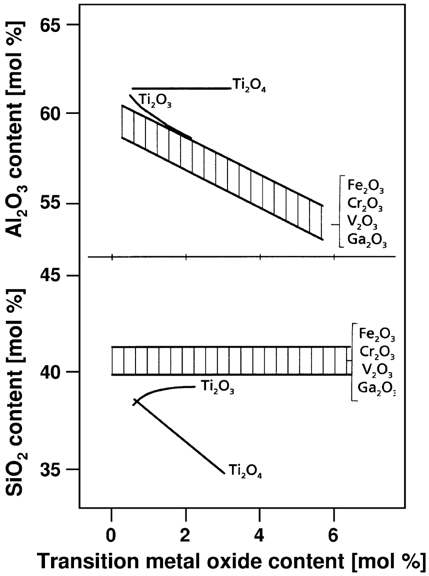

Fig. 1.3.4 Titanium oxide (Ti_2O_3, TiO_2), vanadium oxide (V_2O_3), chromium oxide (Cr_2O_3), manganese oxide (Mn_2O_3), and iron oxide (Fe_2O_3) plotted versus Al_2O_3 and SiO_2 contents, respectively. Relationships for gallium oxide (Ga_2O_3) are given for comparison (from Schneider et al. 1994).

Table 1.3.2 Chemical composition and lattice parameters of mullites containing high amounts of transition metal cations.

Chemical composition (wt. %)			**Method**	**Lattice parameters**				**Reference**
				a [Å]	***b*** [Å]	***c*** [Å]	***V*** [Å^3]	
Mullites containing transition metal cations:								
Al_2O_3 : 72.0	SiO_2 : 24.5	TiO_2 : 4.2	EMA	7.5637(5)	7.7009(6)	2.8931(3)	168.51(2)	Schneider (1990)
Al_2O_3 : 63.0	SiO_2 : 28.2	V_2O_3 : 8.7	XFA*	7.5550(2)	7.711(3)	2.8995(9)	168.92(2)	Schneider (1990)
Al_2O_3 : 72.5	SiO_2 : 24.0	V_2O_4 : 3.5	XFA†	7.5510(1)	7.698(1)	2.8936(5)	168.19(7)	Schneider (1990)
Al_2O_3 : 60.0	SiO_2 : 28.4	Cr_2O_3 : 11.5	EMA	7.5697(5)	7.7117(8)	2.9025(2)	169.43(2)	Rager et al. (1990)
Al_2O_3 : 68.4	SiO_2 : 25.9	Mn_3O_4 : 5.7	XFA‡	7.5630(2)	7.721(2)	2.8828(7)	168.33(6)	Schneider and Vasudevan (1989)
Al_2O_3 : 62.1	SiO_2 : 27.4	Fe_2O_3 : 10.3	EMA	7.5740(1)	7.726(1)	2.9004(5)	169.73(4)	Schneider (1987)
Reference mullite:								
Al_2O_3 : 71.2	SiO_2 : 28.6	–	EMA	7.5461(8)	7.6918(9)	2.8829(4)	167.33(3)	Schneider (1990)

Spectroscopic data and microchemical analyses suggest that samples marked *, †, and ‡ contain essentially V^{3+}, V^{4+} and Mn^{3+}, respectively. Therefore, chemical compositions are given as V_2O_3, V_2O_4 and Mn_3O_4, respectively.

EMA = Electron microprobe analysis; XFA = X-ray fluorescence analysis.

have been resolved at Q-band but not at X-band frequency. These two components were assumed to be due to at least two non-equivalent but structurally very similar Ti^{3+} centers in mullite. A structural model of mullite with two ordering patterns with different local atomic configurations was used to explain the EPR patterns. Rager et al. (1993) believed that the splitting of the Ti^{3+}-EPR is due to slightly different distortions of octahedra. Two octahedral positions with slightly different distortions have also been observed in iron-doped mullite by means of Mössbauer spectroscopy (see Section 1.3.1.5).

Interfacial reactions between titanium metal and mullite have been studied in the temperature range between 200 and 650 °C by Yue et al. space (1998) using secondary ion mass spectrometry (SIMS), Auger electron spectroscopy (AES) and X-ray diffractometry (XRD). At temperatures below 450 °C interfacial reactions are very slow, producing very thin interfacial layers only. The first deposited titanium atoms form Ti-O bonds with the oxygen on the mullite surface. However, intense interfacial reactions occur above about 650 °C and Ti-O-, Ti-Al- and Ti-Si-bonds can be identified.

1.3.1.2 **Vanadium Incorporation**

Only few data are available on vanadium-doped mullites. Schneider (1990) mentioned that maximally about 9 wt.% V_2O_3 and 3.5 wt.% V_2O_4 (Fig. 1.3.1) can be incorporated into mullite (Table 1.3.2).

Comparison of the lattice constants of V^{3+}-doped mullites prepared from reaction-sintered oxide mixtures with undoped mullites yields relatively high **c**, lower **b** and very low **a** expansion (Table 1.3.2, Schneider, 1990). The intense **b** cell edge expansion was correlated with the entry of V^{3+} ions at octahedral lattice sites. It was explained in a similar way to the thermal expansion of mullite, with a considerable lengthening of the long and "elastic" octahedral M(1)-O(D)[3] bond lying to about 30° to either side of **b** in mullite but with a much weaker M(1)-O(A) lengthening (Fig. 1.1.17, Schneider and Eberhard, 1990).

Plots of mol SiO_2 versus V_2O_3 concentrations of V^{3+}-substituted mullites yielded no dependence, whereas reciprocal correlations occur between Al_2O_3 and V_2O_3 (Fig. 1.3.4). This indicates that the entry of V^{3+} into mullite is associated with removal of the same number of Al^{3+} from the structure. Relationships are less clear in the case of V^{4+} substitution, probably because of low foreign cation concentrations and the occurrence of different oxidation states of vanadium.

The above-described observation of V^{3+} and V^{4+} incorporation into mullite has been supported by EPR studies. Vanadium-rich mullites synthesized under a strong reducing atmosphere yield EPR spectra with a weak and broad signal near

---

[3] Different designations of the oxygen positions of mullite have been described in literature: 01, 02, 03, 04 which corresponds to O(A,B), O(D), O(C) and O(C*), (Table 1.1.7). The first setting follows strict geometrical rules and allows an easy description of members of the mullite family being in group-subgroup relationship to the aristotype with the highest symmetry (Tables 1.1.2 to 1.1.10, 1.1.17 and Fig. 1.1.4). Since the second setting has frequently been cited in the crystal chemical literature of mullite it has been used in the following.

$g_{eff} = 4.1$ and a stronger peak near $g_{eff} = 1.9$. The EPR signal group near $g_{eff} = 4.1$ is attributed to V^{3+} in an octahedral environment. The band near $g_{eff} = 1.9$ with little fine structure has been correlated to the occurrence of a small amount of V^{4+} (Schneider, 1990). Vanadium-rich mullites synthesized in a moderately reducing atmosphere exhibit EPR signals near $g_{eff} = 2.0$ with characteristic hyperfine splitting. The EPR bands are attributed to isolated V^{4+} ions, probably localized in octahedral coordination.

1.3.1.3 **Chromium Incorporation**

Chromium-doped mullites were synthesized by Gelsdorf et al. (1958), Murthy and Hummel (1960) and Rager et al. (1990). It has been stated that up to 12 wt.% Cr_2O_3 is incorporated in mullite.

A detailed study of the crystal chemistry of chromium-doped mullites, prepared by reaction sintering of Al_2O_3, SiO_2 and Cr_2O_3 (0.5 to 11 wt.%) powders, was performed by Rager et al. (1990). Rager and coworkers found a reciprocal and equimolar dependence between Cr_2O_3 and Al_2O_3 in mullite, but not between Cr_2O_3 and SiO_2 content. They concluded that Cr^{3+} is incorporated by replacement of Al^{3+}. The structural formula of chromium-doped mullite, which corresponds to that of 3/2-type mullite indicates that the variation of chromium incorporation is not correlated with a change of the amount of O(C) oxygen vacancies (structural state x) in mullite. Chromium entry into mullite causes the largest linear lattice expansion along the crystallographic **c** axis, followed by smaller linear expansions parallel to **a** and **b** (Table 1.3.2). The incorporation-induced structural expansion of mullite, with $\Delta a > \Delta b$, does not fit with a simple $Cr^{3+} \rightarrow Al^{3+}$ substitution at octahedral sites, which should give $\Delta b > \Delta a$.

Electron paramagnetic resonance studies carried out by Rager et al. (1990) provided further information on the structural distribution of chromium in mullite. Chromium-doped mullites exhibit two rather sharp EPR signals near $g_{eff} = 5$, and a broad signal near $g_{eff} = 2.2$ (Fig.1.3.5). The peaks near $g_{eff} = 5$ were assigned to Cr^{3+} in slightly distorted octahedral M(1) positions in mullite, whereas the broad slightly asymmetric signal near $g_{eff} = 2.2$ may indicate coupling between localized magnetic moments. Rager et al. (1990) explained the signal at $g_{eff} \approx 2.2$ in terms of interstitial Cr^{3+} incorporation in mullite. According to the EPR peak intensities the entry of Cr^{3+} into the regular $M(1)O_6$ octahedra is favored at low bulk-Cr_2O_3 contents of mullite, whereas interstitial incorporation with formation of chromium clusters becomes more important at higher Cr_2O_3 contents (Fig. 1.3.5).

The strong preference of Cr^{3+} for octahedral coordination (Wells, 1984) suggests that interstitial Cr^{3+} is located in distorted, octahedral environments. Such sites in mullite are (1) the structural vacancies formed by removal of O(C) oxygen atoms that bridge adjacent tetrahedra near (0.1, 0.25, 0) (substitution model Cr I, Fig. 1.3.6b), and (2) the structural sites in the relatively wide structural channels running along near (0.2, 0.5, 0) (substitution model Cr II, Fig. 1.3.6c). Possible chromium octahedral sites in the O(C) vacancies are strongly distorted but become

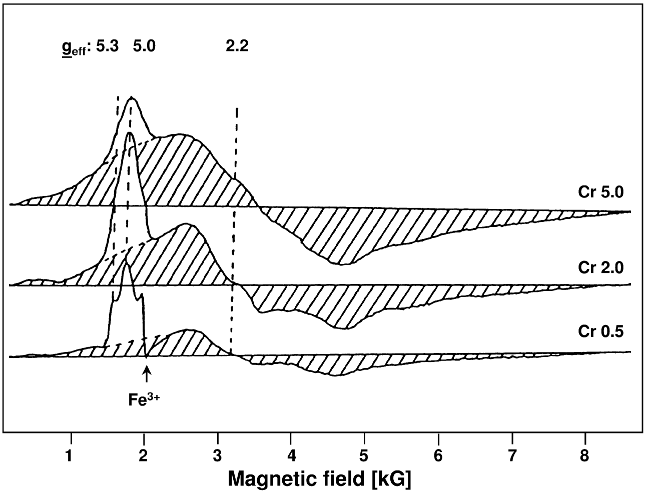

Fig. 1.3.5 EPR spectra of chromium-substituted mullites (Cr_2O_3 contents Cr 0.5 = 0.5 wt.%, Cr 2.0 = 2 wt.%, Cr. 5.0 = 5 wt.%). The hatched areas correspond to the EPR signal denoted by $g_{eff} = 2.2$. The arrow labeled Fe^{3+} indicates that traces of "free" Fe_2O_3 occur in the samples (from Schneider et al. 1994).

more regular if the O(C*) oxygen position is occupied. This is the case near the characteristic oxygen vacancies of the mullite structure. Such sites become almost completely regular by a small additional O(C*) oxygen shift toward the center of the octahedron. Incorporation of Cr^{3+} on equipoint near (0.1, 0.25, 0) implies that the nearest $^{[4]}Al^*$ position cannot be occupied, which is equivalent to the substitution $^{[6]}Cr^{3+} \rightarrow {}^{[4]}Al^{(*)3+}$. In addition, adjacent $Al(2)O_4$ tetrahedra, which would share an edge with the new octahedron, must be vacant, or the Al(2)-ion must occupy an additional Al* site. Chromium incorporation into the structural channels in a distorted octahedral environment near (0.2, 0.5, 0) does not require any severe changes in the configuration of adjacent polyhedra. It can be described by the substitution scheme $^{[6]}Cr^{3+} \rightarrow {}^{[4]}Al(2)^{3+}$. Both types of interstitial octahedra form pairs with the $Al(1)O_6$ octahedra by sharing common faces, as in the α-alumina structure. Furthermore, the proposed substitution schemes do not need any charge compensation mechanism. Therefore, the broad EPR signal at $g_{eff} \approx 2.2$ has been interpreted by Rager et al. (1990) as being mainly due to chromium pairs, where the formation of pairs may occur via occupation of neighboring regular octahedral sites, or through occupation of adjacent regular and interstitial sites, or both.

Unpolarized crystal field spectra measured by Ikeda et al. (1992) in the wavelength range of 340 to 1540 nm by reflection from polycrystalline mullite doped with 8 wt.% Cr_2O_3 yielded further evidence for the structural distribution model of Cr^{3+} developed by Rager et al. (1990). Crystal-field spectra show two pairs of absorption peaks. One of them was attributed to Cr^{3+} ions replacing Al^{3+} at octahe-

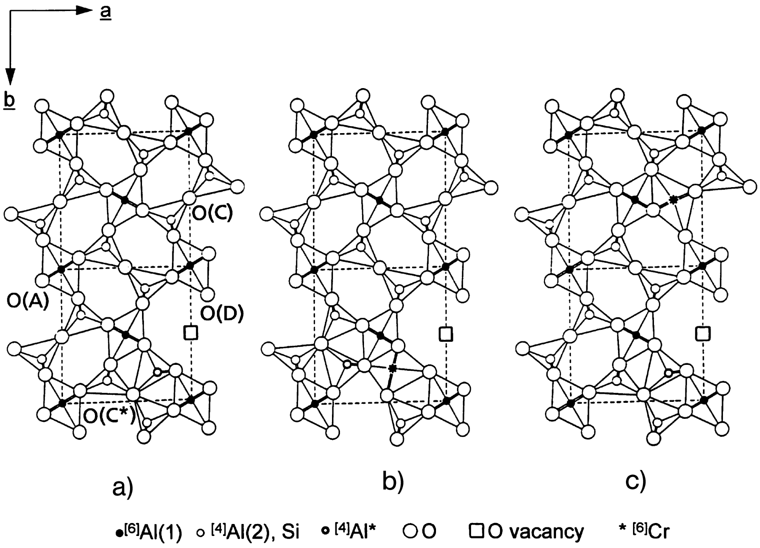

Fig. 1.3.6 Structural models for chromium incorporation in mullite shown in projections down the **c** axis; (a) Transition metal-free mullite, or Cr^{3+} substitution for octahedrally bound Al^{3+} in M position; (b) Substitution of Cr^{3+} for tetrahedrally bound Al^{3+} in T* position near the oxygen vacancy (substitution model Cr I); (c) Substitution of Cr^{3+} for tetrahedrally bound Al^{3+} in T position in the structural channels running parallel to to the **c** axis (substitution model II, see Rager et al. 1990, from Schneider et al. 1994).

dral M(1) sites (Fig. 1.1.17). The other pair of absorption peaks was assigned to Cr^{3+} ions occurring at interstitial octahedral lattice sites. Crystal field spectroscopic data revealed the presence of two kinds of interstitial CrO_6 octahedra corresponding to the EPR-derived substitution model Cr II (Fig. 1.3.6). Integrated absorption intensities yielded estimated Cr^{3+} site occupancies of ≈ 40% in M(1) position, and of ≈ 30% in both of the interstitial channel positions (Ikeda et al. 1992). Becker and Schneider (2005) re-investigated the Cr^{3+} incorporation in mullite single crystals. Although they obtained similar results to those of Ikeda et al. they suggested that the spectra can also be interpreted by a single Cr^{3+} position in mullite (Fig. 1.3.7).

Data on time-resolved fluorescence spectroscopy of chromium-doped mullites (about 2 to 11 wt.%) have been provided by Piriou et al. (1996). They showed that depending on the chromium concentration and on the excitation frequency a low-field site (LFS) transition ($^4T_2 \rightarrow {}^4A_2$), and a high-field site (HFS) transition ($^2E \rightarrow {}^4A_2$) can be distinguished. Mullites with low chromium contents (≤2 wt.% Cr_2O_3) exhibit high- and low-field sites, and an intermediate site with ^2E character with a long decay time. Mullites with high chromium contents (≥5 wt.% Cr_2O_3) produce emission spectra with one low-field site only, having the lowest $^4T_2$ level. Accord-

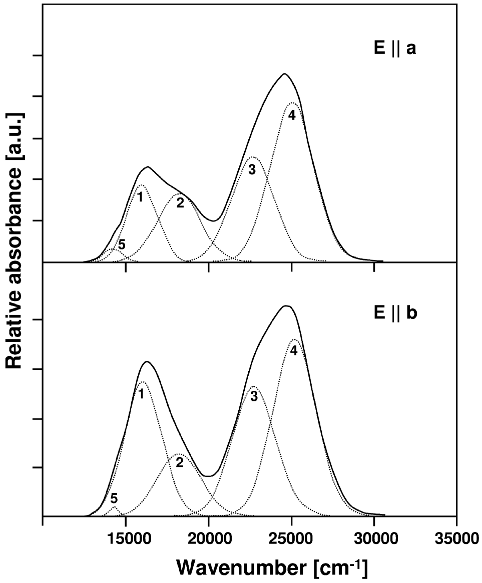

Fig. 1.3.7 Crystal field spectra of a chromium-substituted mullite single crystal plate (0.6 wt.% Cr_2O_3), cut parallel to (001), with the electrical vectors oscillating parallel to to the **a** (E//**a**) and **b** (E//**b**) axes. Full lines: Measured data, dotted lines: Fitted curves. Ikeda et al. (1992) assigned peaks 1 and 3 to interstitial Cr^{3+}, referring to substitution model Cr I and Cr II (see Fig. 1.3.6 and Rager et al. 1990), while peaks 2 and 4 were assigned to substitution of Cr^{3+} for octahedrally bound Al^{3+}. According to Becker and Schneider (2005) a single Cr^{3+} position should also be considered (according to Becker and Schneider, 2005).

ing to Piriou et al. (1996) the low-field site can be attributed to a distorted interstitial octahedral environment of chromium. The HFS peaks occurring additionally in low-chromium mullite spectra lie close to lines in chromium-doped α-alumina (ruby). They are therefore ascribed to Cr^{3+} in undistorted $M(1)O_6$ octahedra in mullite. Obviously, fluorescence spectroscopy supports the earlier suggestion of a bimodal Cr^{3+} distribution in mullite, including undistorted $M(1)O_6$ octahedra and distorted interstitial octahedral sites. According to these results, at low Cr_2O_3 concentrations mullite preferentially incorporates chromium in the $M(1)O_6$ octahedra, whereas the second substitution mode becomes more important at higher chromium contents.

Measurements of the extended X-ray absorption fine structure (EXAFS) of the Cr_K edge were performed by Bauchspiess et al. (1996) for mullites doped with Cr_2O_3 ranging between 5 and 11 wt.%. For all spectra the Fourier transform (FT), which is directly related to the radial distribution function (rdf), is characterized by two pronounced peaks. The first peak near $R = 1.65$ Å was ascribed to oxygen atoms nearest to chromium, and the second peak to those nearest to aluminum and/or silicon. The chromium-oxygen peak yielded a satisfactory fit of measured and calculated values. Although the fit of the chromium-aluminum (silicon) peak is less perfect no asymmetry of the coordination shell has been detected. However, the EXAFS data are not contradictory to the previously reported spectroscopic results, which yielded evidence for a bimodal structural distribution of chromium in mullite. Obviously, the resolution of the EXAFS spectrum is not high enough to distinguish the structurally very similar octahedral chromium sites in mullite. Bauchspiess et al. (1996) on the basis of their studies mentioned that the chromium-aluminum (silicon) distances in mullite increase with the degree of chromium incorporation by 0.007 Å from the 5 wt.% Cr_2O_3 sample to the 11 wt.% Cr_2O_3 mullite.

The Rietveld refinement of chromium-doped mullite (10 wt.% Cr_2O_3) revealed that Cr^{3+} resides preferentially in the octahedral M(1) site (Fischer and Schneider, 2000, see also Parmentier et al. 1999), with a mean octahedral M(1)-O distance close to that of the calculated alumina to chromia (Al_2O_3/Cr_2O_3) mole fraction. The predominance of the incorporation of the relatively large Cr^{3+} ions in the place of Al^{3+} should produce the strongest expansion along the long and elastic M(1)-O(D) bond with associated strong **b** axis lengthening. Since chromium incorporation produces $a > b$ expansion (see Rager et al. 1990) this obviously is not the case. According to Fischer and Schneider a possible explanation of the problem is that the strong M(1)-O(D) expansion is partially compensated by a simultaneous shortening of tetrahedral T-O bonds.

There remains, however, the discrepancy between X-ray diffraction and spectroscopic data. The latter yield evidence for two different structural Cr^{3+} positions in mullite, one at "normal" octahedral M(1) sites and the other at interstitial octahedral sites, as shown in Fig. 1.3.6. Fischer and Schneider (2000) presented a new model including both diffraction and spectroscopic data. It starts from the presence of $\ldots Cr^{3+}\text{-}Cr^{3+}\text{-}Cr^{3+}\ldots$ clusters in the octahedral chains running along the **c** axis. CrO_6 octahedra then can have either CrO_6 units as next-nearest neighbors ("cluster CrO_6") or, alternatively, CrO_6 and AlO_6 polyhedra ("non-cluster CrO_6"). Since the two types of CrO_6 octahedra display slightly different distortions they may produce split signals in the respective spectra. Although this incorporation model is consistant with diffraction and spectroscopic results it is in fundamental disagreement with the chromium incorporation model published by Rossouw and Miller (1999). These authors, starting from the "Atom location by channelling enhanced microanalysis (ALCHEMI)" technique, stated that in Cr_2O_3-rich mullites (10 wt.% Cr_2O_3) most of the chromium enters an interstitial site at 0, 0.25, 0. This, however, is unlikely, since the next-nearest distance between two adjacent octahedral sites then becomes extremely short (1.93 Å). This must lead to a very high (Al^{3+}, Cr^{3+})-Cr^{3+} repulsion, which in turn should produce a very high temperature factor for these cation sites. However, this obviously is not the case.

In spite of the many detailed diffraction and spectroscopic studies, the manner of structural incorporation of Cr^{3+} in mullite remains an open question.

1.3.1.4 **Manganese Incorporation**

Schneider and Vasudevan (1989) provided data on manganese-doped mullites, which were synthesized from metal organic starting materials by a modified sol-gel technique at low temperature (≥700 °C). Schneider and Vasudevan suggested that up to 6 wt.% Mn_2O_3 can enter the mullite structure. Manganese was believed to be incorporated into mullite as Mn^{3+}, which is reasonable considering the charge and size of the cation and because of the "low" temperature stability of Mn^{3+} (see Fig. 1.3.2).

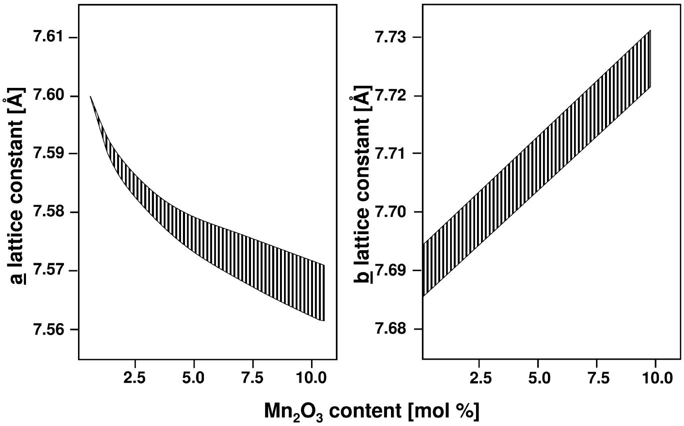

Fig. 1.3.8 Schematic dependence of lattice constants *a* (left) and *b* (right) of mullite from the degree of manganese incorporation (given as Mn_2O_3 content). The hatched areas correspond to the scatter of experimentally determined values. Note that this scatter depends on the Mn_2O_3 content in the case of *a* but not of *b* constants (from Schneider et al. 1994).

With respect to the lattice constants of sinter-mullite the **a** cell edge of the undoped sol-gel mullite is considerably expanded, while **b** and **c** edge lengths are similar to those of the reference mullite (see Table 1.3.2). The strong **a** edge expansion is caused by the high Al_2O_3 content of the low-temperature-produced sol-gel mullite (see Sections 1.1.3.7 and 2.5.1). As manganese is incorporated, the *a* constant first displays strong contraction, which later becomes weaker. The **a** cell edge contraction correlates with a strong and linear **b** expansion, while the **c** cell edge length is less dependent on manganese incorporation (Fig. 1.3.8).

X-ray diffraction line profile analyses carried out by Schneider and Vasudevan (1989) indicate crystallographically controlled strain in mullite: With manganese incorporation this first decreases and later increases again along the [110] direction, while it gradually decreases parallel to [001]. The incorporation-induced strain distribution is explained by the overlapping of a strain relaxation mode, and a mode inducing strain increase. Schneider and Vasudevan (1989) attributed the strain relaxation mode to partial rearrangement of the distorted crystal structure of the undoped sol-gel mullite, due to manganese incorporation. The mode that increases strain was correlated with the substitution of octahedrally bound Al^{3+} by Mn^{3+}: The $3d^4$ electrons of Mn^{3+} in an octahedral crystal field are split from the energetic ground state to the high-spin state $(t_{2g})^3(e_g)^1$. Considering that the e_g electron occupies the d_{z2} orbital and not the $d_{(x2-y2)}$ orbital, this has the effect of lengthening the octahedron's **z** axis. This may be explained by repulsion of the d_{z2} electron from the electrons of the respective oxygen ligands (Jahn-Teller distortion). Taking into account that the octahedron's **z** axis is parallel to the M(1)-O(D) bond, and that **z** lies about 30° to either side of the crystallographic **b** axis (Fig. 1.1.14), this may also explain the strong Mn^{3+} incorporation-induced **b** expan-

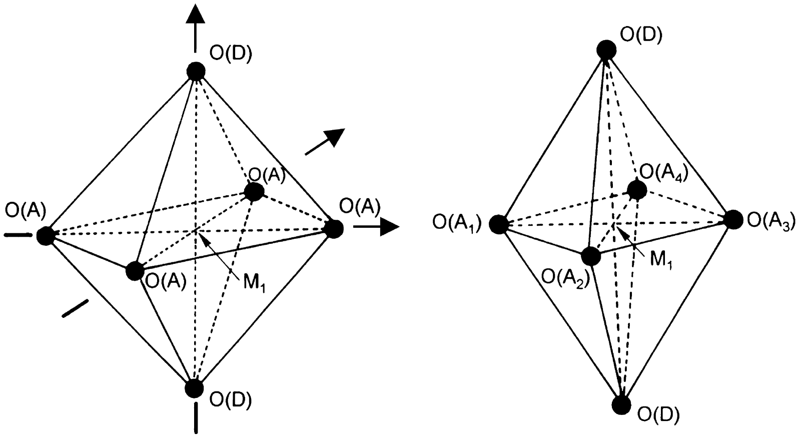

Fig. 1.3.9 Deformation of the oxygen octahedra in mullite by substitution of Al^{3+} by Mn^{3+} (right). Note that the symmetrically equivalent O(A) sites in the non-substituted less deformed octahedron (left) degenerate to non-equivalent sites in the distorted state (labeled as O(A_1), O(A_2), O(A_3) and O(A_4); from Schneider et al. 1994).

sion and the high standard deviations of the *b* spacings. The deformation of the oxygen octahedra by Mn^{3+} incorporation with associated M-O(D) lengthening can also be responsible for the **a** axis shortening in sol-gel mullites. Substitution of Al^{3+} by Mn^{3+} obviously degenerates the symmetrically equivalent O(A) positions of the octahedron to four non-equivalent states O(A_1), O(A_2), O(A_3) and O(A_4), by shortening of the O(A_1)-O(A_4) and O(A_2)-O(A_3) bonds lying close to **a**. Since no incorporation-induced change of the *c* parameter was observed, the lengths of the O(A_1)-O(A_2) and O(A_3)-O(A_4) bonds lying parallel to **c** are less affected by the entry of Mn^{3+} into the mullite structure (Fig. 1.3.9).

Undoped sol-gel mullites form very small crystallites. The incorporation of small amounts of Mn^{3+} in the sol-gel mullites induces tabular crystal growth parallel to the crystallographic **c** axis, while higher amounts of Mn^{3+} incorporated in mullite cause the formation of more equiaxed but smaller crystallites. Crystallite sizes of sol-gel mullites along [110] are similarly small over the whole manganese solid-solution range.

1.3.1.5 **Iron Incorporation**

A survey of literature data shows that mullite incorporates up to about 12 wt.% Fe_2O_3 (Muan, 1957, Brownell, 1958, Gelsdorf et al. 1958, Murthy and Hummel, 1960, Razumowski et al. 1977, Bohn, 1979, Schneider and Rager, 1986). The crystal chemistry of iron-doped synthetic sinter-mullites and of commercially produced fused-mullites was studied by Schneider and Rager (1986) with chemical, X-ray diffraction (XRD) and electron paramagnetic resonance (EPR) techniques. Iron incorporation into mullite causes relatively low *a*, but stronger *b* and *c* lattice constant expansions (Table 1.3.2). The observation was interpreted in terms of an octahedral substitution of Al^{3+} by Fe^{3+} which causes the most “elastic” bond of the octahedron, i.e. M(1)-O(D), lying about 30° to either side of **b**, but about 60° to either side of **a** (Fig. 1.1.17) to expand most strongly. The reciprocal dependence between Fe_2O_3 and Al_2O_3 but not between Fe_2O_3 and SiO_2 (Fig. 1.3.4) also indicates preferred Fe^{3+} substitution for Al^{3+}.

Schneider et al. (1994) published a Mössbauer spectrum from an iron-rich mullite (about 11 wt.% Fe_2O_3). It consists of two relatively broad symmetric lines, similar to the spectrum published by Cameron (1977c). A one-doublet computer fit yields a quadrupole splitting (QS) of about 1.10 mm sec^{-1}, an isomer shift (IS) of about 0.40 mm sec^{-1} versus α-iron, and a line width of about 0.60 mm sec^{-1} (liquid N_2 conditions: 80 K). The isomer shift is appropriate for Fe^{3+} in octahedral coordination. According to these studies there is no clear evidence for tetrahedral Fe^{3+} incorporation in mullite, although Mössbauer spectra of natural sillimanites suggest that about 80% of the incorporated iron can be in octahedral, and about 20% in tetrahedral, coordination (Rossman et al. 1982; see also the results on the electron paramagnetic resonance studies on iron-doped mullite). Since the quadrupole splitting of the Fe^{3+} doublet is moderately large in mullite, a moderately distorted octahedral iron site has been be expected, in comparison to the low distorted octahedral Fe^{3+} sites in pyroxenes, garnets, amphiboles and micas (QS: about 0.4 to 0.6 mm/sec) and the more distorted Fe^{3+} sites in epidote (QS: about 2.0 mm/sec or higher, Rossman et al. 1982). The revision of Mössbauer measurements of iron-doped mullite provides a new detailed view of the Fe^{3+}-incorporation mode in mullite: Attempts to fit a single Mössbauer doublet with a Lorentzian line shape fail (Cardile et al. 1987, Parmentier et. al. 1999, Mack et al. 2005). Mack et al. (2005) on the basis of temperature-dependent Mössbauer measurements propose a three-doublet Mössbauer curve deconvolution (Fig. 1.3.10): Two structurally very similar sites (labelled A and B) with an isomer shift of about 0.32 mm sec^{-1}, and a third somewhat deviating site (labelled C) with an isomer shift of about 0.10 mm sec^{-1} versus α-iron (relationships refer to room temperature). While site A can readily be assigned to octahedral Fe^{3+}, the temperature-dependent evolution of site B suggests that it should equally be attributed to Fe^{3+} in octahedral coordination. The third site, C, is assigned to a minor amount of Fe^{3+} in tetrahedral sites. Making use of this approach, the octahedral site A (occupancy about 65%) is slightly more distorted than octahedral site B (occupancy about 30%), while the tetrahedral site C is of minor importance. It is not clear whether both octahedral sites (A and B) reflect inherently existing differences in the structural arrangement of the octahedral chains in mullite, which, however, are so weak that they cannot be resolved with structure refinements, or if these differences are produced by the iron incorporation itself. The Mössbauer studies of Mack et al. give neither evidence for a temperature-induced increase of the amount of tetrahedrally coordinated iron, nor for significant changes of the distortion of iron oxygen polyhedra. This documents the very high thermal stability of the Fe^{3+} distribution in mullite. The finding of a favored incorporation of iron at octahedral sites has also been stressed in studies

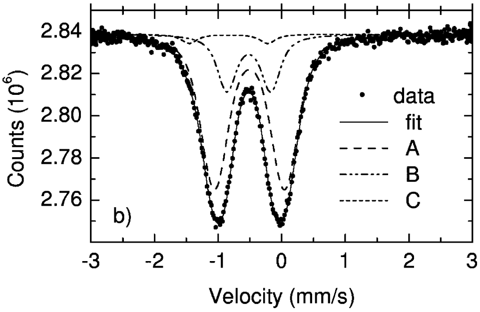

Fig. 1.3.10 Mössbauer transmission spectrum of iron-substituted mullite (10.3 wt.% Fe_2O_3) at 100 °C. Sites A and B have been assigned to octahedrally bound Fe^{3+}, while site C is assigned to tetrahedrally coordinated Fe^{3+}. Fit to the data has been carried out by Voigt profile analysis (after Mack et al. 2005).

investigating the role of iron in mullite formation from kaolin using Mössbauer spectroscopy and Rietveld refinement (Soro et al. 2003) and by extended X-ray absorption fine structure (EXAFS) measurements (Ocana et al. 2000).

Cameron (1977b), referring to reflectance spectra of Faye and Harris (1969) from titaniferous varieties of andalusite, stressed the idea of preferred octahedral incorporation of Fe^{3+} and Ti^{4+} in mullite. The pleochroism from lilac (moderate iron/titanium ratios) to pale yellow (high iron/titanium ratios) was ascribed to $Fe^{2+} \rightarrow Fe^{3+}$, $Ti^{3+} \rightarrow Ti^{4+}$, and $Ti^{3+} + Fe^{3+} \rightarrow Ti^{4+} + Fe^{2+}$ charge transfer. For charge transfer to take place, it is considered necessary that most of the titanium and iron substitute for octahedral aluminum in mullite.

Electron paramagnetic resonance studies on iron-doped mullite have been carried out by Schneider and Rager (1986). Different Fe^{3+} centers could be distinguished in the mullite electron paramagnetic resonance (EPR) spectra: Signals with g_{eff}-values near 6.8 and 5.1 belonging to a common electron paramagnetic resonance center designated as center I, and a signal near $g_{eff} = 4.2$, which was designated as center II (Fig. 1.3.11). The temperature dependence of the spectra was found to be similar for all mullites: The intensity of the signals near $g_{eff} = 4.2$ (center II), and 5.1 and 6.8 (center I) increases with decreasing temperature. The distortion factor $\lambda \approx 0.12$ of center I indicates a rather axially symmetric crystal field, while center II has a λ-value of about 1, which is attributed to a completely orthorhombic crystal field. Mullite electron paramagnetic resonance centers II and I were attributed by Schneider and Rager (1986) to isolated Fe^{3+} ions at tetrahedral and octahedral sites, respectively. Bond distances and angles of the octahedron of 3/2-mullite as determined by Saalfeld and Guse (1981) yield approximate axial symmetry, thus confirming the assignment of center I to the octahedral position, which in turn corresponds with a low λ-value. Contrary to the appearance of the iron-rich sinter-mullite patterns, the electron paramagnetic resonance spectra of iron-poor fused-mullite exhibit signals corresponding to center II ($g_{eff} \approx 4.2$), but not those of center I. This is interpreted in terms of nearly exclusive iron incorporation at tetrahedral sites though in very low concentrations. Though Mössbauer spectroscopy and electron paramagnetic resonance analysis prove that iron essentially occurs as Fe^{3+} in mullite, there is evidence for the presence of traces of Fe^{2+} in titanium-rich mullites grown from a melt in a reducing atmosphere (Schneider and Rager, 1984, Rager et al. 1993).

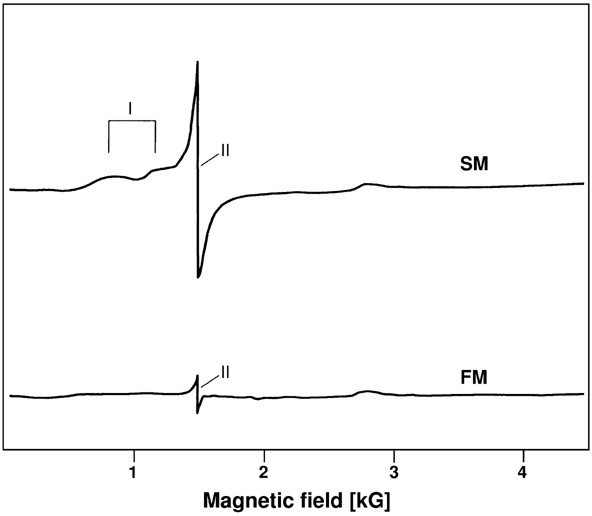

Fig. 1.3.11 Electron paramagnetic resonance (EPR) spectra of iron-substituted mullite. Electron paramagnetic resonance centers I and II are assigned to octahedrally and tetrahedrally coordinated Fe^{3+} in mullite, respectively. SM: Sinter-mullite (0.22 wt.% Fe_2O_3); FM: Fused-mullite (0.10 wt.% Fe_2O_3). Note that the sinter-mullite contains Fe^{3+} at octahedral and tetrahedral sites, while the fused-mullite contains Fe^{3+} preferentially at tetrahedral sites (from Schneider et al. 1994).

The temperature-dependent iron distribution between mullite and a coexisting silicate melt was investigated between 1300 and 1670 °C by Schneider (1987a). The maximum iron content of the mullites strongly decreases from about 10.5 wt.% (6 mol%) Fe_2O_3 at 1300 °C to about 2.5 wt.% (1.5 mol%) Fe_2O_3 at 1670 °C (Fig. 1.3.12). Mullite dissolution in the temperature field under consideration is too low to fit a simple eutectic melting in the system $3Al_2O_3 \cdot 2SiO_2$-"$3Fe_2O_3 \cdot 2SiO_2$" with limited mutual solubility of the compounds. Therefore, a temperature-controlled iron distribution between crystal and melt has to be taken into account (Schneider, 1987a). Further studies on the iron distribution between mullites and coexisting iron-rich silicate glasses were performed between 1350 and 1670 °C by Schneider (1989). They found a reciprocal dependence between iron incorporation into mullite and the annealing temperature, though the amount of iron incorporation was also correlated with the bulk iron content of the samples.

With respect to the iron distribution mechanism two temperature regions could be distinguished:

- A temperature field extending between about 1500 and 1670 °C with small standard deviations of the iron oxide contents of mullite and of the coexisting glass phase. Iron exchange processes between mullite and coexisting glass phase in this temperature region were discussed using Nernst iron distribution patterns (Fig. 1.3.13). Results were interpreted as follows:

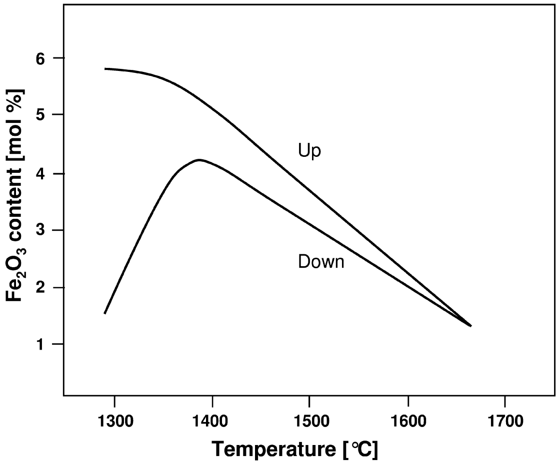

Fig. 1.3.12 Temperature-dependent evolution of iron incorporation in mullite coexisting with a silicate melt. The experiment used a starting mullite with 10.5 wt.% Fe_2O_3. Up: Heating up experiments; down: Back annealing experiments. The strong deviation of "up" and "down" curves at temperatures below about 1400 °C is explained by slow diffusion velocities, which do not allow the iron equilibrium distribution to be established (from Schneider et al. 1994).

- Iron content ratios between mullite (c^s), and coexisting silicate melts (c^l), produce linear curves indicating equilibrium iron distribution;
- In relation to the iron content of the glass phase the amount of iron incorporated into mullite increases with decreasing temperature;
- The iron oxide distribution c^s/c^l ratios increase with increasing iron contents of the bulk samples;
- With increasing annealing temperatures the iron distribution curves approach each other and cross at about 1670 °C. However, it is not clear whether iron incorporation then becomes independent of the bulk iron content of the samples, or whether iron incorporation into mullite is then reciprocally correlated with the bulk iron content of the samples;
- Between 1500 and 1670 °C saturation with iron is reached in any of the mullites.

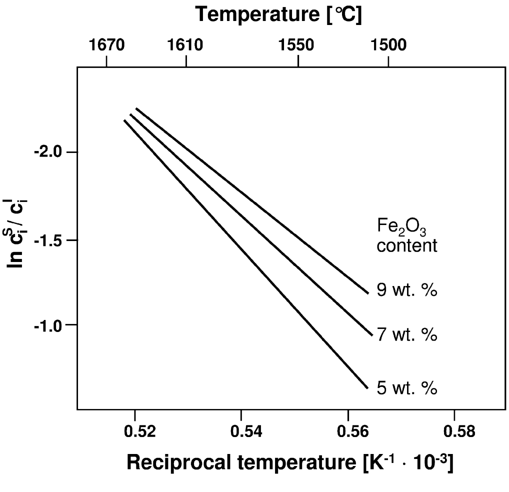

Fig. 1.3.13 Arrhenius plot (Nernst diagram) of the iron distribution between mullite (c^s) and coexisting glass (c^l) for samples with Fe_2O_3 bulk compositions of 5, 7 and 9 wt.%. A ln c^s/c^l versus $1/T$ diagram is given (from Schneider et al. 1994).

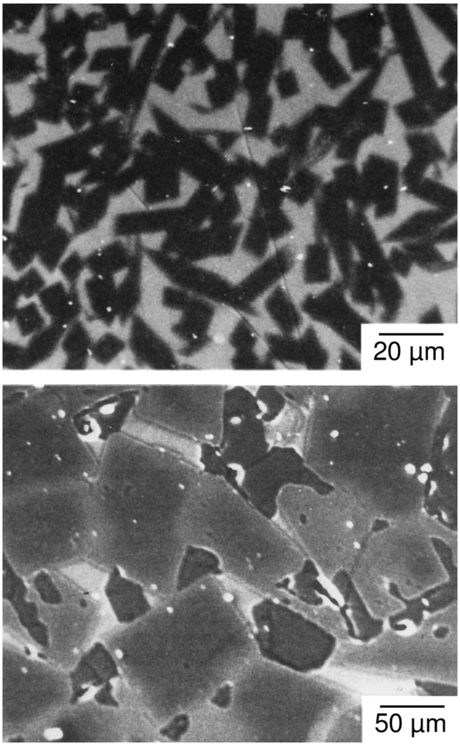

Fig. 1.3.14 Electron microprobe photographs of mullite powder compacts coexisting with an iron-rich glass, corresponding to a bulk Fe_2O_3 content of 7.5 wt.%. Above: Annealed at 1670 °C (7 days); below: Annealed at 1350 °C (22 days). Note the patchy iron distribution in mullite of the "low temperature" sample, indicated by darker ("low" iron contents in the middle of mullite crystals) and lighter areas ("high" iron contents at the mullite crystal rims, from Schneider et al. 1994).

- A temperature field extending below about 1500 °C with widespread iron oxide composition ranges in mullite and between mullite and the coexisting glass phase. This indicates non-equilibrium of iron distribution in mullite and between mullite and the coexisting silicate glass. Electron microprobe analyses show that iron is enriched at the outer rims of mullite, whereas the inner crystals' areas contain less iron (Fig. 1.3.14). Obviously the velocity of diffusion species was too slow below 1500 °C to establish equilibrium iron distribution throughout the crystals (see also Fig. 1.3.12 and Schneider, 1987a).

Things become even more complex if not only iron but multiple foreign cation incorporation in mullite is taken into account. Schneider (1987b) described the temperature-dependent solubility of iron, titanium and magnesium in mullites coexisting with silica-rich partial melts in a used schamotte refractory brick. The mullites of the starting material had relatively high mean titania (TiO_2) but lower iron oxide (Fe_2O_3) and very low magnesia (MgO) contents. Cation removal from mullite to the coexisting glass phase was observed at high temperature though the onset of exsolution is lowest for magnesium and highest for titanium. Cation exsolution curves follow exponential laws with an exsolution rate being considerably higher for Fe_2O_3 than for TiO_2 and MgO (Fig. 1.3.15). The study documents a higher mobility of the iron ion than those of titanium and magnesium.

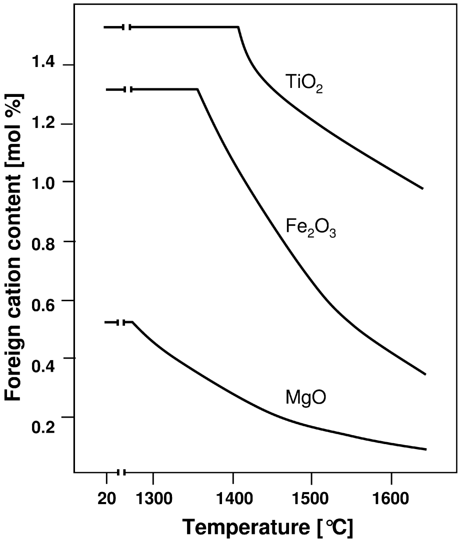

Fig. 1.3.15 Iron, titanium and magnesium incorporation in mullite coexisting with a silicate melt in a used schamotte brick. The Fe_2O_3, TiO_2 and MgO contents are shown versus increasing annealing temperatures. Note that the onset temperature of foreign cation exsolution from mullite follows the sequence $T_{Mg} < T_{Fe} < T_{Ti}$ (from Schneider et al. 1994).

1.3.1.6 **Cobalt Incorporation**

Preliminary data on cobalt incorporation in mullite were published by Schneider (1990). Cobalt-doped mullite produces electron paramagnetic resonance spectra with signals near $g_{eff} = 4.9$ and 2.2. These electron paramagnetic resonance signals are attributed to the occurrence of Co^{2+} in octahedral coordination. Owing to the low CoO content of about 1 wt.%, neither significant incorporation-induced changes of the lattice constants nor microchemical interdependences between Al_2O_3 and SiO_2 on the one hand and CoO on the other hand can be detected. No information on the incorporation of Co^{3+} into the mullite structure is available as yet.

1.3.1.7 **General Remarks on Transition Metal Incorporation**

Dependent on synthesis temperatures and atmospheres, mullite incorporates Ti^{3+}, Ti^{4+}, V^{3+}, V^{4+}, Cr^{3+}, Mn^{3+}, Fe^{2+}, Fe^{3+} and Co^{2+}, though in strongly differing amounts. The upper solubility limit is controlled by radii and oxidation states of transition metal ions, with the highest degrees of incorporation being observed for V^{3+}, Cr^{3+} and Fe^{3+} followed by Ti^{4+}. Only very low amounts of Fe^{2+} and Co^{2+} ions can enter the mullite structure (Schneider, 1990).

The transition metal ions are preferably incorporated into the $M(1)O_6$ octahedra in mullite. Two differently distorted octahedral sites have been revealed by spectroscopic methods in the case of Ti^{3+} and Fe^{3+}. Fe^{3+} also enters the oxygen tetrahedra in small amounts, while Cr^{3+} is possibly distributed over the $M(1)O_6$ oxygen octahedra and octahedral interstitial lattice sites, or, alternatively forms Cr^{3+}-Cr^{3+} clusters in the octahedral chains in the **c** direction (see Section 1.3.1.3). Mn^{3+}-substituted mullites are characterized by major changes of lattice spacings and associated increased lattice strains. Both observations are explained by Jahn-Teller distortion of Mn^{3+} in an octahedral environment (Schneider, 1990).

The relatively large cation sizes and high octahedral but lower tetrahedral crystal-field splitting parameters of most transition metal cations may explain their preference for octahedral coordination. Fe^{3+} and Mn^{2+} ions in the middle of the 3d transition metal series are exceptional: these cations have a stable d^5 electron configuration, with a spherically symmetrical charge distribution similar to those of noble gases. Consequently Mn^{2+} and Fe^{3+} exhibit no site preference and their incorporation behavior is mainly controlled by the sizes of the cations. Actually a small amount of Fe^{3+} does enter the oxygen tetrahedra in mullite at high temperature. On the other hand, Mn^{2+} is obviously too large to be tetrahedrally incorporated in mullite (Schneider, 1990).

Entry of the relatively large transition metal cations into the oxygen octahedra in place of aluminum should produce greater expansion of *b* than of *a*, because the most elastic bond of the octahedron (M(1)-O(D)) lies about 30° to either side of **b** (Fig. 1.1.14). Greater **b** than **a** expansion has actually been observed for V^{3+}, Mn^{3+} and Fe^{3+} substituted mullites (Table 1.3.2). The extreme **b** lengthening (and **a** shortening) of Mn^{3+}-substituted mullites is believed to be due to repulsion of singly occupied d_{z2} electron orbitals of Mn^{3+} by the electrons of the O(D) ligands along the octahedral M(1)-O(D) bonds (Jahn-Teller distortion, Fig. 1.3.9). The intense **a** expansion of Ti^{4+}-doped mullites may be explained by substitution of tetrahedral Si^{4+} by Al^{3+}, which occurs along with the octahedral incorporation of Ti^{4+} for charge compensation. The anomalously high **a** expansion of chromium- substituted mullites can possibly be explained by partial entry of Cr^{3+} into interstitial structural channels parallel to the crystallographic **c** axis. Possibly the unique tendency of Cr^{3+} to occupy interstitial lattice positions in mullite can be explained by its ability to produce metastable octahedral oxygen environments in glass and silicate matrices (Schneider, 1990).

While the structural position of 3d transition metals in mullite seems to be controlled essentially by electron configuration and size of cations, the amount of cation incorporation is also dependent on the oxidation state of the ions. Obviously maximum incorporation can be observed if the transition metal occurs as an M^{3+} ion. This can be understood, taking into account that octahedral transition metal incorporation is associated with removal of Al^{3+} from the structure (Fig. 1.3.4). The entry of cations with deviating oxidation states (e. g.: Ti^{4+} and V^{4+}) is less favorable, even if their radii are closer to that of Al^{3+}, since it requires simultaneous tetrahedral substitution of Si^{4+} by Al^{3+} in order to compensate for the excess positive charge.

1.3.2
Other Foreign Cation Incorporation

Besides transition metals the mullite structure is able to incorporate a variety of other foreign cations, although in variable concentrations. Synthesis experiments on the incorporation of Ga^{3+} in mullite were described by Schneider (1986a). A maximum of about 12 wt.% Ga_2O_3 was determined. According to microchemical relationships (Fig. 1.3.4), and because Ga^{3+}-doped mullites display strongest incorporation-induced expansion parallel to the crystallographic **b** axis (Fig. 1.1.14), it has been suggested that Ga^{3+} substitutes Al^{3+} favorably at octahedral lattice positions.

In an early work Scholze (1956) described the solubility of boron in aluminum silicon mullite. Grießer (2005) re-studied the potential boron incorporation into mullite at 950 and 1300 °C. According to this work mullite has a strong tendency to incorporate B^{3+}. B_2O_3 contents up to about 20 mol% have been reported (Fig. 1.3.16). Incorporation of B^{3+} in mullite probably occurs interstially or at tetrahedral sites. Substitution of Al^{3+} by B^{3+} is charge neutral, while substitution of Si^{4+} produces excess negative charge and therefore is less probable. Incorporation of boron in mullite should cause a reduction of lattice spacings, which was, in fact, is observed. In contrast to boron incorporation into mullite no significant silicon incorporation into boron aluminate $Al_{6-x}B_xO_9$ has been described (see Section 1.1.3.14). The excess positive charge produced by Si^{4+} for Al^{3+} replacement may be one reason for this. Thus, there exists a clear solubility gap between mullite and boron aluminate of the composition $Al_{6-x}B_xO_9$. This is understood in terms that although both end members belong to the mullite family, they are distinguished by structural details that do not allow complete and continuous solid solution (see also Section 1.1.3).

Microchemical studies have shown that alkali or alkaline earth cations can enter the mullite structure, though in small quantities (should not be mixed up with the alkali aluminates with mullite-type structure, see Section 1.1.3.7). Owing to its large cation size, Na^+ ($^{[8]}Na^+$: 1.16 Å) can only be incorporated into the thermally expanded mullite structure at very high temperature (up to about 0.4 wt.% Na_2O, Fig. 1.3.17). The Na_2O content of mullite rapidly decreases with decreasing temperature (Schneider, 1984). Mullite incorporates up to about 0.5 wt.% MgO (Schneider, 1985). Magnesium incorporation decreases with temperature and is

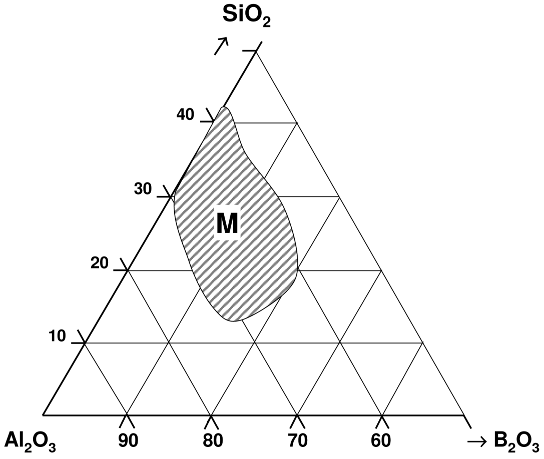

Fig. 1.3.16 Boron incorporation in mullite (M). Note the extended mixed crystal range with B_2O_3 contents of up to 20 mol% being incorporated into mullite at 1300 °C (after Grießer, 2005).

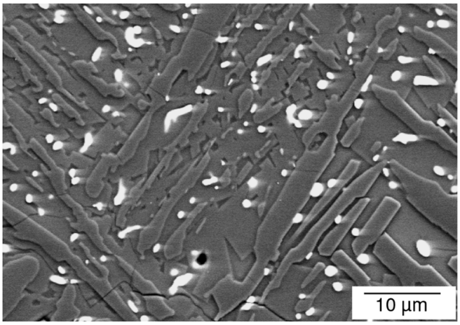

Fig. 1.3.17 Scanning electron micrograph of a fused-mullite refractory brick consisting of mullite (matrix), α-alumina (acicular phases), zirconia (light grains) and silicate glass (at grain junctions). The elongated crystals of α-alumina are the result of rapid crystallization at the outer rim of the refractory brick.

reciprocally correlated with the aluminum content of the phase. These observations have been interpreted in terms of an interstitial incorporation of Na^+ and of a substitution of octahedral Al^{3+} ions by Mg^{2+} ($^{[6]}Mg^{2+}$: 0.72 Å, Schneider, 1984, 1985). In a recent study on the thermal decomposition of muscovite, Rodriguez-Navarro et al. (2003) reported more than 1.5 wt.% of MgO into the newly formed mullite. Similarly high incorporation of MgO were described by Rubie and Brearley (1987) and Worden et al. (1987) in mullites derived from the thermal breakdown of magnesium-rich muscovites. No explanation of these high magnesium oxide contents in mullite with correlated charge compensation mechanisms has yet been provided.

Zirconium enters the mullite structure in low amounts (≤0.8 wt.% ZrO_2, Schneider, 1986b). Schneider suggested that zirconium incorporation increases with temperature rather than with the bulk ZrO_2 content, and that "high" zirconium contents can be preserved in mullite only if the material is quenched rapidly to room temperature. It has also been stated that zirconium incorporation increases with the Al_2O_3 content of mullite. Only a very small amount of zirconium (< 0.1 wt.% ZrO_2) is incorporated into 3/2-type mullite, whereas slightly higher zirconium contents (< 0.5 wt.% ZrO_2) can enter 2/1-type mullite. The conclusion of both observations is that the large Zr^{4+} cations ($^{[8]}Zr^{4+}$: 0.84 Å) is incorporated at thermally expanded structural O(C) oxygen vacancies in a similar way to Na^+ (Schneider, 1984). Charge excesses or deficiencies produced by Na^+, Zr^{4+} and Mg^{2+} entry into mullite may be compensated by $Al^{3+} \rightarrow Si^{4+}$, or by $Si^{4+} \rightarrow Al^{3+}$ substitution, respectively.

Caballero and Ocana (2002) investigated the incorporation of tin into mullite synthesized from aerosols. They stated that Sn^{4+} substitutes Al^{3+} at octahedral sites. The authors provided no direct data on the maximum SnO_2 content in mullite, but believed that it is in the same range than that of other foreign tetravalent cations.(i. e. about 3 mol%). Our own synthesis experiments yielded significantly lower SnO_2 incorporation into mullite.

Tomsia et al. (1998), investigating functionally graded molybdenum/mullite composites, mentioned that more than 2 wt.% of molybdenum enters the mullite structure. However, they gave no information on the charge and structural sites of molybdenum in mullite.

Europium-doped mullites have achieved increasing research interest in recent years, owing to their potential application in fluorescent lamps, since Eu^{2+}-doped mullites emit in the blue region. Photoluminescence emission and excitation may also serve as a tool to provide information on the local structural environment of europium in mullite, because of associated electron transitions. Effects are strongly influenced by the crystal fields of the ligands surrounding the europium centers (see Kutty and Nayak, 2000). Piriou et al. (1977) analyzed Eu^{3+}-incorporation into mullite by emission spectroscopy. They described the "unusual" character of the spectra, which they attributed to the strong and anisotropic field arising from the presence of the Eu^{3+} bonds. Kutty and Nayak (2000) studied europium-doped 3/2-mullite (0.41 wt.% Eu_2O_3) and 2/1-mullite (0.67 wt.% Eu_2O_3). They demonstrated that Eu^{3+} in mullite is easily reduced to Eu^{2+} at high temperature and low oxygen partial pressure, and that this process is reversible. Their conclusion was that Eu^{2+} and Eu^{3+} are both incorporated into the relatively large oxygen vacancies in mullite. No model explaining the mechanisms necessary for charge compensation of the interstitial europium ions was provided by the authors. Possibly it is effected by simultaneous Al^{3+} for Si^{4+} substitution. Charge excesses or deficits, caused by $Eu^{2+} \rightarrow Eu^{3+}$ oxidation or $Eu^{3+} \rightarrow Eu^{2+}$ reduction can also be explained by elimination or formation of O(C) oxygen vacancies.

1.4
Mullite-type Gels and Glasses
M. Schmücker and H. Schneider

Instead of natural raw materials like andalusite, sillimanite and refractory-grade bauxite, synthetic precursors have been increasingly used to produce mullite ceramics of high chemical purity, high sinterability and low mullitization temperatures (below 1250 °C).

Since mullite formation mechanisms are strongly affected by the constitution and structure of precursors, knowledge of their temperature-dependent development allows us to design the microstructure and properties of the final mullite ceramics. As an example, mullite ceramics designated for structural applications at moderate temperatures should have a microstructure with small crystal size and a minimum amount of pores, while small amounts of glassy phase can be accepted. In contrast, mullite ceramics for high temperature structural applications have to be glass-free, and a greater crystal size is favored. Moreover, mullite matrices of fiber-reinforced ceramics have to be processed at relatively low temperature (<1350 °C) to avoid fiber degradation (see Section 7.2.1.2), while optical window materials are fabricated at high temperatures (>1600 °C) to achieve dense, optically transparent ceramics. Thus, the precursors must be designed with respect to mullite formation rate, sinterability, composition or additives in order to obtain a final product which best fits the specific applications.

It is generally accepted that two types of mullite precursors exist. One type displays direct mullitization from the amorphous state at temperatures as low as about 950 °C, while the other type shows mullitization above 1200 °C by reaction of transient spinel-type alumina with silica. The former precursor type has been designated as single phase (Hoffman et al. 1984), polymeric (Yoldas, 1990) or type I (Schneider et al. 1993c) while the latter one is called diphasic, colloidal, type II, or NM (no mixing, Okada and Otsuka, 1986, Schneider et al. 1993b). The type of mullite precursor depends on the starting materials and on synthesis conditions. Colloidal suspensions of aluminum and silicon compounds lead to diphasic precursors, whereas true solutions of salts or organometallic compounds give rise to single phase precursors. However, homogeneous solutions of the starting compounds can also produce diphasic mullite precursors. For instance, ethanol diluted admixtures of tetraethyloxysilane plus aluminum-*sec*-butylate can produce single phase or diphasic gels, depending on the process route (see below and Schneider et al.1993c, Voll, 1995). This special case of diphasic mullite precursor has been been designated as rapid hydrolysis gel or type III precursor (Okada and Otsuka, 1986, Schneider et al. 1993c). They are amorphous up to about 950 °C, then form spinel-type alumina plus silica, and mullitization is observed above about 1200 °C.

In the following an overview on the different mullite precursors and their thermal evolution is given. The main emphasis of this section is on the structure (atomic arrangement, short- range-order) of the non-crystalline aluminum silicate phases, structural development before mullitization, correlation between precursor homogeneity and crystallization process, and the mechanisms of mullite formation.

1.4.1
Type I (Single Phase) Mullite Precursors and Glasses

Non-crystalline aluminosilicate precursors transforming directly to mullite at temperatures below 1000 °C have been designated as single phase (e. g. Hoffman et al. 1984). In more recent studies, however, the single phase character of these precursors was a point of controversy: Huling and Messing (1992) mentioned that spinodal phase separation in the amorphous state preceedes mullite crystallization, while Okada et al. (1996) and Schmücker et al. (2001) showed that diphasic precursors may also directly transform to mullite at low temperatures under special circumstances. None the less, cation mixing at the atomic level, i. e. occurrence of Al-O-Si sequences, can in general be assumed for all these precursors. Thus, in the following, to avoid misunderstandings, this type of mullite precursor will be designated as type I, according to Schneider's nomenclature (Schneider et al. 1993c).

1.4.1.1 Preparation of Type I Mullite Precursors and Glasses

Various kinds of type I mullite precursors can be distinguished, depending on their synthesis routes: Chemical methods, sol-gel route, co-precipitation or spray hydrolysis. Aluminosilicate glasses with mullite composition can also be regarded as type I precursors, since their structural short-range order and crystallization behavior is virtually the same as that of the gels. The preparation of mullite glasses is difficult, since the glass-forming ability of aluminosilicate melts is low, and hence extremely high quenching rates are required to suppress crystallization. Recently it has been shown that ultra homogeneous type I mullite precursors can also be produced by vapor deposition techniques, such as high frequency sputtering (Schmücker et al. 2001, Taake, 1999). In addition, non-crystalline aluminosilicate powders with atomic short-range orders similar to that of mullite gels and glasses can be prepared by mechanical amorphization of mullite carried out via long-term ball milling (Schmücker et al. 1998). Thus, starting materials of ultra homogeneous non-crystalline type I mullite precursors can be liquids (solutions, melts), vapor phases or crystalline solids, as indicated in Fig. 1.4.1.

Chemically derived type I mullite precursors A number of routes to process type I mullite precursors have been described in the literature. In general, solutions containing the aluminum and silicon species have to be prepared, which, in a second step, are transformed into solids by precipitation or condensation. An overview of methods and techniques leading to type I mullite precursors is given by Schneider et al. (1994a) and Voll (1995).

Ossaka (1961) was among the first to describe a precursor forming mullite below 1000 °C. This precursor was prepared by dissolving sodium silicate and potassium aluminate in sulfuric acid. Addition of hexamethylene tetramine led to aluminosilicate precipitates which were filtered and washed to remove residual alkali and amine components. The main disadvantages of this process are a poor yield of aluminosilicate precipitate and the occurrence of residual alkali ions. A sol-gel method starting with an organometallic silicon source was introduced by Hoffman et al. (1984) for the preparation of type I mullite precursors. They used a solution of tetraethyloxysilane ($Si(OC_2H_5)_4$, TEOS) and aluminum nitrate nonahydrate ($Al(NO_3)_3 \cdot 9H_2O$, ANN) in ethanol, which had been gelled at 60 °C for several days by a hydrolysis-polymerization reaction. The mullite precursor derived by this method has been designated "single-phase xerogel". A similar process was used by Okada and Otsuka (1986). They emphasized that the aluminosilicate gel transforms directly to mullite in the case of slow hydrolysis ("SH xerogel"). Rapid hydrolysis, on the other hand, produces a gel that forms transition alumina as the first crystalline phase (see below, type III mullite precursors). The same results are

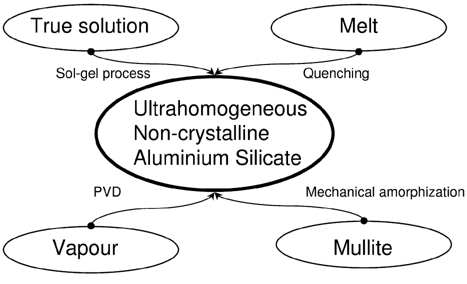

Fig. 1.4.1 Flow chart showing starting materials and processes leading to ultrahomogeneous type I non-crystalline mullite precursors and glasses.

achieved if the gels are aged for more than one month (Okada and Otsuka, 1990), or if gelation is carried out at temperatures below 60 °C (Okada et al. 1996).

Mullite precursor preparation by hydrolysis of organometallic aluminum and silicon compounds is also described in the literature. Alkoxides such as aluminum-isopropylate, aluminum-*sec*-butylate, tetraethyloxysilane (TEOS) or tetramethyloxysilane (TMOS) have been used as starting materials. The preparation of these type I precursors from alkoxides of aluminum and silicon is difficult and very sensitive to the reaction conditions. This is due to the different rates of hydrolysis and polycondensation of the starting compounds, which may cause demixing effects. The problems arising from different reactivities of aluminum and silicon species during the sol-gel process can be minimized by:

- Very slow hydrolysis, e. g. by ambient humidity (Yoldas 1990, Okada and Otsuka, 1986, Colomban, 1989)
- Prehydrolysis of silicon (Voll, 1995)
- Reduction of the hydrolysis rate of aluminum alkoxides using β-diketone (e. g. acetylacetone), as a chelating agent (Heinrich and Raether, 1992)

Spray drying or spray pyrolysis provides an alternative to the hydrolysis-based sol-gel process. Spraying small droplets of a solution containing aluminum and silicon species into a hot reaction chamber causes simultaneous evaporation of the solvents, thermal decomposition and polymerization of the compounds. Thereby the rapid reaction process successfully suppresses demixing effects. The small droplets produced by atomizers or ultrasonicators, yield a precursor powder with particles of spherical shape in the (sub-)micrometer range. Kanzaki et al. (1985) were the first to describe ultra homogeneous type I mullite precursors prepared by spray pyrolysis. Tetraethyloxysilane (TEOS) and aluminum nitrate dissolved in water-methanol solution were atomized and subsequently sprayed into a furnace heated at temperatures between 350 and 650 °C.

Melt-derived type I mullite glasses Gani and McPherson (1977a) showed that aluminosilicate glasses with mullite composition are suitable precursors for mullite ceramics. However, since the glass-forming ability of aluminosilicate melts with alumina contents >20 % is low, extremely high cooling rates are required to suppress the crystallization of melts during the cooling process. Essentially, two methods of mullite glass preparation have been applied. In the first route small melt droplets produced by flame spheroidisation (Takamori and Roy, 1973), plasma spraying (Gani and McPherson, 1977b), or melt atomization (Morikawa et al. 1982) are quenched in water or oil. In an alternative method, the melt is splat cooled between two rollers made of steel (MacDowell and Beall, 1969), titanium (Risbud et al. 1987) or aluminum (Schmücker et al. 1997). Mullite crystallization in the latter case can be suppressed only if particle sizes or flake thicknesses are below about 20 μm (Gani and McPherson, 1977b, Schmücker et al. 1995). Critical particle sizes or glass-flake thicknesses are controlled by the thermal conductivity of the supercooled melt rather than by the cooling medium. Fig. 1.4.2 shows a rapidly solidified aluminosilicate flake produced by roller quenching of the melt. Thin

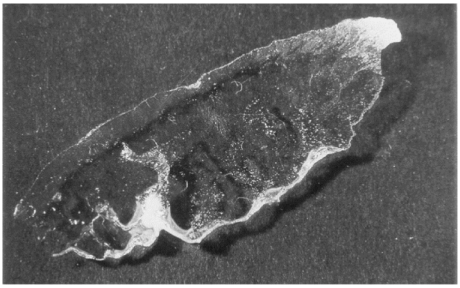

Fig. 1.4.2 Rapidly solidified aluminosilicate glass prepared by roller quenching. Thin and transparent areas are vitreous, while thicker flake areas are partially crystalline (mullite) due to insufficient cooling rates.

areas are transparent and non-crystalline, while thicker areas appear white due to light scattering by micron-sized mullite crystals formed during cooling.

1.4.1.2 **Temperature-induced Structural Evolution of Type I Mullite Precursors and Glasses**

Wet (solution) stage of type I mullite precursors Little information exists about the structural evolution during hydrolysis and gelation (“wet stage”) of type I mullite precursors: Fukuoka et al. (1993) investigated the aluminum coordination of sols and wet gels derived from tetraethyloxysilane (TEOS) plus various aluminum sources by means of ^{27}Al NMR spectroscopy. According to these studies the aluminum ions are octahedrally coordinated in aluminosilicate sols and wet gels derived from aluminum nitrate nonahydrate (ANN) and from boehmite sol, while octahedrally and tetrahedrally bound Al^{3+} is found when aluminum formoacetate is used. Four-, five-, and sixfold coordinated Al^{3+}, on the other hand, occur in gels derived from aluminum di-(butoxide)-ethylacetoacetic ester chelate. Pouxviel and Boilot (1989) investigated the early gelation stages of aluminum silicon esters. Small angle X-ray scattering (SAXS) reveals aggregation of 5 to 8 Å sized elementary clusters. In the case of precursors derived from tetraethyloxysilane (TEOS) plus aluminum *sec*-butylate using acetylacetone as chelating agent, primary particles of 21 to 34 Å form and the condensation is a reaction-limiting cluster-cluster aggregation (Pouxviel et al. 1987). Particles of similar size (about 20 Å) are observed in aluminum nitrate/tetraethyloxysilane (TEOS)-derived sols by means of dynamic light scattering (Jaymes and Douy, 1996; for more details see Section 6.2.1, which deals with mullite fibers).

Dried gel stage of type I mullite precursors The development of dried mullite gels prior to crystallization was investigated by Schmücker and Schneider (1999). These investigations focus on the development of primary particles, volatilization of water and organic groups, condensation of the network, and on the evolution of aluminum oxygen polyhedra. By means of high resolution scanning electron microscopy (SEM), submicron-sized particles are identified in dried or calcined aluminum silicate gels (Fig. 1.4.3). The micrographs show a uniform microstructure of the gel consisting of 20 to 50 nm spherulites. This microstructure remains

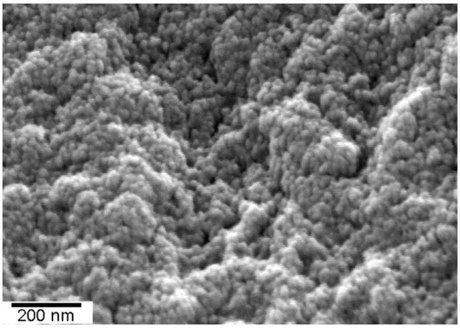

Fig. 1.4.3 Scanning electron micrograph of single phase type I gel showing spherical particles about 20 to 50 nm in size.

unchanged up to 800 °C, indicating no change in particle size and agglomeration behavior. The findings agree well with density data based on refractive index determinations, which reveal a density gain of only 7% after calcination at 900 °C (Okuno et al. 1997). Similar results have been reported by Li and Thomson (1990) on the basis of surface area measurements.

Dehydration and condensation of type I mullite precursors The temperature-dependent removal of water, hydroxyl groups and organic residuals from type I mullite precursors has been studied by means of Fourier transform infrared (FTIR) spectroscopy and mass spectrometry (Voll et al. 1998, Mackenzie et al. 1996). Fig. 1.4.4 shows the analytically determined water loss of tetraethyloxysilane (TEOS)/aluminum *sec*-butylate-derived single phase mullite gels as a function of calcination temperatures together with the integral absorbances of water and hydroxyl groups. Up to annealing temperatures of about 600 °C mullite gels lose virtually all molecular water which is weakly bound at the gel surface and in open pores, whereas the stronger, structurally bound hydroxyl groups are less affected. At temperatures above 700 °C the thermal energy is high enough for dehydroxylation and for subsequent recombination of hydroxyl groups to water ($2OH^- \rightarrow H_2O + 0.5\ O_2$). Some of the newly formed water is trapped in nanopores giving rise to a relative increase of the water content. Temperatures above 800 °C are required for the diffusion of water molecules through the gel network, with the consequence that at 900 °C the mullite precursors are almost water-free.

Investigations of the temperature-dependent decomposition and combustion of organic residuals performed by means of in-situ mass spectrometry reveal that organic species can be retained in mullite gels up to about 900 °C. Released residual organic species formed by prolonged heating below about 250 °C are predominantly straight chains or cyclic hydrocarbons, whereas heating at about 350 °C leads to their conversion into aromatic species. Prolonged heating above 350 °C gradually destroys the aromatic species by oxidation (Mackenzie et al. 1996).

^{29}Si NMR spectroscopic investigations have been used to describe the temperature-induced condensation of the network of mullite gels (Schneider et al. 1992, Mackenzie et al. 1996). Fig. 1.4.5 shows a series of ^{29}Si NMR spectra of calcined

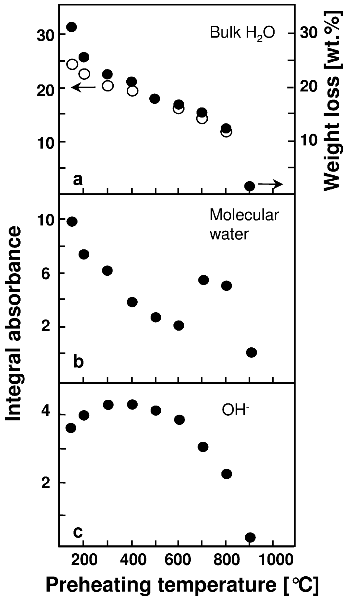

Fig. 1.4.4 Temperature-induced dehydroxylation of single phase (type I) mullite gels: (a) Analytical H_2O contents. Open circles: Data from moisture evolution analysis (MEA), filled circles: Data derived from thermobalance (TG). (b) Integral absorbance values of the infrared H_2O combination band centered at 5160 cm^{-1}. (c) Integral absorbance values of the infrared (Si,Al)-OH combination band at 4540 cm^{-1} (after Voll et al. 1998).

aluminosilicate gels prepared by slow hydrolysis of tetraethyloxysilane (TEOS) and aluminum *sec*-butylate. The NMR spectra contain a major resonance centered at about –88 ppm and two broad shoulders at about –55 and –110 ppm, respectively. The spectral region around –88 ppm is typical for tetrahedrally coordinated silicon in aluminosilicates such as mullite or mullite glass (Risbud et al. 1987, Schneider et al. 1992). The broad shoulder at –110 to –115 ppm is usually very weak in type I mullite gels and glasses, and indicates the presence of a silica-rich phase, while the –55 ppm signal is attributed to residual organo-silicon species and to their transient combustion products (Mackenzie et al. 1996). The temperature-dependent increase of the –110 ppm signal may reflect gradual demixing of the gel into silica-rich and alumina-rich domains (e.g. Huling and Messing, 1992, see below). The major resonance, on the other hand, shows a slight but significant up-field shift from about –84 ppm at 250 °C to –91 ppm at 650 °C. According to Mägi et al. (1984) and Engelhardt and Michel (1987) an up-field peak shift in the ^{29}Si-NMR spectrum of aluminosilicates is either due to a decreasing number of next-nearest aluminum atoms around silicon or due to an increasing number of bridged (Al,Si)-O-(Si,Al) oxygen atoms. Since the major resonance position of the gel approaches the position in corresponding aluminosilicate glasses (e.g. Schmücker et al. 1997) it can be assumed that the temperature-induced upfield shift reflects a gradual condensation process of the gel network accompanied by the evaporation of volatile compounds.

The low increase in the gel density during calcination (see below) indicates that the overall porosity is not dramatically reduced by the precursor network condensation, and a rigid oxide skeleton is formed in an early stage of the precursor evolution. Calculations of radial distribution functions (RDF) have provided fur-

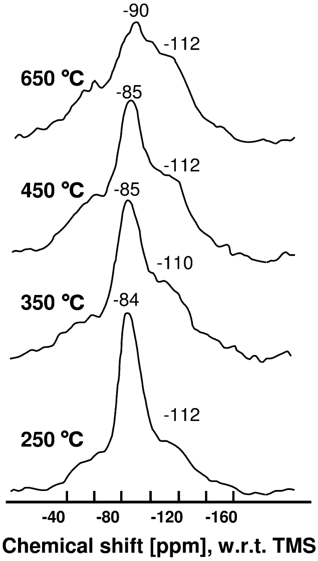

Fig. 1.4.5 ^{29}Si NMR spectra of single phase (type I) mullite gels heat-treated at different temperatures prior to crystallization (after MacKenzie et al. 1996).

ther evidence for a temperature-induced condensation of the network of aluminosilicate gels. As-prepared mullite type I precursors have RDF patterns with a prominent peak at 1.8 Å, and broad peaks of low intensity near 2.9, 3.2 and 4.2 Å (Fig. 1.4.6). On the basis of the ionic radii of Al^{3+}, Si^{4+} and O^{2-}, the peak near 1.8 Å was asssigned to T-O (T = Al^{3+}, Si^{4+}) atomic pairs, whereas those at 2.9, 3.2 and 4.2 Å are associated with O-O, T-T (i.e. T(1)-O(1)-T(2)), and T-O(2) (i.e. T(1)-O(1)-T(2)-O(2)) pairs, respectively. The maxima near 3.2 and 4.2 Å gradually become more intense with heat treatment. This again was interpreted as an increasing condensation of the precursor network (Okuno et al. 1997).

^{27}Al NMR spectroscopy has also been used as a tool to provide information on the mode and distribution of AlO polyhedra in aluminosilicate gels. Ultra homogeneous type I mullite precursors display ^{27}Al NMR spectra with three peaks centered near 0, 30 and 60 ppm (Fig. 1.4.7). In the as-dried gel the 0 ppm signal is stronger than the 60 ppm signal, while the 30 ppm peak is very weak. With heat

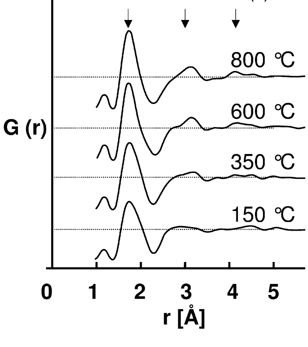

Fig. 1.4.6 Pair distribution functions of single phase (type I) gels heat-treated at different temperatures prior to crystallization (after Okuno et al. 1997).

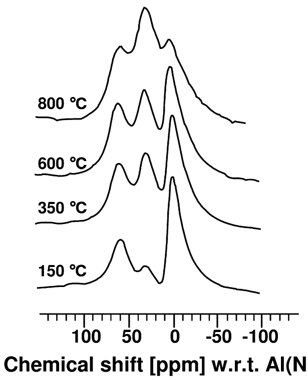

Fig. 1.4.7 ^{27}Al NMR spectra of single phase (type I) mullite gels heat-treated at different temperatures prior to crystallization (after Schmücker and Schneider, 1996).

treatment, a strong increase of the 30 ppm signal intensity is observed, approaching a spectrum very similar to that of aluminosilicate glasses. ^{27}Al NMR data on glasses of the system Al_2O_3–SiO_2 was first published by Risbud et al. (1987). They assigned the ^{27}Al NMR signals near 0 ppm and 60 ppm to octahedral ($Al^{[6]}$) and tetrahedral ($Al^{[4]}$) aluminum, respectively. The 30 ppm resonance was attributed to fivefold coordinated aluminum ($Al^{[5]}$) because of its intermediate position between those of $Al^{[6]}$ and $Al^{[4]}$, and because it exhibits a chemical shift similar to the isotropic shift of andalusite$^{4)}$. A large number of NMR spectroscopic studies carried out on aluminosilicate gels and glasses refer to the paper of Risbud et al. and mention the presence of $Al^{[4]}$, $Al^{[5]}$ and $Al^{[6]}$ in these materials. On the contrary, Schmücker and Schneider (1996, 2002) believe that the 30 ppm ^{27}Al NMR signal has to be attributed to tetrahedral triclusters. However, the final assignment of the 30-ppm resonance in the ^{27}Al NMR spectrum is still a point of discussion (see 1.4.4.2).

Gerardin et al. (1994) and Schneider et al. (1994b) pointed out that there is a correlation between the 30 ppm NMR signal and mullite formation. If aluminum sites corresponding to the 30 ppm signal are predominant, mullite formation is preferred to transition alumina crystallization or, in other words, the intensity of the 30 ppm peak in sol-gel-derived mullite precursors is assumed to correlate with their degree of structural homogeneity. Taylor and Holland (1993), on the other hand, reported that aluminum is tetrahedrally coordinated in very homogeneous gels, while diphasic gels are characterized by high amounts of octahedrally coordinated aluminum. Fivefold coordinated aluminum was believed to occur in interfacial regions between homogeneous and less homogeneous domains.

Metastable immiscibility in the system SiO_2–Al_2O_3 Demixing occurring in noncrystalline materials of the system Al_2O_3–SiO_2 has been well established for many

---

4) Andalusite contains chains of AlO_6 octahedra running parallel to the **c** axis. These octahedral chains are connected by double chains consisting of SiO_4 tetrahedra and AlO_5 polyhedra (Burnham and Buerger, 1961).

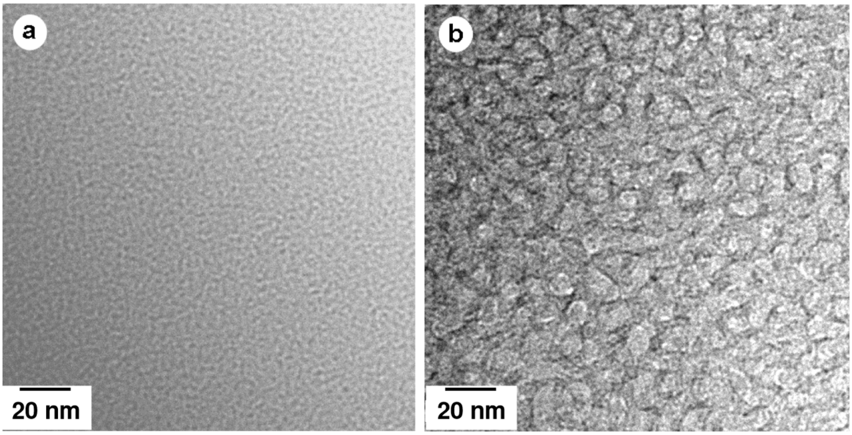

Fig. 1.4.8 Transmission electron micrographs of aluminosilicate glasses. (a) After rapid quenching; (b) After rapid quenchnig and calcination below crystallization temperature (890 °C). Note the occurrence of unmixing zones (Courtesy M. Schmücker).

years. MacDowell and Beall (1969) and Galakhov (1976) were among the first reporting the existence of a metastable immiscibility region deduced from microstructural investigations of rapidly quenched aluminum silicate glasses. They obtained a miscibility gap extending from about 15 to 70 mol% Al_2O_3, and estimated the upper consolute temperature as near 1650 °C. Their results, however, are not without problems, since phase separation was heavily disturbed by simultaneous mullite crystallization. Jantzen et al. (1981) studied ultrarapid quenching from melts and the kinetics of demixing. They obtained a consolute temperature as low as about 725 °C at a composition of about 46 mol% Al_2O_3. Fig. 1.4.8 shows the microstructure of a rapidly solidified aluminosilicate glass with mullite composition. The as-quenched glass appears featureless (Fig. 1.4.8a) while annealing at 890 °C produces significant segregation effects (Fig. 1.4.8b).

Ban et al. (1996) emphasize that mullite crystals formed in glasses and ultrahomogeneous gels at temperatures below 1000 °C are supersaturated in Al_2O_3, irrespective of the bulk chemical composition of the starting material. Ban et al. assume that the unusual crystallization behavior of mullite is caused by phase separation in the amorphous state, and that the composition of mullite formed at 950 °C corresponds to the Al_2O_3-rich demixing zones existing at this temperature. Rapid mullite crystallization at temperatures above 950 °C, however, disturbs the observation of metastable phase separation. It is therefore extremely difficult to determine the high temperature region of the immiscibility gap by experimental methods.

There have been several approaches for calculating the immiscibility region from thermodynamic data. Risbud and Pask (1977) calculated the immiscibility gap for the pseudo-binary system silica-mullite using a regular solution model. Ban et al. (1996) also assumed a regular solution model but considered the binary system Al_2O_3–SiO_2. Takei et al. (2000), on the other hand, used thermodynamic

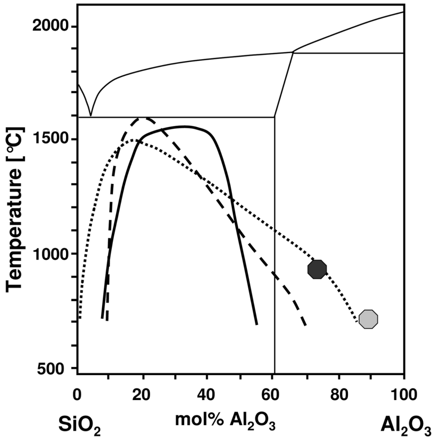

Fig. 1.4.9 Metastable immiscibility in the system Al_2O_3–SiO_2. Curves refer to results of Risbud and Pask (1977; full line), Ban et al. (1996; dotted line), and Takei et al. (2000; dashed line). Data points correspond to mullite compositions formed at 980 °C (dark) and 700 °C (light), respectively (after Fischer et al. 1994).

parameters derived from molecular dynamics simulations. The calculations confirmed the existence of metastable immiscibiltity in the Al_2O_3–SiO_2 system. Miscibility gaps display critical compositions near 20 mol% Al_2O_3 and consolute temperatures ranging between 1500 and 1700 °C. The shape of gaps is asymmetric and tail towards the Al_2O_3-rich composition side of the system. Hillert and Jonsson (1992) simulated the miscibility gap with the CALPHAD method. Their upper consolute point at about 1600 °C fitted well with the other models. However, its critical composition, near 50 mol% Al_2O_3, is obviously too Al_2O_3-rich.

The calculated immiscibility regions are plotted in Fig. 1.4.9 together with typical compositions of mullite formed at 980 °C and 700 °C (Fischer et al. 1994), respectively. The results calculated by Ban et al. (1996) fit well with the crystallization temperature and the composition data determined for mullite. However, the extension of the immiscibility gap towards SiO_2 may correspond to calculations of Risbud or Takei rather than to the curve of Ban, since no phase separation could be observed in silica glasses with 5 mol% Al_2O_3 prior to mullitization (Schmücker, unpublished results). Djuric and Mihajlov (1996) working on theoretical criteria and using data along the liquidus curves of mullite and α-alumina suggested immiscibility regions at both ends of the phase diagram. This observation has not been confirmed by other workers.

1.4.1.3 **Mechanisms of Mullite formation From Type I Precursors and Glasses**

Takei et al. (1999) studied mullite crystallization in commercial aluminosilicate glass fibers that were relatively SiO_2-rich (49 mol% Al_2O_3) and Al_2O_3-rich (69 mol% Al_2O_3), respectively. Mullite formation from the amorphous state is believed to take place in three steps.

- In the first stage, below 1000 °C, mullite nucleation is the dominant process, characterized by activation energies ranging between about 850 kJ mol^{-1} (SiO_2-rich) and 1000 kJ mol^{-1} (Al_2O_3-rich).The higher activation energy of the Al_2O_3-rich system is surprising, since the viscosity of aluminosilicate glass decreases with the Al_2O_3 content and the correlated mobility of atomic species increases as well. Takei et al. explained this discrepancy by a phase separation occurring in the liquid state of the Al_2O_3-rich glass fibers.

- In the second stage, between about 1000 and 1200 °C, mullite nucleation and growth are controlling mechanisms. Activation energies range between about 1200 kJ mol^{-1} (SiO_2-rich) and 1100 kJ mol^{-1} (Al_2O_3-rich). The activation energies of this stage have been explained by the slow diffusion of species.
- In the third stage, above about 1200 °C, the main effect is mullite grain growth via coalescence. Processes in this mullitization stage proceed more rapidly because of the higher temperatures, and as a result the activation energies become lower (SiO_2-rich: about 700 kJ mol^{-1}, Al_2O_3-rich: about 650 kJ mol^{-1}).

Wei and Rongti (1999) studied the crystallization kinetics of other aluminosilicate glass fibers with 67 mol% Al_2O_3 (79 wt.%). They observed first mullite crystallization at about 1250 °C, with maximum mullite precipitation at 1280 °C. and a rather low activation energy of crystallization (about 650 kJ mol^{-1}). Takei et al. (2001) and Okada et al. (2003) investigated the mullite formation process from type I single-phase gels of stoichiometric composition (60 mol% Al_2O_3) and from aluminosilicate glasses with Al_2O_3 contents varying between 15 and 50 mol%. The activation energies of mullite nucleation and growth have been calculated to be about 1200 kJ mol^{-1}, or from 900 to 1300 kJ mol^{-1}, respectively. Diffusion-controlled mechanisms of mullite formation are assumed for these gels and glasses. Tkalcec et al. (1998) starting from a gel of stoichiometric mullite composition (60 mol% Al_2O_3) obtained similar activation energies of mullitization (>1050 kJ mol^{-1}). They discuss a two-step mullite formation model, attributed to phase separation in the precursor, and suggest that mullitization is controlled by phase separation rather than by nucleation and growth of mullite. From literature data it can be concluded that the nucleation density of mullite is extremely high (see also Fig. 1.4.24, below) and that crystal growth occurs isotropically. The kinetic results of Takei et al., Okada et al. and Tkalcec et al. are in a clear contrast to the data published by Li and Thomson (1990) with activation energies between about 300 and 350 kJ mol^{-1} and without any induction branch of the transformation curves, while all other studies observe distinct nucleation periods. A possible explanation is that Li and Thomson measured only the activation energies of nucleation, whereas the other studies measured those of nucleation and growth (see Okada et al. 2003). Similar reasons may account for the low activation energy published by Wei and Pongti (1999).

A time-temperature correlation of the incubation time (τ) was used to estimate the activation energy of nucleation (about 980 kJ mol^{-1}) which is somewhat smaller than the activation energy determined for subsequent crystal growth (about 1100 kJ mol^{-1}). Johnson et al. (2001) stated that aluminosilicate glass samples are fully nucleated by the time they reach 850 °C, and hence crystallization occurs with a constant number of nuclei. James et al. (1997), on the other hand, reviewing the nucleation rates of various silicate glasses, found that the maximum nucleation temperature (T_M) is strongly correlated with the liquidus temperature (T_L), thus leading to T_M/T_L ratios scattered in a remarkably narrow range of 0.54 to

0.58. Using these data, the nucleation temperature of mullite glasses has been determined to range between 895 and 980 °C, suggesting that the formation of mullite at temperatures above 900 °C is not only due to the growth of pre-existing nuclei but involves both nucleation and growth. Inconsistencies in Johnson's findings are caused by the moderate quenching rates, which may have caused mullite nucleation during cooling also.

1.4.2
Type II (Diphasic) Mullite Precursors

Although in type I (single phase) mullite precursors mullitization takes place below 1000 °C this material is not without problems: As diffusion in mullite is very sluggish, sintering-induced densification of ceramics becomes difficult. Diphasic mullite precursors of type II can provide the solution to this problem.

These mullite precursors consist of transitional alumina and non-crystalline silica (type II, Schneider et al. 1993c) and thus allow densification prior to mullitization by viscous flow sintering. The particle size of constituents of diphasic mullite precursors range from a few to several hundreds of nanometers. The precursors are usually prepared by sol-gel or precipitation techniques, but well homogenized and heavily ground powders of alumina and silica phases may also come into this category.

1.4.2.1 Synthesis of Type II Mullite Precursors

Most preliminary work on diphasic mullite precursors via sol-gel techniques originates from the pioneering study of Hoffman et al. (1984). They synthesized diphasic mullite precursors with aqueous silica and boehmite sols as starting materials. Gelation was carried out by gradual solvent evaporation. In alternative approaches admixtures of boehmite sol plus alcoholic tetraethyloxysilane (TEOS) solutions or silica sol plus aqueous aluminum nitrate solutions, have been employed. Okada and Otsuka (1986) used demixed alcoholic solutions of tetraethyloxysilane (TEOS) plus aluminum chloride and gelled them after slow hydrolysis. More recently, Voll (1995) prepared diphasic mullite precursors starting with alcoholic solutions of tetraethyloxysilane (TEOS) and aluminum *sec*-butylate. Tetraethyloxysilane (TEOS) solutions are prehydrolyzed by addition of water under strongly basic conditions (pH = 13) to induce silica self-condensation. After a short aging time the silica sol, containing a considerable amount of excess water, is put into the aluminum-bearing solution, leading to rapid hydrolysis of aluminum *sec*-butylate and subsequent formation of pseudo-boehmite colloids. Transmission electron microscopy of the dried gel reveals the existence of relatively large spherical silicaparticles and nanometer-sized pseudo-boehmite aggregates intimately embedded in a non-crystalline silica matrix (Fig. 1.4.10).

A novel preparation method for type II mullite precursors has been developed by Sacks et al. (1991) by means of transient viscous sintering (TVS) techniques (see Section 4.2.6). According to their concept the powder particles of the mullite pre-

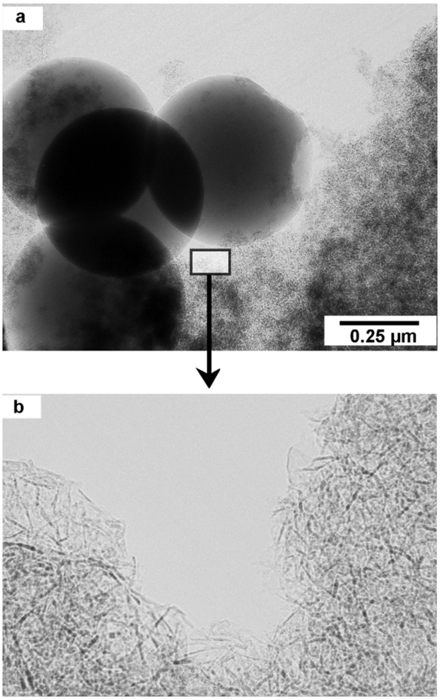

Fig. 1.4.10 Transmission electron micrographs of a diphasic mullite precursor consisting of relatively large spherical silica particles and nanometer-sized pseudo-boehmite aggregates, intimately embedded in a non-crystalline silica matrix. (a) Overview, (b) Detail showing pseudo-boehmite aggregates.

cursor are “microcomposites” consisting of α-alumina cores enveloped by amorphous silica layers. These microcomposites are prepared by dispersing the submicron alumina particles in an alcoholic solution of tetraethyloxysilane. In the next step silica is precipitated at the surface of the alumina particles by the addition of ammoniated water. Compacts of the composite particles are sintered to almost full density at about 1300 °C by viscous flow of the amorphous silica layer. On the other hand, the relatively long diffusion paths necessary for full mullitization (about 200 nm) still require temperatures of about 1600 °C. Based on the idea of microcomposite powders, Bartsch et al. (1999) improved the transient viscous sintering process by preparing “nanocomposite” mullite precursors consisting of γ-alumina particles coated by nanometer-thick silica layers (Fig. 1.4.11). These nanocomposites exhibit a similar densification behavior by transient viscous flow as the α-alumina/silica microcomposites but mullite forms at temperatures as low as 1300 °C. This enhancement of sintering has been explained by diffusional distances required for mullitization which are about one order of magnitude smaller in the latter case.

1.4.2.2 **Temperature-induced Structural Evolution of Type II Mullite Precursors**

The transformation of diphasic type II mullite precursors involves two steps:

- The development of spinel-type transition alumina (“γ-alumina”) phases below about 1200 °C
- Mullite formation by reaction of γ-alumina and silica above about 1200 °C.

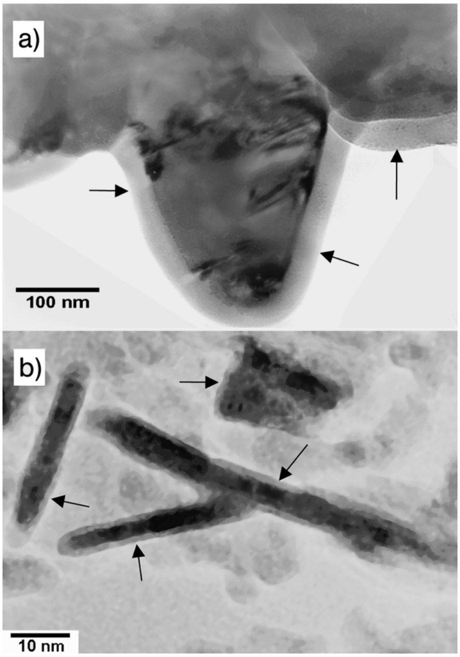

Fig. 1.4.11 Transmission electron micrograph of a diphasic mullite precursor prepared by coating (a) α-alumina powder and (b) γ-alumina powder with amorphous silica according to the transient viscous sintering technique (see also Section 4.2.6. Courtesy M. Bartsch).

The spinel-type transition alumina phase Diphasic mullite precursors prepared by sol-gel methods typically consist of pseudo-boehmite (γ-AlOOH) plus amorphous silica (e.g. Hoffman et al. 1984). By dehydration above about 500 °C pseudo-boehmite converts to γ-alumina, the latter transforming into the structurally related δ- and θ-alumina at elevated temperatures (Wefers and Misra, 1987). The composition of the γ-alumina phases has been a point of controversy for many years. The spinel-type transition phase occurring during the kaolinite-mullite transformation was found to incorporate considerable amounts of silicon. This derives from the analyses of leached samples that reveal aluminum-silicon spinels with compositions approaching that of mullite (e.g. Chakraborty and Ghosh 1978, Srikrishna et al. 1990). Brown et al. (1985), on the other hand, using ^{29}Si NMR spectroscopy established virtually silicon-free γ-alumina as the transient phase in the kaolinite-mullite reaction sequence. Contradictory results have also been reported for the spinel-type transition phase in gel-derived mullite precursors. Low and McPherson (1989), from infrared spectroscopic investigations, assumed a composition corresponding to that of 2/1-mullite (i.e. 33 mol% SiO_2), while Wei and Halloran (1988a) and Komarneni and Roy (1986) on the basis of analytical transmission electron microscopy (TEM) and ^{29}Si NMR spectroscopy concluded that the spinel phase is essentially pure aluminum oxide. Okada and Otsuka (1986) compared the IR spectrum of pure γ-alumina with that of the gel-derived spinel phase and reported a high silicon incorporation, with an Al_2O_3/SiO_2 ratio in the spinel phase of about 6 to 1.

Schneider et al. (1994c) re-examined the composition of the transition spinel

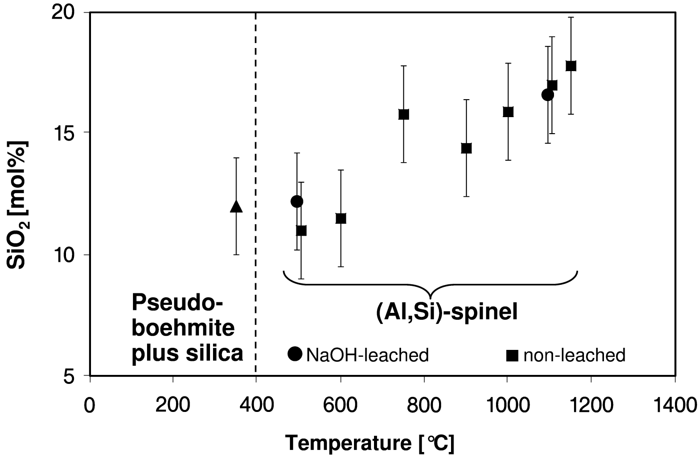

Fig. 1.4.12 SiO_2 content of pseudo-boehmite plus silica phase assemblages and of spinel-type transition alumina ("γ-alumina") determined by the energy dispersive X-ray (EDX) technique. As leaching of the spinel phase has no influence on the composition, it is concluded that silicon has been incorporated in the spinel phase (after Schneider et al. 1994c).

phase that develops in mullite precursors derived from tetraethyloxysilane (TEOS) plus aluminium *sec*-butylate (see above) by combining spectroscopic methods with analytical transmission electron microscopic results on non-leached and leached samples that had been calcined between 350 and 1150 °C. The dried precursor powder consists of relatively large spherical silica particles and much finer grained agglomerates of pseudo-boehmite embedded in a silica matrix (Fig. 1.4.10). Above about 350 °C the pseudo-boehmite and silica admixture converts completely to aluminum-silicon spinel with about 12 mol% SiO_2. Up to 750 °C the composition of the spinel phase remains constant, and above this temperature the SiO_2 content gradually increases up to about 18 mol% at 1150 °C (Fig. 1.4.12), obviously triggered by partial dissolution of the larger SiO_2 spherules.

Mechanisms of mullite formation from type II precursors The kinetics and mechanisms of mullite crystallization from diphasic type II precursors in the system Al_2O_3–SiO_2 have been studied by several research groups. Wei and Halloran (1988b) were the first to describe the kinetics of mullite formation from pseudo-boehmite and tetraethyloxysilane (TEOS) with an activation energy of the overall process of about 1070 kJ mol^{-1}. These authors believe that mullite forms by a direct solid-state reaction between transition alumina and the silica-rich non-crystalline phase by an interface- or, alternatively, a diffusion-controlled process. Mullite formation is preceded by an incubation period, corresponding to nucleation. Mullite nucleation has an activation energy of about 990 kJ mol^{-1}, which is very close to that of the overall process (see above). Scanning electron microscopic analyses reveal a nucleation density of the type II precursors of about 2×10^{11} cm^{-3} which is signicantly smaller than that of type I single-phase mullite precursors (about 10^{17} cm^{-3}, see Fig. 1.4.24 below). The growth of mullite grains follows a $t^{-0.63}$ law. Li and Thomson (1991) used the same starting materials and achieved similar activation energies of mullitization (about 1040 to 1080 kJ mol^{-1}).

Huling and Messing (1991) started from aluminum nitrate nonahydrate and tetraethyloxysilane (TEOS) for their precursor synthesis. They give an activation energy of mullite formation of about 1030 kJ mol^{-1}. Ivankovic et al. (2003) investigating the influence of the particle size of the aluminum sources (boehmite, γ-alumina, aluminum nitrate nonahydrate) on the reaction kinetics, suggested that the mullitization is a two-step process: In a first step Al_2O_3-rich 2/1-mullite (66 mol% Al_2O_3) forms, which, in a second step, is transformed to stoichiometric mullite (60 mol% Al_2O_3) with the activation energy of the overall reaction ranging between about 900 and 1150 kJ mol^{-1} (see also Tkalcec et al. 2003). Finally Boccaccini et al. (1999), starting from boehmite and fumed silica nanopowders obtained activation energies of about 880 kJ mol^{-1}. The latter authors suggest that mullitization is characterized first by an induction period during which mullite nucleation takes place, followed by the main transformation regime, in which mullite nucleation and growth occur simultaneously.

The activation energies of mullitization in type I (single phase) and type II (diphasic) gels and glasses of mullite composition are similar in value. This may indicate that similar mechanisms of mullitization are active. In diphasic precursors dissolution of γ-alumina in the coexisting silica phase and reprecipitation of mullite are rate-controlling steps, being more probable than direct solid-state reactions between transitional alumina and silica as quoted by Wei and Halloran (1988b). Acceleration of mullite formation and associated reduction of the activation energy below 900 kJ mol^{-1} is possible if precursors of higher reactivity are used, as in the case of Boccaccini et al. (1999). Their diphasic mullite precursor was prepared by admixing nanometer-sized fumed silica (aerosol) with boehmite sol. Microcomposites consisting of sub-micron α-alumina particles enveloped by nanometer-thick silica glass coatings behave quite similarly to diphasic gels (see Sacks et al. 1996). These systems have typical activation energies of mullitization of 1040 kJ mol^{-1}. Sacks et al. suggest that mullite formation in this case proceeds via solution of aluminum in amorphous silica with subsequent nucleation and growth of mullite.

A suitable way to further drastically reduce the activation energies of diphasic type II mullite precursors is doping of the starting compounds with foreign atoms. In this way, the viscosity of the amorphous silica is reduced drastically. This causes higher diffusion rates, and as a consequence, induces accelerated nucleation and crystal growth of mullite. Hong et al. (1996) and Hong and Messing (1997, 1999) studied the mullite formation kinetics of sol-gel-derived diphasic gels, doped with phosphorus oxide (P_2O_5), boria (B_2O_3) and titania (TiO_2, see Table 1.4.1). Low activation energies for enhanced mullitization have also been observed by Hildmann et al. (1996) in commercial fibers consisting of γ-alumina plus silica-rich amorphous phase containing a small amount of boria (see Table 1.4.1). The fact that the nucleation barrier of mullite is clearly lowered by boria addition goes along

Table 1.4.1 Activation energy of mullite formation from precursors and glasses.

Composition [wt. %]	Starting compounds	Investigation technique	Effective activation energy [kJ mol^{-1}]	Reference
Single-phase (type I) precursors and glasses				
Al_2O_3: 72% SiO_2: 28%	Al nitrate nonahydrate + TEOS	DXRD	300	Li and Thomson (1990)
Al_2O_3: 49% SiO_2: 51%	Commercial glass fiber	XRD	≈ 1200	Takei et al. (1999)
Al_2O_3: 69% SiO_2: 31%	Commercial glass fiber	XRD	≈ 1100	Takei et al. (1999)
Al_2O_3: 79% SiO_2: 21%	Arc-furnace produced from α-Al_2O_3 + quartz	DTA	≈ 650	Wei and Rongti (1999)
Al_2O_3: 23–72% SiO_2: 77–28%	Al nitrate nonahydrate + TEOS	DTA	≈ 1200	Takei et al. (2001)
Al_2O_3: 72–87% SiO_2: 28–13%	Al nitrate nonahydrate + TEOS	DTA	≈ 900–1300	Okada et al. (2003)
Al_2O_3: 72% SiO_2: 28%	Al nitrate nonahydrate + TEOS	DSC	≈ 1050	Tkalcec et al. (1998)
Diphasic precursors (type II) and single phase/diphasic (type III) precursors				
Al_2O_3: 46–84% SiO_2: 54–16%	Boehmite + TEOS	DXRD	≈ 1040–1080	Li and Thomson (1991)
Al_2O_3: 63–77% SiO_2: 37–23%	Pseudoboehmite + TEOS	XRD	≈ 1070	Wei and Halloran (1988b)
Al_2O_3: 72% SiO_2: 28%	Al nitrate nonahydrate, γ-Al_2O_3, boehmite, TEOS	XRD	≈ 890–1060	Tkalcec et al. (2003)
Al_2O_3: 73% SiO_2: 27%	Al nitrate nonahydrate + TEOS	DTA	≈ 1030	Huling and Messing (1991)
Al_2O_3: 72% SiO_2: 28%	Boehmite sol + silica nanopowder	DTA	≈ 880	Boccaccini et al. (1999)
Al_2O_3: 72% SiO_2: 28%	Al nitrate nonahydrate, γ-Al_2O_3, boehmite, TEOS	XRD	≈ 950–1090	Ivankovic et al. (2003)
Hybrid precursors (types I and III)				
Al_2O_3: 70–73% SiO_2: 30–27%	Al nitrate nonahydrate, silica sol, boehmite, TEOS	DTA	≈ 930–1090	Huling and Messing (1991)

with the observation of a significantly increased nucleation density of boria-doped systems (about 10^{15} cm^{-3}) in comparison to that in undoped systems (about 2×10^{11} cm^{-3}). In the case of boria addition Hong and Messing argue that the boron aluminate $9Al_2O_3 \cdot 2B_2O_3$ is intermediately formed. Since this phase has a crystal structure belonging to the mullite family (Ihara et al. 1980, Garsche et al. 1991) it

Table 1.4.1 (continued).

Composition [wt. %]	Starting compounds	Investigation technique	Effective activation energy [kJ mol^{-1}]	Reference
Foreign cation oxide-doped diphasic precursors				
Al_2O_3: 70% SiO_2: 28% B_2O_3: 2%	Commercial fiber (Nextel 440, 3M)	XRD	≈ 900	Hildmann et al. (1996)
Al_2O_3: 3/2 plus Na_2O	Al nitrate plus Na metasilicate	XRD	≈ 730	Campos et al. (2002)
Al_2O_3: 27% SiO_2: 53% ZnO: 10% B_2O_3: 4% Li_2O: 0.7% ZrO_2: 2.5–3.0% TiO_2: 1.7–2.5%	$Al(OH)_3$, quartz sand, H_3BO_3, ZnO, TiO_2, ZrO_2, Li_2O	DTA	≈ 465	Tkalcec et al. (2001)
Al_2O_3: 73% SiO_2: 24% TiO_2: 3%	Boehmite, silica sol, TiO_2	DTA	≈ 1020	Hong and Messing (1997)

(D)XRD: (Dynamic) X-ray diffraction, DTA: Differential thermal analysis, DSC: Differential scanning calorimetry.

may provide sites for topotactical or epitactical nucleation of mullite. Unfortunately Hong and Messing gave no experimental evidence supporting this interesting approach. The crystallization of mullite from multicomponent silicate glasses of the system $Li_2O–ZnO–Al_2O_3–B_2O_3–ZrO_2–SiO_2$ with different ZrO_2/TiO_2-ratios has been described by Tkalcec et al. (2001). Mullitization at temperatures as low as 800 °C with activation energies below 500 kJ mol^{-1} indicates the high reactivity of the low-viscosity precursor caused by the presence of foreign cations (see Table 1.4.1). Campos et al. (2002) described a similar although less significant trend due to the occurrence of sodia (Na_2O, see Table 1.4.1).

Sundaresan and Aksay (1991) re-examined the kinetics of mullite formation from type II (diphasic) precursors published by Wei and Halloran. They emphasize that the reported time-dependent growth rate is not consistent with interface- or diffusion-controlled transformations but is in excellent accord with a dissolution and precipitation mechanism. In this scenario the alumina particles dissolve in the silica phase and mullite nuclei form when the vitreous aluminosilicate phase exceeds a critical concentration. The solution plus precipitation process can be illustrated in a free enthalpy versus composition diagram (Fig. 1.4.13). It turns out that the equilibrium composition of the amorphous phase is richer in Al_2O_3 when coexisting with alumina (SA) than when coexisting with mullite (SM). Mullite nucleation occurs if the critical nucleation concentration (CNC) is reached at a composition beyond SM. According to Sundaresan and Aksay, mullite nucleation within the non-crystalline silica implies that dissolution of alumina is the rate-

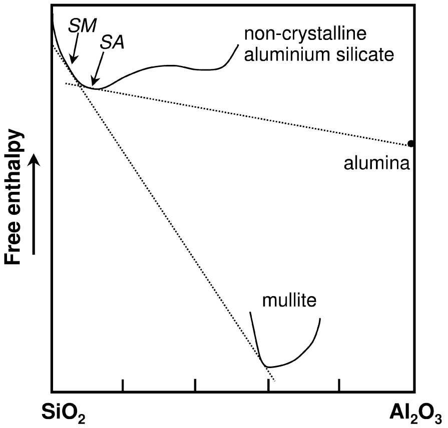

Fig. 1.4.13 Schematic free enthalpy diagram of the system Al_2O_3–SiO_2 (after Sundaresan and Aksay, 1991). SM and SA are the compositions of the non-crystalline aluminosilicate phase coexisting with mullite and alumina, respectively.

controlling step in mullite growth. Diffusion of aluminum ions through the vitreous phase as the rate-controlling step is ruled out: If that were the case a compositional gradient would be expected within the silica-rich phase, giving rise to mullite formation at the alumina/silica interface rather than in the bulk of the non-crystalline silica-rich phase.

Mullite as an interfacial product is observed in sapphire/silica reaction couples heated at temperatures above 1678 °C (Aksay and Pask, 1975). As a conclusion from experimental observations, Sundaresan and Aksay (1991) predict a change of the rate-limiting effects at some point between 1350 and 1650 °C, such that dissolution is rate-controlling below this temperature and diffusion is rate-controlling above. Microscopic evidence for the solution/precipitation mechanism and for a change of mullite formation mode from dissolution- to diffusion-controlled was given for the first time by Schmücker et al. (1994) investigating the mullitization of α-alumina/quartz powder admixtures. The starting powders used in this study were coarse (>100 nm) compared with the alumina and silica particles occurring in gel-derived mullite precursors, and hence mullitization temperatures are shifted to about 1500 °C. Since quartz grains form (metastable) viscous melt layers at their peripheries upon (rapid) heating at temperatures above about 1300 °C, the mullitization reaction takes place between α-alumina and amorphous silica rather than between α-alumina and quartz (Fig. 1.4.14a). Upon heating the powder admixtures to 1550 °C, mullite crystallites form randomly within the non-crystalline silica-rich phase (Fig. 1.4.14b).

The compositional evolution of the vitreous phase as determined by energy dispersive X-ray (EDX) analyses is shown in Fig. 1.4.15. About 4 mol% Al_2O_3 is incorporated into the viscous silica melt at about 1450 °C. Firing temperatures of 1500 °C produce a bimodal compositional distribution with maxima at about 4 and 2.5 mol% Al_2O_3. The obvious reduction of the Al_2O_3 content of the non-crystalline phase with temperature is attributed to mullite crystallization from this phase. The composition of the silica-rich melt coexisting with mullite (SM) is about 97.5 mol% SiO_2 and 2.5 mol% Al_2O_3, while the critical concentration of mullite nucleation

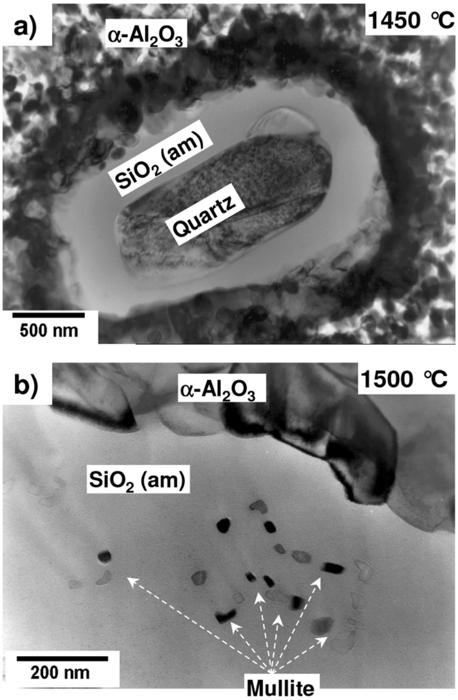

Fig. 1.4.14 Transmission electron micrographs of heat-treated α-alumina/quartz powder compacts. (a) 1450 °C – Formation of a metastable viscous melt layer at the periphery of quartz grains; (b) 1500 °C – Formation of randomly oriented mullite crystallites within the liquid siliceous phase (arrows, Courtesy M. Schmücker).

(CNC) is about 4 mol% Al_2O_3 at 1550 °C (Fig. 1.4.16). The microstructure of quartz/alumina powder admixtures heat-treated at 1600 °C indicates a change in the mullite formation mechanism: Although silica has converted completely to cristobalite, the extension of previous outer melt zones can be recognized by ori-

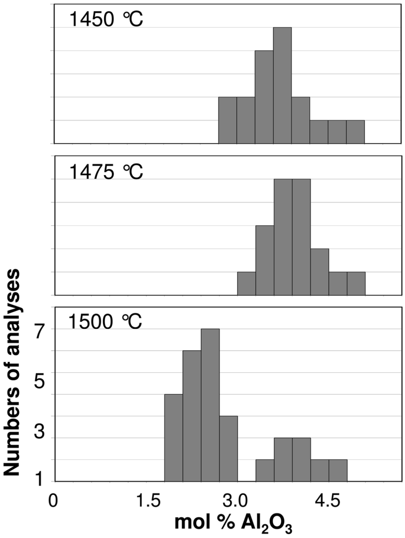

Fig. 1.4.15 Composition of aluminosilicate melts formed at the periphery of quartz grains during reaction sintering of mullite. The primarily existing silica melt incorporates up to 4 mol% Al_2O_3 prior to mullite nucleation. After mullite nucleation (1500 °C) the Al_2O_3 content of the liquid phase is about 2.5 mol% (after Schmücker et al. 1994).

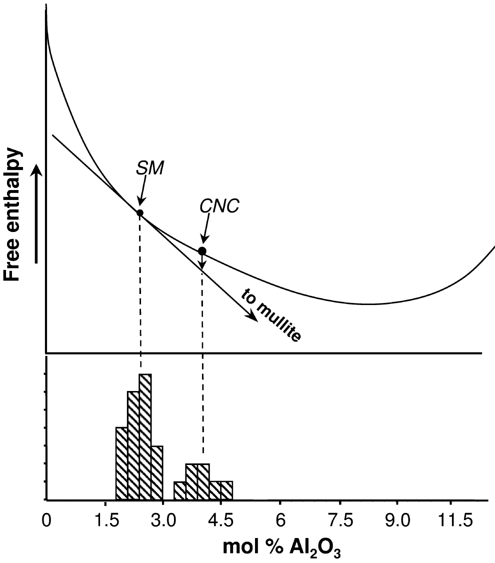

Fig. 1.4.16 Plot of the free energy versus Al_2O_3 content of aluminosilicate melts formed at the periphery of quartz grains during reaction sintering of mullite. The bimodal compositional distribution of the aluminosilicate phase occurring during reaction sintering of quartz plus α-alumina (see Figs. 1.4.14 and 1.4.15) suggests that the silicate melt coexisting with mullite (i. e. SM, see Fig. 1.4.13) contains about 2.5 mol% Al_2O_3, while the critical nucleation concentration (CNC) is about 4 mol% Al_2O_3.

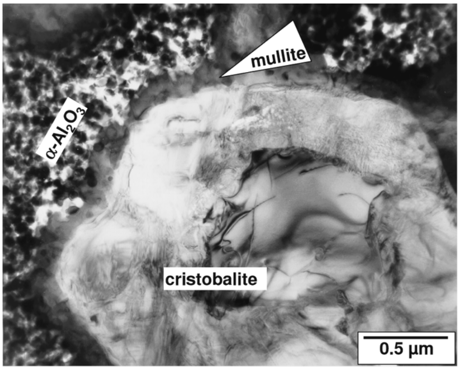

Fig. 1.4.17 Transmission electron micrograph of an α-alumina/quartz powder compact sintered at 1600 °C The picture indicates a different reaction mechanism with respect to firing conditions at 1500 °C (Fig. 1.4.14) No mullite crystals occur in the peripheral amorphous silica zone enveloping the cristobalite grains, but a mullite layer forms at the α-alumina/silica contact instead (Courtesy M. Schmücker).

entational contrasts of the cristobalite. It is noteworthy that no mullite crystals are incorporated in the outer cristobalite zone, but a mullite layer forms at the α-alumina/silica contact (Fig. 1.4.17), which is consistent with the model of Sundaresan and Aksay suggesting diffusion-controlled mullite growth at high temperatures.

1.4.3
Type III (Single Phase/Diphasic) Mullite Precursors

Type I single phase mullite precursors are non-crystalline and convert to Al_2O_3-rich mullite at about 950 °C (see Section 1.4.1), while diphasic type II precursors typically consist of poorly crystalline aluminum hydroxides and oxides and non-crystalline silica, which react to mullite above 1200 °C (see Section 1.4.2). A further

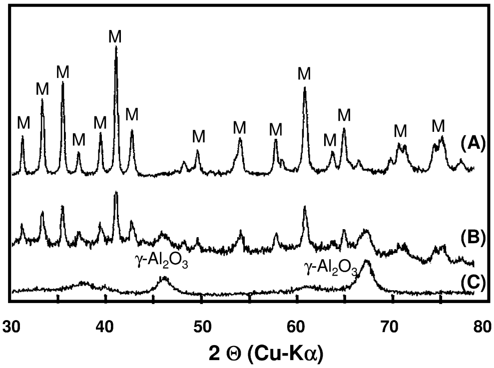

Fig. 1.4.18 X-ray diffraction traces of mullite precursors prepared from tetraethyloxysilane (TEOS) and aluminum nitrate nonahydrate solutions gelled at (A) 60 °C; (B) 40 °C and (C) 20 °C, respectively, and after firing at 1000 °C. At low gelation temperatures the precursor converts into transition alumina ("γ-alumina") plus amorphous silica rather than into mullite.

non-crystalline mullite precursor type has been described in the literature and was designated as rapid hydrolysis gel (Okada and Otsuka, 1986) or type III gel (Schneider et al. 1993c). The crystallization temperature of type III aluminosilicate gels corresponds to type I mullite precursors. However, transitional alumina ("γ-alumina") forms at a first stage, while mullite crystallizes by reaction of the aluminum and silicon compounds only at about 1200 °C. The latter reaction is similar to that of diphasic type II precursors (see Section 1.4.2). There exist gradual transitions between type I and type III precursors, resulting in mullite, mullite plus γ-alumina, or γ-alumina crystallization (Voll, 1995, Taake, 1999; see also Fig. 1.4.18).

1.4.3.1 Synthesis of Type III Mullite Precursors

Type III mullite gels can be prepared by various routes. Okada and Otsuka (1986) and Hyatt and Bansal (1990) used tetraethyloxysilane (TEOS) and aluminum nitrate nonahydrate solutions as starting compounds. Slow hydrolysis at 60 °C was reported to produce type I single phase mullite precursors (see above), but type III gels can be achieved by slow hydrolysis if the sol is aged at room temperature instead of 60 °C (Okada et al. 1996, Taake, 1999). The mullite gels gradually change from type III to type I on increasing the aging temperature from room temperature to 60 °C (Fig. 1.4.18). Voll (1995) prepared type III mullite precursors starting with alcoholic solutions of tetraethyloxysilane (TEOS) and aluminum *sec*-butylate by a similar method to that described for the preparation of diphasic gels. The tetraethyloxysilane (TEOS) solution is pre-hydrolyzed but mild basic conditions (pH 7-10) are used in order to prevent silica self-condensation.

1.4.3.2 Temperature-induced Structural Evolution of Type III Mullite Precursors

The structural development of tetraethyloxysilane (TEOS) plus aluminum nitrate nonahydrate-derived type III gels synthesized by aging at room temperature and calcined between 900 and 1200 °C has been investigated by Schmücker and Hoffbauer (unpublished results) with ^{29}Si NMR spectroscopy (Fig. 1.4.19). The 900 °C precursors show a single resonance centered at about 90 ppm which is typical for

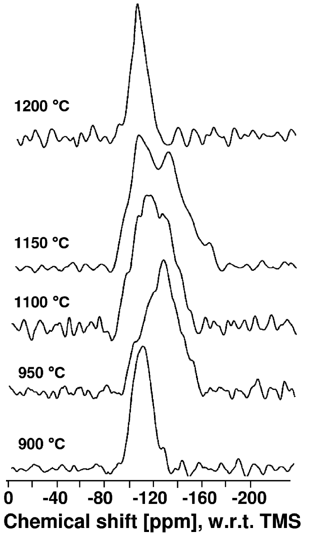

Fig. 1.4.19 ^{29}Si NMR spectra of type III mullite gels heat-treated between 900 and 1200 °C. Gels calcined at 900 °C (amorphous) and 1200 °C (after mullite formation) show a single resonance centered at about 90 ppm, typical of tetrahedrally coordinated silicon in aluminosilicates. Between 950 and 1100 °C a signal centered at about –110 ppm is observed with a shoulder in the –90 ppm region. The corresponding silicon sites are attributed to vitreous silica (–110 ppm) and to a minor extent to an incorporation of silicon into the spinel-type transient phase (–90 ppm).

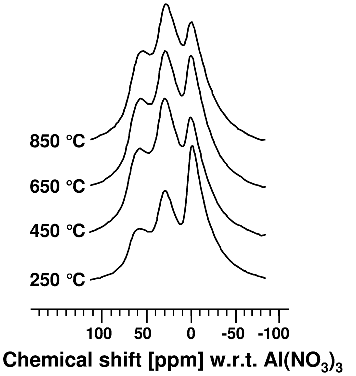

Fig. 1.4.20 ^{27}Al NMR spectra of type III mullite gels heat-treated at different temperatures prior to crystallization (250 to 850 °C). The structural development corresponds closely to type I gels (Fig. 1.4.7). NMR peaks near 0 and 60 ppm have been attributed to aluminum with sixfold (Al$^{[6]}$), and fourfold (Al$^{[4]}$) coordination, while that near 30 ppm was assigned either to fivefold aluminum (Al$^{[5]}$) coordination, or to tetrahedral triclusters.

tetrahedrally coordinated silicon in mullite and in type I single phase aluminosilicate gels and glasses (see Section 4.1.1). Obviously the silicon environments of type I and type III gels are very similar, and significant phase separation in the amorphous state prior to crystallization can be ruled out. Between 950 and 1100 °C a ^{29}Si NMR signal centered at –110 ppm appears with a shoulder in the –90 ppm region. The corresponding silicon sites are attributed to a spinel-type transition phase with minor silicon incorporation (–90 ppm), and to coexisting vitreous silica (–110 ppm). Above 1100 °C the spinel phase and silica gradually react to mullite, indicated by a gradual increase of the –90 ppm resonance. Aluminum nuclear magnetic resonance (^{27}Al NMR) spectroscopy indicates a slightly higher amount of sixfold coordinated aluminum (Al$^{[6]}$) in type III than in type I gels. It was argued that Al$^{[6]}$ may facilitate formation of γ-alumina phases (Schneider et al. 1993c). Aluminum nuclear magnetic resonance spectra of type III mullite gels in the noncrystalline stage (150–900 °C) are shown in Fig. 1.4.20. The spectral development is virtually the same as that observed in single-phase type I mullite gels (see Fig. 1.4.7), supporting the suggestion of a high structural similarity between noncrystalline type I and type III mullite gels.

1.4.3.3 Mechanisms of Mullite Formation From Type III Mullite Precursors

Mullite formation as a reaction between γ-alumina and non-crystalline silica proceeds in type III precursors in a similar way as in type II materials above about 1200 °C (see Section 1.4.2.2).

1.4.4

General Remarks on the Structure and Crystallization Behavior of Mullite Precursors and Glasses

1.4.4.1 Mullite Precursors: Similarities and Differences

In order to understand the differences between type I single phase and type III mullite precursors and to check possible demixing effects in non-crystalline aluminosilicate gels and glasses, Schmücker et al. (2001) studied non-crystalline aluminosilicate materials with a well-defined degree of chemical inhomogeneity ranging from nanometer to almost atomic scale. For that purpose aluminosilicate films consisting of thin (about 30 nm) to ultrathin (about 2 nm) alumina and silica sublayers were physical vapor deposited by two-source evaporation using a jumping electron beam physical vapor deposition technique (EB-PVD). Four series of non-crystalline physical vapor deposited (PVD) films with bulk compositions ranging between 50 and 63 mol% Al_2O_3 are produced by varying the electron beam jumping frequencies (Tab. 1.4.2). Transmission electron microscopic cross sections of the vapor-deposited films show periodic contrasts perpendicular to the deposition direction. The contrast periodicities correspond reasonably with the calculated thicknesses of the respective alumina/silica double layers. Line scans confirm that the physical vapor deposited films actually consist of Al_2O_3- and SiO_2-rich sublayers (Fig. 1.4.21). Silicon nuclear magnetic resonance spectra (^{29}Si NMR) ob-

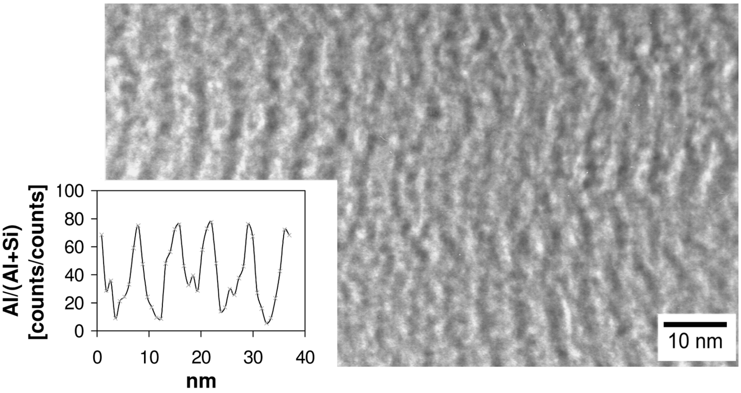

Fig. 1.4.21 Cross section transmission electron micrograph of physical vapor deposited aluminosilicate double layers (series 2, see text) in high magnification with the energy dispersive X-ray (EDX) line scan perpendicular to the observed contrast modulations. The EDX profile yields evidence for periodical chemical variations (Courtesy M. Schmücker).

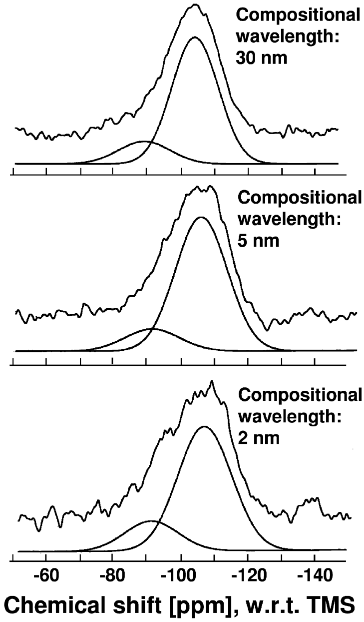

Fig. 1.4.22 ^{29}Si NMR spectra of physical vapor deposited aluminosilicate double layers with nominal thicknesses of 30, 5 and 2 nm, respectively. The three spectra are very similar, showing a main resonance at –110 ppm and a shoulder centered at –90 ppm, indicating the occurrence of "free" silica and atomically "mixed" alumina and silica (after Schmücker et al. 2001).

tained from series with about 30, 5, and 2 nm silica/alumina double-layer thicknesses are shown in Fig. 1.4.22: All spectra are very similar and exhibit a resonance in the –110 ppm region. The peak profiles, however, are slightly asymmetric indicating a resonance of minor intensity in the –90 ppm region.

Deconvolution of the asymmetric resonances into two signals centering at about –110 and –90 ppm, respectively, results in a peak area ratio of about 9/1. This means that virtually pure silica layers (–110 ppm resonance) occur in all PVD aluminosilicate films. The minor fraction of silicon sites surrounded by aluminum (–90 ppm resonance) is interpreted in terms of interfacial silicon, taking into account that the multilayer thickness is in the nanometer range. The occurrence of virtually aluminum-free silica sub-layers in all samples indicates the absence of any significant atomic mixing during deposition. The 30 nm thick alumina/silica double layers calcined at 1000 °C consist of transitional alumina. Transitional alumina plus small amounts of mullite appear in couples of 9 and 5 nm thickness. Only mullite forms in the 2 nm thick alumina/silica system. Above 1200 °C, couples with thicknesses of 30, 9, and 5 nm yield mullite by reaction of transitional alumina with silica. While the crystallization behavior of the 2 nm thick couple corresponds to that of type I single phase mullite precursors, the 30, 9, and 5 nm double layer systems behave like diphasic type II mullite precursors. This is a remarkable result, since all starting alumina/silica double layers are diphasic though on a nanometer scale. The different crystallization behavior has been explained by interdiffusion-induced chemical homogenization between adjacent alumina and silica layers prior to crystallization. Obviously at 1000 °C the complete homogenization necessary for mullitization occurs in reaction couples being about

2 nm thick. Relationships are completely different if the double layers become thicker. In that case zones of atomic mixing are separated by much broader areas of alumina and silica. It is assumed that the extension of the homogenized zones (about 1 to 2 nm) is below the critical size of a mullite nucleus, starting from the suggestion that stable growing mullite nuclei should be at least several unit cell dimensions in size.

To learn more about the crystallization of mullite precursors, the microstructures of type I and type III gels prepared either from tetraethyloxysilane (TEOS) plus aluminum *sec*-butylate (Voll, 1995) or aluminum nitrate nonahydrate solutions (Taake, 1999), respectively, were re-examined by transmission electron microscopy (Schmücker, unpublished results). Fig. 1.4.23 reveals the significant morphological differences between type I and type III mullite gels: Irrespective of the

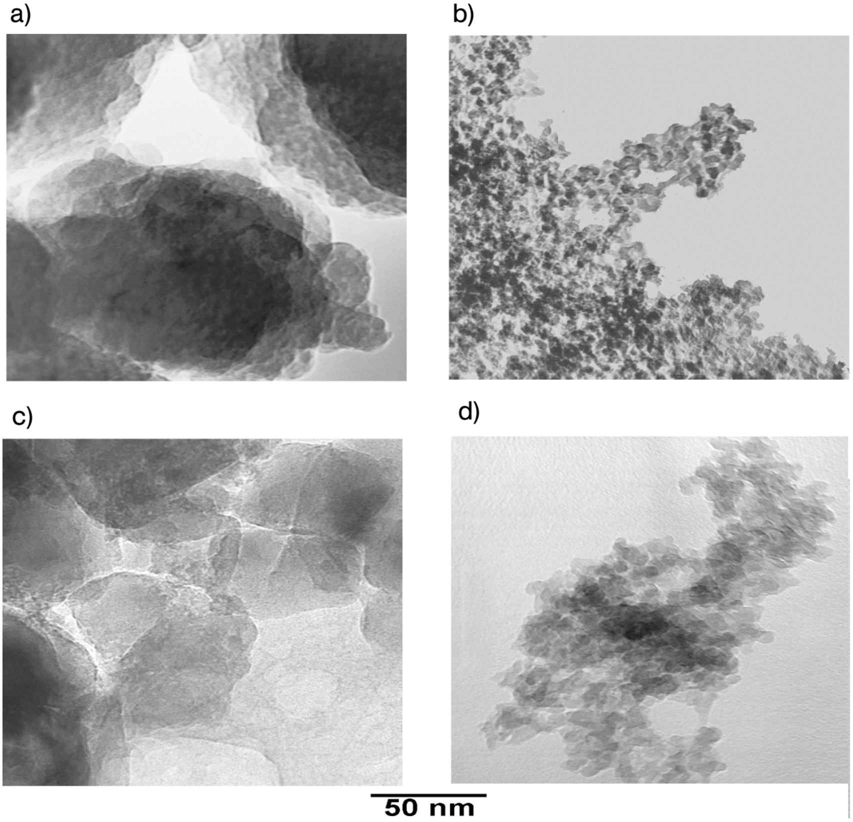

Fig. 1.4.23 Transmission electron micrographs of (a), (c) Single phase type I gels, and (b), (d) Diphasic type III gels. Starting materials are tetraethyloxysilane (TEOS) plus aluminum *sec*-butylate solutions (a,b) and tetraethyloxysilane) plus aluminum nitrate nonahydrate solutions (c,d). In contrast to type I gels, type III gels consist of primary particles smaller than 10 nm (Courtesy M. Schmücker).

Table 1.4.2 Experimental conditions of electron beam physical vapor deposition (EB-PVD) runs.

	Series 1	Series 2	Series 3	Series 4
Film thickness [μm]	70	75	30	29
Average deposition rate [nm s^{-1}]	190	125	75	50
Jumping beam frequency [Hz]	7	14	14	25
Nominal thickness of Al_2O_3–SiO_2 double layer [nm]	27	9	5.5	2

From Schmücker et al. (2001).

starting compounds, primary particles of 5 to 10 nm can be resolved in type III gels (Fig. 1.4.23b,d). In contrast, only faint contours of nanometer-sized primary particles become visible in tetraethyloxysilane (TEOS) plus aluminum *sec*-butylate-derived type I gels (Fig. 1.4.23a) indicating intense particle aggregation. Tetraethyloxysilane (TEOS) plus aluminum nitrate nonahydrate-derived type I gels (Fig. 1.4.23c), on the other hand, consist of agglomerated particles of about 30 to 100 nm (see also Fig. 1.4.3). Small-angle X-ray scattering reveals particles sizes of 7 nm and 39 nm for type III and type I mullite gels, respectively (Okada, unpublished results), in good accordance with microscopic data.

Microstructural analyses of type I and type III mullite gels suggest that their crystallization behavior is influenced by their particle sizes. Obviously, gels with intense aggregation of primary particles or with primary particles several tens of nanometers in size tend to transform directly into mullite, while particulate gels with primary particles below 10 nm form transitional alumina as the first crystalline phase. This finding is explained in terms of critical crystal nucleus sizes, which are assumed to be larger than 10 nm for mullite but smaller than 10 nm for γ-alumina. Actually, there is experimental evidence, from mullite crystal size data reported for early mullitization stages, that stable mullite crystallites exceed 10 nm. Interestingly, crystallite sizes determined by various methods all range from about 10 to 40 nm (Table 1.4.3). Transitional alumina crystals, on the other hand, are well known to be as small as 3 nm (e. g. Wefers and Misra, 1987). Thus homogeneous aluminosilicate gels with particles greater than a stable mullite nucleus (about 10 nm) can directly convert to mullite, while gels consisting of smaller particles should form transitional alumina.

1.4.4.2 The Coordination of Aluminum in Mullite Precursors and Glasses

The structure of gels and glasses in the system Al_2O_3–SiO_2, and the coordination of aluminum has been a point of interest for many years. In the 1960s, Lacy (1963) assumed on the basis of charge balance considerations that tetrahedral triclusters,

Table 1.4.3 Mullite crystallite sizes in early stages of crystallization.

Mullite crystal size [nm]	Method	Reference
20	XRD	Takamori and Roy (1973)
26–42	XRD	Tkalcec et al. (1998)
≈ 15	SEM	Takei et al. (1999)
25–40	XRD	Thom (2000)
10–20	TEM	Bartsch et al. (1999)
12.6	TEM	Johnson et al. (2001)
≈ 20	TEM	This chapter, Figure 1.4.14
20–50	TEM	This chapter, Figure 1.4.24

XRD = X-ray diffractometry
SEM = Scanning electron microscopy
TEM = Transmission electron microscopy

i. e. three tetrahedra linked together by one common oxygen atom, are formed, if silicon is partially replaced by aluminum in melts and glasses. Years later, however, with the introduction of magic angle spinning (MAS) nuclear magnetic resonance (NMR) spectroscopy another structural model became popular. In the pioneering work of Risbud et al. (1987) three ^{27}Al NMR signals are observed, which center at 0, 60 and 30 ppm. These resonances have been attributed to AlO polyhedra in octahedral ($Al^{[6]}$), tetrahedral ($Al^{[4]}$) and fivefold ($Al^{[5]}$)coordination, respectively (see above). In another approach Meinhold et al. (1993) attributed the 30 ppm peak to tetrahedrally bound aluminum ($Al^{[4]}$) with elongated Al-O bonds rather than to $Al^{[5]}$. This suggestion was obtained on the basis of ^{27}Al NMR line shape analyses together with radial distribution functions (RDFs) and extended X-ray absorption fine structure (EXAFS) data. The assignment of the aluminum 30 ppm NMR signal is still a point of controversy: Bodart et al. (1999) supported the idea of the presence of $Al^{[5]}$ on the basis of recent multiple quantum ^{27}Al NMR studies, while Peeters and Kentgeris (1997), for example, provided evidence for the model of distorted tetrahedra. According to McManus et al. (2001), the experimental data do not allow the questionable resonance to be assigned unambiguously.

Schmücker and Schneider (1996) reactivated the tricluster model of Lacy. Starting from the observation that mullite forms within the bulk of aluminosilicate gels or glasses in extremely high nucleation densities (Fig. 1.4.24), structural short-range-order similarities are believed to occur in mullite and the non-crystalline counterparts. Since no $Al^{[5]}$ occurs in mullite but tetrahedral triclusters instead, it was argued that (Si,Al)O_4-triclusters rather than AlO_5 polyhedra exist in aluminosilicate gels and glasses. There is also evidence for short-range-order similarities between non-crystalline aluminosilicates and mullite from similar ^{27}Al NMR spectra (Fig. 1.4.25). It has been suggested that the two different tetrahedrally bound aluminum ($Al^{[4]}$) sites in mullite cause a splitting of the ^{27}Al NMR signal into two peaks at about 60 ppm and 43 ppm, the latter being attributed to tricluster-forming aluminum (Al*) sites (Merwin et al. 1991). The intense upfield shift of the Al*

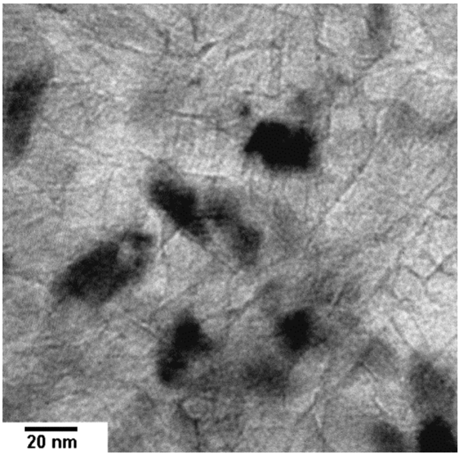

Fig. 1.4.24 Mullite crystals formed after calcination of aluminosilicate glass. Note the numerous crystallites with sizes of 20 to 30 nm (dark areas) which account for a high nucleation density (Courtesy M. Schmücker).

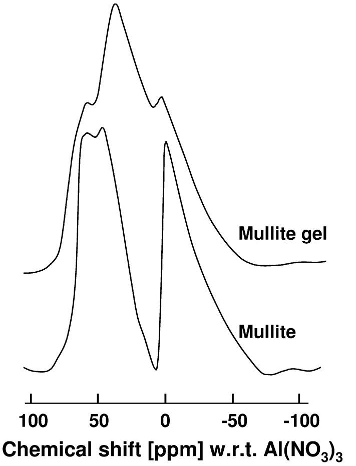

Fig. 1.4.25 ^{27}Al NMR spectra of a single phase (type I) mullite gel. The spectrum of mullite is given for comparison (after Schmücker and Schneider, 1996).

resonance in mullite is close to the 30 to 35 ppm signal occurring in non-crystalline aluminosilicates, and therefore the latter is attributed to triclustered AlO_4 tetrahedra by Schmücker and Schneider (1996).

Table 1.4.4 presents the mean coordination numbers of different aluminosilicate glasses on the basis of ^{27}Al NMR spectroscopy and on pair distribution function studies. From the results of NMR spectroscopy, two structural models have been developed: Model 1 with 20 % of the total aluminum in fourfold ($Al^{[4]}$), 55 % in five-fold ($Al^{[5]}$) and 25 % in six-fold coordination ($Al^{[6]}$) and model 2 with 75 % of the total aluminum in fourfold ($Al^{[4]}$) and 25 % in six-fold coordination ($Al^{[6]}$). Coordination numbers calculated on the basis of model 1 (with $Al^{[5]}$) are higher than values derived from pair distribution functions. On the other hand, it turns out that the coordination numbers calculated from model 2 (without $Al^{[5]}$) agree reasonably with the values resulting from the pair distribution functions (PDFs). In a

Table 1.4.4 Mean cation coordination numbers derived from models 1 and 2 (see the text) compared with values from pair distribution function (PDF) data.

Glass composition [mol% Al_2O_3]	Model 1 (AlO_4, AlO_5, AlO_6)	Model 2 (AlO_4, AlO_6)	Calculated from PDF
60	4.80	4.38	4.3
50	4.70	4.33	4.2
35	4.54	4.26	4.1

After Schmücker et al. (1999).

further step Schmücker and Schneider (1996) fitted the first pair distribution function (PDF) maximum of the glasses to either four gaussian functions according to model 1 ($Si^{[4]}$-O, $Al^{[4]}$-O, $Al^{[5]}$-O, $Al^{[6]}$-O) or with three gaussian functions according to model 2 ($Si^{[4]}$-O, $Al^{[4]}$-O, $Al^{[6]}$-O), using interatomic distances calculated from ionic radii and the site occupancies derived from nuclear magnetic resonance (NMR) spectra. The calculations clearly show that pair distribution function data can be fitted well for all three glass compositions if AlO_4 and AlO_6 polyhedra in addition to SiO_4 are proposed. On the other hand, if AlO_5 is included in the fitting procedure, the shapes of the PDFs and the calculated distance distributions match only poorly (Fig. 1.4.26).

A further fitting strategy has been used by Schmücker and Schneider (1996) for the first maxima of type I gels calcined at different temperatures (see Fig. 1.4.6). The maxima are fitted to two normal functions without parameter constraints

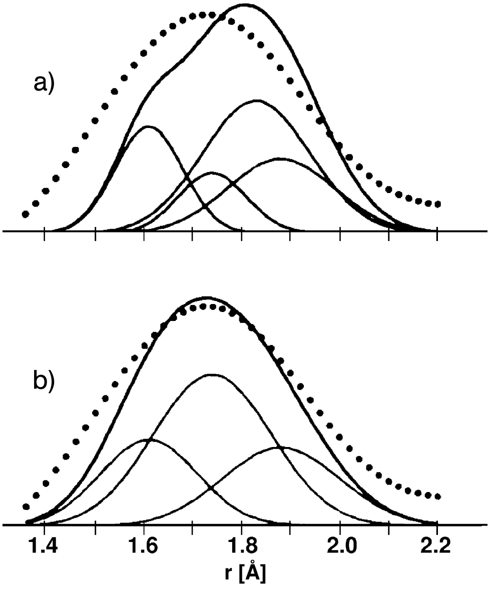

Fig. 1.4.26 Simulation of the first pair distribution function (PDF) maximum of mullite glass by (a) Four, and (b) Three gaussian functions corresponding to ($Si^{[4]}$-O, $Al^{[4]}$-O, $Al^{[5]}$-O, $Al^{[6]}$-O) distances, and ($Si^{[4]}$-O, $Al^{[4]}$-O, $Al^{[6]}$-O) distances, respectively Dotted lines: Measured data. Full lines: Calculated curves (after Schmücker et al. 1999).

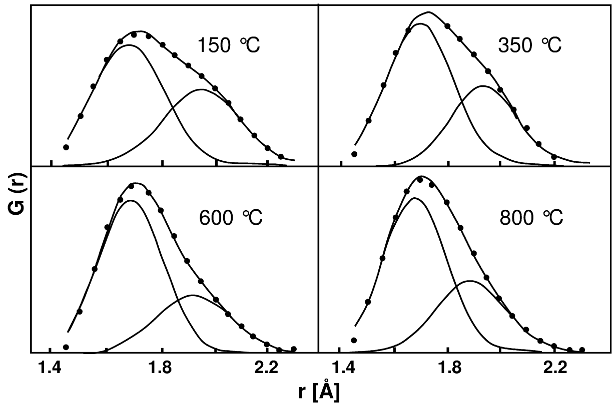

Fig. 1.4.27 Simulation of the first pair distribution function (PDF) maximum of mullite gels heat-treated at different temperatures (after Schmücker and Schneider, 1996).

(Fig. 1.4.27). The following conclusions can be drawn from the positions and intensities of the calculated normal functions: Position of function 1 (maximum at 1.69 Å) corresponds exactly to the mean tetrahedral (Al,Si)-O distance in mullite (Saalfeld and Guse, 1981). Its relative intensity increases with the calcination temperature, which implies a gradual increase of the relative amount of tetrahedrally coordinated aluminum. The intensity of the second normal function decreases with annealing temperature, and the peak maximum position shifts from 1.95 to 1.89 Å. The 1.89 Å distance is typical for $Al^{[6]}$-O bond lengths in crystalline aluminosilicates (Saalfeld and Guse, 1981), while the elongated 1.95-Å distance in the 150 °C and 350 °C samples may rather be attributed to Al-OH bonds. The ratio of $(Si,Al)^{[4]}$ to $Al^{[6]}$ changes slightly from about 60/40 at 150 °C to about 70/30 at 600 to 800 °C. Thus, the ratio of tetrahedrally to octahedrally coordinated cations in the calcined gels is very similar to that of mullite (67/33). The increase of fourfold-coordinated cations with the calcination temperature corresponds to the tendency noted in the NMR spectral development (Fig. 1.4.7), provided the 30 ppm signal is attributed to $Al^{[4]}$.

The assignment of the 30 ppm resonance to distorted AlO_4 tetrahedra and Lacy's charge balance considerations are self-consistent. Schmücker et al. (1997) show that a reciprocal dependence exists between the 30 ppm signal intensity and the Na_2O content in glasses and gels of the system Na_2O-Al_2O_3-SiO_2, suggesting that tricluster formation and incorporation of alkali ions are competitive mechanisms to achieve charge neutrality (Fig. 1.4.28; see also Taake, 1999). It has also been demonstrated that sodium addition to aluminosilicate glasses or melts has a strong influence on mullite nucleation (Schmücker and Schneider, 2002). Fig. 1.4.29 shows reaction couples consisting of Al_2O_3-rich mullite single crystals ($Al_2O_3/SiO_2 \approx 2/1$) and aluminosilicate glasses with and without sodium addition after firing at 1650 °C. While stoichiometric 3/2-mullite ($3Al_2O_3 \cdot 2SiO_2$) nucleates

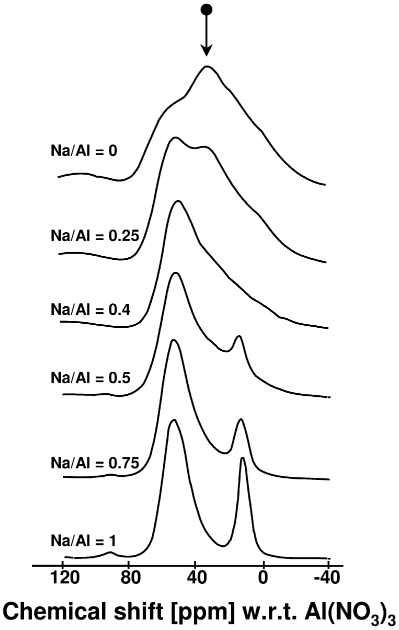

Fig. 1.4.28 ^{27}Al MAS NMR spectra of aluminosilicate glasses containing 10 mol% Al_2O_3 and varying amounts of Na_2O, given as Na/Al ratio. Note the decreasing intensity of the 30 ppm resonance (arrow) with increasing sodium content (after Schmücker et al. 1997).

within the pure Al_2O_3–SiO_2 melt (see also Schmücker et al. 2002), 3/2-mullite forms epitactically at the surface of the parent 2/1-mullite crystal if the aluminum silicate melt contains sodia (Na_2O). To explain these findings, it was suggested that sodium addition to Al_2O_3–SiO_2 glasses suppresses the population of tetrahedral triclusters and as a consequence the difference in the structural short-range-order of mullite and the aluminosilicate melt is high. Therefore, the nucleation barrier of mullite in Na_2O–Al_2O_3–SiO_2-melts is higher than in undoped Al_2O_3–SiO_2 melts. Thus, mullite crystallization in the bulk of the silicate melt becomes unfavorable if sodium is present, and epitactic growth of mullite needles from the surface of the single-crystal substrate occurs instead.

1.4.4.3 **The Origins of Mullite Crystallization**

High density nucleation within the bulk of non-crystalline aluminosilicates indicates that the energy barrier for mullitization is low. This has been attributed to short-range-order similarities between mullite and its non-crystalline counterparts. According to Schmücker and Schneider (1996) mullite and the non-crystalline aluminosilicates both consist of the same type of cation-oxygen polyhedra (SiO_4-tetrahedra, AlO_4-tetrahedra, AlO_6-octahedra, triclustered (Si,Al)O_4-tetrahedra), which display similar polyhedral distribution frequencies. In terms of the classical nucleation theory it is argued that a high degree of structural similarity, on the one hand, reduces the surface energy (σ) of the nucleating phase, but, on the other hand, lowers the driving force of transformation (ΔG). However, since

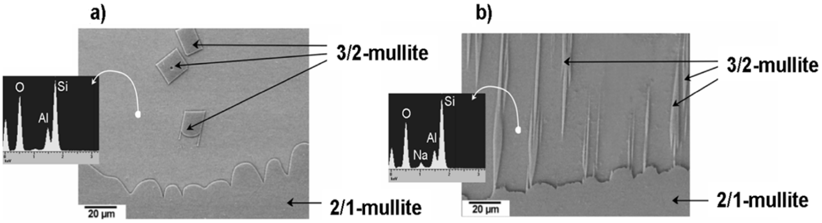

Fig. 1.4.29 Cross-section scanning electron micrograph of (a) Mullite single crystal / SiO_2-Al_2O_3 glass and (b) Mullite single crystal / Na_2O-Al_2O_3-SiO_2 glass reaction couples. Both systems have been heat-treated at 1650 °C (100 h). Note that newly formed mullite crystallites appear in the bulk of the pure aluminosilicate glass (a), but grow epitactically from the substrate surface into the sodium silicate melt (b). Inserts: EDX spectra of the vitreous phases (Courtesy M. Schmücker).

the surface energy dominates the free enthalpy of transformation (σ^3 versus ΔG^2)[5], in total the activation energy of nucleation should be lowered.

Analogous correlations between the structural arrangments of glasses and crystals and nucleation behavior have been reported by several authors. Müller et al. (1993), reviewing literature data, stated that silicate glasses displaying "homogeneous" nucleation have short-range-order similarities with their crystalline phase, in contrast to glasses typically transforming by heterogeneous nucleation events. The same was reported by Mastelaro et al. (2000) and Schneider et al. (2000) investigating $Na_2Ca_2Si_3O_9$-, $CaSiO_3$-, $CaMgSi_2O_6$-, and $PbSiO_3$-glasses by means of extended X-ray absorption fine structure (EXAFS) and silicon nuclear magnetic resonance (^{29}Si NMR) spectroscopy.

Mullitization of type I single phase aluminosilicate glasses and gels at temperatures below 1000 °C is obviously the result of rapid nucleation and very short diffusion distances. It is noteworthy that the close structural relation between crystalline and non-crystalline materials does not only affect the mullite nucleation but also enhances subsequent crystal growth, which then may be considered as polyhedral rearrangement rather than a diffusion-controlled reaction over a distance of several nanometers. In contrast, diphasic mullite precursors require dissolution of alumina and subsequent diffusion of the aluminum species in the silica phase prior to mullite nucleation. Depending on reaction temperature, dissolution (below about 1600 °C) or diffusion (above about 1600 °C) are rate-controlling steps, leading to mullite formation either in the bulk of the siliceous melt or at the alumina/silica interface. Only minor Al_2O_3 supersaturation of the amorphous silica phase is required to induce mullite nucleation (Fig. 1.4.16) which again shows that the nucleation barrier of mullite is low. Mullite crystal growth in diphasic precursors requires relatively long-distance diffusion of aluminum species

---

[5] Derived from classical nucleation theory where the activation energy of nucleation (E_A) is given by $E_A \propto \sigma^3 / T\,\Delta G^2$.

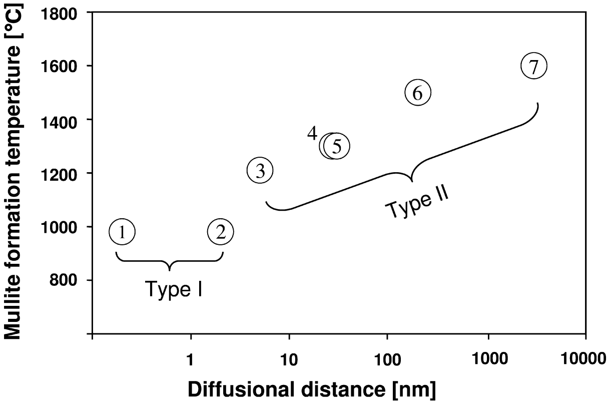

Fig. 1.4.30 Diagram showing the degree of alumina to silica segregation plotted versus the mullitization temperature. Data point 1 corresponds to aluminosilicate glasses or gels with compositional homogeneity on the atomic level. Data points 2 to 4 are from vapor deposited alumina/silica multilayers with layer thickness of 2, 5, and 30 nm, respectively. Data points 5 to 7 refer to literature data obtained from diphasic gels (Wei and Halloran, 1988 a,b), silica-coated alumina particles (Wang and Sacks, 1996), and alumina and silica powder admixtures (Albers, 1994).

through the silica-rich melt or, alternatively at high temperatures, aluminum and silicon interdiffusion through the interfacial mullite layer.

The interdependence between diffusion distance and mullitization temperature is depicted in Fig. 1.4.30. Data point 1 corresponds to type I aluminosilicate glasses or gels with compositional homogeneity on an atomic level. The assumed "diffusional distance" is 0.2 nm. Data points 2 to 4 come from vapor-deposited alumina/silica multilayers (see Section 1.4.4.1) with layer thickness of 2, 5, and 30 nm, respectively. Data points 5 to 7, finally, refer to literature data obtained for diphasic gels (data point 5), silica-coated alumina particles (data point 6) and alumina/silica powder admixtures (data point 7). Obviously, the transformation temperature of type I mullite-forming precursors is not affected by nanometer-sized segregation. In this case homogenization takes place prior to crystallization (see Section 1.4.4.1).

In contrast, data for true type II diphasic materials display mullite formation at significantly higher temperatures, since diffusional distances become larger. The following factors may have a crucial influence on the mullitization process of type II diphasic precursors:

- *Dissolution of alumina*: Small (highly curved) alumina particles display higher solubility in the non-crystalline silica phase than coarser particles owing to the Gibbs-Thompson effect. Moreover, the solubility of metastable transient alumina phases (γ-alumina) is higher than that of the stable α-alumina.
- *Critical nucleation concentration (CNC)*: The smaller the silica zones, the more

rapid the critical Al_2O_3 concentration is achieved necessary for mullite nucleation.

- *Growth of mullite crystals:* The diffusional distance of aluminum species in a silica-rich melt or the aluminum-silicon interdiffusion through the interfacial mullite layer, respectively, are directly controlled by the degree of alumina/silica segregation.

References

Abrahams, I., Bush, A. J., Hawkes, G.E and Nunes, T. (1999). Structure and oxide ion conductivity mechanism in $Bi_2Al_4O_9$ by combined X-ray and high-resolution neutron powder diffraction and ^{27}Al solid state NMR. J. Solid State Chem. **147**, 631–636.

Aksay, I. A. and Pask, J. A. (1975). Stable and metastable equilibria in the system SiO_2–Al_2O_3. J. Am. Ceram. Soc. **58**, 507–512.

Albers, W. (1994). Reaktionsintern von α-Al_2O_3 und verschiedenen SiO_2-Modifikationen zu Mullit. Ph. D. Thesis, Univ. Hannover.

Alonso, J. A., Casais, M. T., Martínez-Lope, M. J. and Rasines, I. (1997a). High oxygen pressure preparation, structural refinement, and thermal behavior of RMn_2O_5 (R = La, Pr, Nd, Sm, Eu). J. Solid State Chem. **129**, 105–112.

Alonso, J. A., Casais, M. T., Martínez-Lope, M. J., Martínez, J. L. and Fernández-Díaz, M. T. (1997b). A structural study from neutron diffraction data and magnetic properties of RMn_2O_5 (R = La, rare earth). J. Phys. Cond. Matter **9**, 8515–8526.

Anderson, J. S. and Kahn, A. S. (1975) quoted in: Levin, E. M. and McMurdie, H. F.: Phase diagrams for ceramists. The American Ceramic Society 1975 Supplement, p. 16, Fig. 1470.

Angel, R. J. and Prewitt, C. T. (1986). Crystal structure of mullite: A re-examination of the average structure. Amer. Min. **71**, 1476–1482.

Angel, R. J. and Prewitt, C. T. (1987).The incommensurate structure of mullite by Patterson synthesis. Acta Cryst. **B 42**, 116–126.

Angel, R. J., McMullan, R. K. and Prewitt, C. T. (1991). Substructure and superstructure of mullite by neutron diffraction. Amer.Min. **76**, 332–342.

Angerer, P. (2001). Alkalialuminate und Alkaligallate mit Mullitstruktur. Ph. D. Thesis Univ. Hannover.

Baerlocher, C., Hepp, A. and Meier, W. M. (1976). DLS-76, a program for the simulation of crystal structures by geometric refinements. ETH Zürich, Switzerland.

Balzar, D. and Ledbetter, H. (1993): Crystal structure and compressibility of 3:2 mullite. Amer. Min. **78**, 1192–1196.

Ban, T. and Okada, K. (1992). Structure refinement of mullite by the Rietveld method and a new method for estimation of chemical composition. J. Am. Ceram. Soc. **75**, 227–230.

Ban, T., Hayashi, S., Yasumori, A. and Okada, K. (1996). Calculation of metastable immiscibility region in the Al_2O_3–SiO_2 system. J. Mater. Res. **11**, 1421–1427.

Bärnighausen, H. (1980). Group-subgroup relations between space groups: A useful tool in crystal chemistry. Communications in mathematical chemistry MATCH, **9**, 209–233.

Bartsch, M., Saruhan, B., Schmücker, M. and Schneider, H. (1999). Novel low-temperature processing route of dense mullite ceramics by reaction sintering of amorphous SiO_2 coated γ–Al_2O_3 particle nanocomposites. J. Am. Ceram. Soc. **82**, 1388–1392.

Basso, R., Palenzona, A., Zefiro, L. (1989): Crystal structure refinement of a Sr-bearing term related to copper vanadates and arsenates of adelite and descloizite groups. N. Jb. Miner. Mh. 1989, 300–308.

Bauchspiess, R., Schneider, H. and Kulikov, A. (1996). EXAFS studies of Cr-doped mullite. J. Europ. Ceram. Soc. **16**, 203–209.

Baudin, C., Osendi, M. I. and Moya, J. S. (1983) Solid solution of TiO_2 in mullite. J. Mater. Sci. Lett. **2**, 185–187.

Baur, W.H. (1994). Rutile-type derivatives. Z. Krist. **209**, 143–150.

Baur, W.H. and Fischer, R.X. (2000). Zeolite-Type Crystal Structures and their Chemistry. Zeolite Structure Codes ABW to CZP. Subvolume B in Landolt-Börnstein, New Series, Group IV, Microporous and other Framework Materials with Zeolite-Type Structures, Springer, Berlin, Vol. 14 2000.

Baur, W.H. and Fischer, R.X. (2002). Zeolite-Type Crystal Structures and their Chemistry. Structure Codes DAC to LOV. Subvolume C in Landolt-Börnstein, New Series, Group IV, Microporous and other Framework Materials with Zeolite-Type Structures, Springer, Berlin, Vol. 14 2002.

Becker, H.-D. and Schneider, H. (2005). High temperature crystal field spectroscopy of chromium-doped mullite. Unpublished results.

Birkenstock, J., Fischer, R.X. and Messner, T. (2004). BRASS, the Bremen Rietveld Analysis and Structure Suite. University of Bremen, Germany.

Birx, J. and Hoppe, R. (1991). $Na_2Li_3CoO_4$, das erste quaternaere Oxocobaltat(III) der Alkalimetalle. Z. Anorg. Allg. Chemie **597**, 19–26.

Boccaccini, A.R., Khalil T.K. and Bücker M. (1999). Activation energy for the mullitization of a diphasic gel obtained from fumed silica and boehmite sol. Mater. Sci. Lett. **38**, 116–120.

Bock, O. and Müller, U. (2002). Symmetrieverwandtschaften bei Varianten des Perowskit-Typs. Acta Cryst., B**58**, 594–606.

Bodart, P. R., Parmentier, J., Harris R. K. and Thompson, D. P. (1999). Aluminium environments in mullite and an amorphous sol-gel precursor examined by ^{27}Al triple quantum MAS NMR. J. Phys. Chem. Solids **60**, 223–228.

Böhm, H. (1977). Eine erweiterte Theorie der Satellitenreflexe und die Bestimmung der modulierten Struktur des Natriumnitrits. Habilitation Thesis, Univ. Münster.

Bohn, D. (1979). Gleichgewichte zwischen Korund, Mullit und Tialit im System Al_2O_3–SiO_2–Fe_2O_3–TiO_2. Diploma Thesis, Univ. Aachen.

Bowen, N.L., and Greig, J.W. (1924). The system Al_2O_3 – SiO_2. J. Am. Ceram. Soc. **7**, 238–254.

Boysen, H.; Frey, F. and Jagodzinski, H. (1984). Diffuse scattering and disorder in crystals. Rigaku **1**, 3–14.

Brown, I. W. M., MacKenzie, K. J. D., Bowen, M.E. and Meinhold, R. H. (1985). Outstanding problems in the kaolinite-mullite reaction sequence investigated by ^{29}Si and ^{27}Al solid-state nuclear magnetic resonance: II. High-temperature transformations of metakaolinite. J. Am. Ceram. Soc. **68**, 298–301.

Brownell, J. (1958). Subsolidus relations between mullite and iron oxide. J. Am. Ceram. Soc. **41**, 226–230.

Brunauer, G., Boysen, H., Frey, F., Hansen, T., Kriven, W. (2001). High temperature crystal structure of a 3:2 mullite from neutron diffraction data. Z. Krist. **216**, 284–290.

Burnham, C.W. (1963a). Crystal structure of mullite. Annual Report Geophys. Lab. Carnegie Inst. Wash., **63**, 223–227.

Burnham, C.W. (1963b). Refinement of the crystal structure of sillimanite. Z. Krist. **118**, 127–148.

Burnham, C.W. (1964a). Composition limits of mullite and the sillimanite – mullite solid solution problem. Carnegie Inst. Wash. Yearb. **63**, 223–227.

Burnham, C.W. and Buerger, M.J. (1961). Refinement of the crystal structure of andalusite. Z. Krist. **115**, 269–290.

Burns, P.C. and Hawthorne, F.C. (1995). Rietveld refinement of the crystal structure of olivenite: A twinned monoclinic structure. Canad. Min. **33**, 885–888.

Butler, B.D. and Welberry, T.R. (1994). Analysis of diffuse scattering from the mineral mullite. J.Appl.Cryst. **27**, 742–754.

Caballero, A. and Ocana, M. (2002). Synthesis and structural characterization by X-ray absorption spectroscopy of tin-doped mullite solid solutions. J. Am. Ceram. Soc. **85**, 1910–1914.

Cameron, W.E. (1976a). A mineral phase intermediate in composition between sillimanite and mullite. Amer. Min. **61**, 1025–1026.

Cameron, W.E. (1976 b) Coexisting sillimanite and mullite. Geol. Mag. **113**, 497–514.

Cameron, W.E. (1977a). Mullite: A substituted alumina. Amer. Min. **62**, 747–755.

Cameron, W.E. (1977b). Nonstoichiometry in sillimanite: Mullite compositions with sillimanite-type superstructures. Phys. Chem. Minerals **1**, 265–272.

Cameron, W. E. (1977c). Composition and cell dimensions of mullite. Amer. Ceram. Soc. Bull. **56**, 1003–1011.

Campos, A. L., Silva, N. T. Melo, F.C.L., Oliveira, M.A.S. and Thim G. P. (2002). Crystallization kinetics of orthohombic mullite from diphasic gels. J. Non-Cryst. Solids **304**, 19–24.

Cesbron, F. P., Ginderov, D., Girand, R., Pelisson, P. and Pilard, F. (1987). La nickelanstiute Ca (Ni, Zn) (AsO_4) (OH): nouvelle espèce minérale du district cobalto-nickelifère de Bon-Azzer, Marvc. Canad. Min. **25**, 401–407.

Chakraborty A. K. and Ghosh D. K. (1978). Reexamination of kaolinite-to-mullite reaction series, J. Am. Ceram. Soc. **61**, 170–173.

Chater, R. and Gavarri, J.-R. (1985). Evolution structurale entre 2 et 300 K de l'oxyde $MnSb_2O_4$: Propriétés élastiques et magnétiques anisotropes. J. Solid State Chem. **59**, 123–131.

Chater, R., Gavarri, J. R. and Hewat, A. (1985). Structures isomorphes MeX_2O_4 – Evolution structurale entre 2 K et 300 K de l'antimonite $FeSb_20_4$: Elasticité et ordre magnétique anisotropes. J. Solid State Chem. **60**, 78–86.

Clark, L. A., Pluth, J. J., Steele, I., Smith, J. V. and Sutton, S. R. (1997). Crystal structure of austinite, $CaZn(AsO_4)OH$. Min. Mag. **61**, 677–683.

Colomban, Ph. (1989). Structure of oxide gels and glasses by infrared and Raman scattering, J. Mater. Sci. **24**, 3011–3020.

Cooper, M. A. and Hawthorne, F. C. (1995). The crystal structure of mottramite, and the nature of Cu ⇆ Zn solid solution in the mottramite-descloizite series. Canadian Mineral. **33**, 1119–1124.

Cordsen, A. (1978). A crystal-structure refinement of libethenite. Canad. Min. **16**, 153–157.

Cowley, J. M. and Moodie, A. F. (1957). The scattering of electrons by atoms and crystals. I. A new theoretical approach. Acta Cryst. **10**, 609–619.

Daniel, V. and Lipson, H. (1944). The dissociation of an alloy of copper, iron and nickel. Further X-ray work. Proc. Royal Soc. London **A128**, 378–387.

Darken, L. S. and Gurry, R. W. (1945). The system iron-oxygen. I. The wustite field and related equilibria. J. Am. Ceram. Soc. **28**, 1398–1412.

Darken, L. S. and Gurry, R. W. (1946). The system iron-oxygen. II. Equilibrium and thermodynamics of liquid oxide and other phases. J. Am. Ceram. Soc. **29**, 798–816.

Deville, S. C. and Caron, D. (1865). Cited in: Pask, J. A. (1990). Critical review of phase equilibria in the $Al_2O_3 - SiO_2$ system. Ceramic Trans. **6**, 1–13.

De Wolff, P. M. (1974). The pseudo-symmetry of modulated crystal structures. Acta Cryst. **A30**, 777–785.

Ďurovič, S. (1962a). A statistical model of the crystal structure of mullite. Kristallografiya **7**, 339–349.

Ďurovič, S. (1962b). Isomorphism between sillimanite and mullite. J. Am. Ceram. Soc. **45**, 157–162.

Ďurovič, S. (1969). Refinement of the crystal structure of mullite. Chemicke Zvesti **23**, 113–128.

Ďurovič, S. and Fejdi, P. (1976). Synthesis and crystal structures of germanium mullite and crystallochemical parameters of D-mullites. Silikaty **2**, 192.

Duvigneaud, P. H. (1974). Existence of mullite without silica. J. Am. Ceram. Soc. **57**, 224.

Engelhardt, G. and Michel, D. (1987). High Resolution Solid State NMR of Silicates and Zeolites. John Wiley and Sons, New York.

Epicier, T. (1991). Benefits of high-resolution electron microscopy for the structural characterization of mullites. J. Am. Ceram. Soc. **74**, 2359–2366.

Epicier, T., O'Keefe, M. A. and Thomas, G. (1990). Atomic imaging of 3:2 mullite. Acta Cryst. **A46**, 948–962.

Faye, G. H. and Harris, D. C. (1969). On the origin of colour and pleochroism in andalusite from Brazil. Canad. Min. **10**, 47–56.

Fischer, R. X. and Baur, W. H. (2004). The standardization of zeolite-type crystal structures. Proceedings of the 14th International Zeolite Conference, In press.

Fischer, R. X., Kahlenberg, V., Voll, D., Mac Kenzie, K. J. D., Smith, M. E. and Schneider, H. (2005). Cation coordination in synthetic boron aluminate, $Al_{6-x}B_xO_9$ ($x = 2$), studied by ^{11}B and ^{27}Al MAS NMR spectroscopy and Rietveld analyses. Abstracts Jahrestagung Deutsche Gesellschaft für Kristallographie (DGK), Köln, 2005.

Fischer, R.X. and Messner, T. (2004). STRUPLO, a new version of the crystal structure drawing program. University of Bremen, Germany.

Fischer, R. and Pertlik, F. (1975). Verfeinerung der Kristallstruktur des Schafarzikites, $FeSb_2O_4$. Tschermaks Mineral. Petrogr. Mitt. **22**, 236–241.

Fischer, R.X. and Schneider, H. (1992). Crystal chemistry of iron containing germanium andalusites, $Fe_xAl_{8-x}Ge_4O_{20}$. Z. Krist. **201**, 19–36.

Fischer, R.X. and Schneider, H. (2000). Crystal structure of Cr-mullite. Amer. Min. **85**, 1175–1179.

Fischer, R.X., Schneider, H. and Schmücker, M. (1994). Crystal structure of Al-rich mullite. Amer. Min. **79**, 983–990.

Fischer, R.X., Schneider, H. and Voll, D. (1996). Formation of aluminum rich 9 : 1 mullite and its transformation to low alumina mullite upon heating. J. Europ. Ceram. Soc. **16**, 109–113.

Fischer, R.X., Schmücker, M., Angerer, P. and Schneider, H. (2001). Crystal structures of Na and K aluminate mullites. Amer. Min. **86**, 1513–1518.

Foster Jr., P.A. (1959). The nature of alumina in quenched cryolite-alumina melts. J. Electrochem. Soc. **106**, 971–975.

Freimann, S. (2001). Bestimmung der Sauerstoff-Leerstellenverteilung in 2:1-Mullit mit Hilfe der videographischen Methode. Ph. D. Thesis, Univ. Hannover.

Freimann, S. and Rahman, S. (2001). Refinement of the real structures of 2:1 and 3:2 mullite. J. Europ. Ceram. Soc. **21**, 2453–2461.

Freimann, S., Thoke, S. and Rahman, S.H. (1996). Bestimmung der Nahordnungsvektoren in Mullit mit Hilfe der videographischen Rekonstruktion. 4. Jahrestagung DGK Marburg, Abstracts 121.

Fukuoka, M., Onoda, Y., Inoue, S., Wada, K., Nukui, A. and Makashima, A.J. (1993). The role of precursors in the structure of SiO_2–Al_2O_3 sols and gels by the sol-gel-process. Sol-Gel Sci. Tech. **1**, 47–53.

Gani, M.S.J. and McPherson, R. (1977a). Crystallization of mullite from Al_2O_3–SiO_2 glasses. J. Austr. Ceram. Soc. **13**, 21–24.

Gani, M.S.J. and McPherson, R. (1977b). Glass formation and phase transformation in plasma prepared Al_2O_3–SiO_2 powders. J. Mater. Sci. **12**, 999–1009.

Garsche, M., Tillmanns, E., Almen, H., Schneider, H. and Kupčik. V. (1991). Incorporation of chromium into aluminium borate $9Al_2O_3 \cdot 2B_2O_3$ (A_9B_2). J. Europ. Min. Soc. **3**, 793–808.

Gavarri, J.R. (1981). Sur les composes isomorphes MeX_2O_4: evolution structurale par diffraction de neutrons de $NiSb_2O_4$ et $ZnSb_2O_4$ entre 5 et 300 K: anisotropie, rigidite. Compt. Rend. Hebd. Seances Acad. Sci. **292**, 895–898.

Gavarri, J.R., Vigouroux, J.P., Calvarin, G. and Hewat, A.W. (1981). Structure de $SnPb_2O_4$ à quatre températures: relation entre dilatation et agitation thermiques. J. Solid State Chem. **36**, 81–90.

Gavarri, J.-R., and Weigel, D. (1975). Oxydes de Plomb. I. Structure cristaline du minium Pb_3O_4, à température ambiante (293 K). J. Solid State Chem. **13**, 252–257.

Gavarri, J.R., Weigel, D. and Hewat, A.W. (1978). Oxydes de plomb. IV. Evolution structurale de l'oxyde Pb_3O_4 entre 240 et 5° K et mécanisme de la transition. J. Solid State Chem. **23**, 327–339.

Gelato, L.M. and Parthé, E., J. (1987). STRUCTURE TIDY – a computer program to standardize crystal structure data. J. Appl. Cryst. **20**, 139–143.

Gelsdorf, G., Müller-Hesse, H. and Schwiete, H.E. (1958). Einlagerungsversuche an synthetischem Mullit und Substitutionsversuche mit Galliumoxyd und Germaniumoxyd. Teil II. Arch. Eisenhüttenwesen **29**, 513–519.

Gelsdorf, G., Müller-Hesse, H. and Schwiete, H.E. (1961). Untersuchungen zur Frage der Mischkristallbildung in Mulliten und mullitähnlichen Verbindungen. Sprechsaal **94**, 502–508.

Gerardin, C., Sundaresan, S., Benziger, J. and Navrotsky, A. (1994). Structural investigation and energetics of mullite formation from sol-gel-precursors. Chem. Mater. **6**, 160–168.

Giaquinta, D.M., Papaefthymiou, G.C., Davis, W.M. and zur Loye, H.-C. (1992). Synthesis, structure, and magnetic properties of the layered bismuth transition metal oxide solid solution $Bi_2Fe_{4-x}Ga_xO_9$. J. Solid State Chem. **99**, 120–133.

Giaquinta, D.M., Papaefthymiou, G.C. and zur Loye, H.-C. (1995). Structural and magnetic studies of $Bi_2Fe_{4-x}Al_xO_9$. J. Solid State Chem. **114**, 199–205.

Green, C.R. and White, J. (1974). Solid solubility of TiO_2 in mullite in the system Al_2O_3–TiO_2–SiO_2. Trans. Brit. Ceram. Soc. **73**, 73–75.

Grigor'ev, A.P. (1976). Crystallization of the intermediate phases in the series sillimanite-mullite. Neorg. Mater. **12**, 519–521.

Grießer, K.J. (2004). Untersuchungen im System Al_2O_3–SiO_2–B_2O_3 "Bormullite". Master Thesis, Univ. Vienna.

Guse, W. (1974). Compositional analysis of Czochralski grown mullite single crystals. J. Crystal Growth **26**, 151–152.

Guse, W. and Mateika, D. (1974). Growth of mullite single crystals ($2Al_2O_3$ .SiO_2) by the Czochralski method. J. Crystal Growth **22**, 237–240.

Hahn (2002) International Tables for Crystallography, Volume A. Space Group Symmetry. Hahn, T. (ed.). Kluwer Academic Publishers.

Hammonds, K.D., Bosenick, A., Dove, M.T. and Heine, V. (1998). Rigid unit modes in crystal structures with octahedrally coordinated atoms. Amer. Min. **83**, 476–479.

Hariya, Y., Dollase, W.A. and Kennedy, G.C. (1969). An experimental investigation of the relationship of mullite to sillimanite. Amer. Min. **54**, 1419–1441.

Hawthorne, F.C. and Faggiani, R. (1979). Refinement of the structure of descloizite. Acta Cryst. **B35**, 717–720.

Heinrich, T. and Raether, F. (1992). Structural characterization and phase development of sol-gel derived mullite and its precursors. J. Non-Cryst. Solids **147**, 152–156.

Hildmann, B., Schneider, H. and Schmücker, M. (1996). High temperature behaviour of polycrystalline alumo-silicate fibers with mullite bulk composition: II. Kinetics of γ-Al_2O_3 -mullite transformation. J. Europ. Ceram. Soc. **16,** 287–292.

Hill, R.J. (1976). The crystal structure and infrared properties of adamite. Amer. Min. **61**, 979–986.

Hiroi, Y., Grew, E.S., Motoyoshi, Y., Peacor, D.R., Rouse, R.C., Matsubara, S., Yokoyama, K., Miyawaki, R., McGee, J.J., Su, S.C., Hokada, T., Furukawa, N. and Shibasaki, H. (2002). Ominellite, $(Fe,Mg)Al_3BSiO_9$ (Fe^{2+} analogue of grandidierite), a new mineral from porphyritic granite in Japan. Amer. Min. **87**, 160–170.

Hoffman, D.W., Roy, R. and Komarneni, S. (1984). Diphasic xerogels, a new class of materials: phases in the system Al_2O_3–SiO_2. J. Am. Ceram. Soc. **67**, 468–471.

Hong, S.-H. and Messing, G.L. (1997). Mullite transformation kinetics in P_2O_5–B_2O_3– and TiO_2-doped aluminosilicate gels. J. Am. Ceram. Soc. **80**, 1551–1559.

Hong, S.-H. and Messing G.L. (1999). Anisotropic grain growth in boria-doped diphasic mullite gels. J. Europ. Ceram. Soc. **19**, 521–526.

Hong, S.-H., Cermignani, W. and Messing, G.L. (1996). Anisotropic grain growth in seeded and B_2O_3-doped diphasic mullite gels. J. Europ. Ceram. Soc. **16**, 133–141.

Hübner, J.S. and Sato, M. (1970). The oxygen fugacity-temperature relationships of manganese oxide and nickel oxide buffers. Amer. Min. **55**, 934–952.

Huling, J. C. and Messing, G. L. (1991). Epitactic nucleation of spinel in aluminium silicate gels and effect on mullite crystallization. J. Am. Ceram. Soc. **74**, 2374–2381.

Huling, J.C. and Messing, G.L. (1992). Chemistry-crystallization relations in molecular mullite gels. J. Non-Cryst. Solids **147/148**, 213–221.

Hyatt, M.J. and Bansal, N. P. (1990). Phase transformations in xerogels of mullite composition. J. Mater. Sci. **25**, 2815–2821.

Ihara , M., Imai, K, Fukunaga, J. and Yoshida N. (1980). Crystal structure of boraluminate $9Al_2O_3$ $2B_2O_3$. Yogyo Kyokaisi **88**, 77–84.

Ikeda, K., Schneider, H., Akasaka, M. and Rager, J. (1992). Crystal-field spectroscopic study of Cr-doped mullite. Amer. Min. **77**, 251–257.

Ivankovic, H., Tkalcec, E., Nass R. and Schmidt H. (2003). Correlation of the precursor type with densification behavior and microstructure of sintered mullite ceramics. J. Europ. Ceram. Soc. **23**, 283–292.

Jagodzinski, H. (1949). Eindimensionale Fehlordnung in Kristallen und ihr Einfluß auf die Röntgeninterferenzen. I. Berechnung des Fehlordnungsgrades aus Röntgenintensitäten. Acta Cryst. **2**, 201–207.

Jagodzinski, H. (1964a). Allgemeine Gesichtspunkte für die Deutung diffuser Interferenzen von fehlgeordneten Kristallen. Advances in Structure Research by Diffraction Methods, Vol. I, R. Brill. (ed.) Vieweg Braunschweig.

Jagodzinski, H. (1964b). Diffuse disorder scattering by crystals. Advanced Methods of Crystallography, G. N. Ramachandran (ed.). London, New York Academic Press.

James, P. F., Iqbal, Y., Jais, U. S., Jordery, S. and Lee, W. E. (1997). Crystallization of silicate and phosphate glasses. J. Non-Cryst. Solids **219**, 17–29.

Jantzen, C. M., Schwalm, D., Schelten, J. and Herrman, H. (1981). The SiO_2–Al_2O_3 system, Part 1. Later stage spinoidal decomposition and metastable immiscibility. Phys. Chem. Glasses **22**, 122–137.

Jaymes I. and Douy, A. (1996). New aqueous mullite precursor synthesis. Structural study by ^{27}Al and ^{29}Si NMR spectroscopy. J. Europ. Ceram. Soc. **16**, 155–160.

Johnson, B. R., Kriven, W. M. and Schneider, J. (2001). Crystal structure development during devitrification of quenched mullite. J. Europ. Ceram. Soc. **21**, 2541–2562.

Kahlenberg, V., Fischer, R. X. and Baur, W. H. (2001). Symmetry and structural relationships among ABW-type materials. Z. Krist. **216**, 489–494.

Kanzaki, S., Tabata, H., Kumazawa, T. and Ohta, S. (1985). Sintering and mechanical properties of mullite. J. Am. Ceram. Soc. **68**, C-6–C-7.

Keller, P., Lissner, F. and Schleid, T. (2003). The crystal structure of arsendescloizite, $PbZn(OH)[AsO_4]$, from Tsumeb (Namibia). N. Jb. Min. Mh. 2003, 374–384.

Kharisun, Taylor, M. R., Bevan, D.J.M. and Pring, A. (1998). The crystal chemistry of duftite, $PbCuAsO_4(OH)$ and the β-duftite problem. Min. Mag. **62**, 121–130.

Kolitsch, U. (2001). Refinement of pyrobelonite, $PbMn^{II}VO_4(OH)$, a member of the descloizite group. Acta Cryst. E**57**, i119–i121.

Komarneni, S. and Roy, R. (1986). Application of compositionally diphasic xerogels for enhanced densification, the system Al_2O_3–SiO_2. J. Am. Ceram. Soc. **69**, C155–C156.

Korekawa, M. (1967). Theorie der Satellitenreflexe. Habilitation Thesis Univ. München.

Korekawa, M., Nissen, H.-U., and Philipp, D. (1970). X-ray and electronmicroscopic studies of a sodium-rich low plagioclase. Z. Krist. **131**, 418–436.

Kunath, G., Losso, P. Steuernagel, S., Jäger, C. and Schneider H. (1992). ^{27}Al satellite transition spectroscopy (SATRAS) of polycrystalline aluminium borate, $9Al_2O_3$ $2B_2O_3$ (A_9B_2). Solid State NMR **1**, 261–266.

Kunze, G. (1959). Fehlordnungen des Antigorites. Z. Krist. **111**, 190–221.

Kutty, T.R.N. and Nayak, M. (2000). Photoluminescence of Eu^{2+}-doped mullite (xAl_2O_3 $ySiO_2$; $x/y = 3/2$ and $2/1$) prepared by the hydrothermal method. J. Mater. Chem. Phys. **65**, 158–165.

Kvick, Å., Pluth, J. J., Richardson, Jr, J. W. and Smith, J. V. (1988). The ferric ion distribution and hydrogen bonding in epidote: a neutron diffraction study at 15K. Acta Cryst. B**44**, 351–355.

Lacy, E. D. (1963). Aluminium in glasses and melts. Phys. Chem. Glasses **4**, 234–238.

Li, D. X. and Thomson, W. J. (1990). Mullite formation kinetics of a single phase gel. J. Am. Ceram. Soc. **73**, 964–969.

Li, D. X. and Thomson, W. J. (1991). Mullite formation from non-stoichiometric diphasic precursors. J. Am. Ceram. Soc. **74**, 2382–2387.

Low, I. M. and McPherson, R. (1989). The origins of mullite formation. J. Mater. Sci. **24**, 926–936.

MacDowell, J. F. and Beall, G. H. (1969). Immiscibility and crystallization in Al_2O_3-SiO_2 glasses. J. Am. Ceram. Soc. **52**, 17–25.

Mack, D. E., Becker, K. D. and Schneider, H. (2005). High temperature Mössbauer study of Fe-subtituted mullite. Amer. Min., in press.

Mackenzie, K. J. D., Meinhold, R. H., Patterson, J. E., Schneider, H. , Schmücker, M. and Voll, D. (1996). Structural evolution in gel-derived mullite precursors. J. Europ. Ceram. Soc. **16**, 1299–308.

Mägi, M., Lipmaa, E., Samoson, A., Engelhardt, G. and Grimmer, A. R. (1984). Solid state high resolution silicon-29 chemical shifts in silicates. J. Phys. Chem. **88**, 1518–1522.

Mastelaro, V. R., Zanotto, E. D., Lequeux, N.

and Cortès, R. (2000). Relationship between short-range order and ease of nucleation in $Na_2Ca_2Si_3O_9$, $CaSiO_3$ and $PbSiO_3$ glasses. J. Non-Cryst.Solids **262**, 191–199.

Mazza, D., Vallino, M. and Busca, G. (1992). Mullite-type structures in the systems Al_2O_3–Me_2O (Me = Na,K) and Al_2O_3–B_2O_3. J. Am. Ceram. Soc. **75**, 1929–1934.

McConnell, J. D. C. and Heine, V. (1985). Incommensurate structure and stability of mullite. Phys. Rev. **B 31**, 6140–6142.

McManus, J., Ashbrook, S. E., MacKenzie, K.J.D. and Wimperis, S. (2001). ^{27}Al multiple quantum MAS and ^{27}Al {^{1}H} CPMAS NMR study of amorphous aluminosilicates. J. Non-Cryst. Solids **282**, 278–290.

McNear, E., Vincent, M.G. and Parthé, E. (1976). The crystal structure of vuagnatite, $CaAl(OH)SiO_4$. Amer. Min. **61**, 831–838.

Meinhold, R. H., Slade, R. C. T. and Davies, T. W. (1993). High field ^{27}Al MAS NMR studies of the formation of metakaolinite by flash calcination of kaolinite. J. Appl. Magn. Reson. **4**, 141–155.

Mellini, M. and Merlino, S. (1979). Versiliaite and apuanite: derivative structures related to schafarzikite. Amer. Min. **64**, 1235–1242.

Merwin, L. H., Sebald, A., Rager, H. and Schneider, H. (1991). ^{29}Si and ^{27}MAS NMR spectroscopy of mullite. Phys. Chem. Minerals **18**, 47–52.

Moore, P. B. and Smyth, J. R. (1968). Crystal chemistry of the basic manganese arsenates: III. The crystal structure of eveite, $Mn_2(OH)$ (AsO_4). Amer. Min. **53**, 1841–1845.

Moore, J. M., Waters, D. J. and Niven, M. L. (1990). Werdingite, a new borosilicate mineral from the granulite facies of the western Namaqua-land metamorphic complex, South Africa. Amer. Min. **75**, 415–420.

Morikawa, H., Miwa, S., Miyake, M., Marumo, F. and Sata, T. (1982) Structural analysis of SiO_2–Al_2O_3 glasses. J. Am. Ceram. Soc. **65**, 78–81.

Muan, A. (1957). Phase equilibria at liquidus temperatures in the system iron oxide-Al_2O_3–SiO_2 in air atmosphere. J. Am. Ceram. Soc. **40**, 121–133.

Müller, E., Heide, K. and Zanotto, E. D. (1993). Molecular structure and nucleation in silicate glasses. J. Non-Cryst. Solids **155**, 56–66.

Müller-Buschbaum, H. and Chales de Beaulieu, D. (1978). Zur Besetzung von Oktaeder- und Tetraederpositionen in $Bi_2Ga_2Fe_2O_9$. Z. Naturforsch. **B33**, 669–670.

Murthy, M. K. and Hummel, F. A. (1960) X-ray study of the solid solution of TiO_2, Fe_2O_3, and Cr_2O_3 in mullite ($3Al_2O_3$ $2SiO_2$). J. Am. Ceram. Soc. **43**, 267–273.

Nakajima, Y., Morimoto, M and Watanabe, E. (1975). Direct observation of oxygen vacancy in mullite, 1.86 $Al_2O_3 \cdot SiO_2$ by high resolution electron microscopy. Proc. Jpn. Acad. Sci. **51**, 173–178.

Nguyen, N., Legrain, M., Ducouret, A. and Raveau, B. (1999). Distribution of Mn^{3+} and Mn^{4+} species between octahedral and square pyramidal sites in $Bi_2Mn_4O_{10}$-type structure. J. Mater. Chem. **9**, 731–734.

Niizeki, N. and Wachi, M. (1968). The crystal structures of $Bi_2Mn_4O_{10}$, $Bi_2Al_4O_9$ and $Bi_2Fe_4O_9$. Z. Krist. **127**, 173–187.

Niven, M. L., Waters, D. J. and Moore, J. M. (1991). The crystal structure of werdingite, $(Mg,Fe)_2Al_{12}(Al,Fe)_2Si_4(B,Al)_4O_{37}$, and its relationship to sillimanite, mullite, and grandidierite. Amer. Min. **76**, 246–256.

Nyfeler, D., Hoffmann, C., Armbruster, T., Kunz, M. and Libowitzky, E. (1997). Orthorhombic Jahn-Teller distortion and Si-OH in mozartite, $CaMn^{3+}O[SiO_3OH]$; A single-crystal X-ray, FTIR, and structure modeling study. Amer. Min. **82**, 841–848.

Ocana, M., Cabellero, A., Ganzalez-Carreno, T. and Serna, C. J. (2000). Preparation by pyrolysis of aerosols and structural characterization of Fe-doped mullite powders. Mater. Res. Bull. **35**, 775–788.

Okada K. and Otsuka, N. (1986). Characterization of the spinel phase from SiO_2-Al_2O_3 xerogels and the formation process of mullite. J. Am. Ceram. Soc. **69**, 652–656.

Okada K. and Otsuka, N. (1990). Preparation of transparent mullite films by dip-coating method. Ceramic Trans. **6**, 425–430.

Okada K., Aoki, C., Ban, T., Hayashi, S. and Yasumori, A. (1996). Effect of aging temperature on the structure of mullite precursor prepared from tetraethoxysilane and aluminum nitrate in ethanol solution. J. Europ. Ceram. Soc. **16**, 149–153.

Okada, K., Kaneda, J., Kameshima, Y., Yasumori, M. and Takei, T. (2003). Crystallization kinetics of mullite from polymeric $Al_2O_3 - SiO_2$ xerogels. Mater. Lett. **4304**, 1–5.

Okuno, M., Shimada, Y., Schmücker, M., Schneider, H., Hoffbauer, W. and Jansen, M. (1997). LAXS and Al-NMR studies on the temperature-induced changes of non-crystalline single phase mullite precursors. J. Non-Cryst. Solids **210**, 41–47.

Oschatz and Wächter (1847). Cited in: Litzow, K. (1984). Keramische Technik. Vom Irdengut zum Porzellan. Callwey, München.

Ossaka, J. (1961). Tetragonal mullite-like phase from co-precipitated gels. Nature **191**, 1000–1001.

Padlewski, S., Heine, V. and Price, G. D. (1992a). Atomic ordering around the oxygen vacancies in sillimanite. A model for the mullite structure. Phys. Chem. Minerals **18**, 373–378.

Padlewski, S., Heine, V. and Price, G. D. (1992b). The energetics of interaction between oxygen vacancies in sillimanite: A model for the mullite structure. Phys. Chem. Minerals **19**, 196–202.

Park, H. and Barbier, J. (2001). $PbGaBO_4$, an orthoborate with a new structure-type. Acta Cryst. E**57**, 82–84.

Park, H., Barbier, J. and Hammond. R. P. (2002). Crystal structure and polymorphism of $PbAlBO_4$. Solid State Sci. **5**, 565–571.

Park, H., Barbier, J., Hammond, R. P. (2003a). Crystal structure and polymorphism of $PbAlBO_4$. Solid State Sci. **5**, 565–571.

Park, H., Lam, R., Greedan, J. E. and Barbier, J. (2003b). Synthesis, crystal structure and magnetic properties of $PbMBO_4$ (M = Cr, Mn, Fe). A new structure type exhibiting one-dimensional magnetism. Chem. Mater. **15**, 1703–1712.

Parmentier, J. Vilminot, S. and Dormann, J.-L. (1999). Fe- and Cr-substituted mullites: Mössbauer spectroscopy and Rietveld structure refinement. Solid State Sci. **1**, 257–265.

Parthé, E. and Gelato, L. M., (1984). The standardization of inorganic crystal-structure data. Acta Cryst. A**40**, 169–183.

Paulmann, C. (1996). Study of oxygen vacancy ordering in mullite at high temperatures. Phase Transitions **59**, 77–90.

Paulmann, C., Rahman, S. H. and Strothenk, S. (1994). Interpretation of mullite HREM images along [010] and [100]. Phys. Chem. Minerals **21**, 546–554.

Peacor, D. R., Rouse, R. C. and Grew, E. S. (1999). Crystal structure of boralsilite and its relation to a family of boroaluminosilicates, sillimanite, and andalusite. Amer. Min. **84**, 1152–1161.

Peeters, M.P.J. and Kentgens, A.P.M. (1997). A ^{27}Al MAS, MQMAS and off-resonance nutation NMR study of aluminium containing silica-based sol-gel materials, Solid State NMR, **9**, 203–217.

Perez Y Jorba, M. (1968). Les systemès $GeO_2–Al_2O_3$ et $GeO_2–Fe_2O_3$ avec les systèmes correspondants à base de silice. Silicates Ind. **33**, 11–17.

Perez Y Jorba, M. (1969). Contribution a l'étude de phases formées par l'oxyde de germanium avec quelques oxydes d'éléments trivalents. Rev. Int. Hts. Temp. et Réfract. **6**, 283–298.

Permer, L., Laligant, Y. and Ferey, G. (1993). Crystal structure of $(Pb_{2.8}Fe_{1.2})Cu_4O_{1.6}(VO_4)_4(OH)_2$; structural relationships with mineral gamagarite. Europ. J. Solid State Inorg. Chem. **30**, 383–392.

Perrotta, A. J. and Young Jr., J. E. (1974). Silica-free phases with mullite-type structures. J. Am. Ceram. Soc. **57**, 405–407.

Pertlik, F. (1975). Verfeinerung der Kristallstruktur von synthetischem Trippkeit, $CuAs_2O_4$. Tschermaks Mineral. Petrogr. Mitt. **22**, 211–217.

Pertlik, F. (1989). The crystal structure of čechite, $Pb(Fe^{2+}, Mn^{2+})(VO_4)(OH)$ with Fe > Mn. A mineral of the descloizite group. N. Jb. Mineral. Mh. 1989, 34–40.

Pilati, T., Demartin, F. and Gramaccioli, C. M. (1997). Transferability of empirical force fields in silicates: Lattice-dynamical evaluation of atomic displacement parameters and thermodynamic properties for the Al_2OSiO_4 polymorphs. Acta Cryst. B**53**, 82–94.

Piriou, B., Rager, H. and Schneider, H. (1996). Time resolved fluorescence spectroscopy of Cr^{3+}in mullite. J. Europ. Ceram. Soc. **16**, 195–201.

Pouxviel, J. C. and Boilot, J. P. (1989). Gels from a double alkoxide $(BuO)_2$-Al-O-Si-$(OEt)_3$, J. Mater. Sci. **24**, 321–327.

Pouxviel, J. C., Boilot, J. P., Lecomte, A. and Dauger, A. (1987). Growth process and structure of aluminosilicate gels. J. Phys. **48**, 921–925.

Puebla, E.G., Rios, E.G., Monge, A. and Rasines, I. (1982). Crystal growth and structure of diantimony(III) zinc oxide. Acta Cryst. B**38**, 2020–2022.

Qurashi, M.M. and Barnes, W.H. (1963). The structures of the minerals of the descloizite and adelite group. IV: Descloizite and conichalcite (part 2). The structure of conichalcite. Canad. Min. **7**, 561–577

Rager, H., Schneider, H. and Graetsch, H. (1990). Chromium incorporation in mullite. Amer. Min. **75**, 392–397.

Rager, H., Schneider, H. and Bakhshandeh, A. (1993). Ti^{3+} centres in mullite. J. Europ. Min. Soc. **5**, 511–514.

Rahman, S.H. (1991). Die videographische Methode: Ein neues Verfahren zur Simulation und Rekonstruktion fehlgeordneter Kristallstrukturen. Habilitation Thesis Univ. Hannover.

Rahman, S.H. (1992). Real structure image reconstruction from the random phase random amplitude model. X^th^ European Congress on Electron Microscopy Granada Spain. Vol. I. 453–454.

Rahman, S.H. (1993a). The videographic method: A new procedure for the simulation and reconstruction of real structures. Acta Cryst. A**49**, 56–68.

Rahman, S.H. (1993b). Interpretation of mullite HREM images using the potential-exchange method. Z. Krist. **203**, 67–72.

Rahman, S.H. (1994a). The real crystal structure of mullite. In: H.Schneider, K.Okada and J.A.Pask. Mullite and Mullite Ceramics. Wiley and Sons, Chichester, 4–31.

Rahman, S.H. (1994b). Videographic reconstructions and simulation of the real Cu_3Au structure at various temperatures. Z. Krist. **209**, 315–321.

Rahman, S.H. and Rodewald, M. (1992). HRTEM-Kontrastsimulation von Defektstrukturen nach dem Multi-slice Verfahren. Optik Suppl. 4, Vol. 88, 17.

Rahman, S.H. and Rodewald, M. (1995). Simulation of short range order in FCC-alloys. Acta Cryst. **A51**, 153–158.

Rahman, S. H. and Weichert, H.-T. (1990). Interpretation of HREM images of mullite. Acta Cryst. **B46**, 139–149.

Rahman, S. H., Strothenk, S., Paulmann, C. and Feustel, U. (1996). Interpretation of mullite real structure via inter-vacancy correlation vectors. J. Europ. Ceram. Soc. **16**, 177–186.

Rahman, S., Feustel, U. and Freimann, S. (2001). Structure description of the thermic phase transformation sillimanite-mullite. J. Europ. Ceram. Soc. 21, 2471–2478.

Razumovskii, S.N., Tunik, T.A., Fisher, O.N. and Schmitt-Fogelevich, S.P. (1977). X-ray analysis of solid solutions of ferric oxide in mullite. Ogneupory **18**, 46–48.

Rehak, P., Kunath-Fandrei, G., Losso, P., Hildmann, B., Schneider H. and Jäger, C. (1998). Study of the Al coordination in mullites with varying Al:Si ratio by ^{27}Al NMR spectroscopy and X-ray diffraction. Amer. Min. **83**, 1266–1276.

Risbud, S. H. and Pask, J. A. (1977). Calculated thermodynamic data and metastable immiscibility in the system SiO_2–Al_2O_3. J. Am. Ceram. Soc. **60**, 419–424.

Risbud, S. H., Kirkpatrick, R. J., Taglialavore, A. P. and Montez, B. (1987) Solid state NMR evidence of 4-, 5-, and 6-fold aluminium sites in roller-quenched SiO_2-Al_2O_3 glasses. J. Am. Ceram. Soc. **70**, C10–C12.

Rodriguez-Navarro, C., Cultrone, G., Sanchez-Navas, A. and Sebastian, E. (2003). TEM study of mullite growth after muscovite breakdown. Amer. Min. **88**, 713–724.

Ronchetti, S., Piana, M., Delmastro, A., Salis, M. and Mazza, D. (2001). Synthesis and characterization of Fe and P substituted 3:2 mullite. J. Europ. Ceram. Soc. **21**, 2509–2514.

Rossman, G.R., Grew., E.S. and Dollase, W.A. (1982). The colors of sillimanite. Amer. Min. **67**, 749–761.

Rossouw, C.J. and Miller, P.R. (1999). Location of interstitial Cr in mullite by incoherent channeling patterns from characteristic X-ray emission. Amer. Min. **84**, 965–969.

Rubie, D.C. and Brearley, A.J. (1987). Metastable melting during the breakdown muscovite + quartz at 1 kbar. Bull. Mineral. **110**, 533–549.

Rymon-Lipinski, T., Hennicke, H.W. and Lingenberg, W. (1985). Zersetzung von $9Al_2O_3 \cdot 2B_2O_3$ bei hohen Temperaturen. Keram. Z. **37**, 450–453.

Saalfeld, H. (1962). A modification of Al_2O_3 with sillimanite structure. Trans. VIIIth Int. Ceramic Congress Copenhagen, pp 71–74.

Saalfeld, H. (1979). The domain structure of 2:1-mullite (2 Al_2O_3 $1SiO_2$). N. Jb. Miner. Abh. **134**, 305–316.

Saalfeld, H. and Gerlach, H. (1991). Solid solution and optical properties of (Al, Ge)-mullites. Z. Krist. **195**, 65–73.

Saalfeld, H. and Guse, W. (1981). Structure refinement of 3:2-mullite (3 $Al_2O_3 \cdot 2Si0_2$). N. Jb. Min. Mh. 1981, 145–150.

Saalfeld, H. and Klaska, K.H. (1985). A Pb/Nd-stabilized mullite of the composition $Al_{5.03}Ge_{0.97}Pb_{0.15}Nd_{0.06}O_{9.71}$. Z. Krist. **172**, 129–133.

Sacks, M. D., Bozkurt, N. and Scheiffele, G.W. (1991). Fabriction of mullite and mullite matrix composites by transient viscous sintering of composite powders. J. Am. Ceram. Soc. **74**, 2828–2837.

Sacks, M.D., Wang, K., Scheiffele, G.W. and Bozkurt, N. (1996). Activation energy for mullitization of α-alumina/silica microcomposite particles. J. Am. Ceram. Soc. **79**, 571–573.

Sadanaga, R., Tokonami, M. and Takéuchi, Y. (1962). The structure of mullite, $2Al_2O_3 \cdot SiO_2$, and relationship with the structures of sillimanite and andalusite. Acta Cryst. **15**, 65–68.

Schmücker, M. and Schneider, H. (1996). A new approach on the coordination of Al in non-crystalline gels and glasses of the system SiO_2–Al_2O_3, Ber. Bunsenges. Phys. Chem. **100**, 1550–1555.

Schmücker, M. and Schneider, H. (1999). Structural development of single phase mullite gels. J. Sol-Gel Sci. Tech. **15**, 191–199.

Schmücker, M. and Schneider, H. (2002). New evidence for tetrahedral triclusters in alumino silicate glasses, J. Non-Cryst. Solids **311**, 211–215.

Schmücker, M., Albers, W. and Schneider, H. (1994). Mullite formation by reaction sintering of quartz and α-alumina – a TEM study. J. Europ. Ceram. Soc.**14**, 511–515.

Schmücker M., Schneider, H., Poorteman, M., Cambier, F. and Meinhold, R. (1995). Formation of Al_2O_3-rich glasses in the system SiO_2–AI_2O_3. J. Europ. Ceram Soc.**15**, 1201–1205.

Schmücker, M., Mackenzie, K.J.D., Schneider, H., and Meinhold, R. (1997). NMR-studies on rapidly solidified SiO_2–Al_2O_3 -and SiO_2–Al_2O_3–Na_2O glasses. J. Non-Cryst. Solids **217**, 99–105.

Schmücker, M., Schneider, H., Mackenzie, K.J.D. (1998). Mechanical amorphization of mullite and recrystallization. J. Non-Cryst. Solids **226**, 99–103.

Schmücker, M., Schneider, H., Mackenzie, K.J.D. and Okuno, M. (1999). Comparative Al NMR and LAXS studies on rapidly quenched aluminosilicate glasses J. Europ. Ceram. Soc, **19**, 99–103.

Schmücker, M., Hoffbauer, W. and Schneider H. (2001). Constitution and crystallization behaviour of ultrathin physical vapor deposited (PVD) Al_2O_3/SiO_2 laminates. J. Europ. Ceram. Soc. **21**, 2503–2507.

Schmücker, M., Hildmann, B. and Schneider, H. (2002). The mechanisms of 2/1- to 3/2-mullite transformation. Amer. Min. **87**, 1190–1193.

Schmücker., M., MacKenzie, K.J.D., Smith, M.E., Carroll, D.E. and Schneider, H.(2005). AlO_4/SiO_4 distribution in tetrahedral double chains of mullite. J. Am. Ceram. Soc., in press.

Schneider, H. (1981). Infrared spectroscopic investigations on andalusite- and mullite-type structures in the systems Al_2GeO_5–Fe_2GeO_5 and Al_2GeO_5–Ga_2GeO_5. N. Jb. Min. Abh. **142**, 111–123.

Schneider, H. (1984). Solid solubility of Na_2O in mullite. J. Am. Ceram. Soc. **67**, C-130–C-131.

Schneider, H. (1985). Magnesium incorporation in mullite. N. Jb. Min. Mh., 491–496.

Schneider, H. (1986a).Formation, properties and high-temperature behaviour of mullite. Habilitation Thesis Univ. Münster.

Schneider, H. (1986b). Zirconium incorporation in mullite. N. Jb. Min. Mh. **4**, 172–180.

Schneider, H. (1987a). Temperature-dependent iron solubility in mullite. J. Am. Ceram. Soc. **70**, C43–C45.

Schneider, H. (1987b). Solubility of TiO_2, Fe_2O_3 and MgO in mullite. Ceramics Intern. **13**, 77–82.

Schneider, H. (1989). Iron exchange processes between mullite and coexisting silicate melts at high temperature. Glastechn. Ber. **62**, 193–198.

Schneider, H. (1990). Transition metal distribution in mullite. Ceramic Trans. **6**, 135–158.

Schneider, H. and Eberhard, E. (1990). Thermal expansion of mullite. J. Am. Ceram. Soc. **73**, 2073–2076.

Schneider, H. and Rager, H. (1984) Occurrence of Ti^{3+} and Fe^{2+} in mullite. J. Am. Ceram. Soc. **67**, C248–C250.

Schneider, H. and Rager, H. (1986) Iron incorporation in mullite. Ceramics Intern. **12**, 117–125.

Schneider, H. and Rymon-Lipinski, T. (1988). Occurrence of pseudotetragonal mullite. J. Am. Ceram. Soc. **71**, C162–C164.

Schneider, H. and Vasudevan, R. (1989) Structural deformation of manganese substituted mullites: X-ray line broadening and lattice parameter studies. N. Jb. Min. Mh., 165–178.

Schneider, H. and Werner, H. D. (1981). Synthesis and crystal chemistry of andalusite-, kyanite-, and mullite-type structures in the system Al_2GeO_5–Fe_2GeO_5. N. Jb. Min. Abh. **140**, 153–164.

Schneider, H. and Werner, H. D. (1982). Synthesis and crystal chemistry of andalusite- and mullite-type structures in the system Al_2GeO_5–Ga_2GeO_5. N. Jb. Min. Abh. **143**, 223–230.

Schneider, H. and Wohlleben, K. (1981). Microchemical composition and cell dimensions of mullites from refractory-grade South American bauxites. Ceramics Intern. **7**, 130–136.

Schneider, H., Merwin, L., Sebald, A. (1992). Mullite formation from non-crystalline solids. J. Mater. Sci. **27**, 805–812.

Schneider, H., Fischer, R.X. and Voll, D. (1993a). Mullite with lattice constants $a > b$. J. Am. Ceram. Soc. **76**, 1879–1881.

Schneider, H., Schmücker, M., Ikeda, K., and Kaysser, W.A. (1993b). Optically translucent mullite ceramics. J. Am. Ceram. Soc. **76**, 2912–2916.

Schneider, H., Saruhan, B., Voll, D., Merwin, L., and Sebald, A. (1993c). Mullite precursor phases. J. Europ. Ceram. Soc. **11**, 87–94.

Schneider, H., Okada, K, and Pask, J. A. (1994a) Mullite and Mullite Ceramics. John Wiley and Sons, Chichester.

Schneider, H., Voll, D., Saruhan, B., Sanz, J., Schrader, G., Rüscher, C. and Mosset, A. (1994b) Synthesis and structural characterization of non-crystalline mullite precursors, J. Non-Cryst. Solids **17**, 262–271.

Schneider, H., Voll, D., Saruhan, B., Schmücker, M., Schaller, T. and Sebald, A. (1994c). Constitution of the γ-alumina phase in chemically produced mullite precursors. J. Europ. Ceram. Soc. **13**, 441–448.

Schneider, J., Mastelaro, V. R., Panepucci, H. and Zanotto, E. D. (2000). ^{29}Si MAS-NMR studies of Q^n structural units in metasilicate glasses and their nucleating ability. J. Non-Cryst. Solids **273**, 8–18.

Scholze, H. (1956). Über Aluminiumborate. Z. Allg. Anorg. Chemie **284**, 272–277.

Schryvers, D., Srikrishna, K., O'Keefe, M.A. and Thomas, G. (1988). An electron microscopy study of the atomic structure of a mullite in a reaction-sintered composite. J. Mater. Res. **3**, 1355–1366.

Schwerdtfeger, G. and Muan, A. (1975) quoted in: Levin, E.M. and McMurdie, H.F.: Phase Diagrams for Ceramists. The American Ceramic Society, Supplement, p. 8, Fig. 4156.

Shannon, R.D. (1976). Revised effective ionic radii and systematic studies of interatomic distances in halides and chalcogenides. Acta Cryst. A**32**, 751–767.

Soro, N., Aldon, L., Olivier-Fourcade, J., Jumas, J.C., Laval, J.P. and Blanchart. P. (2003). Role of iron in mullite formation from kaolins by Mössbauer spectroscopy and Rietveld refinement. J. Am. Ceram. Soc. **86**, 129–134.

Stephenson, D.A. and Moore, P.B. (1968). The crystal structure of grandidierite, (Mg, Fe)Al_3SiBO_9. Acta Cryst. B**24**, 1518–1522.

Srikrishna, K., Thomas, G., Martinez, R., Corral, M. P., De Aza, S. and Moya, J. S. (1990). Kaolinite-mullite reaction series: A TEM study. J. Mater. Sci. **25**, 607–612.

Sundaresan, S. and Aksay, I. A. (1991). Mullitization of diphasic aluminosilicate gels. J. Am. Ceram. Soc. **74**, 2388–92.

Taake, C. (1999). Synthese und strukturelle Charakterisierung amorpher Festkörper im System SiO_2/Al_2O_3. Ph.D. Thesis, Univ. Hannover.

Takamori, T. and Roy, R. (1973). Rapid crystallization of SiO_2–Al_2O_3 glasses, J. Am. Ceram. Soc. **56**, 639–644.

Takei, T., Kameshima, Y., Yasumori, A. and Okada, K. (1999). Crystallization kinetics of mullite in alumina-silica fibers. J. Am. Ceram. Soc. **82**, 2876–2880.

Takei, T., Kameshima, Y., Yasumori, A. and Okada, K. (2000). Calculation of metastable immiscibility region in the Al_2O_3–SiO_2 system using molecular dynamics simulation. J. Mater. Res. **15**,186–193.

Takei, T., Kameshima, Y., Yasumori, A. and Okada, K. (2001). Crystallization kinetics of mulite from Al_2O_3–SiO_2 glasses under non-isothermal conditions. J. Europ. Ceram. Soc. **21**, 2487–2493.

Taylor, A. and Holland, D. (1993).The chemical synthesis and reaction sequence of mullite. J. Non-Cryst. Solids **152**, 1–7

Thom, M. (2000). Zusammensetzungsänderungen von Mullit-Mischkristallen. Diploma Thesis, Univ. Köln.

Thomas, H. H. (1922). On certain xenolithic tertiary minor inclusions in the island of Mull (Argyllshire). J. Geol. Soc. London **78**, 229–260.

Tkalcec, E., Nass, R., Schmauch, J., Schmidt, H., Kurajica, S., Bezjak, A. and Ivankovic, H. (1998). Crystallization kinetics of mullite from single phase gel determined by isothermal differential scanning calorimetry. J. Non-Cryst. Solids **223**, 57–72.

Tkalcec, E., Kurajica, S. and Ivankovic, H. (2001). Isothermal and non-isothermal crystallization kinetics of zinc-aluminosilicate glasses. Thermochim. Acta **378**, 135–144.

Tkalcec, E., Ivankovic, H., Nass, R. and Schmidt, H. (2003). Crystallization kinetics of mullite formation in diphasic gels containing different alumina components. J. Europ. Ceram. Soc. **23**, 1465–1475.

Toman, K. (1978). Ordering in olivenite – adamite solid solutions. Acta Cryst. B**34**, 715–721.

Tomsia, A. P., Saiz, E., Ishibashi, h., Diaz, M., Requena, J. and Moya, J.DS. (1998). Powder processing of mullite/Mo functionally graded materials. J. Europ. Ceram. Soc. **18**, 1365–1371.

Trömel, G., Obst, K.-H., Konopicky, K., Bauer, H. and Patzak, I. (1957). Untersuchungen im System SiO_2–Al_2O_3. Ber. Dtsch. Keram. Ges. **34**, 397–402.

Vernadsky, W. I. (1890).Cited in: Pask, J. A. (1990). Critical review of phase equilibria in the Al_2O_3 – SiO_2 system. Ceramic Trans. **6**, 1–13.

Voll, D. (1995). Mullitprecursoren. Synthese, temperaturabhängige Entwicklung der strukturellen Ordnung und Kristallisationsverhalten. Ph. D. Thesis, Univ. Hannover

Voll, D., Beran, A. and Schneider, H. (1998). Temperature-dependent dehydration of sol-gel-derived mullite precursors: A FTIR spectroscopy study. J. Europ. Ceram. Soc. **18**, 1101–1106.

Voll, D., Lengauer, C., Beran, A. and Schneider, H. (2001). Infrared band assignment and structural refinement of Al–Si, Al–Ge, and Ga–Ge mullites. J. Europ. Min. Soc. **13**, 591–604.

Voll, D., Beran, A. and Schneider, H. (2005). Local structure of Bi_2 (Al_4Fe_{4-x}) O_9 mixed crystals. Unpublished results.

Wada, H., Sakane, K., Kitamura, T., Sunai, M. and Sasaki, N. (1993). Thermal expansion of aluminium borate. Mater. Sci. Lett. **12**, 1735–1737.

Wada, H., Sakane, K., Kitamura, T. Kayahara, Y., Kawahara, A. and Sasaki, N. (1994). Thermal conductivity of aluminium borate. J. Ceram. Soc. Jp. **102**, 695–701.

Wang, K. and Sacks, M. (1996). Mullite formation by endothermic reaction of α-Al_2O_3/silica microcomposite particles. J. Am. Ceram. Soc. **79**, 12–16.

Wefers, K. and Misra, C. (1987). Oxides and hydroxides of aluminium. Alcoa Technical Paper No. 19, Rev., Alcoa Lab, Pittsburgh PA.

Wei, W.-Ch., and Halloran, J. W. (1988a). Phase transformation of diphasic aluminosilicate gels. J. Am. Ceram. Soc. **71**, 166–172.

Wei, W.-Ch. and Halloran, J. W. (1988b). Transformation kinetics of diphasic aluminosilicate gels, J. Am. Ceram. Soc. **71**, 581–587.

Wei, P. and Rongti, L. (1999). Crystallization kinetics of the aluminum silicate glass fiber. J. Mater. Sci. Eng. **A271**, 298–305.

Weiss, Z., Bailey, S. W. and Rieder, M. (1981). Refinement of the crystal structure of kanonaite, $(Mn^{3+}, Al)^{[6]}(Al,Mn^{3+})^{[5]}$ $O[SiO_4]$. Amer. Min. **66**, 561–567.

Wells, A. F. (1984) Structural Inorganic Chemistry. Clarendon Press, 5th Edition, Oxford.

Werding, G. and Schreyer, W. (1992). Synthesis and stability of werdingite, a new phase in the system MgO – Al_2O_3 – B_2O_3 – SiO_2 (MABS), and another new phase in the

ABS-system. J. Europ. Min. Soc. **4**, 193–207.

Wilhelmi, K.A. (1975) quoted in: Levin, E.M. and McMurdie, H.F. Phase Diagrams for Ceramists. The American Ceramic Society 1975 Supplement, p. 6, Fig. 4152.

Witzke, T., Steins, M., Doering, T. and Kolitsch, U. (2000). Gottlobite, CaMg(VO_4, AsO_4)(OH), a new mineral from Friedrichroda, Thuringia, Germany. N. Jb. Min. Mh., 444–454.

Worden, R.H., Champness, P.E. and Droop, G.T.R. (1987). Transmission electron microscopy of pyrometamorphic breakdown of phengite and chalorite. Min. Mag. **51**, 107–121.

Yamashita, T., Fujino, T., Masaki, N. and Tagawa, H. (1981). The crystal structures of alpha- and beta-$CdUO_4$. J. Solid State Chem. **37**, 133–139.

Yang, H., Hazen, R.M., Finger, L.W., Prewitt, C.T. and Downs, R.T. (1997). Compressibility and crystal structure of sillimanite, Al_2SiO_5, at high pressure. Phys. Chem. Minerals **25**, 39–47.

Ylä-Jääski, J. and Nissen, H.-U. (1983). Investigation of superstructure in mullite by high resolution electron microscopy and electron diffraction. Phys. Chem. Minerals **10**, 47–54.

Yoldas, B. E. (1990). Mullite formation from aluminium and silicon alkoxides. Ceramic Trans. **6**, 255–263.

Yue, R., Wang, Y., Chen, C. and Xu, C. (1998). Interface reaction of Ti and mullite ceramic substrate. Appl. Surf. Sci. **126**, 255–264.

Zha, S., Cheng, J., Liu, Y., Liu, X. and Meng, G. (2003). Electrical properties of pure and Sr-doped $Bi_2Al_4O_9$ ceramics. Solid State Ionics **156**, 197–200.